Novel Thermoresponsive Homopolymers and Amphiphilic Diblock Copolymers

Neuartige thermoresponsive Homopolymere und

amphiphile Diblockcopolymere

Dissertation of

Chia-Hsin Ko

Technische Universität München

Physik-Department

Fachgebiet Physik weicher Materie

Supervised by

Prof. Christine M. Papadakis, Ph.D.

TECHNISCHE UNIVERSITÄT MÜNCHEN

Physik-Department

Fachgebiet Physik weicher Materie

Novel Thermoresponsive Homopolymers and Amphiphilic Diblock Copolymers

Chia-Hsin Ko

Vollständiger Abdruck der von der Fakultät für Physik der Technischen Universität München zur Erlangung des akademischen Grades eines

Doktors der Naturwissenschaften (Dr. rer. nat.)

genehmigten Dissertation.

Vorsitzende:	Prof. Dr. Karen Alim
Prüfer der Dissertation:	1. Prof. Christine M. Papadakis, Ph.D.
	2. Prof. Dr. Friedrich Simmel

Die Dissertation wurde am 31.05.2021 bei der Technischen Universität München eingereicht und durch die Fakultät für Physik am 19.07.2021 angenommen.

Preface

The research presented in this thesis was performed under the supervision of Prof. Christine M. Papadakis in the Soft Matter Physics Group, Physics Department, Technical University of Munich, Germany.

The research was carried out in close collaboration with Prof. Dr. André Laschewsky, Institute of Chemistry, University of Potsdam, Germany, and Prof. Dr. Peter Müller-Buschbaum, Chair of Functional Materials, Physics Department, Technical University of Munich, Germany. The polymer synthesis and preliminary molecular characterization was conducted by Dr. Dirk Schanzenbach and Cristiane Henschel, Institute of Chemistry, University of Potsdam, Germany.

The Raman spectroscopy and optical microscopy investigations were performed in the lab of Prof. Dr. Alfons Schulte, Department of Physics and College of Optics and Photonics, University of Central Florida, U.S.A.

The small-angle neutron scattering (SANS) studies were carried out with the support of instrument scientists Dr. Henrich Frielinghaus and Dr. Lester C. Barnsley at the instrument KWS-1 at the Heinz Maier-Leibnitz Zentrum (MLZ) in Garching, Germany.

The very small-angle neutron scattering experiments were conducted with the support of instrument scientists Dr. Vitaliy Pipich and Dr. Baohu Wu at the instrument KWS-3 at the Heinz Maier-Leibnitz Zentrum (MLZ) in Garching, Germany.

The small-angle X-ray scattering (SAXS) experiments were performed in cooperation with instrument scientists Dr. Martin A. Schroer, Dr. Dmitry Molodenskiy and Dr. Stefano Da Vela at the high brilliance synchrotron beamline P12 at the European Molecular Biology Laboratory (EMBL) at DESY, Hamburg, Germany.

Abstract

Novel thermoresponsive homopolymers and amphiphilic diblock copolymers show intriguing switching behavior. The present thesis investigates the temperature-dependent phase behavior and structural transition of poly(*N*-isopropylmethacrylamide) (PNIPMAM) in aqueous solution. The influence of the additional methyl group in PNIPMAM on the phase transition behavior is examined by comparison with poly(*N*-isopropylacrylamide) (PNIPAM). The self-assembly behavior of poly(methylmethacrylate)-*b*-poly(*N*-isopropylacrylamide) diblock copolymers is studied in aqueous solution and in mixtures of water and methanol. By means of scattering methods, the self-assembled micelles are investigated in dependence on temperature and solvent composition. The influence of the co-nonsolvency effect on the morphological transition of the micelles is determined as well.

Zusammenfassung

Neuartige thermoresponsive Homopolymere und amphiphile Diblockcopolymere zeigen ein faszinierendes Schaltverhalten. In dieser Arbeit wird das temperaturabhängige Phasenverhalten und der strukturelle Übergang von Poly (*N*-isopropylmethacrylamid) (PNIPMAM) in wässriger Lösung untersucht. Der Einfluss der zusätzlichen Methylgruppe von PNIPMAM auf das Phasenübergangsverhalten wird durch Vergleich mit Poly(*N*-isopropylacrylamid) (PNIPAM) bestimmt. Die Selbstassemblierung von Poly(methylmethacrylat)-*b*-poly(*N*-isopropylacrylamid) Diblockcopolymeren wird in wässrigen Lösungen sowie in Mischungen aus Wasser und Methanol untersucht. Mit Streumethoden werden die selbstassemblierten Mizellen in Abhängigkeit von der Temperatur und der Lösungsmittelzusammensetzung untersucht. Der Einfluss des Co-nonsolvency-Effekts auf den morphologischen Übergang der Mizellen wird ebenfalls bestimmt.

List of abbreviations

ATRP	atom transfer radical polymerization
CMC	critical micelle concentration
CMT	critical micelle temperature
CTA	chain transfer agent
DLS	dynamic light scattering
DP	degree of polymerization
DSC	differential scanning calorimetry
FRP	free radical polymerization
FTIR	Fourier transform infrared spectroscopy
IR	infrared
LCST	lower critical solution temperature
NIR	near-infrared
NMR	nuclear magnetic resonance
OM	optical microscopy
OZ	Ornstein-Zernike
PMMA	poly(methyl methacrylate)
PNIPAM	poly(*N*-isopropylacrylamide)
PNIPMAM	poly(*N*-isopropylmethacrylamide)
PS	polystyrene
RAFT	reversible addition fragmentation chain transfer polymerization
REPES	regularized positive exponential sum method
SANS	small-angle neutron scattering
SAXS	small-angle X-ray scattering
SDD	sample-to-detector distance
SEC	size-exclusion chromatography
SLD	scattering length density
TGA	thermogravimetric analysis
UCST	upper critical solution temperature
UV-vis	ultraviolet-visible spectroscopy
VSANS	very small-angle neutron scattering
VSAXS	very small-angle X-ray scattering

Contents

1. Introduction

The physical properties of thermoresponsive polymers are sensitive to, and adjustable by, changes of the temperature [1]. As a result, they have attracted enormous attention in recent decades for a wide range of applications, including drug delivery systems [2-5], sensors [6, 7], catalysis [8, 9], substance separation [10], filtration [11], reactors [12], and tissue engineering [13]. However, to maximize the performance of such applications, it is essential that the physical behaviors of thermoresponsive polymers, and particularly their morphological transitions, are properly understood.

Among the many thermoresponsive polymers available nowadays, poly(*N*-isopropylacrylamide) (PNIPAM) is the most extensively investigated [14, 15]. PNIPAM in aqueous solution has a lower critical solution temperature (LCST) of ~32 °C, which is essentially independent of the molar mass and concentration. The LCST behavior of PNIPAM depends on a delicate balance between the hydrophilic and hydrophobic interactions [16, 17]. Below the LCST, PNIPAM is soluble in aqueous solution, and the water molecules tend to form hydrogen bonds with the hydrophilic amide groups of PNIPAM and form a hydration shell around the hydrophobic isopropyl groups [18-21]. As a result, the polymer chains are stabilized and hydrated, and their chain conformation has the form of expanded coils. Above the LCST, however, the hydrogen bonds between the water molecules and amide groups are weakened, while the intra- and intermolecular hydrogen bonds and the hydrophobic interactions dominate. Thus, the polymer chains strongly dehydrate and collapse; resulting in a globular conformation and the formation of mesoglobules [15, 22-25]. The phase transition of PNIPAM is rapid and reversible, and is compatible with many applications, which demand an abrupt change in physical properties at the transition temperature. Furthermore, the LCST of PNIPAM is easily tuned by the addition of surfactants [26], salts [27], or by copolymerization with hydrophobic/hydrophilic comonomers or end-group modification [28, 29]. In general, increasing the hydrophilic nature of polymer materials results in a higher transition temperature since the overall ability of the material to form hydrogen bonds is enhanced. By contrast, incorporating hydrophobic groups leads to a lower transition temperature. Furthermore, the presence of hydrophobic groups tends to disrupt the water structure around the polymer, which improves the interactions between the hydrophobic groups and further facilitates aggregation [30].

Poly(*N*-isopropylmethacrylamide) (PNIPMAM) is another LCST-type thermoresponsive polymer. It has a similar chemical structure as PNIPAM, but has the additional methyl groups on its backbone. Compared to PNIPAM, the molecular origin of PNIPMAM gives rise to a counterintuitive increase of the transition temperature to approximately 43 °C [31-36]. The exact reason for this higher transition temperature is still under discussion. However, it seems to be associated with the steric hindrance effect originating from the additional methyl groups, which changes both the chain conformation and the hydration behavior [37, 38]. Moreover, the intermolecular and intramolecular interactions among the amide groups of PNIPMAM are weaker than the ones of PNIPAM [39, 40];

possibly due to the presence of the additional methyl groups. As a result, even small changes in the molecular structure can significantly alter the phase behavior around the transition temperature. Even though aqueous PNIPMAM solutions have been studied intensively by turbidimetry [32-36], differential scanning calorimetry (DSC) [36, 38, 41], Fourier transform infrared spectroscopy (FTIR) [39, 42, 43], nuclear magnetic resonance (NMR) [43], Raman spectroscopy [39], and light scattering [37], the understanding of the phase transition behavior of PNIPMAM is still limited compared to that of PNIPAM. Furthermore, in most previous studies, only a few characterization methods have been used, and only single samples investigated. Therefore, the first part of the present thesis reports a systematic study of the phase behavior of PNIPMAM. Various instrumental techniques, including turbidimetry, optical microscopy (OM), differential scanning calorimetry (DSC), Raman spectroscopy, small-angle neutron scattering (SANS) and very small-angle neutron scattering (VSANS), are applied to examine the phase transition behavior of PNIPMAM. The results provide a comprehensive picture of the structural changes which take place around the phase transition point of PNIPMAM, and yield an important understanding of the effects of the additional methyl groups in PNIPMAM on the phase behavior, thermal behavior, hydration behavior, and the structural changes at phase transition compared to those of PNIPAM.

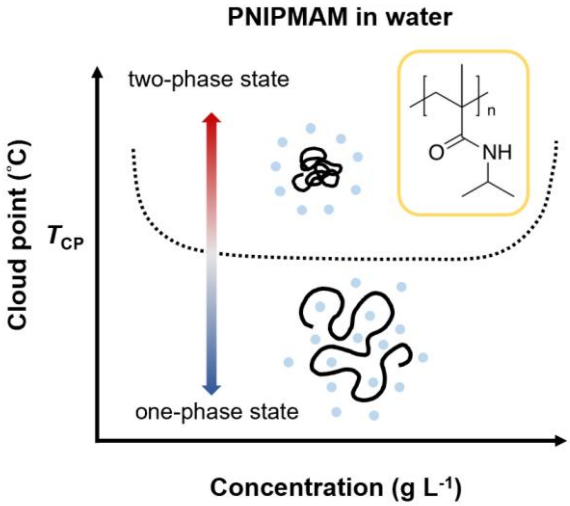

Figure 1.1 Schematic representation of experiments on PNIPMAM homopolymers aimed to investigating temperature-dependent phase behavior of thermoresponsive polymer PNIPMAM in aqueous solutions.

As mentioned above, PNIPAM is often selected for copolymerization with both hydrophobic and hydrophilic blocks. Furthermore, to create more complex and versatile systems, PNIPAM is also frequently chosen for copolymerization with stimuli-responsive polymer blocks [44-47]. Thermoresponsive amphiphilic diblock copolymers are one such class of materials, and consist of both a hydrophobic block and a hydrophilic block, where at least one of these blocks is sensitive to temperature. Due to their amphiphilicity below the phase transition temperature of PNIPAM, they are

able to self-assemble into core-shell micelles in aqueous solution. Furthermore, the morphology of these micelles can be readily adjusted by varying the temperature. As a result, PNIPAM-based block copolymers are promising candidates for a wide range of applications [44, 48, 49]; especially those associated with biomedical applications, such as drug encapsulation and release [50, 51].

Accordingly, the second part of this thesis addresses a novel thermoresponsive amphiphilic diblock copolymer, namely poly(methylmethacrylate)-*b*-poly(*N*-isopropylacrylamide) (PMMA-*b*-PNIPAM). PMMA-*b*-PNIPAM copolymers form core-shell micelles in aqueous solution. The micellar shell collapses at the transition temperature of the PNIPAM block (32 °C) and the aggregates are formed by collapsed micelles, which can potentially be exploited for applications such as drug delivery, microfluidic sensors, and tissue engineering. However, to realize such practical applications, the inner structure and thermal behavior of the micelles must be properly understood. The PNIPAM blocks in the PMMA-*b*-PNIPAM copolymers are sensitive not only to the temperature, but also to the solvent composition in the aqueous solution. For example, adding methanol as a cosolvent causes the PNIPAM blocks to collapse; thereby reducing the transition temperature. In other words, co-nonsolvency is observed. By contrast, the PMMA blocks feature a co-solvency effect in water-methanol mixtures, i.e., the hydrophobicity of the block decreases in the presence of methanol. Thus, the main goal of the second part of this thesis is to elucidate (i) the structure of the self-assembled micelles and their changes upon collapse and aggregation with increasing temperature; and (ii) the co-nonsolvency and co-solvency effects of PMMA-*b*-PNIPAM in pure D_2O and different D_2O/CD_3OD mixtures using turbidimetry, DSC, dynamic light scattering (DLS), and small-angle X-ray scattering (SAXS).

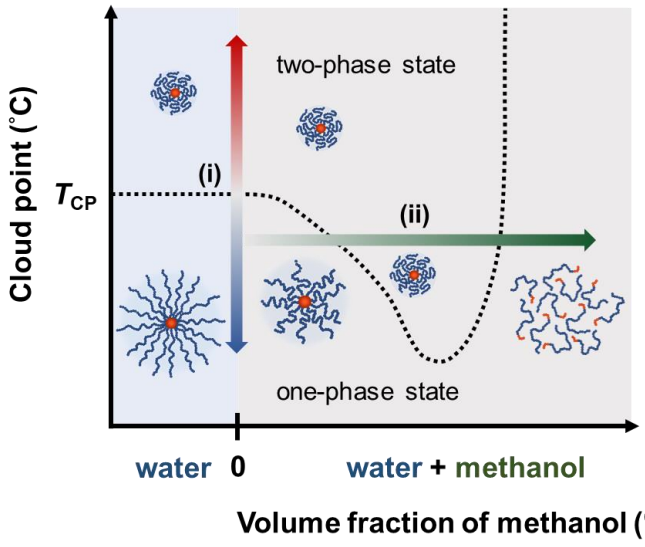

Figure 1.2 Schematic representation of experiments on PMMA-*b*-PNIPAM amphiphilic diblock copolymers aimed at investigating: (i) temperature-dependent structural transition of self-assembled micelles in pure water, and (ii) morphology changes in dependence on solvent composition in water/methanol mixtures at fixed temperature.

2. Background

To facilitate the later discussions in this thesis on the phase transition behavior of thermoresponsive homopolymers and the self-assembly of thermoresponsive amphiphilic diblock copolymers in solution, this chapter introduces the fundamental concepts of polymers in solutions, thermoresponsive polymers, and the self-assembly of amphiphilic diblock copolymers.

2.1 Polymers in solutions

When a polymer chain is fully stretched, it has a maximum end-to-end distance of R_{max}. This distance is referred to as the contour length, L, and is defined as [52]:

$$L = n\, l \cos\frac{\theta_b}{2} \tag{2.1}$$

where n is the number of C-C bonds, l is the C-C bond length (l = 0.154 nm), and θ_b is the bond angle (θ_b =109.5°).

When polymers are dissolved in solvent, the conformation of the polymer chain is not fully stretched, and the chains behave as random coils. For ideal chains, the mean-square end-to-end distance is given by (Figure 2.1) [52]:

$$R_{ee}{}^2 = C_\infty n l^2 \tag{2.2}$$

where C_∞ is the characteristic ratio.

For ideal chains, the end-to-end distance can be represented as (Figure 2.1) [52]:

$$R_{ee} = bN^{\frac{1}{2}} \tag{2.3}$$

where N is the number of Kuhn monomers, and b is the Kuhn length. Furthermore, the contour length L, can be obtained as $L = bN$.

For infinitely long polymer chains, the radius of gyration of the polymer chain is given as (Figure 2.1) [52]:

$$R_g = \frac{R_{ee}}{\sqrt{6}} \tag{2.4}$$

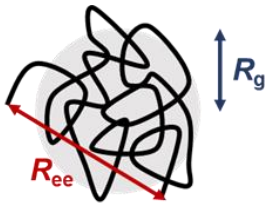

Figure 2.1 Schematic representation of polymer chain with end-to-end distance R_{ee} and radius of gyration R_g.

For real chains, interactions exist between the monomers in the chain. In a θ solvent, the polymer chain can be regarded as an ideal chain and the excluded volume effects are neglected, as described in eq. 2.3. In a good solvent, the polymer chain has a swollen chain conformation, as given by [52]:

$$R_{ee} \cong bN^{\frac{3}{5}} \tag{2.5}$$

By contrast, in a poor solvent, the polymer chain has a collapsed globular conformation [52]:

$$R_{ee} \cong bN^{\frac{1}{3}} \tag{2.6}$$

For the case of polymers dissolved in a good solvent, the polymer solutions can be classified into three different concentration regimes (Figure 2.2) [52]. In dilute solution ($c < c^*$), the polymer chains resemble coils, and are well-separated without interactions. The solvent viscosity thus dominates the properties of the solution. At the overlap concentration, c^*, the polymer chains approach one another and start to overlap. At higher concentrations ($c > c^*$), the chains become entangled. The resulting solutions are referred to as semi-dilute solutions, and exhibiting a strong viscoelastic behavior. Finally, in highly-concentrated solutions ($c >> c^*$), the polymer chains are strongly entangled, and the solution behavior is dominated by the elastic properties of the chains.

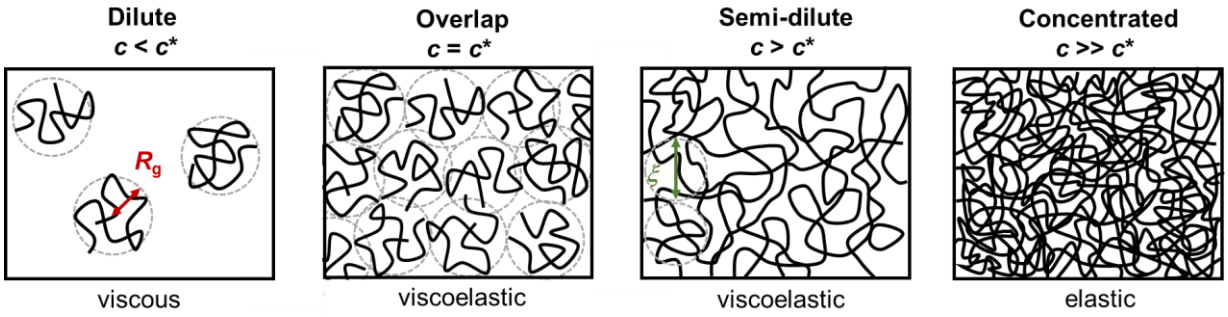

Figure 2.2 Concentration regimes of polymer solutions. From left to right: dilute solution, semi-dilute solution, and concentrated solution. Note that c^* indicates the overlap concentration.

For dilute polymer solutions, the polymer chains are separated from one another, and hence the

structure of solution is determined by the radius of gyration of the polymer chains. The overlap concentration can be estimated from the radius of gyration in accordance with [53]:

$$\frac{3M_{\mathrm{w}}}{4\pi N_{\mathrm{A}}(R_{\mathrm{g}})^3} < c^* < \frac{M_{\mathrm{w}}}{N_{\mathrm{A}}\left(\sqrt{2}R_{\mathrm{g}}\right)^3} \tag{2.7}$$

where M_{w} is the weight-average molar mass of the polymer chains and N_{A} is the Avogadro constant. In semi-dilute solutions, the polymer chains start to overlap, and the the structure of the solution is characterized by the distance between the overlap points, i.e., ξ (Figure 2.2), where ξ is referred to as the blob size of the polymer chains, or the correlation length of the concentration fluctuations, and the chain segments of the blobs are unperturbed without interactions with the chain segments of other blobs. Studies have shown that ξ varies with the solution concentration as $\xi \sim c^{-0.75}$ [54]. The spatial correlation between the monomers in the chains can be represented by the following Ornstein-Zernike pair correlation function:

$$g(r) = A_r \frac{\xi}{r} exp(-\frac{r}{\xi}) \tag{2.8}$$

where A_{r} is a constant [54].

In concentrated solutions, movement of the chain segments is restricted. Consequently, monomer-monomer interactions dominate, and the local chain conformation deviates from eq. 2.8 [54, 55].

Based on the principles of thermodynamics, the general phase behavior of polymer solutions can be described by the free energy of mixing. In Flory-Huggins theory, the free energy of mixing is written as

$$\Delta G_{\mathrm{m}} = \Delta H_{\mathrm{m}} - T\Delta S_{\mathrm{m}} \tag{2.9}$$

where ΔH_{m} is the enthalpy of mixing, ΔS_{m} is the entropy of mixing, and T is the temperature.

For a polymer solution, the free energy of mixing of the polymer-solvent mixture is given by

$$\Delta G_{\mathrm{m}} = k_{\mathrm{B}}T\left[\frac{\phi_{\mathrm{p}}}{N}\ln\phi_{\mathrm{p}} + \left(1-\phi_{\mathrm{p}}\right)\ln\left(1-\phi_{\mathrm{p}}\right) + \chi\,\phi_{\mathrm{p}}\left(1-\phi_{\mathrm{p}}\right)\right] \tag{2.10}$$

where k_{B} is the Boltzmann constant, N is the degree of polymerization of the polymer, ϕ_{p} is the volume fraction of polymer in the solution and χ is the interaction parameter between the polymer and the solvent.

It is noted that the first and second terms in eq. 2.10 originate from the entropy of mixing ΔS_{m}, which always has a positive value, and thus favors mixing. By contrast, the third term is associated with the enthalpy of mixing ΔH_{m}, which can either promote or prevent mixing, depending on the interaction parameter. In accordance with Flory-Huggins theory, χ is defined as

$$\chi = \frac{z}{k_{\mathrm{B}}T}\left[u_{\mathrm{AB}} - \frac{1}{2}\left(u_{\mathrm{AA}} + u_{\mathrm{BB}}\right)\right] \tag{2.11}$$

where u_{AB}, u_{AA}, and u_{BB} are pairwise interactions energies (A and B denote monomers and solvent molecules, respectively), and z is the coordination number.

For $\chi > 0$, the interactions between the monomers and solvent molecules are unfavorable and repulsive. However, for $\chi < 0$, the interactions are favorable and attractive, and hence the enthalpy of mixing governs the miscibility of the polymer solution. Empirically, χ can be expressed as the sum of the entropic contribution A and enthalpic contribution B/T. That is,

$$\chi = A + \frac{B}{T} \tag{2.12}$$

In general, the solubility of polymers depends on the solvent quality, which is strongly dependent in turn on the interaction between the polymer and the solvent. Thus, in the case of $\chi = 1/2$, the polymers are ideal chains, and the solvent is referred to as θ solvent. For $\chi < 1/2$, the polymer chains are swollen and behave like real chains, and the solvent is regarded as a good solvent. For $\chi > 1/2$, the polymer chains tend to collapse and the solvent is considered to be a poor solvent [55].

For a polymer solution, χ is related to the solubility parameters of the polymer and solvent as follows [56]:

$$\chi = \frac{V_{\mathrm{ref}}}{k_{\mathrm{B}}T}\left(\delta_{\mathrm{p}} - \delta_{\mathrm{s}}\right)^2 + \chi_{\mathrm{s}} \tag{2.13}$$

with V_{ref} is a reference volume, δ_{p} and δ_{s} are the solubility parameters of the polymer and solvent, respectively; and χ_{s} is a constant that estimates the entropic contribution to the interaction parameter. $\chi_{\mathrm{s}} = 0.34$ is often applied [56].

2.2 Thermoresponsive polymers

Thermoresponsive polymers undergo a sudden change in solubility and chain conformation at a certain temperature known as the transition temperature. This change is often referred to as a coil-to-globule transition (Figure 2.3) since at lower temperatures, the polymer chains are soluble and swollen like random coils, whereas at the transition temperature, they become insoluble and collapse into globules. The transition temperature is commonly called the cloud point, T_{CP}, and depends on the particular concentration of the polymer solution.

Generally speaking, thermoresponsive polymers can be classified into two types. For polymers with a lower critical solution temperature (LCST) behavior (Figure 2.3a), the coil-to-globule transition is triggered by an increasing temperature. Polymers with such an LCST behavior are soluble at low temperatures, but undergo phase transition upon heating to the LCST, i.e., the lowest temperature at which phase transition occurs. Conversely, for polymers with an upper critical solution temperature (UCST) behavior (Figure 2.3b), phase transition takes place with a decreasing temperature. Such polymers are insoluble at low temperatures, but become soluble upon heating to the UCST, i.e., the highest temperature at which phase transition occurs. UCST behavior is commonly observed for polymers in organic solvents, whereas LCST behavior is generally observed for polymers in aqueous solutions. For both LCST- and UCST-type polymers, the transition temperature (T_{c} or T_{CP}) usually

depends on the polymer concentration. In particular, the LCST or UCST generally shifts toward a lower polymer concentration with an increasing molar mass.

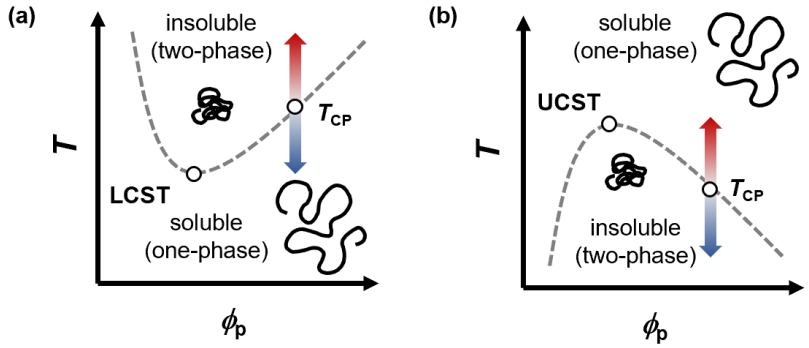

Figure 2.3 Temperature-concentration phase diagram of thermoresponsive polymers with: (a) LCST and (b) UCST behavior.

Thermodynamically, the phase transition behavior of a polymer solution depends on the free energy of mixing, ΔG_m, as shown in eq. 2.9. According to classical Flory-Huggins theory, the entropy of mixing always has a positive value (i.e., $\Delta S_m > 0$), and hence mixing is favored. As a result, the miscibility of the polymer solution is governed by the sign and magnitude of the enthalpy of mixing, ΔH_m. As shown in eq. 2.10, ΔH_m depends on the Flory-Huggins interaction parameter χ. In particular, ΔH_m is given by

$$\Delta H_m = k_B T \chi \phi_p (1 - \phi_p) \tag{2.14}$$

The empirical form of the Flory-Huggins interaction parameter χ is given in eq. 2.12. When $B > 0$, χ decreases with increasing T, leading to an UCST behavior. This causes a reduction of ΔH_m with an increasing temperature, and thus results in an overall smaller ΔG_m upon heating. Consequently, the miscibility is improved at high temperatures. Conversely, when $B < 0$, χ increases with increasing T; giving rise to an LCST behavior. However, this cannot allow an LCST or type-II behavior, i.e., T_{CP} is nearly independent of the polymer concentration at high molar mass due to the assumption of classical Flory-Huggins theory that ΔS_m is always positive. In addition, the free volume change after mixing, the free volume change after temperature change, and the entropy of the solvent molecules are all neglected in classical Flory-Huggins theory. Finally, the additional monomer-monomer and monomer-solvent interactions, e.g., the hydrogen bonds and hydrophobic interactions, are also ignored in Flory-Huggins theory. However, these interactions are crucial for polymers with an LCST behavior in aqueous solution.

The entropy of the water molecules in an aqueous solution also plays an important role in determining the free energy of mixing, ΔG_m. In particular, the water molecules tend to form an ordered hydration shell around the hydrophobic groups on the polymer chains, which decreases the entropy of the water molecules upon mixing. Therefore, for polymers with an LCST behavior, the free energy of

mixing, ΔG_m in eq. 2.9 can be rewritten as [57, 58]:

$$\Delta G_m = \Delta H_m - T\Delta S_m - T\Delta S_{water} \tag{2.15}$$

where ΔH_m is always negative due to the presence of hydrogen bonds between the polymer and water molecules, while ΔS_{water}, i.e., the entropy of the water molecules upon mixing, is always negative due to the formation of an ordered hydration shell. For polymers with an LCST behavior, the ΔH_m term dominates at low temperatures, and mixing of the polymer solution is favored. However, upon heating, the absolute value of ΔH_m reduces due to the increased thermal motion, which weakens the hydrogen bonds between the polymer and water molecules. By contrast, $T\Delta S_m$ and $T\Delta S_{water}$ both increases in magnitude; leading to an overall negative entropy value. Consequently, at temperatures higher than the LCST, the $T\Delta S_{water}$ term dominates, and demixing of the polymer solution is favored.

To consider all the additional contributions, including those of the hydrogen bonds and hydrophobic interactions, the empirical interaction parameter χ in eq. 2.12 can be replaced with $\chi_{\text{type-II}}(\phi_p, T)$ [15], i.e.,

$$\chi_{\text{type-II}}\left(\phi_p, T\right) = \sum_{i=0}^{2} B_i(T)\,\phi_p^i \tag{2.16}$$

$$B_i(T) = b_{i0} + \frac{b_{i1}}{T} + b_{i2}T + b_{i3}\ln T \tag{2.17}$$

where b_{ij} are constants. Notably, $\chi_{\text{type-II}}(\phi_p, T)$ is applicable to both polymers with an LCST behavior and those with a type-II behavior, where the latter class of polymers are defined as polymers for which the transition temperature (T_c or T_{CP}) is essentially independent of the molar mass and concentration.

2.3 Amphiphilic diblock copolymers in diluted solutions

Diblock copolymers are polymers consisting of two blocks that are chemically different. For example, amphiphilic diblock copolymers comprise a hydrophilic block and a hydrophobic block. For diblock copolymers, selective solvents are defined as solvents which are good solvents for one block, but poor solvents for the other. Thus, in the case of amphiphilic diblock copolymers, water serves as a good solvent.

In selective solvents at a fixed temperature, amphiphilic diblock copolymers are molecularly dissolved, and usually behave as unimers below the critical micelle concentration (CMC). When the concentration increases beyond the CMC, the fraction of unimers remains constant and the additional diblock copolymers self-assemble into micelles [59, 60], where the fraction of these micelles increases with increasing concentration. Figure 2.4 shows a schematic representation of a typical amphiphilic diblock copolymer. As shown, for concentrations less than the CMC, the amphiphilic diblock

copolymers are present as unimers, wherein the hydrophobic B blocks collapse and are screened by swollen hydrophilic A blocks in the selective solvent. However, for concentrations greater than the CMC, the unimers coexist in equilibrium with micelles consisting of a core formed by the hydrophobic blocks and a hydrated shell formed by the hydrophilic blocks.

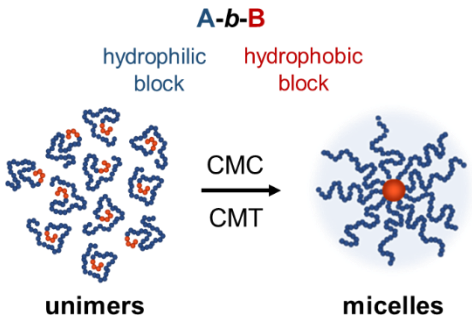

Figure 2.4 Schematic representation of unimers and spherical micelles formed by amphiphilic diblock copolymers in selective solvent below (left) and above (right) the critical micelle concentration (CMC) or critical micelle temperature (CMT).

The micellar morphology of amphiphilic diblock copolymers is determined by their structure (e.g., block lengths). However, external stimuli, such as the temperature and solvent quality, also play a crucial role in determining the micelle morphology. The driving force for micelle formation is the entropy gain of the water. By contrast, the driving force for the morphological transition of the micelles is the force required to minimize the overall free energy of the micelle [61-64], i.e.,

$$F_{\text{micelle}} = F_{\text{core}} + F_{\text{shell}} + F_{\text{interface}} \tag{2.18}$$

where F_{core} is the free energy of the micellar core, which is related to the deformation of the core-forming block; F_{shell} is the free energy of the micellar shell, which is associated with the deformation of the shell-forming block; and $F_{\text{interface}}$ is the free energy of the interface between the core and the shell, which depends on the surface area of the core and the interaction between the solvent and the core-forming block.

In general, the morphology of micelles, and their structural transition, can be qualitatively elucidated by the F_{core}, F_{shell}, and $F_{\text{interface}}$ terms. Generally speaking, F_{core} is small, and can often be neglected. For star-like micelles, i.e., micelles in which the shell thickness, t_{shell} is substantially larger than the core radius, R_{core} ($t_{\text{shell}}/ R_{\text{core}} >> 1$), both F_{shell} and $F_{\text{interface}}$ dominate. Conversely, for crew-cut micelles, i.e., micelles in which the shell thickness t_{shell} is significantly smaller than the core radius R_{core} ($t_{\text{shell}}/ R_{\text{core}} << 1$), the overall free energy is dominated by $F_{\text{interface}}$. Star-like micelles are generally

of spherical shape, whereas crew-cut micelles can be either spherical, cylindrical, or lamellar shape. In practice, the micellar shape can be predicted using the following packing parameter, P:

$$P = \frac{V_{\text{core}}}{sL_{\text{core}}} \tag{2.19}$$

where s is the surface area per chain at the interface between the core and the shell, V_{core} and L_{core} are the volume and contour length of the core-forming hydrophobic blocks, respectively. In the case of $P \leq 1/3$, the micelles are spherical. By contrast, for $1/3 < P < 1/2$, the micelles are cylindrical, while for $1/2 \leq P < 1$, the micelles are bilayers or vesicles. Finally, for $P > 1$, inverse micelles are formed [65, 66].

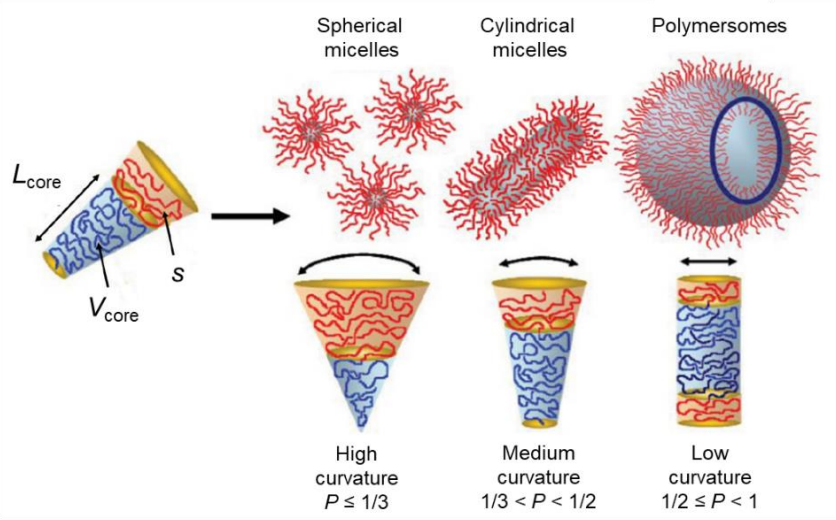

Figure 2.5 Schematic representation of possible shape of micelles formed by amphiphilic diblock copolymers in selective solvent for different values of packing parameter P. (Adapted with permission from Ref. [67]. Copyright (2009) WILEY-VCH Verlag GmbH & Co. KGaA, Weinheim.)

For amphiphilic diblock copolymers with a long hydrophilic block and short hydrophobic block that form star-like spherical micelles, i.e., $N_{\text{shell}} >> N_{\text{core}}$, the core radius R_{core} and shell thickness t_{shell} of the micelles can be estimated by the following power functions [62]:

$$R_{\text{core}} \sim N_{\text{core}}^{\frac{3}{5}} \tag{2.20}$$

$$t_{\text{shell}} \sim N_{\text{shell}}{}^{\nu} N_{\text{core}}^{\frac{2(1-\nu)}{5}} \tag{2.21}$$

where N_{core} and N_{shell} are the degree of polymerization of the core- and shell-forming blocks,

respectively. In addition, ν is the exponent, and has a value of $\nu = 3/5$ for a good solvent and $\nu = 1/2$ for a θ solvent.

The aggregation number, N_{agg}, i.e. the average number of polymer chains in a micelle, can be predicted as [64]

$$N_{\text{agg}} \cong N_{\text{core}}{}^{\frac{4}{5}} \left(\frac{s^2 \gamma_{\text{core-solvent}}}{k_{\text{B}} T} \right)^{\frac{6}{5}} \tag{2.22}$$

where $\gamma_{\text{core-solvent}}$ is the surface energy of the interface between the core-forming blocks and the solvent, and is proportional to the interaction parameter between the blocks and the solvent, i.e., $\chi_{\text{core-solvent.}}$ As a result, N_{agg} depends not only on the degree of polymerization of the core-forming hydrophobic blocks, but also on the strength of the interactions between the hydrophobic blocks and the solvent molecules.

The above-mentioned discussion holds for amphiphilic diblock copolymers that are in thermodynamically equilibrium, i.e., a continuous exchange of polymer chains take place between the micelles. However, in reality, the polymer chains within the micelles may exhibit a retarded mobility. In other words, the exchange dynamics of the micelles may be slow. The extent to which the dynamics are slowed depends on the glass transition temperature T_g of the core-forming hydrophobic blocks, which may lead to the formation of either equilibrium or non-equilibrium self-assembled micelles [68-70]. In particular, for core-forming hydrophobic blocks with a high T_g, micellar chain exchange is suppressed [59]. As a result, the micelles are kinetically frozen, and micellar chain exchange is impossible [71]. By contrast, amphiphilic diblock copolymers containing hydrophobic blocks with high T_g often form non-equilibrium micelles with a compact glassy core in aqueous solutions. Such amphiphilic diblock copolymers usually exhibit a very low CMC, or cannot be directly dissolved in aqueous solution at all.

2.4 Thermoresponsive amphiphilic diblock copolymers

Thermoresponsive amphiphilic diblock copolymers, consisting of a hydrophobic block and a hydrophilic block which is sensitive to temperature, can self-assemble into micelles in aqueous solution. Furthermore, the morphology of these self-assembled micelles can be adjusted by altering the temperature (Figure 2.6). Thermoresponsive amphiphilic diblock copolymers have thus drawn extensive attention for both fundamental research and practical applications [48, 72, 73]. One of the most well-known thermoresponsive polymers is poly(*N*-isopropylacrylamide) (PNIPAM) PNIPAM exhibits an LCST behavior at 32 °C in aqueous solution [15, 16], and is thus often chosen for copolymerization with both hydrophobic and hydrophilic blocks as well as stimuli-responsive polymer

blocks [44-46]. In addition to the temperature, the morphology of the self-assembled structures can also be generated, destroyed or altered by changing the solvent quality, i.e., tuning the solvent composition [74-76].

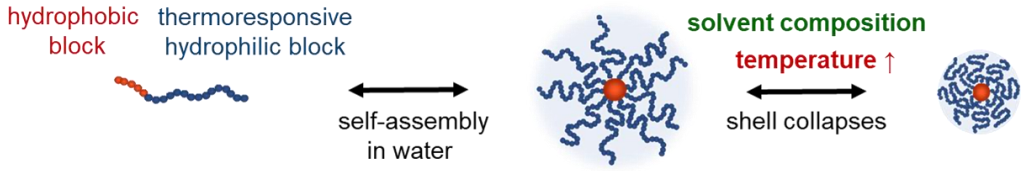

Figure 2.6 Schematic representation of morphological transition of micelles formed by thermoresponsive amphiphilic diblock copolymers in aqueous solution in response to changes in temperature or solvent composition.

Due to their unique responsive properties, thermoresponsive amphiphilic diblock copolymers are promising candidates for a wide variety of applications, including drug release or delivery systems [2-5], microsensors for bioanalysis or diagnosis [6, 7], tunable catalysis [8, 9], and substance separation/purification technologies [10]. Figure 2.7 illustrates their potential use in drug delivery system, wherein the thermoresponsive block of amphiphilic diblock copolymer may be designed in either the shell (see Figure 2.7A) or the core (see Figure 2.7B); thereby facilitating two different drug-release mechanisms.

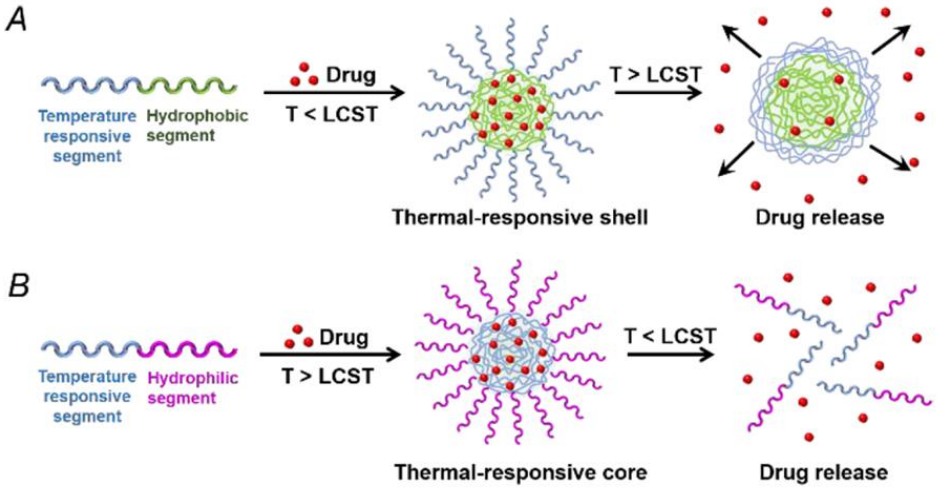

Figure 2.7 Schematic representation of micellar formation and trigger-release behavior of PNIPAM-based amphiphilic diblock copolymers with thermoresponsive block in shell (A) or core (B). (Reprinted with permission from Ref. [46]. Copyright (2020) American Chemical Society.)

3. Systems under investigation

This chapter provides an overview of the polymers under study in this thesis and their analogous polymers. The chapter commences by describing the phase behavior of thermoresponsive homopolymers in aqueous solutions. Previous studies on thermoresponsive amphiphilic diblock copolymers are then briefly discussed. Finally, the main goals of the thesis, and the details of the systems under investigation, are introduced and explained.

3.1 Poly(*N*-isopropylacrylamide)

Poly(*N*-isopropylacrylamide) (PNIPAM) is a widely investigated thermoresponsive polymer, which features an LCST of ~32 °C in aqueous solution [15, 16]. Figure 3.1a shows the chemical structure of PNIPAM. As shown, the vinyl backbone contains a side group consisting of a hydrophilic amide group and a hydrophobic isopropyl group. Heating across the LCST prompts an abrupt coil-to-globule transition (Figure 3.1b). This sharp collapse occurs for a wide range of molar masses and concentrations, and indicates that PNIPAM has a so-called type-II LCST behavior [14, 15]. Upon heating through the cloud point (T_{CP}), the chains dehydrate strongly and form mesoglobules [15, 22-25]. These mesoglobules contain only little water and are long-lived, which can be attributed (among other things) to the viscoelastic effect [77-79]. PNIPAM is able to form hydrogen bonds; both with water and with other PNIPAM repeat units [18-21]. The LCST behavior of PNIPAM has been attributed to a delicate balance between hydrogen bonding with water and hydrophobic hydration [16, 17].

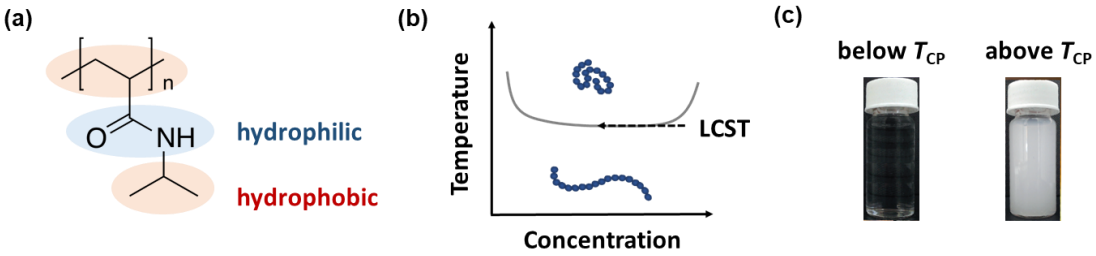

Figure 3.1 (a) Chemical structure of poly(*N*-isopropylacrylamide), PNIPAM. Note that hydrophobic groups are shown in red, while hydrophilic groups are shown in blue. (b) Schematic representation of phase diagram of a PNIPAM aqueous solution (c) Photos of PNIPAM aqueous solutions below (left) and above (right) T_{CP}, respectively. (Reprinted with permission from Ref. [15]. Copyright (2015) WILEY-VCH Verlag GmbH & Co. KGaA, Weinheim.)

At temperatures lower than the transition temperature, the hydrophilic groups tend to form hydrogen bonds with water molecules, and the hydrophobic groups are surrounded by an ordered hydration shell. Thus, PNIPAM is soluble in aqueous solutions, and its chain conformation is swollen. Furthermore, the solution has a transparent appearance, which indicates that it is in a one-phase state (Figure 3.1c). At temperatures higher than the transition temperature, a small portion (~ 13%) of the hydrogen bonds between the hydrophilic groups and the water molecules are broken and form intramolecular hydrogen bonds between the carbonyl and amide groups [42]. The remaining portion (~ 87%) of the hydrophilic groups remain hydrated and the hydration shells around the hydrophobic groups become disordered. As a result, PNIPAM becomes insoluble and transits to collapsed globules. In addition, the solution turns turbid; indicating the existence of a two-phase state (Figure 3.1c).

The LCST behavior of PNIPAM was explained theoretically by Tanaka et al. [80, 81], who showed that the coil-to-globule transition of PNIPAM in aqueous solution occurs abruptly at the transition temperature due to a process of cooperative hydration. In particular, if a hydrogen bond between an amide group and a water molecule is formed on the polymer chain, a neighboring space for hydrogen bonds is created. Since the formation of the first hydrogen bond leads to a displacement of the hydrophobic isopropyl groups, the neighboring space is more accessible for water molecules to form hydrogen bonds. Therefore, a second water molecule preferentially forms another hydrogen bond adjacent to the first hydrogen bond. In this way, a consecutive sequence of hydrogen bonds is formed along the length of the polymer chain. Between these sequences, the polymer chain is dehydrated and has a globule-like conformation, which results in a pearl-necklace chain conformation, as shown in Figure 3.2. At the cloud point, T_{CP}, the sequences of hydrogen bonds dehydrate entirely almost at once; giving rise to a sharp collapse of the polymer chain.

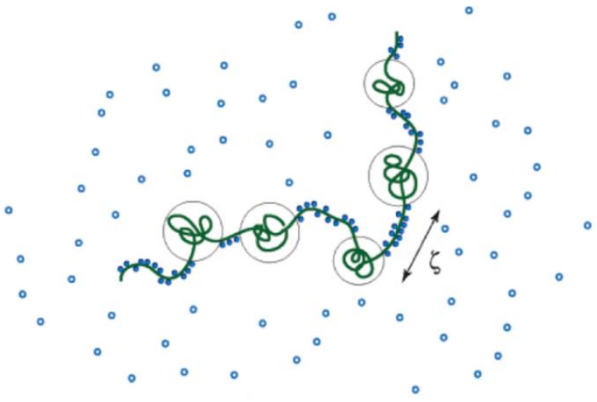

Figure 3.2 Schematic representation of pearl-necklace conformation of PNIPAM chain produced by formation of sequential hydrogen bonds under effects of cooperative hydration. (Reprinted with permission from Ref. [81]. Copyright (2005) American Chemical Society.)

Co-nonsolvency effect of PNIPAM

PNIPAM is sensitive to not only the temperature, but also to the solvent composition. The behavior of PNIPAM in binary mixtures of water and water-miscible cosolvent (e.g., methanol, ethanol, acetone, tetrahydrofuran and dimethylformamide) has been amply investigated [82-88]. Most studies have focused on the behavior of PNIPAM in water/methanol mixtures. Although PNIPAM is soluble in both pure water and pure methanol at room temperature, it becomes insoluble in a certain range of mixing ratios (Figure 3.3a) [83, 89]. In this miscibility gap, the PNIPAM chains collapse. However, they reswell when methanol becomes the majority component in the water/methanol mixture (Figure 3.3a). At room temperature, the PNIPAM chains undergo a reentrant coil-to-globule-to-coil transition with a miscibility gap spanning from ca. 25-65 vol% of methanol (Figure 3.3b) [90, 91]. This phenomenon is termed the co-nonsolvency effect. Moreover, the chain size of PNIPAM homopolymers gradually decreases with an increasing methanol content towards the phase transition point when water is the majority component in the water/methanol mixture [92].

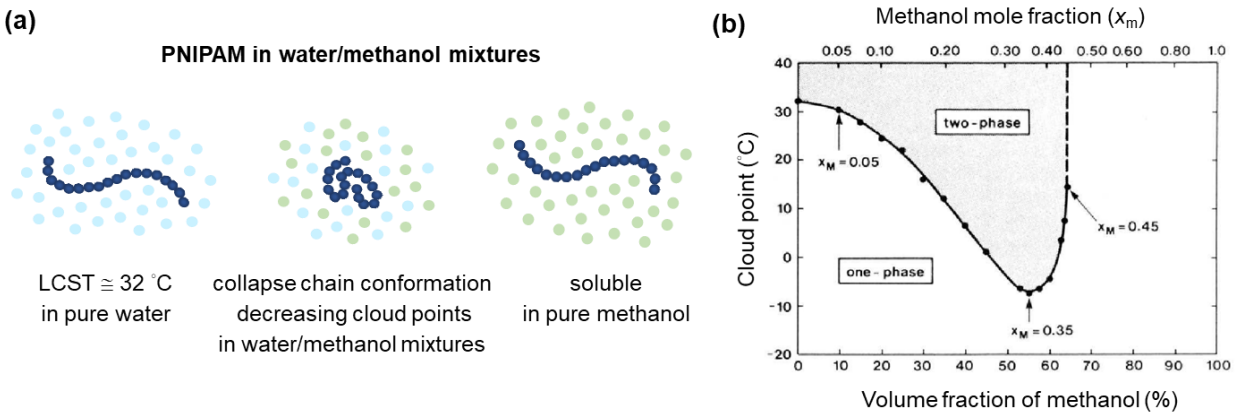

Figure 3.3 (a) Schematic representation of co-nonsolvency effect on the chain conformation of PNIPAM at 20 °C in water/methanol mixtures. (b) Cloud point of PNIPAM in water/methanol mixtures. (Reprinted with permission from Ref. [89]. Copyright (1990) American Chemical Society.)

The molecular origin of the co-nonsolvency effect of PNIPAM remain unclear. However, generally speaking, the theories and mechanisms which have been proposed for explaining the chain collapse which occurs upon adding the cosolvent can be divided into two main categories. One category is related to the structure or local concentration fluctuations of the solvent mixture. For instance, Zhang and Wu attributed the co-nonsolvency effect of PNIPAM to the formation of water/methanol complexes [90], while Mukherji and Kremer suggested that the reentrant collapse and swelling transition of PNIPAM is triggered by local concentration fluctuations of the water/methanol mixture [93]. The second category is based on polymer-solvent interactions and the preferential

adsorption of the cosolvent on the chains. For example, Tanaka et al. claimed that the cooperativity and competitive hydrogen bonding processes of water and methanol molecules with the PNIPAM chains lead to a dehydration of the chains in water/methanol mixtures [94, 95]. Mukherji et al. reported that preferential interactions of the cosolvent with the chain result in a bridging of the polymer chain and the formation of segmental loops [96]. Rodríguez-Ropero et al. suggested that the preferential binding of methanol to PNIPAM causes a significant increase in the configurational entropy of the globules [97]. Pica and Graziano argued that geometric frustration originates from a competition process between the preferential interaction of the water molecules with the amide groups of PNIPAM and the preferential interaction of the methanol and isopropyl groups of PNIPAM, and ultimately gives rise to the collapse of the chain [98]. Dalgicdir et al. found that polymer hydration plays a key role in determining the co-nonsolvency effect of PNIPAM since methanol geometrically impedes the formation of hydrogen bonds between the water molecules and the amide groups of PNIPAM [99]. Based upon the evidence obtained from high-sensitivity differential scanning calorimetry measurements, Grinberg et al. contended that PNIPAM possesses cooperative hydro-solvation structures formed by water/methanol complexes, which lead to a decreasing enthalpy with an increasing methanol content [100]. Tavagnacco et al. carried out atomistic simulations of PNIPAM chains in a water/ethanol mixture, and found that the chemical potential of the water in the bulk of the mixture and the competition between the water and ethanol molecules in the interactions with the polymer both have a driving role in determining the transition behavior [101].

3.2 Poly(*N*-isopropylmethacrylamide)

Poly(*N*-isopropylmethacrylamide) (PNIPMAM) is very similar to PNIPAM, but has an additional methyl group on the backbone, as shown in Figure 3.4. As for PNIPAM, PNIPMAM shows a type-II LCST behavior in aqueous solution. However, the coil-to-globule collapse transition occurs at a higher temperature of ~44 °C, where this temperature depends only weakly on the molar mass, solution concentration, and added electrolytes [15, 31].

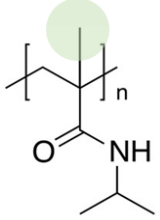

Figure 3.4 Chemical structure of poly(*N*-isopropylmethacrylamide), PNIPMAM. Note that the green circle indicates the additional methyl group on the backbone.

The molecular origin of the counter-intuitive increase of the T_{CP} of PNIPMAM is still under discussion. However, it appears to be related to the steric demand of the methyl group altering the chain conformation and hydration behavior. PNIPMAM solutions have been intensively examined by turbidimetry [32-36], differential scanning calorimetry (DSC) [36, 38, 41], Fourier transform infrared spectroscopy (FTIR) [39, 42, 43], nuclear magnetic resonance (NMR) [43], Raman spectroscopy [39], and light scattering. In general, the results have shown that, below T_{CP}, the PNIPMAM chains are more hydrated and expanded than PNIPAM chains [37], while above T_{CP}, the aggregates are more loosely packed than those formed by PNIPAM [38]. In addition, molecular dynamics simulations and quantum mechanical calculations have revealed that both the intermolecular interactions and the intramolecular interactions among the amide groups of PNIPMAM are weaker than those of PNIPAM as a result of the steric hindrance effect caused by the additional methyl groups [39, 40]. Thus, even very small changes in the molecular structure can strongly affect the behavior around the coexistence line.

3.3 Polystyrene-*b*-poly(*N*-isopropylacrylamide)

Polystyrene (PS) is a hydrophobic polymer with a glass transition temperature of around 100 °C and the chemical structure shown in Figure 3.5. It is often chosen as the hydrophobic block of amphiphilic diblock copolymer on account of its hydrophobic and glassy nature in water.

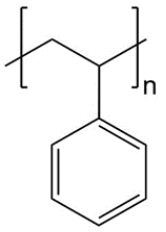

Figure 3.5 Chemical structure of polystyrene, PS.

Polystyrene-*b*-poly(*N*-isopropylacrylamide) (PS-*b*-PNIPAM) diblock copolymer is composed of a permanently hydrophobic PS block and a thermoresponsive PNIPAM block, and is one of the most frequently studied thermoresponsive amphiphilic diblock copolymers. PS-*b*-PNIPAM copolymers are capable of forming self-assembled structures in aqueous solution, where the morphology of these structures is critically dependent on the block length ratio between the hydrophobic PS blocks and the thermoresponsive PNIPAM blocks [62, 102]. Table 3.1 shows the morphology of the self-assembled structures formed by PS-*b*-PNIPAM diblock copolymers with different PNIPAM weight fractions. At temperatures lower than the LCST of PNIPAM, PS_{207}-*b*-$PNIPAM_{176}$ with a PNIPAM weight fraction

of w_{PNIPAM} = 0.48 self-assembles into vesicles in aqueous solution [103], while PS_{36}-*b*-$PNIPAM_{37}$ with a weight fraction of w_{PNIPAM} = 0.53 forms kinetically stable, large spherical aggregates [104]. The self-assembled structures of PS_{77}-*b*-$PNIPAM_{120}$ with w_{PNIPAM} = 0.63 [105], PS_{90}-*b*-$PNIPAM_{150}$ with w_{PNIPAM} = 0.64 [106], PS_{207}-*b*-$PNIPAM_{375}$ with w_{PNIPAM} = 0.65 [103], and PS_{48}-*b*-$PNIPAM_{159}$ with w_{PNIPAM} = 0.78 [107] all have the form of core-shell spherical micelles in aqueous solution. However, PS_{65}-*b*-$PNIPAM_{360}$ with w_{PNIPAM} = 0.86 [108] and PS_{50}-*b*-$PNIPAM_{376}$ with w_{PNIPAM} = 0.88 [105] form a mixture of cylinders and spheres and unstructured large aggregates, respectively. In other words, spherical micelles are obtained only within a narrow w_{PNIPAM} range of approximately 0.63-0.78.

Table 3.1 Morphology of self-assembled structures formed by PS-*b*-PNIPAM.

Polymer	**PNIPAM weight fraction, w_{PNIPAM}**	**Morphology of self-assembled structures**		**Reference**
		below T_{CP}	above T_{CP}	
PS_{328}-*b*-$PNIPAM_{98}$	0.25	crew-cut spheres	-	[109]
PS_{207}-*b*-$PNIPAM_{176}$	0.48	vesicles	hollow vesicles	[103]
PS_{36}-*b*-$PNIPAM_{37}$	0.53	spherical aggregates	-	[104]
PS_{77}-*b*-$PNIPAM_{120}$	0.63	core-shell spheres	core-shell spheres with a subtle shrinkage shell	[105]
PS_{90}-*b*-$PNIPAM_{150}$	0.64	core-shell spheres	clusters formed by core-shell spheres with a partially collapsed shell	[106]
PS_{207}-*b*-$PNIPAM_{375}$	0.65	core-shell spheres	core-shell spheres with a collapse shell	[103]
PS_{48}-*b*-$PNIPAM_{159}$	0.78	core-shell spheres	clusters formed by core-shell spheres with a partially collapsed shell	[107, 110]
PS_{65}-*b*-$PNIPAM_{360}$	0.86	mixtures of cylinders and spheres	spheres	[108]
PS_{50}-*b*-$PNIPAM_{376}$	0.88	unstructured large aggregates	collapsed aggregates	[105]

The temperature-dependent morphology of the self-assembled structures produced by PS-*b*-PNIPAM in aqueous solution at temperatures close to the transition temperature of PNIPAM has been extensively investigated [45, 103, 105, 106]. In general, the results have shown that the size of the micelles increases upon heating below the LCST-transition point, but then shrinks upon heating across the spinodal of PNIPAM. The increasing micellar size at temperatures lower than the transition temperature may be attributed to the hydrophobic PS blocks and the interchain interactions between the PNIPAM blocks, which both hinder the collapse of the micellar shell [103, 105, 106]. Troll et al. and Adelsberger et al. examined on the collapse transition and aggregation behavior of spherical micelles formed by PS_{48}-*b*-$PNIPAM_{159}$ (w_{PNIPAM} = 0.78) upon heating [107, 110].The results showed that as the temperature increased, the core-shell micelles shrank slightly; resulting in a partially collapsed shell. The micelles then formed small clusters, which retained their size upon further heating until the temperature reached a point far greater than the LCST transition temperature of PNIPAM, at which point they began to grow in size [107]. This behavior was attributed to the hydrophobic and glassy nature of the PS blocks, which hamper equilibration of the micelles and result in a non-typical aggregation behavior upon the collapse of the shell. A similar aggregation behavior was observed by Cao et al. for PS_{90}-*b*-$PNIPAM_{150}$ with a lower PNIPAM weight fraction of w_{PNIPAM} = 0.64 [106].

3.4 Poly(methylmethacrylate)-*b*-poly(*N*-isopropylacrylamide)

Most nonionic diblock copolymers with a degree of polymerization of the PS blocks higher than 14 (DP_n>14) are not directly soluble in water. Moreover, their self-assembled structures in aqueous solution are usually not in equilibrium, but are kinetically frozen. This seems to be the case for PS-*b*-PNIPAM diblock copolymers as well [45]. As for PS, poly(methyl methacrylate) (PMMA) is an amorphous glassy hydrophobic polymer with a glass transition temperature just above 100 °C. However, PMMA is slightly less hydrophobic, more polar, and more biocompatible than PS [111, 112]. Hence, it appears to be an attractive alternative hydrophobic block. The chemical structure of PMMA is shown in Figure 3.6.

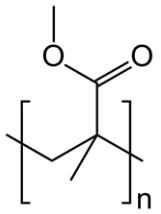

Figure 3.6 Chemical structure of poly(methyl methacrylate), PMMA.

Amphiphilic thermoresponsive diblock copolymers with a strong asymmetry of the block size, e.g., a small permanently hydrophobic PMMA block and a much larger thermoresponsive PNIPAM block, are particularly attractive for many applications since they are readily dissolved in water and self-assemble into stable spherical micelles. In addition to the implications of self-assembly [105, 113], increasing the polarity of the hydrophobic blocks can improve the loading efficiency of water-insoluble but polar substances in the core of the self-assembled micelles, and modulate the substance releasing process [5]. As a result, the drug loading efficiency is enhanced and the drug releasing process is impeded.

Table 3.2 Morphology of self-assembled structures formed by PMMA-*b*-PNIPAM.

Polymer	**PNIPAM weight fraction, w_{PNIPAM}**	**Self-assembled structures**		**Reference**
		below T_{CP}	above T_{CP}	
$PMMA_{35}$-*b*-$PNIPAM_{33}$ $PMMA_{34}$-*b*-$PNIPAM_{34}$	0.50-0.55	spherical aggregates	shrinking spherical aggregates	[114]
$PMMA_{\sim 120}$-*b*-$PNIPAM_{\sim 340}$	0.76	aggregate structures	-	[115]
$PMMA_{14}$-*b*-$PNIPAM_{106}$	0.88	ordered packed spherical micelles	shrinking spherical micelles	[113]
$PMMA_{16}$-*b*-$PNIPAM_{172}$	0.92	core-shell spherical micelles	large aggregates	[113]

Despite these potential advantages, surprisingly few studies have explored the micellar self-assembly of PMMA-*b*-PNIPAM diblock copolymers (Table 3.2) [105, 113, 115, 116]. However, $PMMA_{16}$-*b*-$PNIPAM_{172}$ diblock copolymers were synthesized by reversible addition fragmentation chain transfer (RAFT) polymerization, and their aggregation was then studied by SANS and surface tensiometry [113, 116]. The results showed that, unlike PS-*b*-PNIPAM diblock copolymers, $PMMA_{16}$-*b*-$PNIPAM_{172}$ forms spherical core-shell micelles in dilute aqueous solution in spite of its rather high PNIPAM weight fraction (w_{PNIPAM} = 0.92). Furthermore, $PMMA_{14}$-*b*-$PNIPAM_{106}$ with a weight fraction of w_{PNIPAM} = 0.88 forms gel structures with ordered packed micelles at a polymer concentration of 10 wt% [113]. Wei et al. prepared PMMA-*b*-PNIPAM block copolymers with a weight fraction of w_{PNIPAM} = 0.76 by coupling carboxyl-terminated $PMMA_{\sim 120}$ with primary amine terminated $PNIPAM_{\sim 340}$, and then investigated their use for the thermally-triggered delivery of the drug prednisone acetate [115]. However, the aggregate structures were only rudimentarily

characterized. Thus, in later studies, the same group incorporated a small number of reactive groups into the PNIPAM block in order to fabricate shell-crosslinked micelles with the objective of improving the drug release kinetics [117, 118]. Recently, Razavi et al. recently synthesized small, nearly-symmetrical PMMA-*b*-PNIPAM block copolymers with weight fractions in the range of w_{PNIPAM} = 0.50-0.55 using an atom transfer radical polymerization (ATRP) method [114]. The copolymers were found to self-assemble into spherical large aggregates in aqueous media, and were both temperature- and light-responsive due to the spiropyrane dye-functionalized initiator employed. The encapsulation and controlled release of the drug doxorubicin from the micelles of $PMMA_{35}$-*b*-$PNIPAM_{33}$ and $PMMA_{34}$-*b*-$PNIPAM_{34}$ diblock copolymers with w_{PNIPAM} = 0.50-0.55 were comprehensively examined [114]. However, only a rudimentary analysis of the aggregate structures was performed.

Due to their thermoresponsive property, PNIPAM-based amphiphilic diblock copolymers and their self-assembled structures have been used in a wide range of applications, including drug encapsulation and release systems [4, 5], microsensors [6, 7], catalysis [8, 9], and substance separation [10]. Thus, undertaking a comprehensive temperature-dependent phase and structural investigation of the self-assembled micelles produced by PMMA-*b*-PNIPAM diblock copolymers in aqueous solution is of significant interest. Moreover, a comparison between PMMA-*b*-PNIPAM and PS-*b*-PNIPAM is also useful in understanding the impact of the specific hydrophobicity of the core-forming block on the inner structure, correlation, and aggregation of the micelles.

For PMMA-*b*-PNIPAM diblock copolymers, the PNIPAM block is not only sensitive to the temperature, but also to the solvent composition. For example, for water and methanol mixtures at room temperature, the PNIPAM chains experience a reentrant coil-to-globule-to-coil transition with a miscibility gap ranging from ca. 25-65 vol% of methanol [90, 91, 119] (Figures 3.3a and b). In other words, PNIPAM features a co-nonsolvency effect in water and methanol mixtures. Consequently, besides changing the temperature, tuning the solvent composition also serve as an effective alternative approach for adjusting the self-assembled structures formed by PNIPAM-based amphiphilic diblock copolymers, e.g., inducing the formation and disintegration of micelles and tuning their morphology [74-76].

Co-solvency effect of PMMA

PMMA is insoluble in water and poorly soluble in methanol at room temperature (Figure 3.7a). However, the solubility of PMMA is improved in mixtures of water and methanol containing ~80-95 wt% of methanol (ca 85-98 vol% of methanol) [119, 120] (Figure 3.7b). This phenomenon is referred to as the co-solvency effect, and is the opposite of the co-nonsolvency effect. The co-solvency behavior

of PMMA in homopolymers has been observed both experimentally [121] and numerically [122], while that in diblock copolymers has also been observed experimentally [121, 123], and can be exploited to enable the self-assembly of double hydrophobic diblock copolymers.

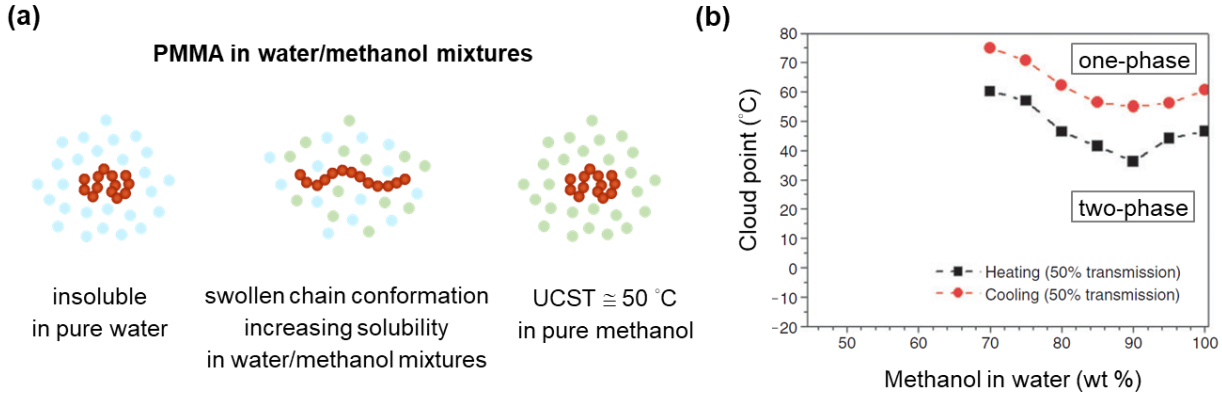

Figure 3.7 (a) Schematic representation of co-solvency effect on chain conformation of PMMA in water/methanol mixtures. (b) Cloud point of PMMA in water/methanol mixtures. (Reprinted from Ref. [121]. Copyright (2010) CSIRO Publishing.)

Due to the co-solvency effect of PMMA, the behavior of PMMA-*b*-PNIPAM in water/methanol mixtures may be more complicated than that of PS-*b*-PNIPAM. Therefore, the effect of the solvent composition on the thermal and structural properties of PMMA-*b*-PNIPAM diblock copolymers in water/methanol mixtures with different methanol volume fractions is of significant interest. As shown in Figure 3.8, the interplay of the co-nonsolvent and co-solvency effects on the morphologies of the micelles or molecularly-dissolved chains formed by PMMA-*b*-PNIPAM is also of great interest.

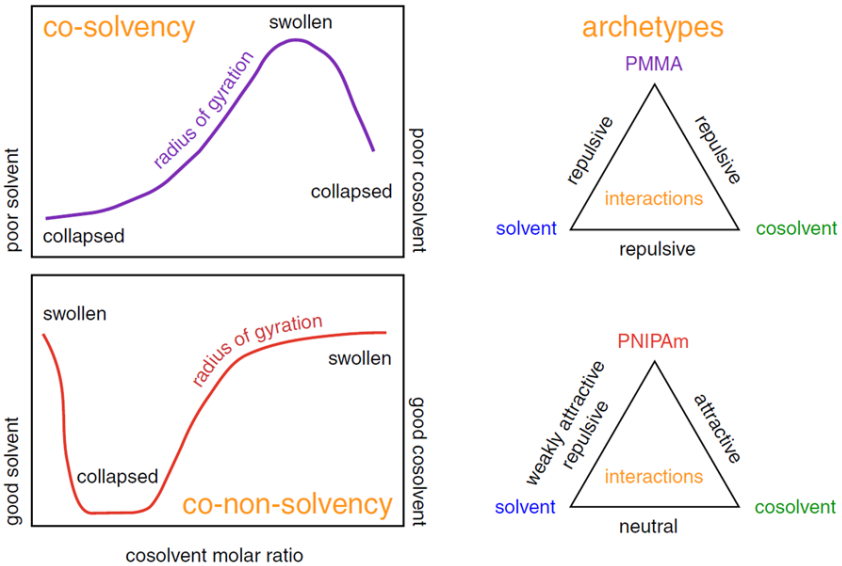

Figure 3.8 Schematic representation of co-solvency effect for PMMA and co-nonsolvency effect for PNIPAM. (Reprinted with permission from Ref. [119]. Copyright (2017) IOP Publishing, Ltd.)

3.5 Main goals of this thesis

The thesis commences by investigating the temperature-dependent phase behavior of thermoresponsive polymer PNIPMAM in aqueous solutions. As described in Section 3.2, compared to PNIPAM, PNIPMAM has a higher phase transition temperature (i.e., ~43 °C rather than 32 °C) [15, 31]. Moreover, PNIPMAM has a similar chemical structure as PNIPAM, but has the additional methyl groups on its vinyl backbone, which may result in steric hindrance [37, 38] and weaker intramolecular interactions [39, 40]. In other words, small changes in the molecular structure may have a significant impact on the phase behavior around the coexistence line. This thesis therefore conducts a detailed examination of the phase behavior of aqueous PNIPMAM solutions in order to clarify how these effects impact the thermal and structural behavior of PNIPMAM aqueous solutions.

Although several studies have investigated the behavior of PNIPMAM in aqueous solutions [32-36, 38, 39, 41-43], most of these studies considered only a single sample, or used only one or two characterization methods. Accordingly, the present thesis conducts a more systematic investigation into the phase behavior of aqueous PNIPMAM solutions over a broad concentration range of 2 to 150 g L^{-1}. In addition, a large number of instrumental techniques are used to address different aspects of the phase transition behavior. For example, the cloud point, T_{CP}, is identified using turbidimetry and optical microscopy (OM), while the thermal properties are studied by differential scanning calorimetry (DSC). Small-angle neutron scattering (SANS) and very small-angle neutron scattering (VSANS) techniques are additionally used to obtain structural information over a broad range of length scales and a wide range of temperatures. Finally, Raman spectroscopy is used to unravel the hydrophobic hydration behavior of PNIPMAM around the phase transition point.

The second part of this thesis addresses PMMA-*b*-PNIPAM amphiphilic thermoresponsive diblock copolymers. Previous studies have shown that PMMA-*b*-PNIPAM forms core-shell micelles in aqueous solution [46]. The shells of these core-shell structures collapse at the transition temperature of the PNIPAM block (32 °C), and the collapsed micelles then form aggregates. Theis property renders PMMA-*b*-PNIPAM copolymers ideally suited to applications such as drug delivery [2-5], microfluidic sensors [6, 7], and tunable catalysis [8, 9]. However, to optimize the practical performance of such applications, a fundamental investigation into the inner structure, thermal behavior and dynamics of the micelles is required.

Additionally, PMMA-*b*-PNIPAM is not only sensitive to the temperature, but also to the solvent composition. For example, adding methanol to the aqueous solution as a cosolvent causes the PNIPAM blocks to collapse; thereby reducing the transition temperature as a result of the so-called co-nonsolvency effect (Section 3.1) [91, 92]. However, PMMA also features a co-solvency effect in

water/methanol mixtures [120-123], i.e., the hydrophobicity of the PMMA block decreases as the methanol concentration increases (Section 3.4). As a result, the impact of the interplay between the co-nonsolvent and co-solvency effects on the morphologies of the self-assembled micelles or molecularly-dissolved chains formed by PMMA-*b*-PNIPAM is also of interest (Figure 3.8).

The present thesis therefore investigates: (i) the structure of the self-assembled micelles formed by PMMA-*b*-PNIPAM in aqueous solution and the changes which occur upon the collapse and aggregation of these micelles with an increasing temperature; and (ii) the co-nonsolvency/co-solvency interplay effect in a water/methanol mixture. The inner structure and correlations of the correlated micelles are systematically characterized by means of turbidimetry, differential scanning calorimetry (DSC), dynamic light scattering (DLS) and synchrotron small-angle X-ray scattering (SAXS).

3.6 Systems under investigation

3.6.1 Poly(*N*-isopropylmethacrylamide)

In this present work, poly(*N*-isopropylmethacrylamide) (PNIPMAM) homopolymer used in the present research was synthesized by Dr. Dirk Schanzenbach from the group of Prof. Laschewsky at the University of Potsdam, Germany.

Briefly, PNIPMAM homopolymer with an apparent number average molar mass of M_n^{app} = 17,000 g mol^{-1} (equivalent to an apparent number average degree of polymerization of 133) and a dispersity index of $Đ$ = 1.74 was synthesized by free radical polymerization (FRP). (Full details of the synthesis process are provided in Ref. [124].)

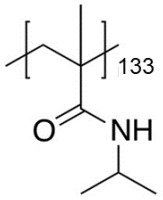

Figure 3.9 Chemical structure of poly(*N*-isopropylmethacrylamide), PNIPMAM.

Sample preparation

For all measurements, $PNIPMAM_{133}$ was dissolved in D_2O (Deutero GmbH, purity 99.95%, Kastellaun, Germany) at concentrations between 2 and 150 g L^{-1}. All solutions were left to equilibrate at room temperature for at least 48 h.

3.6.2 Poly(methylmethacrylate)-*b*-poly(*N*-isopropylacrylamide)

Synthesis and molecular characterization

The poly(methylmethacrylate)-*b*-poly(*N*-isopropylacrylamide) (PMMA-*b*-PNIPAM) diblock copolymer used in the present work was synthesized and molecularly characterized by Cristiane Henschel from the group of Prof. Laschewsky at the University of Potsdam, Germany.

Amphiphilic diblock copolymer PMMA-*b*-PNIPAM with a short hydrophobic PMMA block and a long thermoresponsive PNIPAM block was synthesized by reversible addition fragmentation chain transfer (RAFT) polymerization [125]. The chemical structure of the PMMA-*b*-PNIPAM copolymer is shown in Figure 3.10. (Full details of the synthesis process and molecular characterization results are available in Ref. [126].)

Table 3.3 lists the molar mass values obtained for PMMA and PMMA-*b*-PNIPAM by ^{1}H nuclear magnetic resonance (NMR), ultraviolet-visible (UV-vis) spectroscopy, and size-exclusion chromatography (SEC). The molar mass values obtained from the different methods agree reasonably

well with the theoretical predictions and one another. As designed, the hydrophobic PMMA block is short, with around 20 MMA repeating units, while the hydrophilic thermoresponsive PNIPAM block is much longer, with approximately 300 NIPAM repeating units. It is noted that this particular design allows the direct dissolution of the diblock copolymer in water. The remainder of the thesis employs the M_n^{NMR-R} values in Table 3.3; meaning that the synthesized PMMA-*b*-PNIPAM diblock copolymers are expressed as $PMMA_{21}$-*b*-$PNIPAM_{283}$.

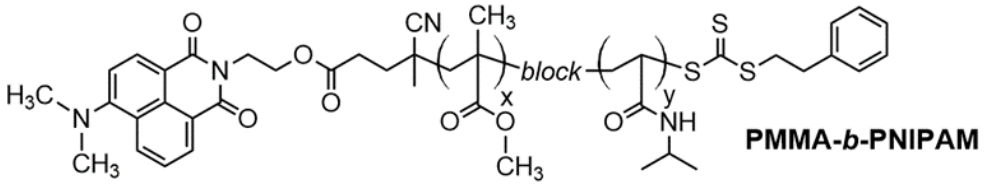

Figure 3.10 Chemical structure of diblock copolymer PMMA-*b*-PNIPAM synthesized via successive RAFT polymerization of MMA and NIPAM. According to ^{1}H NMR analysis, x = 21, and y = 283.

Table 3.3 Characteristics of synthesized polymers.

Polymer	yield (%)	M_n^{theo} (kg mol^{-1})	M_n^{NMR-R} (kg mol^{-1})	M_n^{NMR-Z} (kg mol^{-1})	M_n^{vis} (kg mol^{-1})	M_n^{SEC} (kg mol^{-1})	Dispersity *Đ*
PMMA (macro-CTA)	40 %	2.2	2.7	2.7	3.5	2.3	1.38
PMMA-*b*-PNIPAM	92 %	28	35		36.5	41	1.39

Sample preparation

$PMMA_{21}$-*b*-$PNIPAM_{283}$ were dissolved in D_2O (99.95 %, Deutero GmbH) at concentrations of 0.2, 0.5, 1, and 10 g L^{-1}. All the solutions were prepared and kept at room temperature for equilibration for 48 h.

For the measurements regarding co-nonsolvency/co-solvency effects, the mixtures of deuterated water D_2O (99.95 %, Deutero GmbH) and fully deuterated methanol CD_3OD (99.8 %, Deutero GmbH) in different v/v D_2O/CD_3OD mixing ratio were prepared and shaken at room temperature for 24 h before preparing the polymer solutions. $PMMA_{21}$-*b*-$PNIPAM_{283}$ were dissolved in D_2O/CD_3OD mixtures at different v/v mixing ratios of 100:0, 95:5, 90:10, 85:15, 80:20, 75:25, 35:65, 30:70, 20:80, 10:90 and 0:100, respectively, at a concentration of 10 g L^{-1}. All the polymer solutions were shaken at room temperature for 24 h and kept at ~ 4 °C for equilibration before the measurements.

Characterization in aqueous solution

Due to its relatively short hydrophobic block, the present $PMMA_{21}$-*b*-$PNIPAM_{283}$ diblock copolymer can be directly dissolved in water without the need for ultrasonication or a cosolvent. To obtain a crude estimate of the critical micelle concentration (CMC) of the copolymer in aqueous solution, the concentration-dependence of the solutions was investigated at room temperature (20-23 °C) by UV-vis spectroscopy [126]. The results indicated that the absence of any transition behavior pointing to a CMC down to a concentration of at least 0.05 g L^{-1}. This finding is consistent with the correlations established for nonionic amphiphilic block copolymers with similar architectures. Thus, the hypothetical CMC for the $PMMA_{21}$-*b*-$PNIPAM_{283}$ diblock copolymer in aqueous solution was inferred to be very low (around 10^{-9} M, i.e., less than 0.001 g L^{-1}) [127]. Consequently, in characterizing the structural information of the micelles formed by the $PMMA_{21}$-*b*-$PNIPAM_{283}$, all of the following measurements were taken at concentrations far higher than this concentration.

Contour length calculation and micellar size estimation

The contour lengths, L, of the PMMA and PNIPAM blocks were calculated in order to estimate the upper limit, R_{max}, of the size of the micelles formed by the $PMMA_{21}$-*b*-$PNIPAM_{283}$ diblock copolymer. According to the results presented in Table 3.4. the maximum size of the micelles, R_{max}, can be estimated as $L_{PMMA}+L_{PNIPAM}$ = 76.6 nm (i.e., for fully stretched polymer chains). In addition, the end-to-end distances, R_{ee}, of the PMMA and PNIPAM blocks can also be calculated from Table 3.4 under the assumption of ideal conformations. In particular, the size of the micelles, $R_{ee,ideal}$, can be estimated as $(R_{ee}^2{}_{,PMMA}+R_{ee}^2{}_{,PNIPAM})^{0.5}$= 12.3 nm.

Table 3.4 Calculated contour lengths and the end-to-end distances of diblock copolymers.

Polymer	Monomer length b[(a)] (nm)	Degree of polymerization N	Contour length L[(b)] (nm)	End-to-end distance R_{ee}[(c)] (nm)
PMMA	0.252	21	5.3	3.0
PNIPAM	0.252	283	71.3	11.9

(a) Calculated using the C-C bond length of l = 0.154 nm and bond angle of 109.5°; (b) Calculated using $L= bN$; (c) Calculated using $R_{ee}^2 = C_\infty n l^2$ with characteristic ratios C_∞ = 9.0 for PMMA [52] and C_∞ = 10.6 for PNIPAM [128]. Note that n is the number of the C-C bonds, and can be estimated as $n \sim 2N$.

4. Characterization techniques

This chapter describes the characterization methods and experimental techniques employed in the present thesis. Dynamic light scattering was used to determine the hydrodynamic radius of the micelles and molecularly-dissolved polymer chains in solution, while small-angle neutron and X-ray scattering were used to gain insights into the structures of the various systems under investigation. Turbidimetry was employed to identify the cloud points of the various solution. Finally, differential scanning calorimetry was used to characterize the thermal behavior of the phase transition, while Raman spectroscopy was employed to examine the molecular structure of the polymer and their interactions in the considered systems.

4.1 Dynamic light scattering (DLS)

Dynamic light scattering (DLS) provides a powerful technique for investigating the size and dynamic diffusional behavior of dispersed particles in suspensions or polymer solutions. When the solution is illuminated by coherent light, the scattered intensity fluctuates with time due to the continuous Brownian motion of the particles (i.e., translational diffusion). Generally speaking, the faster the particles move, the more rapidly the scattered light intensity fluctuates. The rate of the scattered light intensity fluctuation is therefore strongly associated with the diffusional behavior of the particles. Figure 4.1 presents a schematic illustration of the typical DLS experimental setup. As shown, the sample is illuminated by a laser source with a wavelength λ, and the scattered light intensity, $I(t)$, is recorded as a function of time t at a scattering angle θ by a photodetector. The normalized autocorrelation function, $g_2(q,\tau)$, is then computed by a correlator. (Note that full details of the measurement and analytical methods are available on Refs. [129] and [130].)

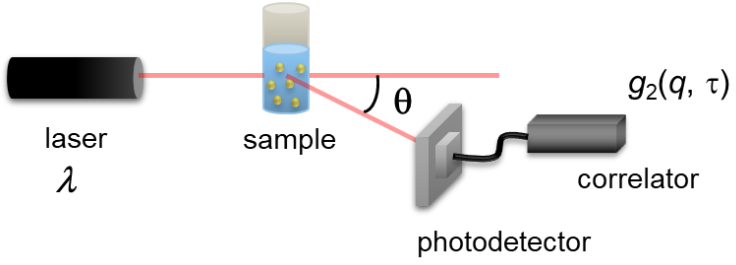

Figure 4.1 Schematic representation of dynamic light scattering setup.

4.1.1 Principles of DLS

In dilute solutions containing particles, the scattered intensity fluctuations originate from

Brownian motion. The structural and diffusional information of the particles can be obtained from the normalized autocorrelation function, $g_2(q,\tau)$, recorded during the measurements, i.e.,

$$g_2(q,\tau) = \frac{\langle I(t) \cdot I(t+\tau) \rangle}{\langle I(t) \rangle^2} \tag{4.1}$$

where $g_2(q,\tau)$ correlates the scattered light intensity at time t with the scattered light intensity after a certain delay time τ.

For short delay times, the intensities at the initial time t and after the delay time τ, respectively, are strongly correlated since the particles change their positions only very slightly during a short time interval. As a result, the fluctuation of the scattered light intensity is small. However, for long delay times, the correlation decays exponentially since the particles are liable to move through a far greater distance. In other words, the correlation between the scattered intensity of the initial and final states is destroyed, or is extremely weak. Thus, the exponential decay of $g_2(q,\tau)$ provides a meaningful insight into the diffusional behavior of the particles. For convenience, DLS analysis is commonly performed using the normalized field autocorrelation function, $g_1(q,\tau)$, which is related to $g_2(q,\tau)$, via the following Siegert relation [131]:

$$g_2(q,\tau) = 1 + \beta |g_1(q,\tau)|^2 \tag{4.2}$$

where β is a coherence factor with $0 < \beta < 1$ and varies depending on the particular alignment and geometry of the laser light in the DLS instrument.

For monodisperse particles, the autocorrelation curve features a single exponential, and the corresponding normalized field autocorrelation function is given by

$$g_1(q,\tau) = e^{-\Gamma\tau} = e^{-\frac{\tau}{\tau_1}} \tag{4.3}$$

where Γ is the decay rate and τ_1 is the decay time. (Note that Γ is defined as $1/\tau_1$.) The translational diffusion coefficient D of the particles is then defined as

$$D = \frac{1}{\tau_1 q^2} = \frac{\Gamma}{q} \tag{4.4}$$

where q is the scattering vector, and is given as

$$q = \frac{4\pi n_s}{\lambda} \sin\frac{\theta}{2} \tag{4.5}$$

where n_s is the refractive index of the solvent, λ is the wavelength of the incident laser and θ is the scattering angle.

For translational diffusion, D commonly shows no angular dependence, i.e., it is independent of

the scattering angle. Thus, referring to eq. 4.4, Γ depends linearly on q^2, which indicates purely translation diffusion. In this case, the hydrodynamic radii, R_h, of the monodisperse particles can be calculated by the Stokes-Einstein equation as follows:

$$R_h = \frac{k_B T}{6\pi \eta_s D} \tag{4.6}$$

where k_B is the Boltzmann constant, T is the temperature, and η_s is the solvent viscosity.

For polydisperse particles, the autocorrelation function is a sum of multiple exponentials, where each exponential corresponds to a certain size fraction of particles. In this, case, the normalized field autocorrelation function, $g_1(q,\tau)$, is given by the following integral over the decay time distribution, $A(\tau_1)$:

$$g_1(q,\tau) = \int A(\tau_1) e^{-\frac{\tau}{\tau_1}} d\tau_1 \tag{4.7}$$

where $\int A(\tau_1) d\tau_1 = 1$. In eq. 4.7, $g_1(q,\tau)$ is the Laplace transform of $A(\tau_1)$ with respect to τ_1. Thus, to obtain the distribution values of τ_1 from the particles in polymer solution, it is necessary to perform inverse Laplace transformation. However, this operation is difficult due to the well-known ill-conditioned problem for inverse Laplace transformation. Accordingly, in the present thesis, the regularized positive exponential sum (REPES) method is applied instead to analyze the autocorrelation function. As described in Ref. [132], the REPES method aims to minimize the expression

$$E + \kappa_0 R \tag{4.8}$$

where E is an error term, and is defined as

$$E = \sum_k \left[f(t_k) - f_{k,exp} \right]^2 \tag{4.9}$$

in which $f_{k,exp}$ is the experimental data of $g_2(q, t_k)$ and is given by

$$f(t) = \left[a_1 + \sum_{i=2}^{r} a_i \, e^{-\frac{t}{\tau_i}} \right]^2 \tag{4.10}$$

In eq. 4.8, R is a regularizor, and κ_0 is calculated based on a preselected value during fitting called the Probability to Reject (*PtR*). When the value of *PtR* is large, the smoothness of the fit for $A(\tau_1)$ is prioritized. Conversely, when the value of *PtR* is small, minimizing the error of the fit is prioritized. In general, *PtR* is set as 0.5. By fitting the experimental data using the REPES algorithm, the distribution function of $A(\tau_1)$ can be obtained. Moreover, the distribution of the hydrodynamic radii, $A(R_h)$, can also be obtained by converting $A(\tau_1)$ in accordance with eqs. 4.5 and 4.6.

4.1.2 Instrument

In the present thesis, the DLS measurements were obtained using an LS Spectrometer (LS Instruments, Fribourg, Switzerland) in a setup consisting of a laser light source, a goniometer, and two avalanche photodiode detectors. The light source had the form of a polarized HeNe laser (Thorlabs, Dachau, Germany) with a maximum power of 21 mW and a wavelength of 632.8 nm. The solutions under investigation were filled in cylindrical glass tubes with an outer diameter of 5 mm and a wall thickness of 0.4 mm. During the measurement process, the cylindrical tubes or square cuvettes were inserted in a decalin bath connected to a temperature control reservoir by a Julabo CF31 Cryo-Compact Circulator (JULABO, Seelbach, Germany).

Angle-dependent DLS measurements were obtained at a solution temperature of 20 °C with scattering angles, θ, varied in the range of 45° to 135° in steps of 15°. 20 measurements were obtained at each angle; with a measurement time of 30 s in every case. The momentum transfer was evaluated as $q = (4\pi n_s/\lambda) \sin(\theta/2)$ (eq. 4.5), where n_s is the refractive index of the solvent, λ is the wavelength of the laser light, and τ is the delay time. The corresponding normalized intensity autocorrelation functions, $g_2(q,\tau)$ (where τ is the delay time), were analyzed using the REPES algorithm in the Gendist software [132, 133]. The calculated values of τ were then used to derive the related values of the translational diffusion coefficient, D, from the decay rate as $\Gamma = 1/\tau = Dq^2$. Finally, the hydrodynamic radii, R_h, were calculated using the Stokes-Einstein equation given in eq. 4.6. For all of the DLS measurements, the related computations were performed using the refractive index and viscosity values of the corresponding solvent.

Temperature-dependent DLS measurements were obtained at temperatures up to the T_{CP} of the solution in steps of 1 or 2 °C. For each temperature, 20 measurements were obtained; with a measurement time of 30 s in every case. The outliers were removed, and the remaining data were then analyzed and averaged. A thermal equilibration time of 20 min was allowed before the measurement process at each temperature. The temperature-dependent scattered intensity was measured for a constant scattering angle of $\theta = 90°$. The normalized intensity autocorrelation functions, $g_2(q,\tau)$, were again evaluated using the REPES algorithm implemented in Gendist software [132, 133]. For each temperature, the distribution of the hydrodynamic radii was obtained in an equal area representation $A(R_h)$ R_h vs. $\log R_h$. The peaks in the distributions were then used to determine the average hydrodynamic radii, R_h.

4.2 Rolling-ball Microviscometer

To determine precisely the hydrodynamic radius, the viscosity of the D_2O/CD_3OD solvent mixtures was measured using a rolling-ball microviscometer Lovis 2000 M/ME (Anton Paar GmbH, Graz, Austria). Each solvent mixture, 10 measurements were done and averaged. The inclination angle was set at 70°. The ball rolling time t_r was measured. The viscosity of the solvent mixtures, η_s, was obtained by the following equation.

$$\eta_s = K(\rho_b - \rho_s)t_r \tag{4.11}$$

where K is the proportionality constant, r_b is the ball density, and r_s is the density of the solvent mixtures, which was referred to the value in Ref. [134].

The viscosity of the corresponding D_2O/CD_3OD solvent mixtures was measured from 15 to 50 °C in steps of 5 °C.

Table 4.1 Results from viscosity of the solvent mixtures [135]

Solvent composition D_2O/CD_3OD [v/v]	Viscosity of the solvent mixture, η_s (cP)							
	15 °C	20 °C	25 °C	30 °C	35 °C	40 °C	45 °C	50 °C
100:0	1.440	1.251	1.100	0.976	0.873	0.787	0.714	0.652
90:10	1.796	1.538	1.336	1.174	1.043	0.935	0.845	0.770
80:20	2.083	1.769	1.523	1.328	1.169	1.040	0.933	0.844
70:30	2.509	2.114	1.806	1.560	1.362	1.201	1.068	0.957
30:70	2.083	1.817	1.598	1.414	1.259	1.129	1.016	0.920
20:80	1.617	1.439	1.287	1.156	1.044	0.947	0.863	0.790
10:90	1.140	1.036	0.946	0.867	0.797	0.736	0.682	0.634
0:100	0.778	0.722	0.673	0.630	0.591	0.556	0.526	0.498

4.3 Abbe Refractometer

The refractive index of the corresponding D_2O/CD_3OD solvent mixtures was obtained using an Abbe-refractometer (A. KRÜSS Optronic GmbH, Hamburg, Germany), which is connected to a temperature control reservoir by a Julabo F31-HE (JULABO, Seelbach, Germany). The refractive index of the corresponding solvent mixtures was obtained at temperatures from 15 to 50 °C in steps of 5 °C.

Table 4.2 Results from refractive index of the solvent mixtures [135]

Solvent composition D_2O/CD_3OD [v/v]	Refractive index of the solvent mixtures, n_s							
	15 °C	20 °C	25 °C	30 °C	35 °C	40 °C	45 °C	50 °C
100:0	1.327	1.327	1.327	1.326	1.325	1.325	1.324	1.324
90:10	1.329	1.329	1.328	1.328	1.327	1.327	1.326	1.325
80:20	1.331	1.331	1.330	1.330	1.329	1.328	1.327	1.327
70:30	1.334	1.333	1.333	1.332	1.331	1.330	1.329	1.329
30:70	1.340	1.338	1.337	1.336	1.3335	1.335	1.333	1.331
20:80	1.338	1.336	1.335	1.333	1.332	1.331	1.330	1.328
10:90	1.333	1.332	1.330	1.329	1.328	1.326	1.324	1.324
0:100	1.328	1.326	1.326	1.323	1.324	1.320	1.320	1.316

4.4 Small-angle neutron and X-ray scattering (SANS/SAXS)

Small-angle neutron and X-ray scattering (SANS/SAXS) are widely used techniques for investigating the structures of polymer and colloid systems at length scales of ~1-100 nm by analyzing the elastic scattering of neutrons and X-rays, respectively. (Full details both techniques are available in Refs. [131] and [136].)

4.4.1 Principles of SANS and SAXS

The fundamental instrument setup for SANS and SAXS is identical (see Figure 4.2), and comprises a neutron or X-ray source, a collimation system, a sample holder and a two-dimensional detector. The sample is illuminated in transmission mode by the collimated neutrons or X-rays, and the scattered intensity of the neutrons or X-rays is then detected by the 2D detector. Based on the assumption of elastic scattering, $\vec{k}_i$ and $\vec{k}_s$ are defined as the wave vectors of the incident beam and scattered beam, respectively, and have magnitudes of $|\vec{k}_s| = |\vec{k}_i| = 2\pi/\lambda$, where λ is the wavelength of the neutrons or X-rays. The momentum transfer, $|\vec{q}|$, is then defined as the difference between the magnitudes of the wave vectors of the incident and scattered beams, i.e.,

$$|\vec{q}| = |\vec{k}_s - \vec{k}_i| = \frac{4\pi}{\lambda} sin\frac{\theta}{2} \tag{4.12}$$

Thermal neutrons typically have wavelengths of 0.1-1.0 nm, while hard X-rays have wavelengths ranging from 0.1-0.2 nm. For both characterization methods, the scattering intensity is usually recorded at small angles of 0.1-10°. As shown in eq. 4.12, there exists a reciprocal relation between the characteristic size of the sample and the scattering angle. Depending on the angular range over which a good scattering signal can be obtained, SANS and SAXS are able to characterize the structure at length scales of 1-100 nm. Generally speaking, the smaller the measured angle, the larger the sample length scale which can be probed. Thus, very small-angle neutron scattering (VSANS) is capable of resolving even larger length scales. Furthermore, the recorded angular range can be tuned simply by adjusting the sample-to-detector distance (SDD).

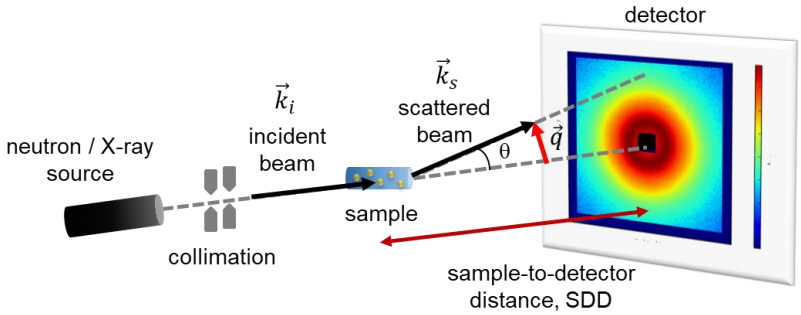

Figure 4.2 Schematic illustration of small-angle neutron or X-ray scattering setup.

4.4.2 Differential scattering cross-section and scattering contrast

To characterize the sample structure, the intensity, $I_m(\theta)$, is measured using the experimental setup is shown in Figure 4.3.

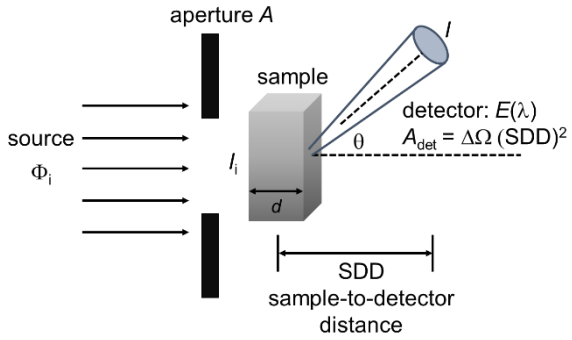

Figure 4.3 Schematic representation of scattering experiment. The incident radiation source has a flux Φ_i, wavelength λ, and incident intensity I_i. The sample has a thickness d and is illuminated through an aperture of area A. Finally, the detector has an efficiency $E(\lambda) < 1$ and a surface area of $A_{det} = \Delta\Omega\ (SDD)^2$ at a sample-to-detector distance SDD and scattering angle θ. (Adapted from Ref. [131].)

The ratio of the incident intensity, I_i, to the scattered intensity, I, is defined as the differential scattering cross-section of the sample per unit solid angle, i.e.,

$$\frac{d\sigma}{d\Omega} = \frac{I(\mathrm{SDD})^2}{I_i} \tag{4.13}$$

The differential scattering cross-section can then be expressed per unit sample volume in units of cm^{-1} by normalizing with respect to the unit sample volume, V, i.e.,

$$\frac{d\Sigma}{d\Omega}\ (\mathrm{cm}^{-1}) = \frac{1}{V}\frac{d\sigma}{d\Omega} \tag{4.14}$$

where $d\Sigma/d\Omega$ is the probability of the incident beam being scattered from the unit sample volume V into the solid angle $\Delta\Omega$. In other words, it represents the interaction between the incident radiation and the sample, and hence provides an understanding of the structure of the sample.

For an isotropic matter with N atoms at individual positions r_i, e.g., a polymer chain, the scattering of neutrons and X-rays represents an interference phenomenon. That is, the incident radiation waves interact with the sample and produce interference of waves scattered from each atom i at position r_i with a wave function A_i. The total scattering amplitude, $A(q)$, is then given as the sum of N wave functions A_i. That is,

$$A(q) \propto \sum\nolimits_N b_i\, exp[-i\ q\ r_i] \tag{4.15}$$

where b_i is the fraction of the incident radiation scattered by atom *i*, and is referred to as the scattering length. For small-angle scattering, the length scales probed are much larger than the interatomic distance. Therefore, eq. 4.15 can be expressed as

$$A(q) \propto \int_V \rho(r_i)\, exp\,[-i\, q\, r_i]\, dr \tag{4.16}$$

where $\rho\,(r_i)$ is the scattering length density. $\rho\,(r_i)$ stems from the electron density for X-rays, but the the scattering length for neutrons. In small-angle scattering, it is conventional to use the scattering length density ρ of a material rather than the scattering length *b* of the atoms. The scattering length density is defined as

$$\rho = \frac{1}{V_m} \sum_i^n b_i \tag{4.17}$$

where V_m is the molecular volume and b_i is the scattering length of all atoms in a molecule.

Neutrons and X-ray photons interact with matter differently. Specifically, X-rays interact with the electrons of atoms, while neutrons interact with the nuclei. The scattering length *b* is related to the strength of the interaction. For X-rays, the scattering length, *b*, depends on the wavelength and increases with an increasing atomic number *Z*. For neutrons, *b* is essentially wavelength-independent, but depends strongly on the isotopes. Table 4.3 lists the valu of *b* for some of the atoms most commonly investigated in polymer systems, e.g., H, D, C, O and N. It is noted that the *b* values of H and D are different for neutrons, but the same for X-rays. Therefore, some form of contrast variation, e.g., solvent matching or deuterium labeling, is often used in neutron scattering [131].

Table 4.3 X-ray and coherent neutron scattering lengths *b* and incoherent neutron cross-sections σ_{inc} of atoms commonly found in polymer systems.

Atom	H	D	C	N	O
$b_{X\text{-}ray}$, 10^{-12} cm [136]	0.282	0.282	1.690	1.970	2.260
$b_{neutron}$, 10^{-12} cm [137]	-0.374	0.667	0.665	0.940	0.580
σ_{inc}, 10^{-24} cm^2 [138]	80.26	2.05	0.001	0.5	0

For the case of *n* polymer chains (each made up of *N* atoms) in solvent, the total scattering effect can be rewritten as the sum of the $k = 1$ to *n* individual chains, i.e.,

$$F(q) \propto \sum_{\mathrm{k}} A_{\mathrm{k}}(q)\, exp[-i\, q\, r_{\mathrm{k}}] \tag{4.18}$$

For isotropic matter, the differential scattering cross-section is given by the product of $F(q)$ and its complex conjugate, $F^*(q)$. That is,

$$\frac{d\Sigma}{d\Omega}(q) \propto \langle F(q)F*(q)\rangle = \langle \sum\sum b_{\mathrm{i}} b_{\mathrm{j}} exp\left[-i\, q\, \left(r_{\mathrm{i}} - r_{\mathrm{j}}\right)\right]\rangle \tag{4.19}$$

Based on the assumption of elastic scattering, only the relative positions of every pair of scattering elements play a role. Thus, eq. 4.19 can be simplified as

$$\frac{d\Sigma}{d\Omega}(q) \propto (\rho - \rho_{\mathrm{s}})^2 \int_V P(r) exp[-i\, q\, r]\, dr \tag{4.20}$$

where $\Delta\rho = \rho - \rho_{\mathrm{s}}$ is the excess scattering length density, in which ρ is the scattering length density of the dispersed polymer and ρ_{s} is the scattering length density of the solvent.

For N particles with volume V_{p} with correlations in a polymer solution, the scattered intensity is given by

$$\frac{d\Sigma}{d\Omega}(q) = I(q) = \frac{N}{V} {V_{\mathrm{p}}}^2 \Delta\rho^2 P(q) S(q) + I_{\mathrm{bkg}} \tag{4.21}$$

where $P(q)$ is the form factor of the particles, and is related to their shape and size. In addition, $S(q)$ is the structure factor, and describes the correlation between the particles. Finally, I_{bkg} is a constant background, and $\Delta\rho$ is the excess scattering length density (i.e., the scattering contrast). In general, a small value of $\Delta\rho$ may hinder the analysis of $P(q)$ and $S(q)$. Therefore, SANS measurements are usually performed using deuterated solvent or deuterium labeling in order to increase the value of $\Delta\rho$ and simplify the structural analysis task.

4.4.3 Experimental aspects of small-angle scattering

Figure 4.3 shows the experimental setup for small-angle scattering experiments. The scattered intensity, I, is measured at a scattering angle, θ, and sample-to-detector distance SDD within a solid angle ΔΩ on a detector with efficiency $E(\lambda)$ and area $A_{\mathrm{det}} = \Delta\Omega\ (\mathrm{SDD})^2$. The incident intensity per second, I_{i}, is defined as

$$I_{\mathrm{i}} = \Phi_{\mathrm{i}}\, A\, E(\lambda) \tag{4.22}$$

where Φ_{i} is the incident radiation flux, λ is the incident radiation wavelength, and A is the aperture area.

For neutron and X-ray scattering, the measured intensity, $I_{\mathrm{m}}(\theta)$, obtained by experiments can be

simplified as

$$I_{\mathrm{m}}(\theta) = \Phi_{\mathrm{i}}\, A\, E(\lambda)\Delta\Omega\; d\, T\, \frac{d\Sigma}{d\Omega} \tag{4.23}$$

where d is the sample thickness and T is the transmission of the sample. The coefficient C(λ) is related to the configuration of the experimental setup, i.e., $C(\lambda) = \Phi_{\mathrm{i}} AE(\lambda)\Delta\Omega = I_{\mathrm{i}}\Delta\Omega$. In other words, C(λ) depends on the wavelength, the detector, the collimation distance, the type of detector, and the size of the sample aperture. Finally, term $dT\mathrm{d}\Sigma/\mathrm{d}\Omega$ in eq. 4.23 is specific to the sample.

For neutron scattering, the spin coupling of the neutrons and nuclei contributes to an incoherent background, which is represented as the incoherent neutron cross-section, σ_{inc}. The values of σ_{inc} for some of the most commonly found atoms in polymer systems are listed in the bottom row of Table 4.3. It is seen that the H atoms have a very strong neutron incoherent cross-section, compared to the D atoms. However, this effect can be minimized by using deuterated solvents. The total measured differential cross-section of a sample (e.g., a polymer solution) comprises two terms, namely

$$\frac{d\Sigma}{d\Omega} = \left(\frac{d\Sigma}{d\Omega}\right)_{\mathrm{coherent}} + \left(\frac{d\Sigma}{d\Omega}\right)_{\mathrm{incoherent}} \tag{4.24}$$

where $(\mathrm{d}\Sigma/\mathrm{d}\Omega)_{\mathrm{coherent}}$ is q-dependent and contains the structural information of the particles in the polymer solution, and $(\mathrm{d}\Sigma/\mathrm{d}\Omega)_{\mathrm{incoherent}}$ is independent of q and is considered to be a flat background originating from both the solvent and the incoherent scattering of the polymer. For dilute solutions, the incoherent scattering from the polymer is negligible and subtraction of the solvent scattering is thus sufficient. However, for concentrated solutions, the incoherent scattering from the polymer must be measured (or calculated) and then subtracted before the coherent differential scattering cross-section can be analyzed.

Due to the limited instrumental resolution effects originating from the wavelength spread, beam divergence and detector resolution, respectively, the measured intensity, $I_{\mathrm{m}}(\theta)$, is degraded by a smearing effect. Therefore, to analyze the differential scattering cross-section of the sample, it is necessary to employ the following smeared scattering function, $I_{\mathrm{smear}}(q)$ [139]:

$$I_{\mathrm{smear}}(q) = \int_0^\infty R(q, q')I(q')\, dq' \tag{4.25}$$

Where $R(q, q')$ is a Gaussian resolution function with a standard deviation Δq, which accounts for the q-divergence caused by the wavelength spread, beam divergence and detector resolution, respectively. $R(q, q')$ is given mathematically as

$$R(q, q') = \frac{1}{\Delta q\sqrt{2\pi}}\; exp\left[-\frac{(q'-q)^2}{2(\Delta q)^2}\right] \tag{4.26}$$

For SAXS, Δq in eq. 4.26 is usually negligible; particularly when the instrument has a pin-hole geometry. However, for SANS, wavelength spreading usually results in a larger Δq value, and hence the smearing effects must be considered. In other words, when analyzing the scattered intensity, the model function needs to be convoluted with the resolution function.

4.4.4 Instruments

Small-Angle Neutron Scattering (SANS). In the present thesis, the SANS measurements were performed at the KWS-1 instrument operated by the Jülich Centre for Neutron Science (JCNS) at Heinz-Maier-Leibnitz Zentrum (MLZ), Garching, Germany [140, 141]. The neutron source had a wavelength of $\lambda = 0.50$ nm with a spread of $\Delta\lambda/\lambda = 0.1$. The sample-detector distances were set as 1.5, 8.0 and 20 m; resulting in a value of q ranging from 0.03-4.4 nm^{-1}. The momentum transfer was evaluated as $q = 4\pi \sin(\theta/2)/\lambda$, where θ is the scattering angle. The samples were mounted in quartz glass cells (Hellma Analytics) with a light path length of 1 mm. A Peltier thermostated sample stage was used for all of the experiments. The sample transmission was measured and considered. The measurement time was set as 5 min, 20 min and 30 min for SDD values of 1.5 m, 8 m, and 20 m, respectively. Prior to the experiments, the detector sensitivity was evaluated using an empty Plexiglas cell. The background scattering from the empty cell and the dark current measured using boron carbide were then subtracted from the experimental measurements to obtain the absolute intensities for the sample under investigation. All of the data operations including azimuthal averaging were carried out using standard procedures in the software QtiKWS provided by JCNS.

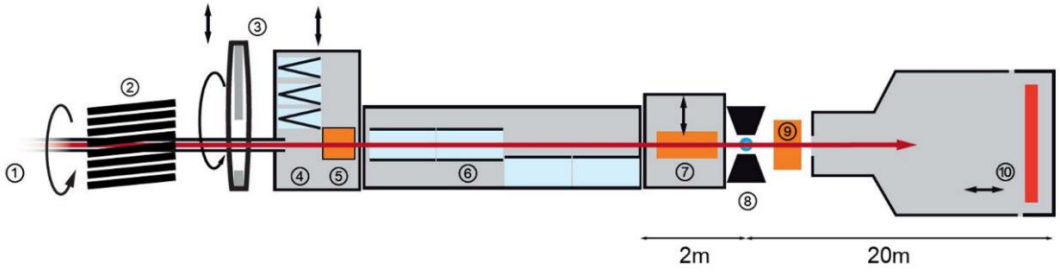

Figure 4.4 Schematic representation of SANS instrument at KWS-1 located at the MLZ, Garching, Germany. (Adapted from [140].)

Very Small-Angle Neutron Scattering (VSANS). VSANS measurements were carried out at the KWS-3 instrument operated by the Jülich Centre for Neutron Science (JCNS) at Heinz-Maier-Leibnitz Zentrum (MLZ), Garching, Germany [142]. The incident neutrons had a wavelength of 1.28 nm with a spread $\Delta\lambda/\lambda$ of 0.18. The SDD distance was set as 9.4 m; giving a q range of 0.002 – 0.02 nm^{-1}. In addition, the measurement time was set as 20 min or 25 min; depending on the concentration of the solution. As for the SANs experiments, the system was calibrated using an empty Plexiglass cell, and data processing was performed using standard procedures implemented in QtiKWS software. For each sample, the neutron transmission was measured using a direct beam on the detector, and T_{CP}^{VSANS} was defined as the temperature at which the transmission started to decay.

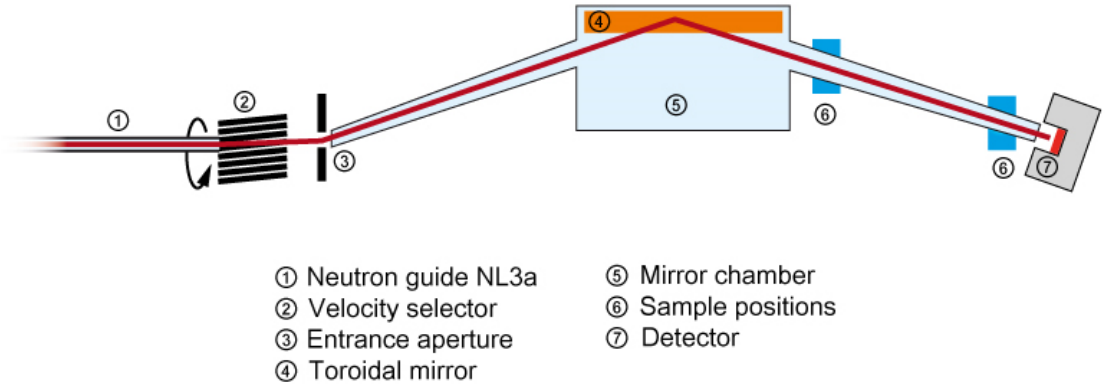

Figure 4.5 Schematic representation of VSANS instrument at KWS-3 located at MLZ, Garching, Germany. (Adapted from Ref. [142].)

Synchrotron small-angle X-ray scattering (SAXS). Synchrotron SAXS measurements were conducted at the high brilliance synchrotron beamline P12 at the European Molecular Biology Laboratory (EBML) at DESY, Hamburg [143]. The measurements were performed using an X-ray wavelength of λ = 0.124 nm and an SDD distance of 3.0 m; leading to a value of q in the range of 0.03-4 nm^{-1}. The scattering patterns were collected using a 2D Pilatus 2M detector. For each measurement, 20 frames were obtained as the solution was flowed continuously through a quartz capillary with a wall thickness of 50 μm and a path length of 1.7 mm using a robotic sample changer [144]. The exposure time of each frame was set as 45 ms. For each measurement, frames without significant differences caused by radiation damage were averaged, and they were then azimuthally integrated by the automated data processing pipeline SASFLOW [145]. The background signals of the solvent and quartz capillary were subtracted. The absolute scattering data of the samples were calibrated using pure water as a standard. All of the experiments were performed in transmission mode.

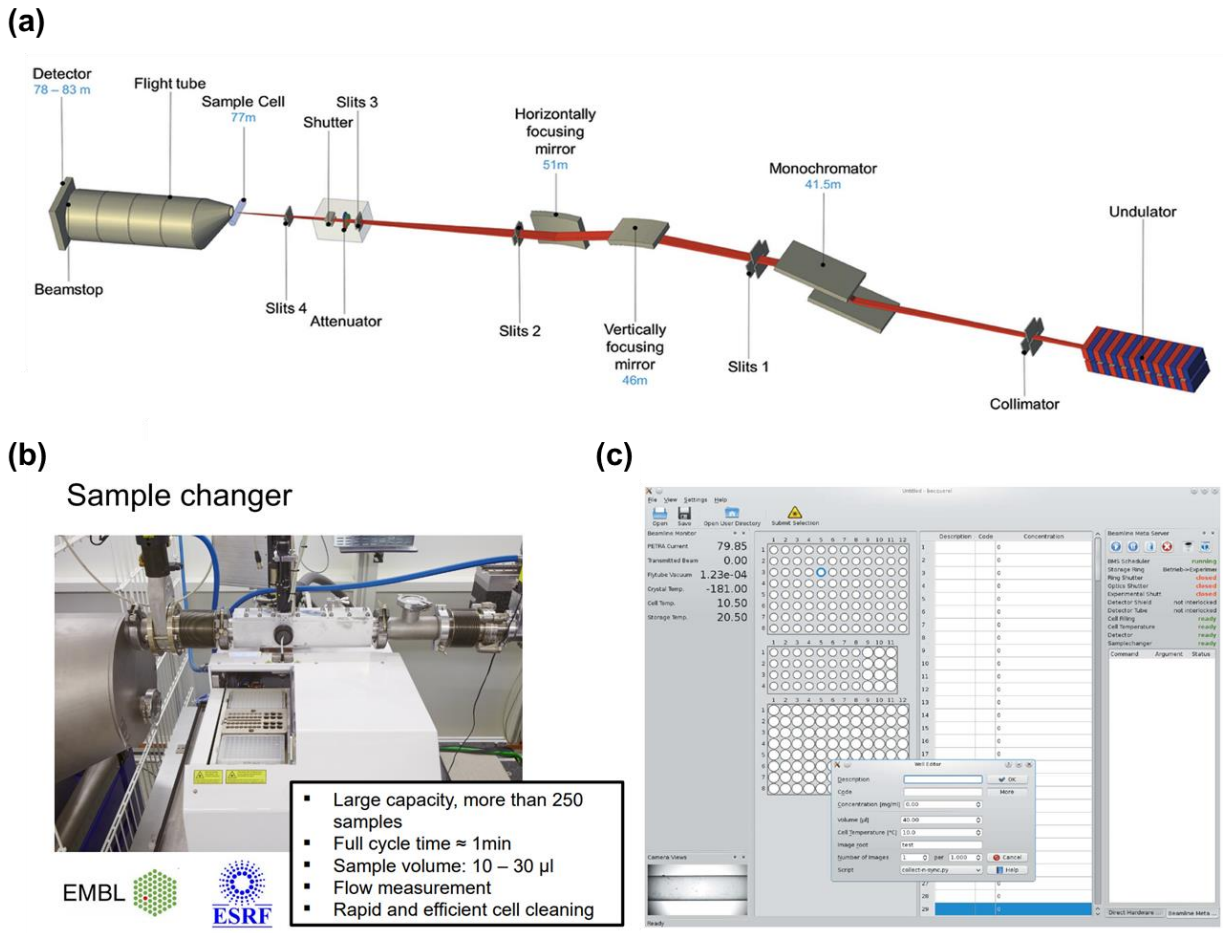

Figure 4.6 (a) Schematic representation of SAXS instrument at beamline P12 located at EMBL, Hamburg, Germany. (Reprinted from Ref. [143].) (b) Robotic sample changer. (Reprinted from Ref. [144].) (c) Screenshot of graphical user interface of P12 beamline. (Reprinted from Ref. [143].)

4.5 Data analysis in small-angle scattering

This section commences by introducing the model used to characterize the structure of PNIPAM homopolymer aqueous solution. The modeling of the molecularly-dissolved polymer chains of PMMA-*b*-PNIPAM is then discussed. Finally, the form factors and structure factors used for the self-assembled micelles produced by PMMA-*b*-PNIPAM are introduced.

4.5.1 Modeling of PNIPMAM homopolymers

Modified Porod term, $I_{agg}(q)$

In most cases, the modified Porod term, $I_{agg}(q)$, can be approximated by the following modified Porod term [146]:

$$I_{\mathrm{agg}}(q) = \frac{K_{\mathrm{P}}}{q^{P}} \tag{4.27}$$

which K_P is a scaling factor and P is the Porod exponent. For PNIPMAM aqueous solutions in a one-phase state, the Porod term describes the large-scale inhomogeneities, and the Porod exponent P describes the fractal dimension of large-scale inhomogeneities [147]. In the two-phase state, P describes the surface structure of the mesoglobules or aggregates, and has a value of $P = 4$ for smooth surfaces, $P < 4$ for rough surfaces and $P > 4$ for concentration gradients near the surface.

Gel term, $I_{gel}(q)$

The gel term, $I_{gel}(q)$, is frequently used to characterize the "frozen-in" crosslinks of gels [148], and is used in the present thesis to identify the size and amount of the static heterogeneities formed by the physical crosslinks in the PNIPMAM solution. The gel term, $I_{gel}(q)$, is given by

$$I_{\mathrm{gel}}(q) = I_{\mathrm{Gel}} exp\,(-\frac{q^2\Xi^2}{2}) \tag{4.28}$$

Where I_{Gel} is a scaling factor related to the quantity of static heterogeneities; and Ξ is the size of the static heterogeneities.

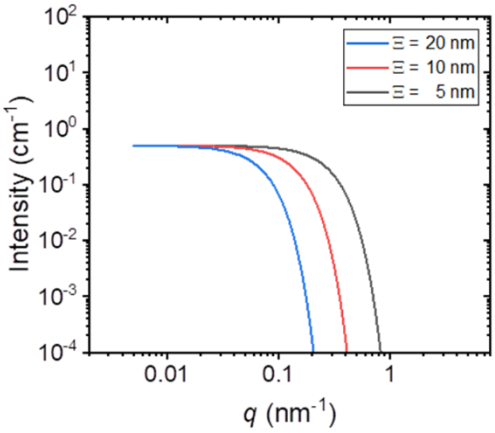

Figure 4.7 Examples of gel terms with different values of Ξ.

Modified Ornstein-Zernike term, $I_{\text{fluct}}(q)$

The term $I_{\text{fluct}}(q)$ is used to describe the chain scattering effect, and takes account of both the correlation length caused by local concentration fluctuations, ξ_{OZ}, and the interactions between polymer chains and the solvent molecules. The present thesis uses the following modified Ornstein-Zernike term [149]:

$$I_{\text{fluct}}(q) = \frac{I_{\text{OZ}}}{1 + (q\xi_{\text{OZ}})^m} \tag{4.29}$$

where I_{OZ} is a scaling factor, and m is the Ornstein-Zernike exponent associated with the chain conformation, which in turn reflects the interactions between the polymer chains and the solvent molecules. For $m = 2$, the normal Ornstein-Zernike function is recovered, which describes polymer chains with a Gaussian chain conformation [150]. However, for $m > 2$, the chains have a more compact local chain conformation due to a poorer solvent quality.

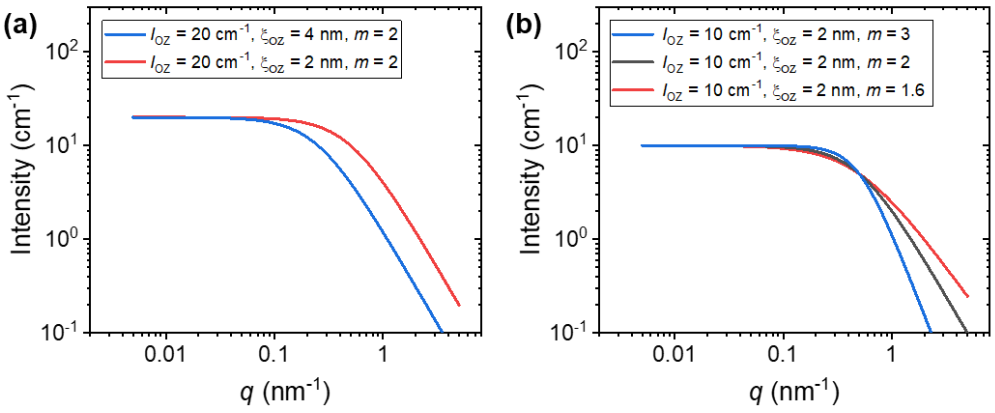

Figure 4.8 Examples of modified Ornstein-Zernike terms with different values of I_{OZ}, ξ_{OZ} and m.

Beaucage model

The Beaucage model combines the modified Porod term and the Guinier term to describe the scattering effect of the mesoglobules or aggregates as follows [151, 152]:

$$I(q) = G\exp\left(-\frac{q^2 {R_g}^2}{3}\right) + B\left\{\left[\mathrm{erf}\left(\frac{qR_g}{\sqrt{6}}\right)\right]^3 / q\right\}^{P'} + I_{bkg} \quad (4.30)$$

where G and B are scaling factors, R_g is the radius of gyration of the mesoglobules, P' is the Porod exponent characterizing the mesoglobule surface roughness [153, 154] and I_{bkg} is the incoherent background with a fixed value of 30 cm^{-1}. Finally, erf(x) is an error function designed to provide a smooth transition between the two contributions.

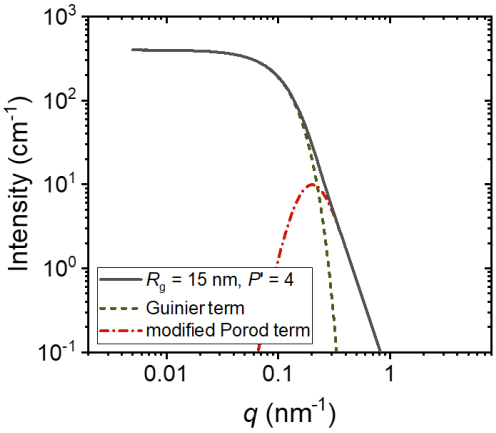

Figure 4.9 Examples of Beaucage model with R_g = 15 nm and P' = 4. Note that the contribution from the Guinier term is given by the green dashed line, while that from the modified Porod term multiplied by the error function is given by the red dashed-dotted line.

The invariant Q^*, used to further estimate the water fraction in the polymer-rich domains, was calculated as follows:

$$Q^* = \int_0^\infty I(q) q^2 dq \quad (4.31)$$

where $I(q)$ is the scattered intensity. For a two-phase system, Q^* reads:

$$Q^* = 2\pi\phi(1-\phi)(\Delta\rho)^2 \quad (4.32)$$

where ϕ is the volume fraction of the polymer-rich domains and $\Delta\rho$ is the scattering length density difference between polymer-rich and solvent-rich domains. It was calculated over the entire q range from the fitted Beaucage model (eq 4.30) without the I_{bkg} term.

4.5.2 Form factor of molecularly-dissolved polymer chains from PMMA-*b*-PNIPAM

For molecularly-dissolved polymer chains subject to an excluded volume assumption, the form factor, $P_{\text{chain}}(q)$, can be expressed as [155, 156]

$$P_{\text{chain}}(q) = 2\int_0^1 dx(1-x)exp\left[-\frac{q^2a^2}{6}n^{2\nu}x^{2\nu}\right] \tag{4.33}$$

where ν is the excluded volume parameter, and is related to the chain conformation exponent, m, by $\nu = 1/m$. In addition, a is the statistical segment length of the polymer chains and n is the degree of polymerization.

The integral expression in eq. 4.33 can be converted into the following rough analytical form. It reads [155]:

$$P_{\text{chain}}(q) = \frac{1}{\nu U^{1/2\nu}}\gamma\left(\frac{1}{2\nu}, U\right) - \frac{1}{\nu U^{1/\nu}}\gamma\left(\frac{1}{\nu}, U\right) \tag{4.34}$$

The incomplete gamma function, $\gamma(x, U)$, has the form

$$\gamma(x,U) = \int_0^U dt\ exp(-t)t^{x-1} \tag{4.35}$$

where U is a variable expressed in terms of the scattering momentum transfer q as follows:

$$U = \frac{q^2a^2n^{2\nu}}{6} = \frac{q^2{R_g}^2(2\nu+1)(2\nu+2)}{6} \tag{4.36}$$

The square of the radius of gyration of the molecularly-dissolved polymer chains is given by

$${R_g}^2 = \frac{a^2n^{2\nu}}{(2\nu+1)(2\nu+2)} \tag{4.37}$$

Finally, the chain conformation exponent, $m = 1/\nu$, describes the fractal dimension of the polymer chains, and has a value of $m < 2$ for swollen chains, $m = 2$ for ideal or Gaussian chains, and $m = 3$ for collapsed chains [155, 157].

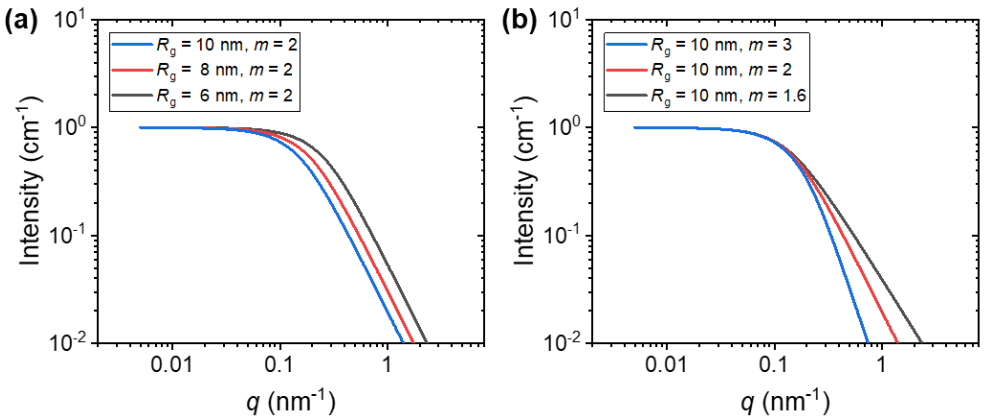

Figure 4.10 (a) Examples of form factors of molecularly-dissolved polymer chains with different values of R_g and m.

4.5.3 Form factors of self-assembled micelles from PMMA-*b*-PNIPAM

This section introduces the form factors used to characterize the shape and size of the self-assembled micelles formed by PMMA-*b*-PNIPAM.

Form factor of homogeneous spheres

The form factor for homogeneous spheres, $P_s(q)$, has the form [158]

$$P_s(q) = \frac{\phi}{V_{mic}}\left[3V_{mic}(\rho_{sphere} - \rho_{solvent})\frac{\sin(qR_{mic}) - qR_{mic}\cos(qR_{mic})}{(qR_{mic})^3}\right]^2 \tag{4.38}$$

where ρ_{sphere} is scattering length density (SLD) of the sphere.

Form factor of core-shell spheres with homogeneous shell

The common form factor for spherical core-shell particles with a homogenous shell SLD, $P'_{CS}(q)$, is expressed as [158]

$$P'_{CS}(q) = \frac{\phi}{V_{mic}}\left[3V_{core}(\rho_{core} - \rho_{shell})\frac{\sin(qR_{core}) - qR_{core}\cos(qR_{core})}{(qR_{core})^3} + 3V_{mic}(\rho_{shell} - \rho_{solvent})\frac{\sin(qR_{mic}) - qR_{mic}\cos(qR_{mic})}{(qR_{mic})^3}\right]^2 \tag{4.39}$$

where R_{core} is the radius of the micellar core, p_{core} is the polydispersity of the core, and R_{mic} is the radius of the micelles. Given the radius values of the micellar core and micelles, respectively, the shell thickness, t_{shell}, can be obtained directly by subtraction. The shell SLD, ρ_{shell}, remains constant along the radial direction and is set as a free fit parameter.

Form factor of core-shell spheres with inhomogeneous shell

The form factor for core-shell spheres, $P_{CS}(q)$, is given by [136]

$$P_{CS}(q) = \frac{1}{V_{mic}}[f_{core}(q) + f_{shell}(q) + f_{solvent}(q)]^2 \quad (4.40)$$

where V_{mic} is the volume of the micelles, and the individual terms in eq. 4.40 are defined as follows:

$$f_{core} = 4\pi \int_0^{R_{core}} \rho_{core} \frac{\sin(qr)}{qr} r^2 dr = 3\rho_{core} V_{core} \left[\frac{\sin(qR_{core}) - qR_{core}\cos(qR_{core})}{(qR_{core})^3}\right] \quad (4.41)$$

$$f_{shell} = 4\pi \int_{\Delta t_{shell}} \rho_{shell}(r) \frac{\sin(qr)}{qr} r^2 dr \quad (4.42)$$

$$f_{solvent} = 4\pi \int_{R_{mic}}^{\infty} \rho_{solvent} \frac{\sin(qr)}{qr} r^2 dr = 3\rho_{solvent} V_{mic} \left[\frac{\sin(qR_{mic}) - qR_{mic}\cos(qR_{mic})}{(qR_{mic})^3}\right] \quad (4.43)$$

where R_{core} is the radius of the micellar core, t_{shell} is the shell thickness of the micelles, R_{mic} is the radius of the micelles (i.e., $R_{mic} = R_{core} + t_{shell}$), and V_{core} is the volume of the micellar core. The polydispersity of the micellar core radius, p_{core}, is described by the following Schultz distribution [159, 160]:

$$G(R_{core}) = \frac{{R_{core}}^Z}{\Gamma(Z+1)} \left(\frac{Z+1}{\bar{R}_{core}}\right)^{Z+1} \times exp\left[-\frac{R_{core}}{\bar{R}_{core}}(Z+1)\right] \quad (4.44)$$

where $\bar{R}_{core}$ is the mean value of the micellar core radius, Z is associated with the width of the distribution, and $\Gamma(x)$ is the gamma function. The polydispersity of the micellar core radius, p_{core}, is given by

$$p_{core} = \frac{1}{(Z+1)^{\frac{1}{2}}} \quad (4.45)$$

This thesis investigates PMMA-*b*-PNIPAM diblock copolymers with PMMA blocks as core-forming blocks in D_2O solution. The scattering length densities (SLDs) of PMMA (ρ_{PMMA} = 10.82 × 10^{-6} Å^{-2}) and D_2O ($\rho_{solvent}$ = 9.44 × 10^{-6} Å^{-2}) are estimated in accordance with their mass densities of 1.18 and 1.10 g/cm^3, respectively. During model fitting, the SLD values of the core ρ_{core} and solvent $\rho_{solvent}$ are set as fixed parameters at equal to those of PMMA and D_2O, respectively.

The SLD of the shell ρ_{shell} (r) is described by the following exponential function:

$$\rho_{shell}(r) = \begin{cases} B \exp\left(\frac{-A_0\,(r - R_{core})}{t_{shell}}\right) + C & \text{for } A_0 > 0 \\ B\left(\frac{r - R_{core}}{t_{shell}}\right) + C & \text{for } A_0 = 0 \end{cases} \quad (4.46)$$

Where B and C are constants, which depend on the boundary conditions of the SLD value at the interfaces between the core and shell and shell and solvent, respectively. In addition, A_0 /t_{shell} is

associated with v_0, and determines the shape of the exponential function. Finally, ρ_{shell}^{o} is the SLD value at the interface between the core and the shell.

Once the SLD of the shell, $\rho_{\text{shell}}(r)$, has been determined, its contribution to eq. 4.42 is given by

$$f_{\text{shell}} = 4\pi \int_{\Delta t_{\text{shell}}} \rho_{\text{shell}}(r) \frac{\sin(qr)}{qr} r^2 dr = 4\pi \sum_{j=1}^{n_{\text{step}}} \rho_{\text{shell}}(r_j) \frac{\sin(qr)}{qr} r^2 dr$$

$$\approx 4\pi \sum_{j=1}^{n_{\text{step}}} \left[3\left(\rho_{\text{shell}}(r_{j+1}) - \rho_{\text{shell}}(r_j)\right) V(r_j) \left[\frac{{r_j}^2 {\beta_{out}}^2 \sin(\beta_{out}) - ({\beta_{out}}^2 - 2)\cos(\beta_{out})}{{\beta_{out}}^4} \right] - \right.$$

$$3\left(\rho_{\text{shell}}(r_{j+1}) - \rho_{\text{shell}}(r_j)\right) V(r_{j-1}) \left[\frac{{r_{j-1}}^2 {\beta_{out}}^2 \sin(\beta_{in}) - ({\beta_{in}}^2 - 2)\cos(\beta_{in})}{{\beta_{in}}^4} \right] +$$

$$\left. 3\rho_{\text{shell}}(r_{j+1}) V(r_j) \left[\frac{\sin(\beta_{out}) - \cos(\beta_{out})}{{\beta_{out}}^4} \right] - 3\rho_{\text{shell}}(r_j) V(r_j) \left[\frac{\sin(\beta_{in}) - \cos(\beta_{in})}{{\beta_{in}}^4} \right] \right] \quad (4.47)$$

where

$$V(a) = \frac{4\pi}{3} a^3 \quad (4.48)$$

with

$$a_{in} \approx \frac{r_j}{r_{j+1} - r_j} \; ; \; a_{out} \approx \frac{r_{j+1}}{r_{j+1} - r_j} \quad (4.49)$$

$$\beta_{in} = q r_j \; ; \; \beta_{out} = q r_{j+1} \quad (4.50)$$

In fitting of the SAXS curves, n_{step}, is assigned to a value of 45, and $\rho_{\text{shell}}(r)$ is approximated to be linear in each step.

In the present research, the PNIPAM blocks form the micellar shell. Once the SLD profile of the shell has been obtained, the D_2O content of the shell along the radial direction is calculated as follows:

$$\phi_{D_2O} = \frac{\rho_{\text{PNIPAM}} - \rho_{\text{shell}}(r)}{\rho_{\text{PNIPAM}} - \rho_{\text{solvent}}} \quad (4.51)$$

where ρ_{solvent} is the SLD value of D_2O (9.44×10^{-6} Å^{-2}) and ρ_{PNIPAM} is the SLD value of dry PNIPAM (10.30×10^{-6} Å^{-2}).

In addition, the aggregation number of the micelles, N_{agg}, is determined from the resulting core radius, R_{core}, as

$$N_{\text{agg}} = \left(\frac{N_{\text{av}}}{DP_{\text{PMMA}} \times V_{\text{PMMA}}}\right) \frac{4\pi}{3} {R_{\text{core}}}^3 \quad (4.52)$$

where N_{av} is the Avogadro number (6.02×10^{23} mol^{-1}), DP_{PMMA} is the degree of polymerization of the PMMA blocks, and V_{PMMA} is the molar volume (21×85.4 cm^3 mol^{-1}) [161].

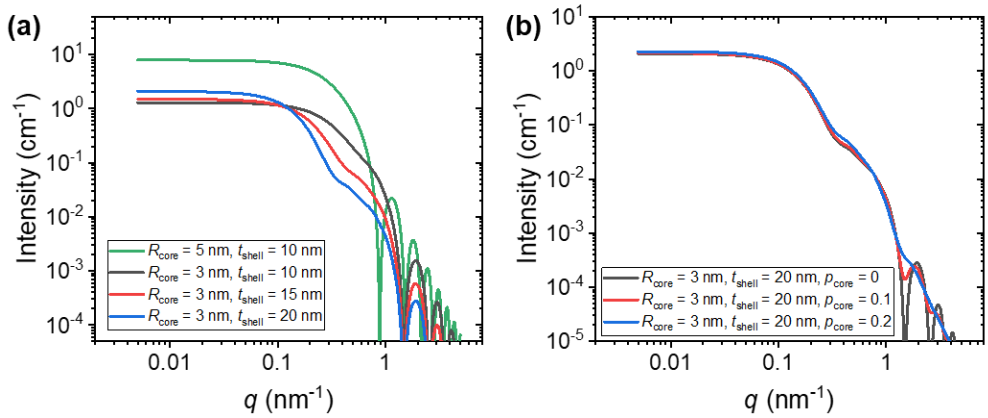

Figure 4.11 Examples of spherical core-shell form factors with inhomogeneous shell SLD with different values of R_{core}, t_{shell} and p_{core}. Note p_{core} = 0 in (a), and v_0 = 3 in (a) and (b). SLD values of the core ρ_{core} and solvent $\rho_{solvent}$ are assumed to be equal to the SLD values of PMMA (ρ_{PMMA} = 10.82 × 10^{-6} Å^{-2}) and D_2O ($\rho_{solvent}$ = 9.44 × 10^{-6} Å^{-2}), respectively. In addition, the SLD value at the interface between the core and the shell, ρ_{shell}^{o}, is assumed to be 9.60 × 10^{-6} Å^{-2}.

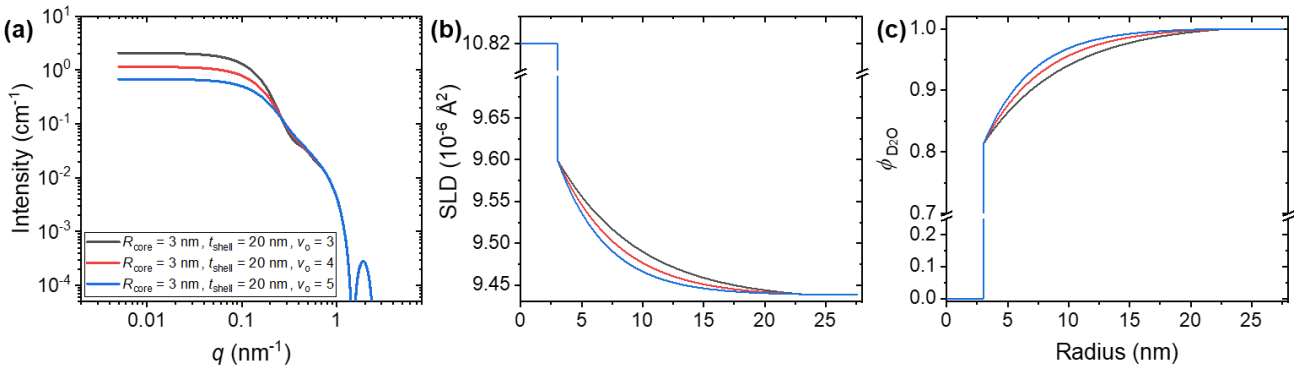

Figure 4.12 (a) Examples of core-shell spherical form factors with inhomogeneous shell SLD with different values of v_0. Note that p_{core} in (a) is zero. Resulting SLD profile (b) and D_2O content (c) along micellar radial direction. SLD values of the core ρ_{core} and solvent $\rho_{solvent}$ are assumed to be equal to the SLD values of PMMA (ρ_{PMMA} = 10.82 × 10^{-6} Å^{-2}) and D_2O ($\rho_{solvent}$ = 9.44 × 10^{-6} Å^{-2}), respectively. In addition, the SLD value at the interface between the core and the shell, ρ_{shell}^{o}, is assumed to be 9.60 × 10^{-6} Å^{-2}.

4.5.4 Structure factors

This section introduces the structure factors used in the present research to characterize the interactions between the correlated micelles formed by PMMA-*b*-PNIPAM.

Hard-sphere structure factor

The spatial correlation between the collapsed micelles is described using the Percus-Yevick hard-sphere structure factor, $S_{\mathrm{HS}}(q)$, which has the form [159, 162]

$$S_{\mathrm{HS}}(q) = \frac{1}{1 + 24\eta G(2R_{\mathrm{HS}}q)/(2R_{\mathrm{HS}}q)} \tag{4.53}$$

with

$$G(x) = \gamma \frac{\sin x - x\cos x}{x^2} + \delta \frac{2x\sin x + (2-x^2)\cos x - 2}{x^3} + \varepsilon' \frac{-x^4\cos x + 4(3x^2 - 6\cos x + (x^3 - 6x)\sin x + 6)}{x^5} \tag{4.54}$$

where the parameters γ, δ and ε' are given respectively by

$$\gamma = \frac{(1+2\eta)^2}{(1-\eta)^4}; \delta = \frac{-6\eta\left(1+\frac{\eta}{2}\right)^2}{(1-\eta)^4}; \varepsilon' = \frac{\gamma\eta}{2} \tag{4.55}$$

Referring to eq. 4.53, $S_{\mathrm{HS}}(q)$ gives R_{HS}, the half-distance between two correlated collapsed micelles, while η is the volume fraction of the correlated collapsed micelles.

The interparticle potential of the Percus-Yevick hard-sphere model, $u_{\mathrm{PY}}(r)$, is expressed as

$$u_{\mathrm{PY}}(r) = \begin{cases} \infty & r < 2R_{\mathrm{HS}} \\ 0 & r \geq 2R_{\mathrm{HS}} \end{cases} \tag{4.56}$$

Sticky hard-sphere structure factor

The sticky hard-sphere structure factor, $S_{\mathrm{SHS}}(q)$, is a perturbative solution of the Ornstein-Zernike equation with the Percus-Yevick closure relation, and is used to describe the intermicellar interactions with short-range attractive potentials. $S_{\mathrm{SHS}}(q)$ has the form [163, 164]

$$S_{\mathrm{SHS}}(q) = \frac{1}{A(q)^2 + B(q)^2} \tag{4.57}$$

where

$$A(q) = 1 + 12\eta\left[\alpha\frac{\sin\kappa - \kappa\cos\kappa}{\kappa^3} + \beta\frac{1-\cos\kappa}{\kappa^2} - \frac{\lambda'}{12}\frac{\sin\kappa}{\kappa}\right] \tag{4.58}$$

$$B(q) = 12\eta\left[\alpha\left(\frac{1}{2\kappa} - \frac{\sin\kappa}{\kappa^2} + \frac{1-\cos\kappa}{\kappa^3}\right) + \beta\left(\frac{1}{\kappa} - \frac{\sin\kappa}{\kappa^2}\right) - \frac{\lambda'}{12}\frac{1-\cos\kappa}{\kappa}\right] \tag{4.59}$$

in which parameters α and β are expressed as

$$\alpha = \frac{1 + 2\eta - \mu}{(1-\eta)^2}\ ;\ \beta = \frac{\mu - 3\eta}{2(1-\eta)^2}\ ;\ \mu = \lambda'\eta(1-\eta) \tag{4.60}$$

$$\lambda_\tau = \frac{1+\eta/2}{(1-\eta)^2} + \lambda' \left(\frac{\eta}{12} - \frac{\eta^2}{1-\eta} \right) ; \ \kappa = q(2R_{\mathrm{HS}} + \Delta) \tag{4.61}$$

Here, λ' is a parameter introduced by Baxter [163]. R_{HS} is the half-distance between two correlated micelles with short-range attractive interactions, and Δ is the well width of the square-well potential. In addition, η is equal to $\pi\rho(2R_{\mathrm{HS}}+\Delta)^3/6$, and is associated with the volume fraction of correlated micelles (ϕ), and ρ is the number density of the correlated micelles.

The "stickiness" parameter, τ_0, is related to the depth of the attractive potential well, and is given by

$$\tau_0 = \frac{1}{12\epsilon} \exp\left(-\frac{u_0}{k_B T}\right) \tag{4.62}$$

where the perturbation parameter, ϵ, is defined as

$$\epsilon = \frac{\Delta}{2R_{\mathrm{HS}} + \Delta} \tag{4.63}$$

in which k_{B} is the Boltzmann constant, T is the temperature, and u_0 is the depth of the attractive potential well in units of $k_{\mathrm{B}}T$. In the present research, ϵ is assigned a constant value of 0.05 in the fitting process.

The interparticle potential of the sticky hard-sphere model $u_{\mathrm{SHS}}(r)$ is given by

$$u_{\mathrm{SHS}}(r) = \begin{cases} \infty & r < 2R_{\mathrm{HS}} \\ -u_0 & 2R_{\mathrm{HS}} \le r \le 2R_{\mathrm{HS}} + \Delta \\ 0 & r > 2R_{\mathrm{HS}} + \Delta \end{cases} \tag{4.64}$$

In other words, a larger value of τ_0 give rise to a weaker the attractive interaction. Given τ_0, the reduced second virial coefficient, b_2, can be inferred simply as $b_2 = 1 - 1/(4\tau_0)$ [165, 166]. For $b_2 > 0$, a the repulsive interaction prevails. By contrast, for $b_2 < 0$, attractive interaction dominates.

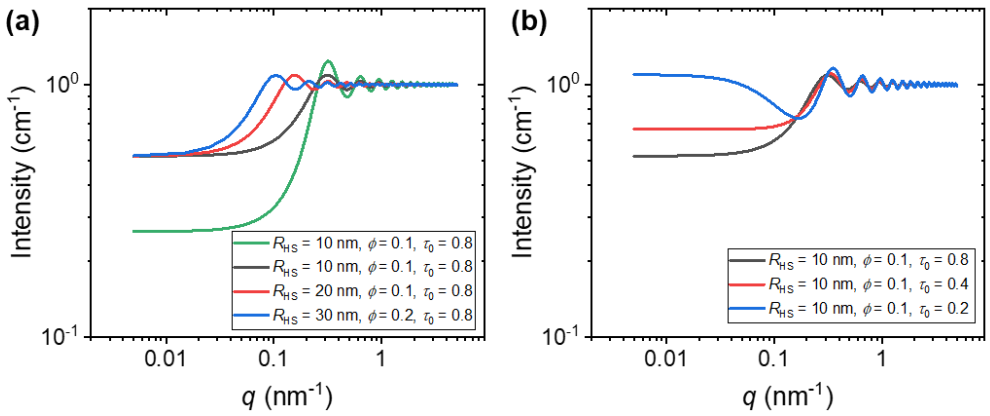

Figure 4.13 (a) Examples of sticky hard-sphere structure factors with different values of R_{HS}, ϕ, and τ_0.

Fractal structure factor

The fractal structure factor, $S_{\text{fractal}}(q)$, describes the clusters formed by the polydisperse core-shell micelles, and is expressed as [147]

$$S_{\text{fractal}}(q) = 1 + \frac{D_{\text{f}}\Gamma(D_{\text{f}} - 1)\sin\left[(D_{\text{f}} - 1)\tan^{-1}\left(q\xi_{\text{f}}\right)\right]}{(qR_{\text{mic}})^{D_{\text{f}}} \times \left(1 + \frac{1}{q^2{\xi_{\text{f}}}^2}\right)^{(D_f-1)/2}} \tag{4.65}$$

where D_{f} is the fractal dimension and ξ_{f} is the fractal correlation length. The radius of gyration of the clusters, R_{cluster}, is defined as [167]

$${R_{\text{cluster}}}^2 = \frac{D_{\text{f}}(D_{\text{f}} + 1){\xi_{\text{f}}}^2}{2} \tag{4.66}$$

4.5.5 Modeling of scattering from aggregates

In evaluating the scattering from the large aggregates formed by the collapsed micelles, the Porod term, I_{Porod} (q), is used to characterize the surface properties of the aggregates, i.e., [146].

$$I_{\text{Porod}} = \frac{I_{\text{P}}}{q^P} \tag{4.67}$$

where I_{P} is a scaling factor, and P is the Porod exponent, which indicates the surface properties of the aggregates, and has a value of $P = 4$ for a smooth surface, $3 < P < 4$ for a rough surface, and $P > 4$ for a surface with a concentration gradient [153, 154].

Finally, the size of the aggregates is evaluated using the Guinier function, $I_{\text{agg}}(q)$, which has the form [158]

$$I_{\text{agg}}(q) = I_{\text{G}} exp\left(-\frac{q^2{R_{\text{agg}}}^2}{3}\right) \tag{4.68}$$

where I_{G} is the scaling factor, and R_{agg} is the radius of gyration of the aggregates.

4.6 Turbidimetry

To identify the cloud points of the various polymer solutions, turbidimetry was performed using a 10 mW HeNe laser with a wavelength of 632.8 nm and a Si photodiode (Thorlabs, CITY). The samples were loaded in quartz glass cells (Hellma Analytics) with a light path length of 1 mm. The cells were inserted into an aluminum sample stage connected to a Julabo F12 thermostat (Julabo GmbH, Seelbach, Germany), and temperature scans were carried out at a heating rate of 0.2 K min^{-1} with a Pt100 resistance thermosensor attached directly to the stage. The transmitted light intensity was normalized to the maximum measured intensity to obtain the transmission of the sample. The cloud point temperature, T_{CP}, was then taken as the temperature at which the transmission reduced abruptly; indicating the collapse of the polymer chains.

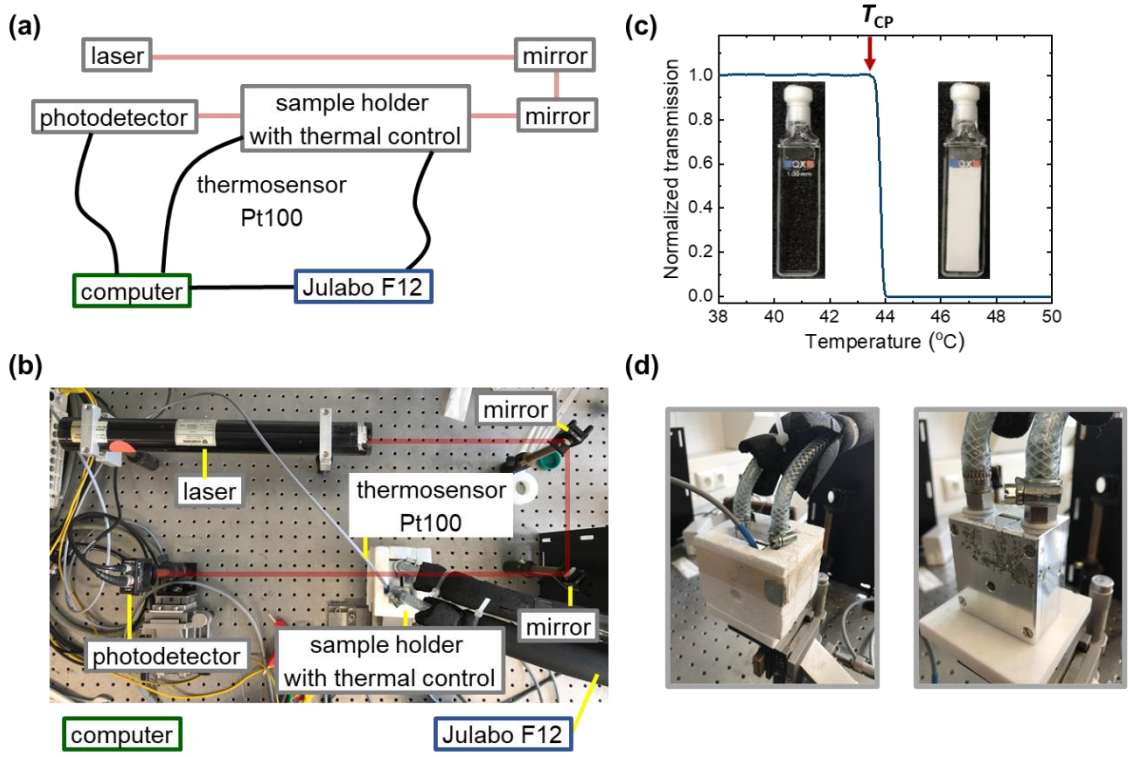

Figure 4.14 (a) Schematic representation of turbidimetry setup. (b) Photograph of turbidimetry setup. (c) Example of transmission data obtained at different temperatures. Note that the red arrow indicates the cloud point, T_{CP}, and the photographs show glass cells containing solutions below T_{CP} (left) and above T_{CP} (right), respectively. (d) Photographs of aluminum sample stage with (left) and without (right) thermal insulation by polystyrene foam.

4.7 Differential scanning calorimetry (DSC)

Differential scanning calorimetry (DSC) is a technique for analyzing the thermal properties of materials; particularly for polymeric materials. It is often used to determine the characteristic temperatures and enthalpies of the physical phase transition and chemical reaction of materials. (Full details of the DSC technique are presented in Ref. [168].)

4.7.1 Principles of DSC

Figure 4.15a presents a schematic illustration of a typical DSC setup, in which the sample and reference are placed in the same furnace and maintained at almost exactly the same temperature throughout the entire measurement process. The reference usually has the form of an inert material or empty crucible, and does not undergo any phase transition over the selected temperature range under investigation. During the measurement process, the sample and reference are treated at the same defined heating or cooling rate in the pre-selected temperature range under the assumption that the sample undergoes phase transition. The temperature difference between the sample and the reference is measured by two thermocouples as a function of time or temperature. For each thermocouple, the heat flow, Φ_{heat}, passes through thermal resistance R_{th} of the sensor, and the DSC signal is written as [168]

$$\Phi_{heat} = \frac{T_s - T_r}{R_{th}} = \frac{\Delta T}{R_{th}} \tag{4.69}$$

where T_s and T_r are temperatures of the sample and reference, respectively. Since the DSC signal is based on temperature differences are measured, the sensitivity of the thermocouple must be considered, i.e., $S = V_{th} / \Delta T$, where V_{th} is the thermoelectric voltage. In other words, the heat flow, Φ_{heat}, is expressed as

$$\Phi_{heat} = \frac{V_{th}}{R_{th} S} = \frac{V_{th}}{E} \tag{4.70}$$

where E is the calorimetry sensitivity, $E = R_{th} S$.

Figure 4.15b shows the typical DSC signal obtained from the heat flow difference between the sample and reference as a function of the time or temperature. For the case where the sample undergoes phase transitions involving endothermic or exothermic effects, such as melting, crystallization, chemical reaction, a prominent peak is formed in the DSC curve and the onset and end temperatures of the phase transition are identified as the intersection points of the tangents of the peak flanks on the extrapolated baseline. Similarly, the peak temperature of the phase transition is taken as the temperature corresponding to the maximum or minimum of the endothermic or exothermic peak.

Finally, the change in enthalpy of the phase transition, ΔH, is identified by integrating the peak area between the endothermic or exothermic peak and the baseline with respect to time, i.e.,

$$\Delta H = \int \Phi_{\text{heat}}\, dt \tag{4.71}$$

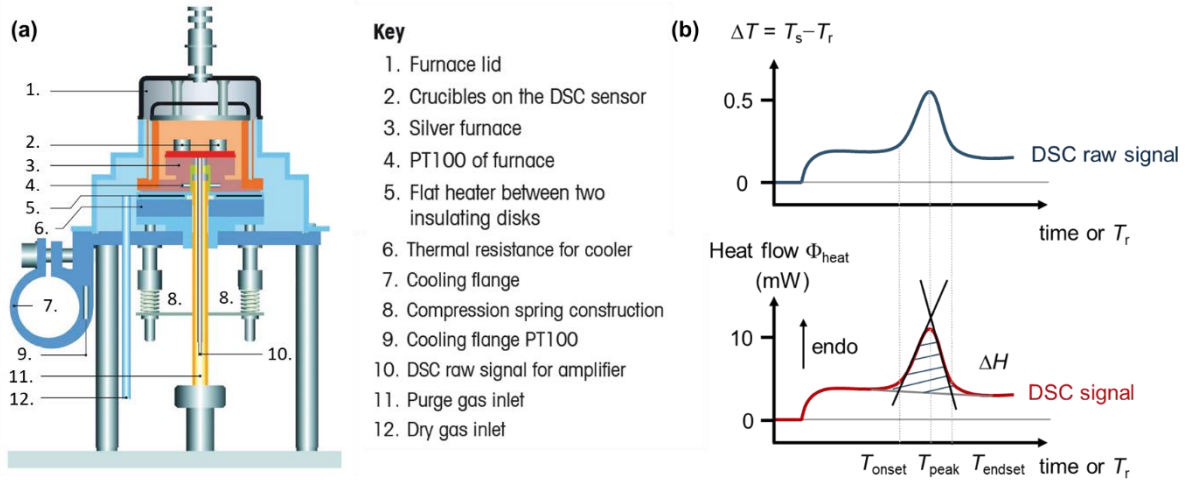

Figure 4.15 (a) Schematic representation of DSC setup. (Adapted from Ref. [169].) (b) Illustrative DSC curve and associated derivations.

4.7.2 Experimental instrument

In the present thesis, the DSC measurements were conducted using a DSC 3 STAR^e system from Mettler Toledo. The system was calibrated using indium and zinc, and nitrogen gas with a flow rate of 50 ml min^{-1} was employed as a standard atmosphere. The aqueous solutions were filled in a 40 µL aluminum pan, and an empty aluminum pan of an identical size was used as the reference sample. The measurements were carried out over a temperature range of T_{CP} - 20 °C to ~ T_{CP} + 20 °C °C. Each sample firstly underwent a heating and cooling cycle at a rate of 10 K min^{-1} to erase the thermal history. The characteristic temperatures were then determined from a second heating scan carried out at a lower rate of 1 K min^{-1}. As described above, the onset temperature of the phase transition was taken as the intersection of the extrapolated baseline with the tangent of the peak, and the peak temperature was taken as that corresponding to the maximum of the endothermic peak. Finally, the enthalpy of the phase transition was obtained from the area under the endothermic or exothermic peak and was normalized to the mass of the polymer solution to give units of J g$_s^{-1}$.

4.8 Raman spectroscopy

Raman spectroscopy is a spectroscopic method used to investigate the vibration modes of molecules, i.e., molecular interactions of samples. The Raman spectra obtained in the measurement process yield useful insights into both the structural properties and the dynamic properties of the investigated sample at the molecular scale. (Full details of the Raman spectroscopy technique are available in Refs. [170] and [171].)

4.8.1 Principles of Raman spectroscopy

Molecular vibration

Molecular vibration is defined as the periodic oscillation of the atoms in a molecule originating from the covalent bonds between them, which serve as springs. For a diatomic model with vibrating masses m_1 and m_2, the stretching vibration can be regarded as harmonic oscillation with a vibrational frequency, ν_F, of [172]

$$\nu_F = \frac{1}{2\pi}\sqrt{\frac{K_s}{\mu_m}} \tag{4.72}$$

where K_s is the spring constant and indicates the strength of the covalent bond between m_1 and m_2. In addition, μ_m is the reduced mass of the atoms, and is given by

$$\mu_m = \frac{m_1 m_2}{m_1 + m_2} \tag{4.73}$$

The stretching vibrational frequency of the molecular vibration in a diatomic molecule is sensitive to both the mass and the binding difference of the atoms, and therefore provides a useful insight into the structural information of the sample at a molecular scale. However, the local environment around the molecule also impacts on the strength of the covalent bonds between the atoms. Thus, the vibrational frequency also provides information on the interactions of the molecule with its environment.

In general, for a nonlinear molecule containing N atoms, the number of possible vibration modes is equal to $3N$-6. By contrast, for a linear molecule, e.g., polymer, the number of vibration modes is reduced to $3N$-5. Considering the large molecular mass of polymers, it is reasonable to expect the molecules to exhibit a huge number of vibration modes and complex vibrational spectra. However, due to the similarity in the repeating units of polymer materials, the total number of vibration modes is in fact quite limited. This phenomenon is proven by the fact that the vibrational spectra of a monomer and polymer, respectively, are similar to one another. In other words, the vibrational bands are assigned to the molecular vibrations of the functional groups, which are features of the repeating unit.

Spectroscopic methods

Infrared (IR), near-infrared (NIR) and Raman spectroscopy are all vibrational spectroscopic techniques used to investigate the molecular vibrations of the atoms in a molecule. However, their working principles are different. In particular, IR and NIR spectroscopy are based on the absorption of light, whereas Raman spectroscopy depends on the scattering of light. Figure. 4.16 shows the basic working principles of the three methods.

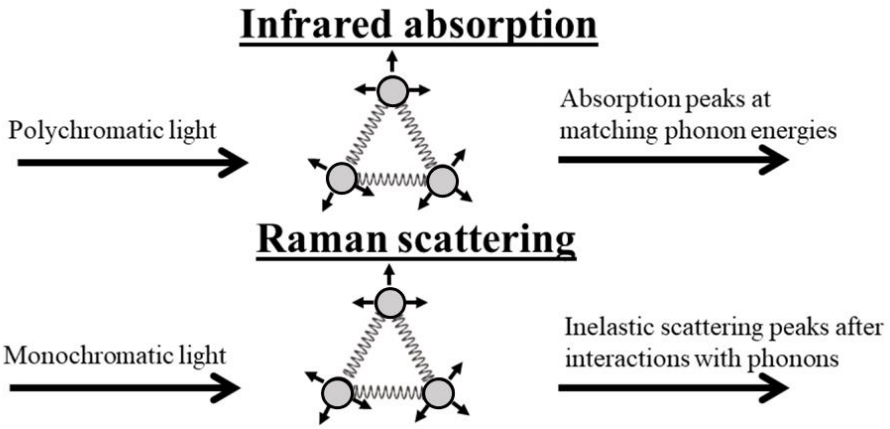

Figure 4.16 Overview of similarities and differences between IR/NIR spectroscopy and Raman spectroscopy [173].

For IR and NIR spectroscopy, polychromatic light is chosen as the incident light to interact with the sample. In practice, different vibration modes are assigned to the absorptions of the incident light at different wavelengths. Therefore, the transmittance spectra provide information on both the sample composition and the interactions between its components. For Raman spectroscopy, by contrast, the sample is illuminated by monochromatic laser light. When the incident light is scattered by the molecules in the sample, the majority of the incident light undergoes Rayleigh scattering, i.e., elastic scattering. That is, the frequency (or wavelength) of scattered light remains the same as that of the incident light (Figure 4.17). However, a small fraction of the scattered light has a slightly different frequency or wavelength from that of the incident light (Figure 4.18). This phenomenon is known as Raman scattering, i.e., inelastic scattering, and is referred to as Stokes Raman scattering when the scattered light has a lower frequency (i.e., a longer wavelength) than the incident light, or anti-Stokes Raman scattering when the scattered light has a higher frequency (i.e., a shorter wavelength). The frequency differences between the incident light and scattered light are related to the molecular vibration modes of the molecules in the sample under investigation. Due to its relatively higher

intensity in Raman scattering, the Raman spectrum at the Stokes side is usually recorded and used in experimental analyses (Figure 4.18).

Although the working principles of IR, NIR and Raman spectroscopy are fundamentally different, IR and Raman spectroscopy both probe the vibration modes over a similar frequency range (~ 200−4000 cm^{-1}). However, NIR spectroscopy probes the vibration modes at a higher frequency range (~ 4000−12500 cm^{-1}). In practice, the selection among IR, NIR and Raman spectroscopy as the experimental method depends mainly on the vibration modes of interest. For instance, the absorption of water is significantly strong in IR spectroscopy, which may hinder the analysis. By contrast, the Raman scattering of water is rather weak in Raman spectroscopy. As a result, Raman spectroscopy is more suitable for characterizing polymers in aqueous solutions. Consequently, in analyzing the present polymer aqueous solutions, this thesis deliberately adopts Raman spectroscopy as the characterization method.

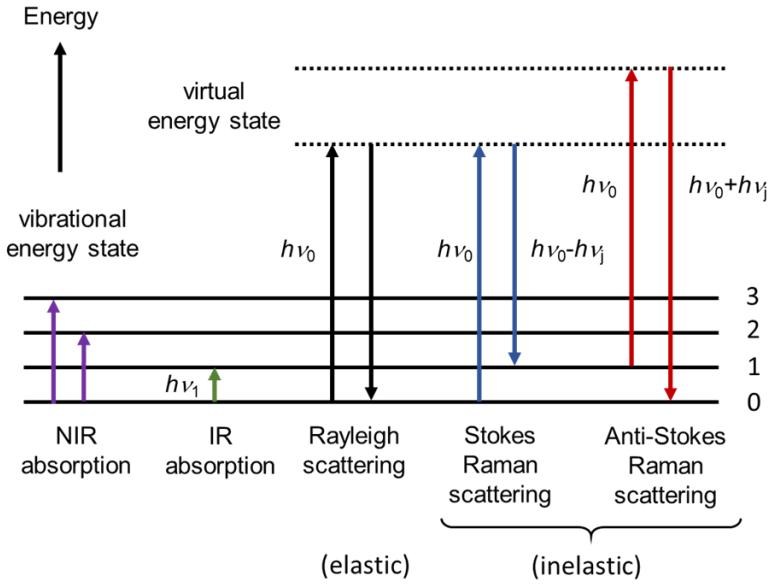

Figure 4.17 Spectroscopic transitions in several types of vibrational spectroscopy methods. Note that ν_0 is the frequency of the incident laser, while ν is the vibrational quantum number. The virtual energy state is a short-lived distortion of the electron distribution produced by the electric field of the incident laser [170].

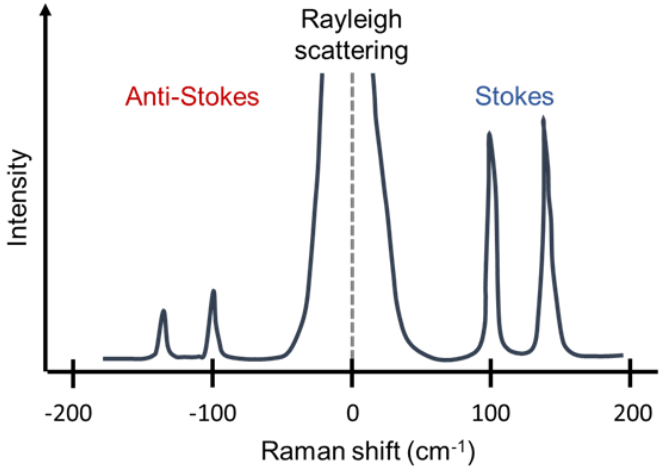

Figure 4.18 Schematic representation of Raman spectrum showing Rayleigh, Stokes and anti-Stokes scattering.

Raman scattering theory

In Raman spectroscopy, the incident photons are scattered by molecules, and a polarization of the molecule is induced by the oscillating electric field of the incident light. The induced dipole then radiates the scattered light with or without energy change with vibrational modes in the molecule. The strength of the induced polarization, P, can be expressed as

$$P = \alpha_{\mathrm{p}} E \tag{4.74}$$

where α_{p} is the polarizability and E is the incident electric field, which is time-dependent and defined as

$$E = E_0 \cos 2\pi \nu_0 t \tag{4.75}$$

where ν_0 is the frequency of the incident laser and t is the time.

When the incident photons are scattered by the molecules, the majority of the photons undergo Rayleigh scattering. In other words, the frequency of the scattered photons remains the same as that of the incident photons. In this case, the polarizability, α_{p}, is a constant. However, for the small fraction of incident photons which undergo Raman scattering, the polarizability, α_{p}, is no longer constant, but is modulated by the molecular vibration. For Raman scattering, α_{p} can be approximated as a Taylor series expansion, i.e.,

$$\alpha_{\mathrm{p}} = \alpha_{\mathrm{p},0} + \left(\frac{\partial \alpha_{\mathrm{p}}}{\partial x_{\mathrm{j}}}\right) x_{\mathrm{j}} + \cdots \tag{4.76}$$

In addition, the vibrational displacement of a particular vibration mode in a molecule, x, can be

expressed as

$$x_j = x_0 \cos 2\pi \nu_j t \tag{4.77}$$

From eq. 4.74, the polarization P is the product of eq. 4.75 and 4.76. After ignoring the higher-order terms in eq. 4.76, and noting that cos a cos b = [cos (a + b) +sin (a - b)]/2, the polarization, P, can be obtained as

$$P = \alpha_{p,0} E_0 \cos 2\pi \nu_0 t + E_0 \, x_0 \left(\frac{\partial \alpha_p}{\partial x_j}\right) \frac{\cos 2\pi(\nu_0 + \nu_j)t + \cos 2\pi(\nu_0 - \nu_j)t}{2} \tag{4.78}$$

As shown, the incident light is scattered with three different frequencies, ν_0, $\nu_0+\nu_j$, and $\nu_0-\nu_j$. The first term in eq. 4.78 describes Rayleigh scattering, while the second and third terms describe anti-Stokes and Stokes Raman scattering, respectively, in which the frequency of the scattered photons is either increased or decreased by the frequency of the vibration mode in the molecule, ν_j. In other words, the second and third terms only occur if the molecular vibration causes a change in polarizability.

Generally, $\alpha_{p,0}$ is much larger than ($\partial\alpha_p/\partial x_j$), which indicates that Rayleigh scattering is much stronger than Raman scattering (Figure 4.17). Therefore, one of the main experimental challenges involved in Raman spectroscopy is to separate the rather weak Raman scattering signal from the relatively stronger Rayleigh scattering signal. Furthermore, there exists an intensity difference between the Stokes and anti-Stokes scattering effects (Figure 4.18). The intensity ratio of the two scattering types is given by the Boltzmann factor, i.e.,

$$\frac{I_{\text{anti-Stokes}}}{I_{\text{Stokes}}} = \frac{(\nu_0 + \nu_j)^4}{(\nu_0 - \nu_j)^4} exp\left(-\frac{h\nu_j}{k_B T}\right) \tag{4.79}$$

where h is the Plank number, k_B is the Boltzmann constant, and T is the temperature. Due to the relatively high intensity, Raman spectroscopy generally records the spectrum at the side of Stokes scattering side.

4.8.2 Raman spectroscopy setup

Figure 4.19 presents a simple schematic illustration of the Raman spectroscopy setup. As shown, a laser light illuminates the sample through a microscope objective, which enables the incident light to be focused on a very small area of the sample surface with a size of just several μm^2. The scattered light travels through the sample path back into the experimental setup, where the Raman scattering signal is separated from the Rayleigh scattering signal by a filter and is then diffracted by a grating. Finally, the diffracted light is incident on a CCD detector, which records the signals of the photons with different frequencies (or wavelengths) at different positions, hence enables the different vibration

modes in the sample to be differentiated.

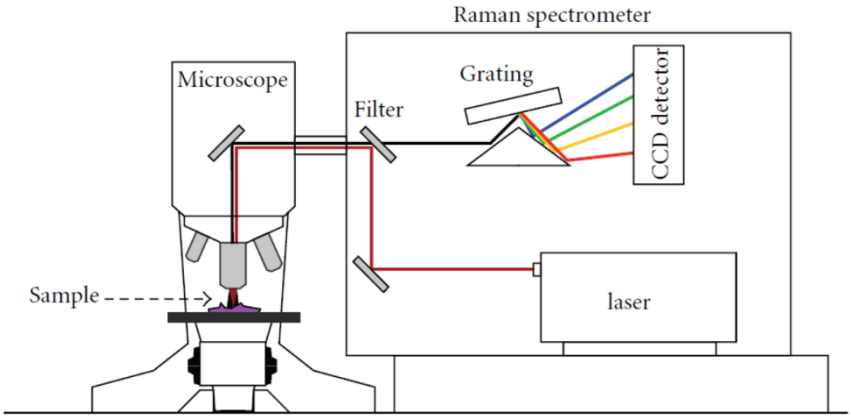

Figure 4.19 Schematic representation of Raman setup. (Adapted from Ref. [174].)

4.8.3 Data analysis of Raman spectroscopy

The Raman spectra provide valuable insights into the molecular composition of the investigated sample. For example, the characteristic peaks in the Raman spectra appear at frequencies correlated with the energies of the vibration modes of the molecules. Therefore, analyzing the Raman spectra yields an understanding of the chemical composition of the molecules. However, the local environment conditions surrounding the molecules, e.g., the molecular hydration, also affect the appearance of the Raman spectra, including the frequency, shape and width of the peaks associated with different vibration modes of the molecules.

Frequency of Raman peak.

The vibration modes of a molecule are affected by its neighboring atoms since these atoms may induce differences in the local charge density distribution. For example, a change in the electron density between two atoms affects the strength of the covalent bond between them, and leads to a corresponding change in the frequency of the related vibration mode. In practice, the interaction effects on the peaks in the Raman spectrum depend strongly on the type of interaction and the involved atoms, and tend to vary from case by case.

Width of Raman peak.

Generally, the measured photons are characteristic of a distribution of energy, which is attributed to the “natural broadening” effect [175], and is an intrinsic trait of Raman scattering that arises from the uncertainty of the excitation energy, E. Based on the Heisenberg uncertainty principle, the uncertainty of E is given by

$$\Delta E\ \tau_v \geq \frac{h}{2} \tag{4.80}$$

with τ_v is the lifetime of the vibration state and h is the Planck constant.

In this case, the Raman signal can be described by the Lorentzian function

$$L(\nu_F) = \frac{1}{2\gamma_L} \frac{{\gamma_L}^2}{\left[\left(\nu_F - \nu_{F,0}\right)^2 + {\gamma_L}^2\right]} \tag{4.81}$$

where $\nu_{F,0}$ is the mean frequency and γ_L is the Lorentzian width.

Collisions between molecules or network formations also lead to a broadening effect. Thus, an increase in the uncertainty of the excitation energy, and a broader width of the measured Raman signal, is observed. In this case, the Raman spectrum also follows a Lorentzian function.

Thermal motion of the molecules also leads to a broadening effect. In particular, the Doppler effect, originating from the velocity of the molecules, results in a difference of the observed excitation energy. Consequently, a spectrum with a broadening effect stemming from thermal motion of the molecules can be described by the following Gaussian function [175]:

$$G(\nu_F) = \frac{1}{\sqrt{2\pi{\sigma_G}^2}} exp\left(-\frac{\left(\nu_F - \nu_{F,0}\right)^2}{2{\sigma_G}^2}\right) \tag{4.82}$$

with σ_G is the Gaussian width.

In practical Raman spectroscopy experiments, all of the mechanisms described above which contribute to a broadening effect may be observed. Thus, the following Voigtian function, which is a convolution of the Lorentzian and Gaussian functions, is commonly applied:

$$V(\nu_F) = \int L(\nu_F') \cdot G(\nu_F - \nu_F')\, d\nu_F' \tag{4.83}$$

Figure 4.20 shows typical Lorentzian, Gaussian, and Voigtian functions, respectively. It is seen that the functions differ mainly in their wings. For example, the Gaussian function decays more sharply than the Lorentzian function, while Voigtian function decays in-between.

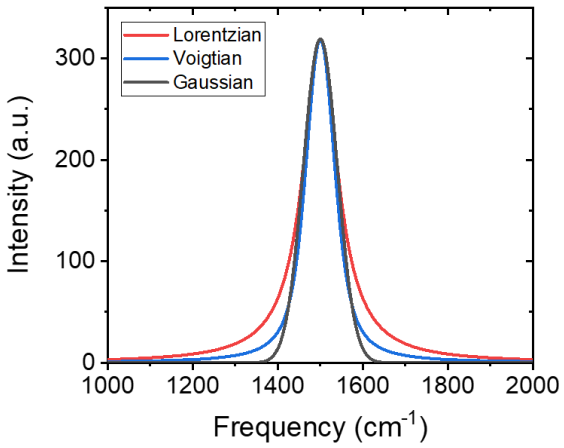

Figure 4.20 Example of Lorentzian (red line), Voigtian (blue line) and Gaussian (black line) functions with similar widths and peak frequency of 1500 cm^{-1}.

4.8.4 Experimental instrument

Optical microscopy and Raman spectroscopy were carried out using the setup described in Ref. [25]. In the present research, the Raman spectra were acquired using a LabRam HR 800 system (JY Horiba) with a HeNe laser with a wavelength of 632.8 nm as the excitation source. The spectra were recorded at a resolution of 2 cm^{-1} with a laser power of less than 3 mW at the sample position and a spot size of 1.5 µm. The polymer solutions were loaded in fused silica micro capillaries with a square cross-section (edge length 100 µm). In the measurement process, the capillaries were embedded in a copper stage connected to a circulating water bath thermostat. The sample temperature was measured by a Pt100 resistance thermosensor attached to the stage. The spectra were obtained with an integration time of 120 s, and the dark current was subtracted before the deconvolution of the spectrum was deconvoluted. The resulting Raman spectra in the frequency region of 2200 to 3100 cm^{-1} were fitted by a superposition of three Gaussian functions assigned to several OD-vibration modes and four Lorentzian functions attributed to various CH-stretching modes. An example of deconvolution of frequency range from 2200 to 3100 cm^{-1} is shown in Figure 4.21.

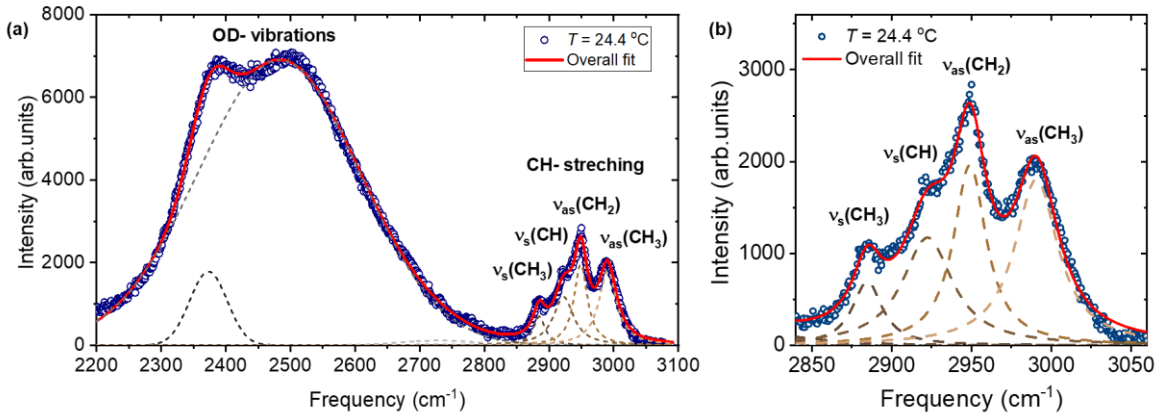

Figure 4.21 (a) Example for the deconvolution of the Raman spectra at 24.4 °C. (b) Zoom of (a) in the deconvolution frequency range from 2850 to 3100 cm^{-1}. Blue open circles: experimental data, full red line: overall fit. Grey dotted lines: individual contributions of the Gaussian distributions. Brown dashed lines: individual contributions of the Lorentzian distributions. (Reprinted from Ref. [124]. Copyright (2020) American Chemical Society.)

We aim to focus on the hydrophobic interactions in the CH-stretching region with frequency range from 2850 to 3100 cm^{-1} (Figure 4.21b). The Gaussian functions were only used to account for the possible overlap of the OD-vibration modes with the CH-stretching region, and are not supposed to give a precise description of the vibration modes in water in the OD-vibration region. Therefore, only the spectral bands in the CH-stretching region with frequency range from 2850 to 3100 cm^{-1} are further discussed.

Prior to obtaining each Raman spectrum, an OM image was taken in the same setup using an Olympus X41 microscope equipped with a CCD camera. Heating scans were then conducted from 24 to 50 °C in steps of 1-2 °C with a thermal equilibration time of 5 min before each measurement. The T_{CP} of the solution was then determined as the average temperature between the temperature just before mesoglobules appeared and the temperature at which mesoglobules they were present, as observed by the OM. As small offset was noted in the temperature measured by the Pt100 resistance thermosensor and the sample temperature; with the latter being a few °C lower. It was speculated that this discrepancy was most probably heat losses of the microscope objective.

5. Phase behavior of PNIPMAM in aqueous solutions

In this chapter, the temperature-dependent phase behavior of the thermoresponsive polymer Poly(*N*-isopropylmethacrylate) (PNIPMAM) in aqueous solution is investigated. At this, turbidimetry, differential scanning calorimetry (DSC), small-angle and very small-angle neutron scattering (SANS and VSANS), Raman spectroscopy measurements are performed. The work presented in this chapter was published in ” Temperature-Dependent Phase Behavior of the Thermoresponsive Polymer Poly(*N*-isopropylmethacrylamide) in an Aqueous Solution” C.-H. Ko et al. *Macromolecules* **2020**, *53*, 6816–6827 [124].

5.1 Introduction

A $PNIPMAM_{195}$ sample in a 50 g L^{-1} solution in D_2O was previously studied by Vishnevetskaya et al. [176]. Due to the rather hydrophobic fluorescence tag used for molar mass characterization, T_{CP} was obtained at a low value of 38.0 °C. At temperatures below T_{CP}, the SANS data were notably more complicated than the SANS data of PNIPAM. Apart from the typically observed chain scattering, inhomogeneities were found at intermediate length scales. In addition, large aggregates were observed. At temperatures just above T_{CP}, scattering from single chains was observed. The collapsed polymer chains from large and compact aggregates. At temperatures far above T_{CP}, single chain scattering was significantly weakened. Very large and compact aggregates dominated. These phenomena took place only in PNIPMAM solutions instead of in PNIPAM solutions. This was due to an improved hydrophobic effect caused by the additional methyl groups.

The phase behavior of PNIPMAM in aqueous solution have investigated by several research groups. However, in most cases, only single samples were investigated or only one or two characterization methods were used. In this chapter, we carry out a systematic investigation of the phase behavior of PNIPMAM in aqueous solution in a wide concentration range (2-150 g L^{-1}). Different aspects of the phase transition are addressed by a few techniques: turbidimetry identifies the T_{CP} values of the solutions. Optical microscopy enables us to observe the phase-separated structures. DSC characterizes the thermal behavior of the phase transition. SANS and VSANS provide structural information on broad-ranging length scales. Raman spectroscopy probes the hydrophobic hydration behavior around the phase transition. Ultimately, all results are summarized. A comprehensive picture of the morphological transition of PNIPMAM aqueous solutions is presented.

5.2 Phase behavior

By means of turbidimetry, the phase diagram of the PNIPMAM solutions in D_2O is constructed. The cloud points T_{CP} of the solutions in the concentration range 2-150 g L^{-1} are determined. A very slow heating rate of 0.2 K min^{-1} is used to prevent non-equilibrium conditions. Figure 5.1a displays the transmission curves. Below T_{CP}, the normalized transmission remains constantly at a value of one, indicating that the solutions are clear and transparent. At T_{CP}, the transmission undergoes a sudden drop, meaning that the solutions become turbid. This is attributed to the formation of large mesoglobules. For the solutions in the concentration range 5-150 g L^{-1}, their phase transitions are all relatively sharp. For the solution at the lowest concentration of 2 g L^{-1}, the phase transition is broad, and the transmission above T_{CP} keeps slightly above zero. The T_{CP} values are observed in the range 42-45 °C (Figure 5.1b, Table 5.1). As increasing polymer concentration, the T_{CP} values are decreased, as expected for LCST type polymers of rather low concentration. The T_{CP} values agree with the reported values in other studies (mostly ~43 °C) [32, 34, 36]. This confirms that the type-II behavior of PNIPMAM solutions. As a result, the cloud points of our sample do not seem to be notably affected by its rather low molar mass (M_n^{app} = 17,000 g mol^{-1}) and relatively high dispersity ($Đ$ = 1.74).

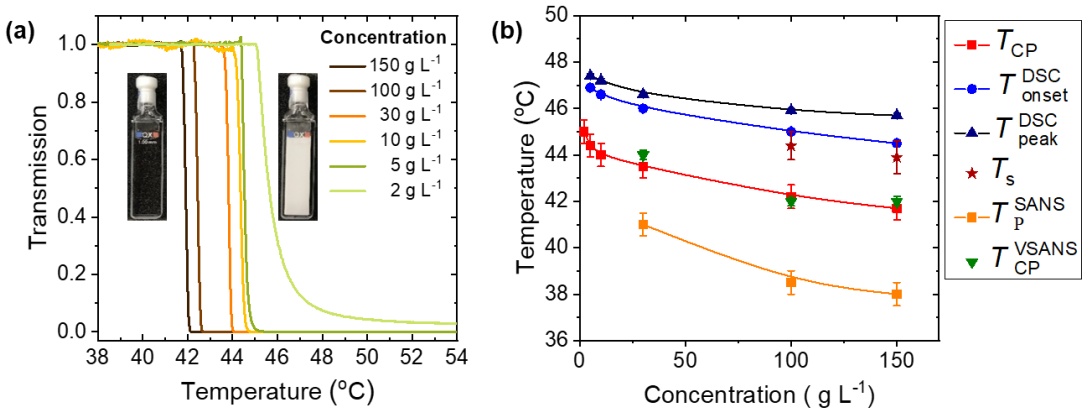

Figure 5.1 (a) Light transmission of PNIPMAM solutions in D_2O in dependence on temperature at a heating rate of 0.2 K min^{-1}. The concentrations are given in the graph. The photos show solutions of the 30 g L^{-1} solution below (left) and above the phase transition (right). (b) Cloud points determined by turbidimetry, onset and peak temperatures from DSC, spinodal temperatures T_s from the Ornstein-Zernike structure factor in SANS and the transition temperatures determined from the Porod exponent and from VSANS, as indicated in the graph. (Reprinted from Ref. [124]. Copyright (2020) American Chemical Society.)

Table 5.1 Results from turbidimetry, DSC and VSANS measurements

Concentrations (g L^{-1})	T_{CP} (°C)	T_{onset}^{DSC} (°C)	T_{peak}^{DSC} (°C)	ΔH (J/g_s)	T_{CP}^{VSANS}(°C)
2	45.0 ± 0.5	-	-	-	-
5	44.4 ± 0.5	46.9 ± 0.2	47.4 ± 0.1	0.17 ± 0.02	-
10	44.0 ± 0.5	46.6 ± 0.2	47.2 ± 0.1	0.39 ± 0.02	-
30	43.5 ± 0.5	46.0 ± 0.2	46.6 ± 0.1	1.29 ± 0.02	44.0 ± 1.0
100	42.2 ± 0.5	45.0 ± 0.2	45.9 ± 0.1	4.54 ± 0.02	42.0 ± 1.0
150	41.7 ± 0.5	44.5 ± 0.2	45.7 ± 0.1	6.40 ± 0.02	42.0± 1.0

5.3 Thermal behavior

DSC measurements were performed in the concentration range 5-150 g L^{-1}. The thermograms are shown in Figure 5.2a. As the temperature is increased, endothermic peaks are observed at 45-47 °C. The onset temperature and the peak temperature of the endothermic phase transition are presented in Figure 5.2b and Table 5.1. Both T_{onset}^{DSC} and T_{peak}^{DSC} decrease with increasing concentration, as found previously [41, 177]. This is also in accordance with the findings from turbidimetry. However, T_{onset}^{DSC} is generally 2-3 °C higher than T_{CP} from turbidimetry. T_{onset}^{DSC} is related to dehydration, whereas T_{CP} is associated with turbidity. Hence, as temperature is increased, the polymer chains in PNIPMAM solutions firstly form large mesoglobules at $T_{CP} \cong$ 42-45 °C and then they dehydrate 2-3 °C above (at $T_{onset}^{DSC} \cong$ 45-47 °C). The enthalpies of the phase transition, ΔH, are obtained by the areas of endothermic peaks. In the studied concentration range, the ΔH values depend linearly on polymer concentration. From the slope, the enthalpy of the polymer independent of concentration is derived as $\Delta H_p = 0.043 \pm 0.006$ J g_s^{-1}/g L^{-1}. Presumably, these findings are only marginally influenced by the dispersity, if at all.

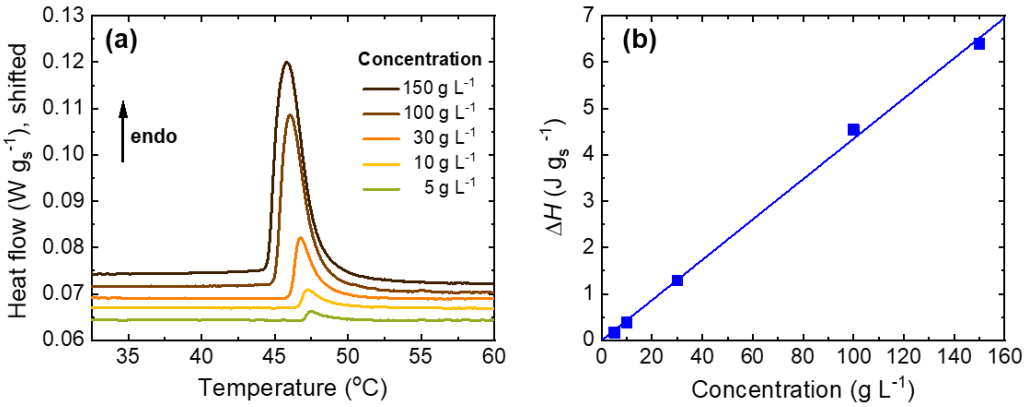

Figure 5.2 (a) DSC thermograms of PNIPMAM solutions in D_2O at a heating rate of 1 K min^{-1} at the concentrations given in the graph. For better visibility, the curves of 100 and 150 g L^{-1} are shifted vertically by 0.0030 and 0.0045, respectively. (b) Resulting concentration-dependent endothermic enthalpy ΔH (symbols). Line: linear fit. (Reprinted from Ref. [124]. Copyright (2020) American Chemical Society.)

5.4 Structural properties around the cloud point

Optical microscopy (OM) provides first insights into the phase-separated structures formed by PNIPMAM in an aqueous solution. Figure 5.3 displays the OM images of a 150 g L^{-1} PNIPMAM solution in D_2O. Below T_{CP}, the solution is homogeneous and transparent (Figure 5.3a). At T_{CP}, mesoglobules with diameters of ~2 µm are observed (Figure 5.3b). Upon heating, the size of mesoglobules increases (Figure 5.3c and d).

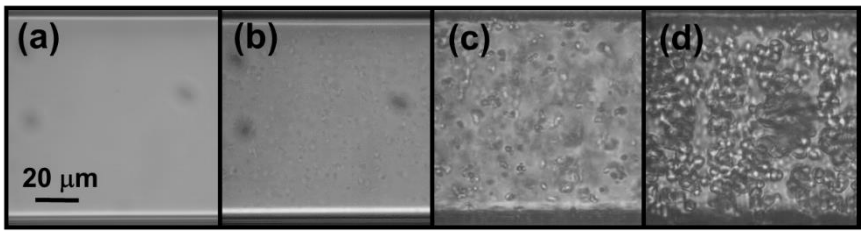

Figure 5.3 OM images of a 150 g L^{-1} PNIPMAM solution in D_2O below T_{CP} (a), at T_{CP} (b), just above T_{CP} (c), and far above T_{CP} (d). The dark spots in (a) and (b) are due to the background. (Reprinted from Ref. [124]. Copyright (2020) American Chemical Society.)

Small-Angle Neutron Scattering (SANS) is employed to study the temperature-dependent mesoscopic structures of PNIPMAM in D_2O. To probe the structures at length scales of ~1-100 nm, SANS measurements are performed. It is not possible in OM to resolve structures at such small length scales. Representative SANS curves from solutions with concentrations of 30, 100 and 150 g L^{-1} are

displayed in Figure 5.4. Below T_{CP}, the scattering curves have a decay at 0.03 – 0.06 nm^{-1} and a shoulder at 0.2 – 2.0 nm^{-1}, which are called "forward scattering" and "chain scattering", respectively. The intensity of the forward scattering increases with increasing temperature. This suggests that large-scale inhomogeneities exist already below T_{CP} and become more pronounced as temperature is raised towards T_{CP}. The intensity of the chain scattering, which is originated from local concentration fluctuations in the semi-dilute polymer solutions, also increases upon heating towards T_{CP}. Above T_{CP}, the intensity of the forward scattering is significantly higher, which attributed to the formation of mesoglobules. However, the intensity of the chain scattering decreases severely upon heating, indicating that the contribution from large mesoglobules prevails.

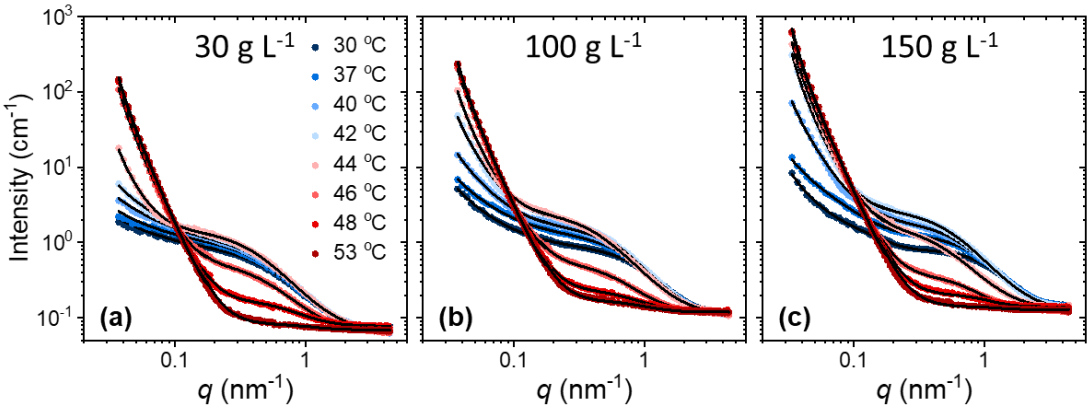

Figure 5.4 Representative SANS data of the (a) 30 g L^{-1}, (b) 100 g L^{-1}, and (c) 150 g L^{-1} PNIPMAM solutions in D_2O (symbols) at temperatures as given in (a). Blue and red color indicate temperatures below and above T_{CP} from turbidimetry, respectively. Black lines: fitting curves. (Reprinted from Ref. [124]. Copyright (2020) American Chemical Society.)

In general, the scattering curves of semi-dilute polymer solutions in the one-phase state only feature chain scattering and very weak forward scattering. For example, the scattering curves of aqueous PNIPAM solutions. Therefore, they are often well described by the (normal) Ornstein-Zernike model with the OZ exponent of 2 [150, 178]. Nevertheless, the SANS curves of aqueous PNIPMAM solutions cannot be successfully fitted with only this model, as displayed in Figure 5.5. This result is in accordance with our previous results [176]. This can be attributed to the fact that the forward scattering is caused by the presence of more pronounced large-scale inhomogeneities. In addition, for 100 and 150 g L^{-1} between 30 and 37 °C, an additional "bump" is observed at $q \cong 0.1$ nm^{-1}, which is possibly due to the structures caused by physical crosslinks of the hydrophobic groups. Moreover, the feature of the chain scattering at $q \cong 0.2 – 2.0$ nm^{-1} is dissimilar to the normal Ornstein-Zernike model. The negative slope of the decay is larger than 2 (Figure 5.5), suggesting a more compact local chain

conformation, presumably due to attractive segment-segment interactions. Thus, the model function given in eq. 5.1 is employed to analyze the SANS curves quantitatively in the one-phase state instead of the Ornstein-Zernike model.

$$I(q) = I_{\mathrm{agg}}(q) + I_{\mathrm{gel}}(q) + I_{\mathrm{fluct}}(q) + I_{\mathrm{bkg}} \tag{5.1}$$

It features a modified Ornstein-Zernike term, $I_{\mathrm{fluct}}(q)$, which explains non-ideal chain conformations, a Porod term, $I_{\mathrm{agg}}(q)$, accounting for the forward scattering from large inhomogeneities, and a gel term, $I_{\mathrm{gel}}(q)$, describing the bump at $q \cong 0.1$ nm^{-1} due to physical crosslinks. Excellent fits are obtained, as demonstrated in Figure 5.4. The contributions and the full fit are shown in Figure 5.6a and b. At temperatures just below T_{CP}, the amplitude of the gel term is insignificant. Thus, it is neglected. In these cases, eq. 5.1 without the gel term is chosen instead. The same model is used for all temperatures at 30 g L^{-1}.

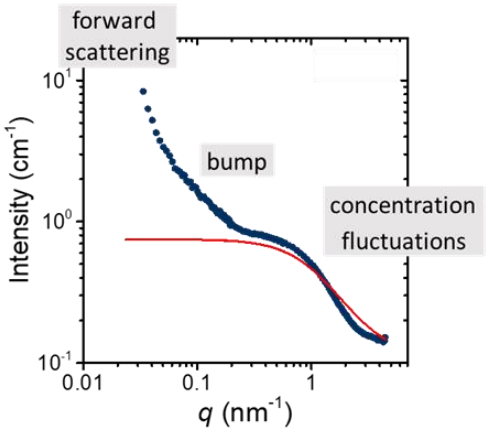

Figure 5.5 SANS data of the 150 g L^{-1} PNIPMAM solution in D_2O at 30 °C (symbols). Red solid line: plot of the (normal) Ornstein-Zernike (OZ) structure factor with the OZ exponent of 2. The grey labels indicate the respective contributions of forward scattering, bump and concentration fluctuations. (Reprinted from Ref. [124]. Copyright (2020) American Chemical Society.)

Likewise, the scattering curves of semi-dilute polymer solutions in the two-phase state (e.g., from aqueous PNIPAM solutions) are typically fitted by a model consisting of the Porod law and the normal Ornstein-Zernike model. The Porod law describes the scattering from large mesoglobules, while the normal Ornstein-Zernike model accounts for local concentration fluctuations [150, 178]. For PNIPMAM solutions, a similar model (eq. 5.1 without the gel term) is applicable for fitting all the scattering curves in the two-phase state, namely the sum of the Porod term, $I_{\mathrm{agg}}(q)$, and the modified Ornstein-Zernike term, $I_{\mathrm{fluct}}(q)$. Excellent fits are obtained in all cases (Figures 5.4 and 5.6b).

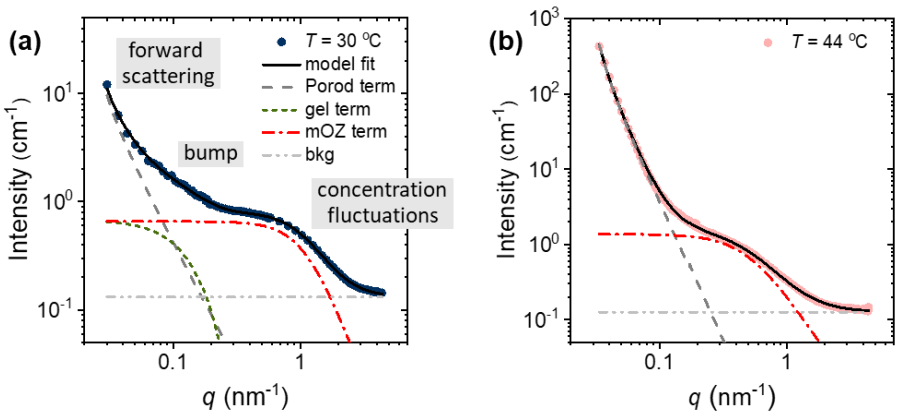

Figure 5.6 Representative SANS data of the 150 g L^{-1} PNIPMAM solutions in D_2O at (a) 30 °C, and (b) 44 °C (symbols). Full black lines: overall model fits. The other lines indicate the contributions to the models as described in the graphs. mOZ stands for modified Ornstein-Zernike model. (Reprinted from Ref. [124]. Copyright (2020) American Chemical Society.)

Concerning the temperature-dependent morphologies, Figure 5.7a and b show the Ornstein-Zernike scaling factor I_{OZ} and correlation length ξ_{OZ}, respectively. In the one-phase state, both I_{OZ} and ξ_{OZ} increase upon heating towards T_{CP}, and they demonstrate the critical behavior expected for semi-dilute LCST-type polymer solutions with a divergence at the spinodal temperature T_s [150]. The values of the critical exponents γ and ν indicate the universality classes of the phase transitions and are obtained by fitting the following power laws:

$$I_{OZ} \propto |T_s - T|^{-\gamma} \tag{5.2}$$

and

$$\xi_{oz} \propto |T_s - T|^{-\nu} \tag{5.3}$$

Figure 5.7a and b show the fits. Figure 5.7d and e show the same data in double-logarithmic representation. The resulting spinodal temperatures and the critical exponents are listed in Table 5.2. For the 30 g L^{-1} PNIPMAM solution, I_{OZ} and ξ_{OZ} increase as well. Nevertheless, due to a lack of data points, fitting the data by eqs. 5.2 and 5.3 is restricted.

For the 100 and 150 g L^{-1} PNIPMAM solutions, T_s values of ~44.5 °C are determined from both I_{OZ} and ξ_{OZ} (Table 5.2). Comparing to T_{CP} from turbidimetry, T_s values are ~ 2 °C higher. In both cases, the critical exponent γ is ~0.7 and the exponent ν is ~0.35. The Ornstein-Zernike exponent, m, is associated with the chain conformation and therefore characterizes the interactions between polymers and solvent molecules. In the one-phase state, m is ~2.4-3.2 for all concentrations studied (Figure 5.7c).

Upon heating above T_{CP}, both I_{OZ} and ξ_{OZ} decrease significantly. This is due to the collapse of the polymer chains. m increases drastically with temperature to values weight larger than in the one-phase state. This suggests that, in the two-phase state, the attractive segment-segment interactions are strongly enhanced, which leads to much more compact chain conformations. However, local concentration fluctuations still exist.

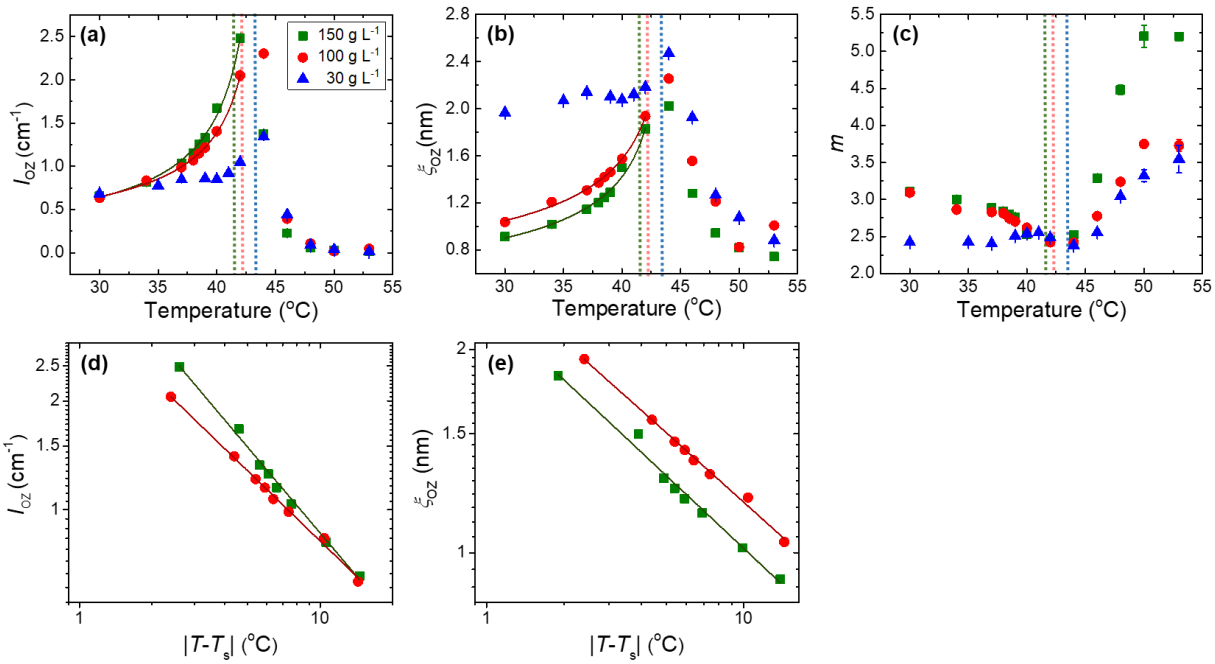

Figure 5.7 Structural parameters from model-fit results of the SANS data on the 30 (blue), 100 (red) and 150 g L^{-1} (green) solutions of PNIPMAM in D_2O in dependence on temperature, as indicated in (a). The dashed lines indicate the T_{CP} values from turbidimetry (same colors as the data). (a) Scaling factor of the mOZ term, I_{OZ}, (b) OZ correlation length ξ_{OZ}, and (c) OZ exponent m. Double-logarithmic representation of I_{OZ} (d) and ξ_{OZ} (e) in dependence on the absolute difference to the spinodal temperature T_s. The solid lines are fits to the data. (Reprinted from Ref. [124]. Copyright (2020) American Chemical Society.)

Table 5.2 Characteristic temperatures and critical exponents determined from SANS measurements on PNIPMAM solutions in D_2O

Concentration (g L^{-1})	T_s (°C) from I_{OZ}	γ	T_s (°C) from ξ_{OZ}	ν
100	44.4 ± 0.4	0.64 ± 0.06	44.4 ± 0.6	0.34 ± 0.04
150	44.6 ± 0.6	0.78 ± 0.10	43.9 ± 0.7	0.36 ± 0.06

Figure 5.8a and b display the scaling factor of the gel term I_{Gel} and the size of the static heterogeneities Ξ . They are attributed to the number density and the size of the static heterogeneities formed by physical crosslinks caused by the hydrophobic groups in PNIPMAM, respectively. At 30 °C, Ξ is ~4 nm for 100 g L^{-1} and Ξ is ~10 nm for 150 g L^{-1}. For 100 g L^{-1}, Ξ and I_{Gel} are almost temperature-independent. For 150 g L^{-1}, both Ξ and I_{Gel} increase remarkably as approaching T_{CP}, indicating that the static heterogeneities consisting of physical crosslinks grow larger and more prominent. This may be attributed to an increase of concentration fluctuations close to T_{CP} and the stronger segment-segment interactions. The number density and the size of the static heterogeneities comprising physical crosslinks increase with polymer concentration. Above 38 °C, the forward scattering originated from the large-scale inhomogeneities becomes very prominent. Therefore, it is no longer possible to further characterize the static heterogeneities.

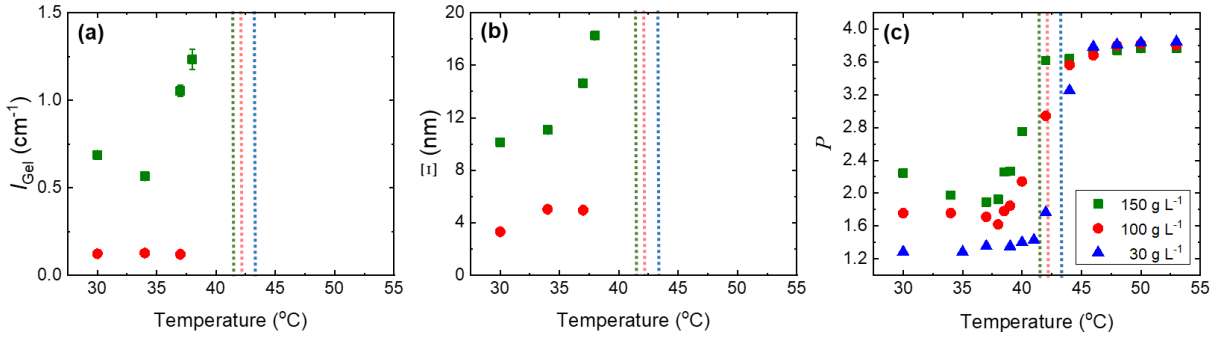

Figure 5.8 Structural parameters from model-fit results of the SANS data on the 30 (blue), 100 (red) and 150 g L^{-1} (green) PNIPMAM solutions in D_2O in dependence on temperature, as indicated in (c). The dashed lines indicate the T_{CP} values from turbidimetry (same colors as the data). (a) Scaling factor of physical crosslinks I_{Gel}, (b) correlation length of physical crosslinks Ξ, and (c) Porod exponent P. (Reprinted from Ref. [124]. Copyright (2020) American Chemical Society.)

The Porod exponent P is displayed in Figure 5.8c. For 150 g L^{-1}, P is ~2 below T_{CP} (at 30-38 °C), meaning that the large-scale inhomogeneities are loose fractals [147]. A few degrees below T_{CP} (at 38-42 °C), P suddenly increases to 3.6, indicating that they become compact. A transition temperature T_P^{SANS} can be determined from the onset of the increase of P. For all concentrations, T_P^{SANS} is 2.5-3 °C below the T_{CP} determined by turbidimetry. As a result, structural changes on the mesoscopic length scale happen consistently ~3 °C below T_{CP}. Above T_{CP}, P is an indicative of the surface structure of the mesoglobules. For all concentrations, P remains constant at ~3.8 above T_{CP}, suggesting that the collapsed polymer chains result in the formation of large mesoglobules with relative smooth surfaces.

Concerning the concentration-dependent morphologies, generally, ξ_{OZ} decreases and I_{OZ} increases with increasing polymer concentration in the one-phase state. In the two-phase state, ξ_{OZ} and I_{OZ} are hardly concentration-dependent (Figure 5.7a and b). Additionally, m increases with increasing concentration. Regarding the static heterogeneities, Ξ is 10-18 nm for 150 g L^{-1}, but Ξ is only 4-5 nm for 100 g L^{-1}. I_{gel} is ~0.75-1.25 cm^{-1} for 150 g L^{-1} and I_{gel} is ~0.12 cm^{-1} for 100 g L^{-1} (Figure 5.8a and b). Therefore, the static heterogeneities formed by physical crosslinks are smaller and less abundant at lower concentration, as expected. At the concentration of 30 g L^{-1}, the static heterogeneities are not observed. Regarding the large-scale inhomogeneities in the one-phase state, P increases with concentration, suggesting that large-scale inhomogeneities are more loosely packed in more dilute solutions. In the two-phase state, the surface of the large mesoglobules is rather smooth independent of the concentration. Moreover, the phase transition temperature T_P^{SANS} decreases with increasing concentration.

Very Small-Angle Neutron Scattering (VSANS) is applied to investigate the size and water content of the mesoglobules. Figure 5.9a shows representative data of the 30 g L^{-1} PNIPMAM solution in D_2O together with the SANS results discussed above (see also Figure 5.12a).

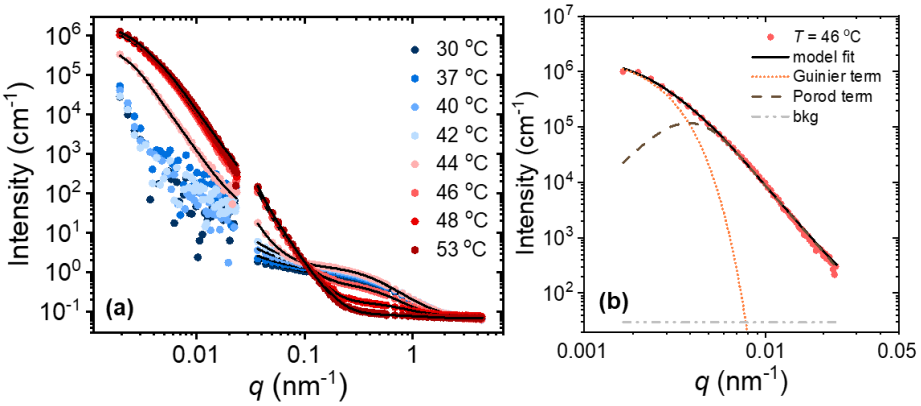

Figure 5.9 (a) Representative VSANS and SANS data of the 30 g L^{-1} PNIPMAM solution in D_2O (symbols). Full black lines: model fits. (b) VSANS data at 46 °C (symbols) including the fits of the Beaucage model. The orange dotted and brown dashed lines indicate the contributions to the model (full black line) as described in the graph. (Reprinted from Ref. [124]. Copyright (2020) American Chemical Society.)

During the VSANS measurements, the neutron transmission was measured at each temperature. The temperature at which it starts to decay abruptly (Figure 5.10), was defined as T_{CP}^{VSANS}. For the 30 g L^{-1} PNIPMAM solution, T_{CP}^{VSANS} is 44.0 ± 1.0 °C (Table 5.1), which is in agreement with the T_{CP} value determined by turbidimetry (43.5 ± 0.5 °C).

For the 100 and 150 g L^{-1} PNIPMAM solution, the transmission is around 0.7 in the one-phase state, but below 0.05 in the two-phase state. This indicates significant multiple scattering, preventing further analysis (Figure 5.10). Thus, only the VSANS data at 30 g L^{-1} are further analyzed quantitatively.

Below T_{CP}^{VSANS}, the VSANS curves feature a decay, verifying the presence of large-scale inhomogeneities already in the one-phase state (Figure 5.9a). Above T_{CP}^{VSANS}, the shape of the VSANS curves becomes a pronounced shoulder and the intensities of the VSANS curves are much higher. This suggests that compact mesoglobules form (Figure 5.9a).

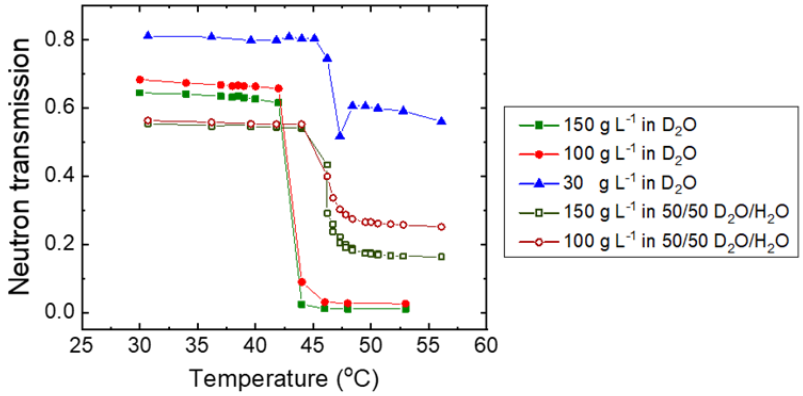

Figure 5.10 Neutron transmission of PNIPMAM in D_2O or in D_2O/H_2O in dependence on concentration, as determined in VSANS measurements for the solutions indicated in the graph. (Reprinted from Ref. [124]. Copyright (2020) American Chemical Society.)

Due to the intensities of the VSANS curves at temperatures below T_{CP}^{VSANS} are relative noisy, they are not evaluated by fitting structural models. Above T_{CP}^{VSANS}, the Beaucage model was applied, which characterizes the size and the surface roughness of the mesoglobules. The invariant Q^* provides information on the water content within the mesoglobules. Figure 5.9b shows exemplarily the contributions to the Beaucage model. At all temperatures above T_{CP}^{VSANS}, excellent fits are obtained (Figure 5.9a).

Figure 5.11a displays the radius of gyration R_g of the mesoglobules. For the 30 g L^{-1} PNIPMAM solution, R_g is ~910-960 nm at 44 and 45 °C and ~750 nm at 46 °C and above. The overall size decreases with increasing temperature, which is due to the release of water. The Porod exponent P' is ~3.9 at all temperatures, indicating that the surface of the mesoglobules is rather smooth (see also Figure 5.18a). This is in agreement with the results for P from SANS (Figure 5.8c). The invariant Q^*, calculated from the fitted Beaucage functions, is an indicative of the fraction of D_2O in the PNIPMAM-rich mesoglobules (Figure 5.11b). Q^* increases abruptly at T_{CP}^{VSANS} and remains constant above ~

T_{CP}^{VSANS} + 1 °C, indicating the dehydration of the mesoglobules that improves the scattering contrast.

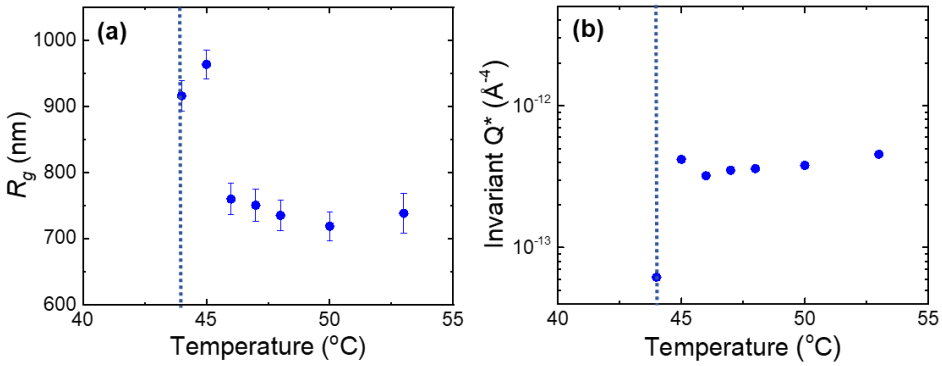

Figure 5.11 (a) Radius of gyration of the mesoglobules R_g and (b) invariant Q^* of the 30 g L^{-1} PNIPMAM solution in D_2O, determined by VSANS. Dashed line: T_{CP}^{VSANS}. (Reprinted from Ref. [124]. Copyright (2020) American Chemical Society.)

To reduce multiple scattering for 100 and 150 g L^{-1} PNIPMAM solutions, the VSANS measurements are carried not only in D_2O (Figure 5.12), but also in 50:50 v/v mixtures of D_2O and H_2O (Figure 5.13). The neutron transmission values are ~0.58 in the one-phase state and ~0.18-0.25 in the two-phase state (Figure 5.10). These values above T_{CP}^{VSANS} are still so low that a reliable analysis of the data is not possible. Thus, only the data at 44 °C are further evaluated since their neutron transmissions are still higher than 0.5. For the 100 and 150 g L^{-1}at 44 °C, the radius of gyration of the mesoglobules may be estimated at ~1.1 µm and 1.0 µm, respectively. These values are slightly larger than the ones from the 30 g L^{-1} PNIPMAM solution in pure D_2O.

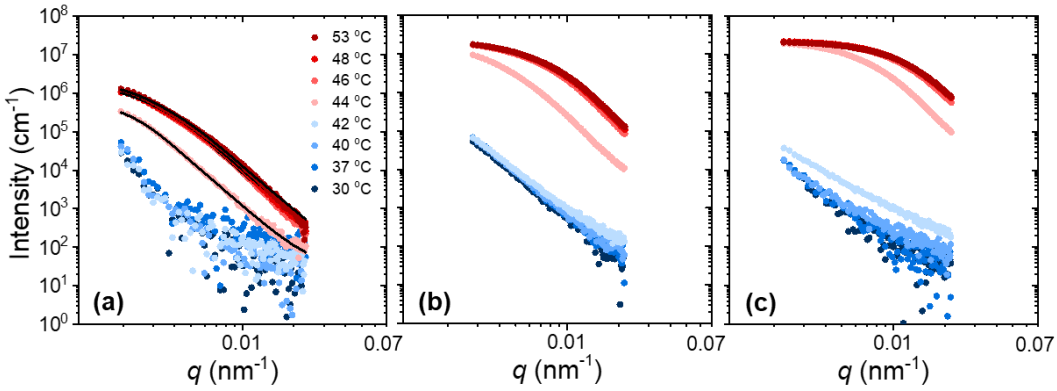

Figure 5.12 Representative temperature-dependent VSANS curves of PNIPMAM solutions in D_2O for concentrations of (a) 30 g L^{-1}, (b) 100 g L^{-1}, and (c) 150 g L^{-1} at the temperatures given in (a) (symbols). Blue and red color indicate temperatures below and above T_{CP}^{VSANS}, respectively. Black lines: fitting curves. (Reprinted from Ref. [124]. Copyright (2020) American Chemical Society.)

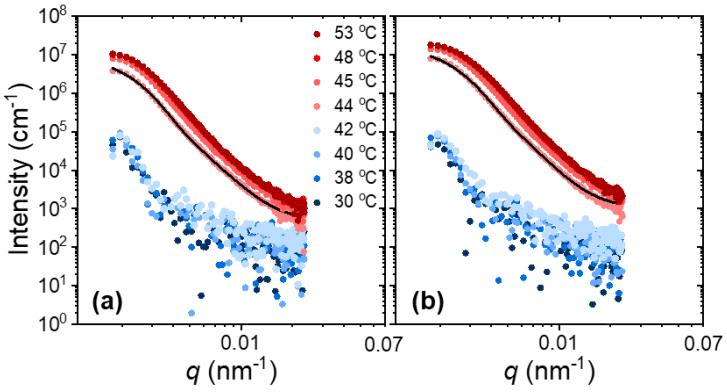

Figure 5.13 Representative temperature-dependent VSANS curves of PNIPMAM solutions in 50:50 v/v D_2O/H_2O for concentrations of (a) 100 g L^{-1}, and (b) 150 g L^{-1} at the temperatures given in (a) (symbols). Blue and red color indicate temperatures below and above T_{CP}, respectively. Black lines: fitting curves to the data at 44 °C. (Reprinted from Ref. [124]. Copyright (2020) American Chemical Society.)

5.5 Dehydration behavior of the hydrophobic groups

For PNIPAM, the hydrophilic amide groups remain hydrated even above the transition temperature, while the hydrophobic interactions play a dominant role for the phase transition [179-181], and the vibrational frequencies of the hydrophobic groups are sensitive to hydration [21, 39, 179, 180]. To characterize the dehydration behavior of the hydrophobic groups in PNIPMAM solutions, we performed temperature-dependent Raman spectroscopy around T_{CP} in the CH-stretching vibration region at a polymer concentration of 150 g L^{-1} in D_2O, as in SANS. The Raman spectra of the CH-stretching region of PNIPMAM around 2950 cm^{-1} are shown in Figure 5.14. Vibrational modes are detected at 2884, 2922, 2948, and 2991 cm^{-1} are attributed to symmetric stretching of the CH_3 groups, $\nu_s(CH_3)$, symmetric stretching of the CH groups, $\nu_s(CH)$, antisymmetric stretching of the CH_2 groups, $\nu_{as}(CH_2)$, and antisymmetric stretching of the CH_3 groups, $\nu_{as}(CH_3)$ [21, 39, 182]. Above T_{CP}, all bands shift to lower frequencies.

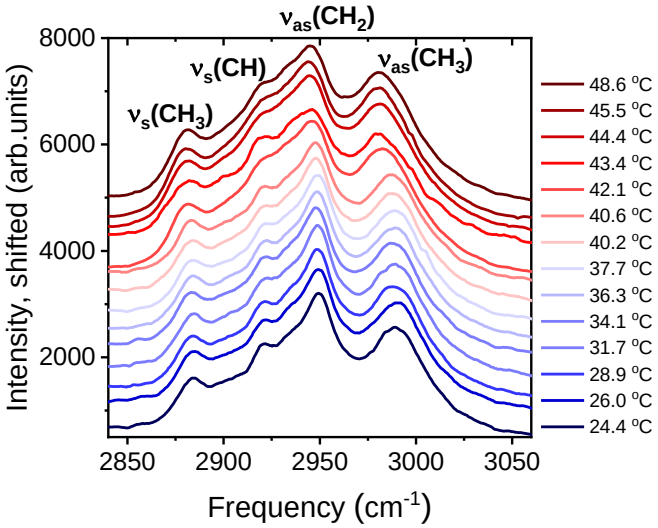

Figure 5.14 Raman spectra of the 150 g L^{-1} PNIPMAM solution in D_2O in dependence on temperature. Temperatures are given in the graphs. T_{CP} is determined at 39.0 °C by in situ optical microscopy. Blue lines: below T_{CP}, red lines: above T_{CP}. For clarity, the spectra were smoothed by the Savitzky-Golay algorithm and are shifted vertically. (Reprinted from Ref. [124]. Copyright (2020) American Chemical Society.)

For a quantitative description of the peak frequencies, the CH-stretch spectral bands in the frequency range from 2850 to 3100 cm^{-1} are fitted using a superposition of four Lorentzian lineshapes. A small background due to the tail of the OD vibrational bands between 2200 and 2800 cm^{-1} is accounted for, as shown in Figure 4.21a. Figure 4.21b shows the deconvolution in the CH-stretching region. The peak frequencies of these four contributions are displayed in dependence on temperature in Figure 5.15. Below T_{CP}, they are constant, while, above T_{CP}, they decrease steadily. This means that the interactions between the hydrophobic substituents of PNIPMAM and D_2O molecules change, as T_{CP} is crossed. In other words, an abrupt red-shift occurs in the two-phase region, especially for the bands related to CH_3, as observed for PNIPAM [21, 179]. Accordingly, the hydrophobic substituents of PNIPMAM undergo a strong dehydration at T_{CP} and the hydrophobic interactions dominate during the phase transition. Moreover, upon heating, the full widths at half maximum of the Lorentzian functions of $\nu_s(CH)$ and $\nu_{as}(CH_3)$ increase significantly, and the one of $\nu_{as}(CH_2)$ increases gradually (Figure 5.16). This indicates that, in the two-phase state, the molecular interactions around the CH groups become more disordered and inhomogeneous.

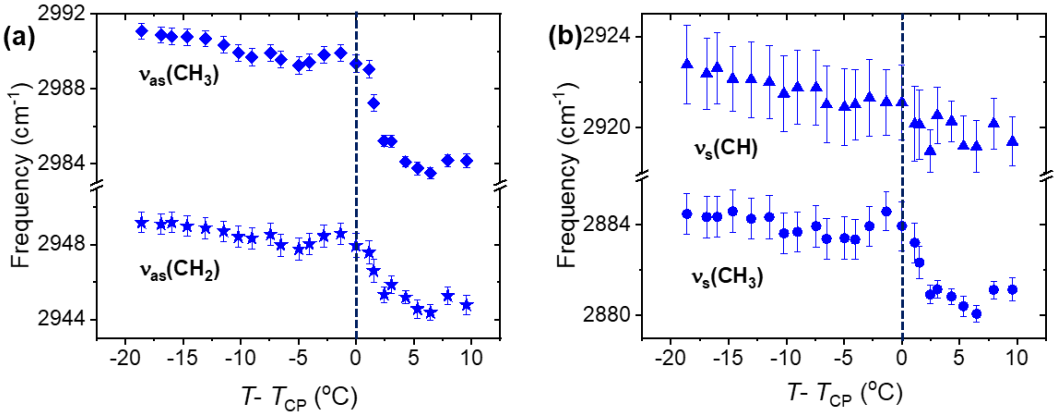

Figure 5.15 Results from Raman spectroscopy on the 150 g L^{-1} PNIPMAM solution in D_2O. Peak frequencies of (a) antisymmetric CH_3 ($\nu_{as}(CH_3)$), and antisymmetric CH_2 ($\nu_{as}(CH_2)$), and (b) symmetric CH ($\nu_s(CH)$), and symmetric CH_3 ($\nu_s(CH_3)$) stretching bands, as indicated in the graphs, in dependence on the temperature difference to T_{CP} from optical microscopy. (Reprinted from Ref. [124]. Copyright (2020) American Chemical Society.)

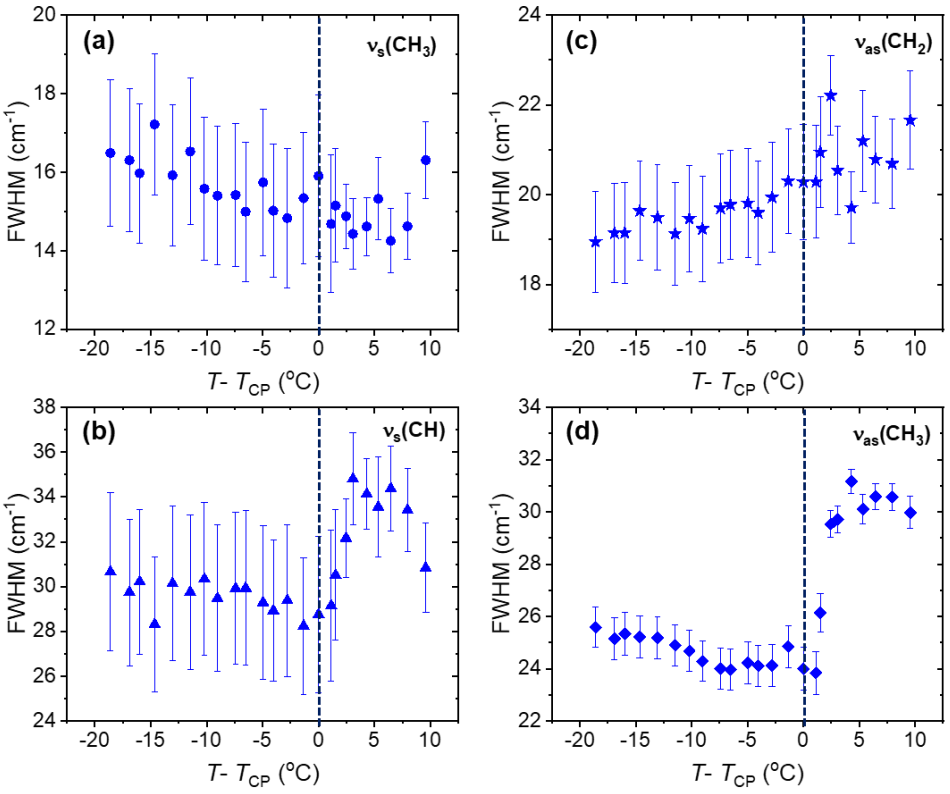

Figure 5.16 Full width at half maximum of the Lorentzian functions fitted to the Raman spectra for (a) $\nu_s(CH_3)$, (b) $\nu_s(CH)$, (c) $\nu_{as}(CH_2)$, and (d) $\nu_{as}(CH_3)$ of 150 g L^{-1} PNIPMAM solution in D_2O in dependence on the temperature difference to T_{CP} from optical microscopy. (Reprinted from Ref. [124]. Copyright (2020) American Chemical Society.)

5.6 Comparison between aqueous PNIPAM and PNIPMAM solutions

To understand how the additional methyl groups in PNIPMAM influence the phase behavior, thermal behavior, hydration behavior of the hydrophobic groups, and structural changes at the phase transition, we compare our results from aqueous PNIPMAM solutions with those of the analogous polyacrylamide PNIPAM. Both polymers exhibit type-II LCST behavior. Accordingly, the results from the PNIPMAM solutions are barely influenced by its dispersity index (here: $Đ = 1.74$).

Turbidimetry and DSC show that PNIPMAM solutions undergo the phase transition at higher temperature ($T_{CP} \cong 43$ °C) than PNIPAM ($T_{CP} \cong 32$ °C). Furthermore, they reveal that T_{onset}^{DSC} is 2-3 °C higher than T_{CP} in the case of PNIPMAM, indicating that mesoglobules are formed before the polymer chains dehydrate. In aqueous PNIPAM solutions, T_{CP} and T_{onset}^{DSC} are equal within the uncertainties (0.5 °C), see Figure 5.17 and Table 5.3. This indicates that, in the PNIPAM solutions, the formation of large mesoglobules and the dehydration occur simultaneously upon heating. Thus, PNIPMAM solutions not only undergo the phase transition at higher temperatures, but also feature a more complex phase transition process than PNIPAM.

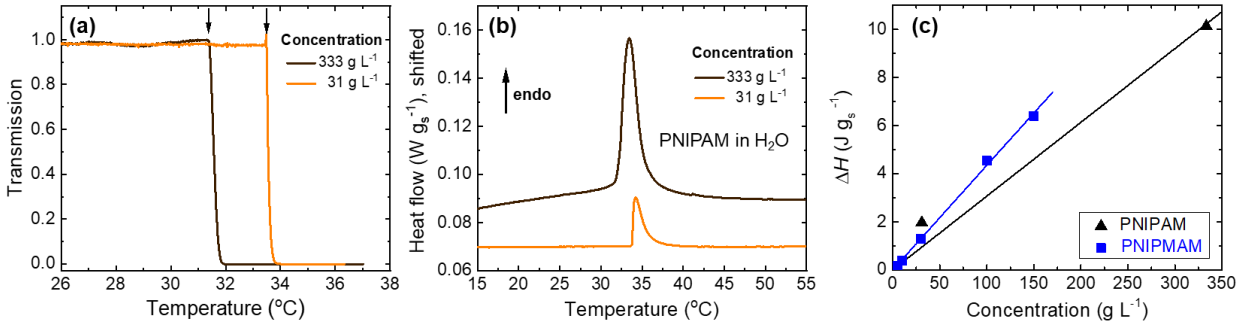

Figure 5.17 (a) Transmission curves of PNIPAM in H_2O in dependence on the temperature and polymer concentration at a heating rate of 0.2 K min^{-1}. The arrows indicate the cloud point temperatures. (b) DSC thermograms for PNIPAM solutions in H_2O at the concentrations given at a heating rate of 1 K min^{-1}. For better visibility, the curve from 333 g L^{-1} is shifted vertically by 0.03. (c) Comparison of the concentration-dependent endothermic enthalpy ΔH of the phase transition derived from the DSC thermograms for PNIPAM and PNIPMAM (symbols). Lines: linear fits. (Reprinted from Ref. [124]. Copyright (2020) American Chemical Society.)

Table 5.3 Results from turbidimetry and DSC measurements on PNIPAM solutions in H_2O.

Concentration (g L^{-1})	T_{CP} (°C)	T_{onset}^{DSC} (°C)	T_{peak}^{DSC} (°C)	ΔH (J/g_s)
31	33.5 ± 0.5	33.7 ± 0.2	34.1 ± 0.1	1.96 ± 0.02
333	32.2 ± 0.5	32.1 ± 0.2	35.3 ± 0.1	10.13 ± 0.02

Additionally, the value of the enthalpy of the polymer independent of concentration, ΔH_p, has a value of 0.043 ± 0.006 J g_s^{-1}/g L^{-1} for the PNIPMAM solutions which is higher than for PNIPAM (ΔH_p = 0.031 ± 0.003 J g_s^{-1}/g L^{-1}, Figure 5.17c). This difference is in accordance with the findings in Ref. [36]. In PNIPAM solutions, the hydrophilic amide groups mostly remain hydrated and the hydrophobic interactions dominate [179-181]. Therefore, the endothermic heat during the phase transition is mainly due to the hydrophobic dehydration. As PNIPMAM has more hydrophobic groups, its enthalpy change at the phase transition is larger than the one from PNIPAM.

The critical behavior when approaching the phase transition differs as well. In the one-phase state, the critical exponents ν and γ of the PNIPMAM solutions are ca. 0.35 and 0.7 and thus significantly smaller than the values predicted by mean-field theory (ν = 0.5 and γ = 1.0) [183, 184]. The deviation may be due to the fact that the phase transition of PNIPMAM is not of first or of higher order. For a purely first-order phase transition, the critical behavior is absent [185]. Though less pronounced values lower than the mean-field ones were reported also for aqueous PNIPAM solutions, namely ν = 0.44 ± 0.01 and γ = 0.81 ± 0.01 [178], it was doubted that this was due to the higher order of the phase transition [57, 58]. A more likely reason may be the long-range concentration fluctuations observed for both polymers which are significantly more pronounced in the PNIPMAM solutions. Furthermore, the segment-segment interactions in the PNIPMAM solutions are enhanced and the chain conformation is more compact, as evidenced by the high values of the Ornstein-Zernike exponent m compared to the values m = 2 found previously for PNIPAM [150, 178]. We ascribe this difference to the additional hydrophobic methyl groups in PNIPMAM.

Overall, three main morphological differences emerge between PNIPMAM and PNIPAM in aqueous solution. Firstly, in the one-phase state, loosely packed large-scale inhomogeneities are much more pronounced for PNIPMAM. Secondly, physical crosslinks give rise to inhomogeneities at intermediate length scales. Thirdly, the chain conformation of PNIPMAM in aqueous solutions below T_{CP} is more compact. All these observations are mainly a consequence of the enhanced attractive

segment-segment interactions between the hydrophobic moieties already in the one-phase state.

OM and VSANS revealed size differences of the mesoglobules from PNIPMAM and PNIPAM solutions above T_{CP}. Comparing the VSANS results of the 30 g L^{-1} PNIPMAM solution (which corresponds to 2.7 wt%) with the ones of a 3 wt% PNIPAM solution, which was measured previously at the same instrument (Figure 5.18) [25], it is seen that the R_g values of the mesoglobules formed by PNIPMAM are consistently larger than the ones from PNIPAM, namely by a factor of ~2-3. Furthermore, the invariant Q^* from PNIPMAM is almost 2 orders of magnitude smaller than the one from PNIPAM, reflecting that the mesoglobules from PNIPMAM contain more D_2O than the ones from PNIPAM. These findings may be attributed to the steric hindrance induced by the additional methyl groups on the polymer backbone, hampering a dense packing.

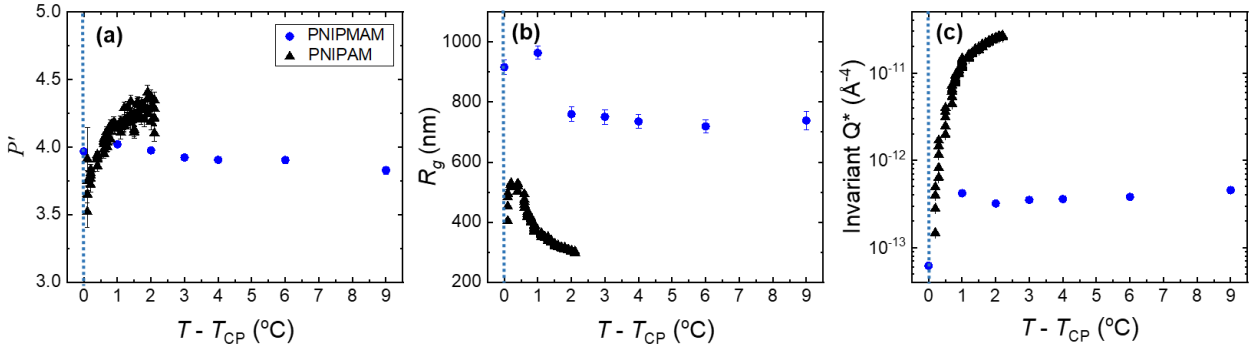

Figure 5.18 (a) Porod exponent P', (b) radius of gyration of the mesoglobules, R_g, and (c) invariant Q^* in dependence on the temperature difference from the respective cloud point temperature T_{CP}. Blue symbols: 30 g L^{-1} PNIPMAM solution in D_2O (2.7 wt%), black symbols: 3 wt% PNIPAM solution in D_2O. The data from the PNIPAM solution are taken from Ref [25]. (Reprinted from Ref. [124]. Copyright (2020) American Chemical Society.)

The difference of the hydration behavior of the hydrophobic groups between PNIPMAM and PNIPAM solutions can be determined by comparing the results from Raman spectroscopy with the ones from a 3 wt% PNIPAM solution in D_2O measured with the same setup and analyzed with the same method (Figure 5.19) [25]. In the one-phase state, the peak frequency of $\nu_{as}(CH_3)$ from PNIPMAM is ~2991 cm^{-1}, while it is ~2989 cm^{-1} for PNIPAM. A similar shift is observed for $\nu_{as}(CH_2)$ and $\nu_s(CH_3)$, but not for $\nu_s(CH)$. Higher peak frequencies suggest that the hydrophobic groups of PNIPMAM are more hydrated than the ones of PNIPAM (Figure 5.19). Previous experiments with infrared spectroscopy addressed the hydration behavior of the hydrophilic amide groups of PNIPMAM and of PNIPAM via the frequency of the amide II band [39]. In the one-phase state, the peak frequency of the amide II groups for PNIPMAM is ~1538 cm^{-1}, whereas the one of PNIPAM is ~1562 cm^{-1}. Accordingly, the amide groups of PNIPMAM are less hydrated than the ones of PNIPAM. Thus, the

hydrophobic groups of PNIPMAM are surrounded by more water molecules, while the hydrophilic amide groups are surrounded by less water molecules (Figure 5.20). This may be attributed to steric hindrances caused by additional methyl groups in PNIPMAM. However, in interpreting these differences, one should keep in mind that the PNIPMAM and PNIPAM samples studied here and in Ref. [25] differ in molar mass (M_n = 17,000 g/mol and 36,000 g/mol, respectively). Computer simulations for PNIPAM suggest that the degree of hydration of the polymer chain decreases with increasing molar mass [186]. Still, this effect levels off for polymers with degrees of polymerization above 30 and is presumably negligible for the polymers discussed here, $PNIPAM_{319}$ and $PNIPMAM_{133}$ [186].

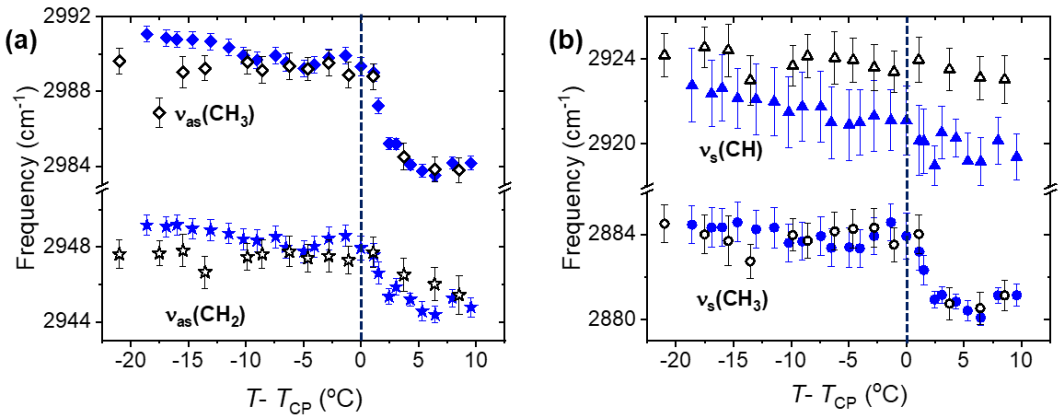

Figure 5.19 Results from Raman spectroscopy on the 150 g L^{-1} (~12 wt%) PNIPMAM solution in D_2O (blue closed symbols) and the 3 wt% PNIPAM solution in D_2O (black open symbols). Peak frequencies of (a) antisymmetric CH_3 ($\nu_{as}(CH_3)$) and antisymmetric CH_2 ($\nu_{as}(CH_2)$), and (b) symmetric CH ($\nu_s(CH)$) and symmetric CH_3 ($\nu_s(CH_3)$) stretching bands, as indicated in the graphs, in dependence on the temperature difference to T_{CP} from optical microscopy. The data from the PNIPAM solutions are taken from Ref [25]. (Reprinted from Ref. [124]. Copyright (2020) American Chemical Society.)

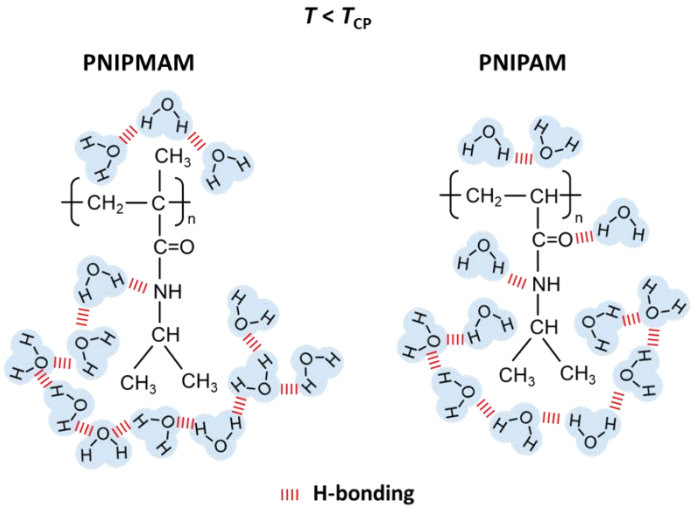

Figure 5.20 Schematic illustration of hydrophilic/hydrophobic interactions in PNIPMAM and PNIPAM in the one-phase state. The number of water molecules in the first hydration shell is based on the simulation results of PNIPAM aqueous solution in Ref. [186]. (Reprinted from Ref. [124]. Copyright (2020) American Chemical Society.)

In the two-phase state, the peak frequency of all CH-stretching bands of PNIPMAM and PNIPAM are shifted to lower wavenumbers, showing that the dehydrated state of the hydrophobic groups from the collapsed PNIPMAM and PNIPAM chains is similar. As for the $\nu_{as}(CH_3)$ band, this is consistent with the infrared spectroscopy results on the $\nu_{as}(CH_3)$ in the two-phase state [39]. Moreover, the infrared spectroscopy results on the amide II band in Ref. [39] indicate that, in the two-phase state, the intermolecular interactions between the amide groups of PNIPMAM are weaker than the ones of PNIPAM. This weakening may be attributed to the steric hindrances caused by the presence of the methyl groups. Moreover, it is consistent with the higher water content and larger size of the mesoglobules formed by PNIPMAM found using VSANS.

To summarize, PNIPMAM solutions feature not only higher phase transition temperatures but also a more complex phase transition process. The additional methyl groups change hydration behavior of the hydrophobic groups from PNIPMAM in the one-phase state. The structural behavior of PNIPMAM and PNIPAM in D_2O around the cloud point is summarized in Figure 5.21. In the one-phase state, loosely packed large-scale inhomogeneities and physical crosslinks caused by hydrophobic groups are present in the PNIPMAM solution. Furthermore, the local chain conformation of PNIPMAM is more compact than the one of PNIPAM, which is attributed to the hydrophobic effect and enhanced attractive segment-segment interactions induced by the additional methyl groups. In the two-phase state, the chains are collapsed and mesoglobules form, which shrink with increasing

temperature. The mesoglobules formed by PNIPMAM are larger and contain more water than the ones of PNIPAM at a similar polymer concentration.

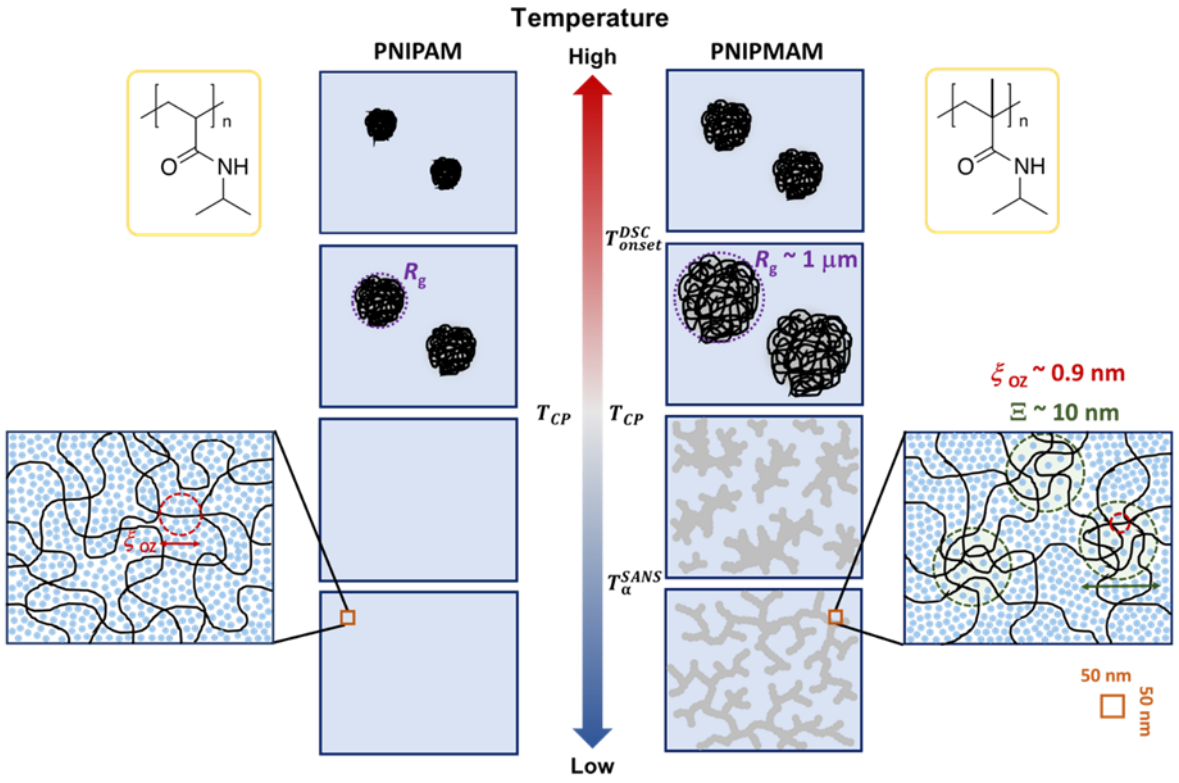

Figure 5.21 Schematic structures of PNIPAM and PNIPMAM in D_2O in dependence on temperature. The polymers are shown as black lines, and the water molecules as light blue dots. The red circles mark the correlation length ξ_{OZ}, the green circles display the size of the physical crosslinks Ξ, and the purple circles illustrate the radius of gyration of the mesoglobules R_g. Characteristic length scales are indicated. The grey regions represent the large-scale inhomogeneities. The chemical structures are shown in the yellow boxes. (Reprinted from Ref. [124]. Copyright (2020) American Chemical Society.)

5.7 Conclusions

The present work addresses the phase transition mechanism of the thermoresponsive polymer PNIPMAM in aqueous solution. The phase diagram is constructed from results of turbidimetry and DSC measurements, revealing that the PNIPMAM chains dehydrate only 2~3 °C above T_{CP}, where macroscopic phase separation sets in. This is in contrast to the behavior of PNIPAM, for which the turbidity and DSC transitions virtually coincide. From Raman spectroscopy, it is concluded that, compared to PNIPAM, the hydration behavior of the hydrophobic groups from PNIPMAM in the one-phase state is altered due to the steric hindrances caused by the additional methyl groups. SANS and VSANS results provide structural information of the temperature-dependent phase transition

mechanism of aqueous PNIPMAM solutions. In the one-phase state, loosely packed large-scale inhomogeneities and the static heterogeneities formed by physical crosslinks are observed, which can be attributed to hydrophobic moieties induced by the additional methyl groups. These hydrophobic methyl groups also give rise to more compact local chain conformations in the one-phase state. The PNIPMAM chains collapse in the two-phase state, as expected for thermoresponsive polymers. Mesoglobules form and shrink with increasing temperature. The mesoglobules formed by PNIPMAM are larger and contain more water inside than the ones from PNIPAM. To conclude, the presence of a single additional methyl group in the backbone segment of the PNIPMAM chain leads to substantially different hydration and structural behavior around the phase transition, which explains the counter-intuitive shift of the transition to higher temperatures.

6. Concentration-dependence of PMMA-*b*-PNIPAM in aqueous solutions

In this chapter, the concentration effect of the micellar structures formed by $PMMA_{21}$-*b*-$PNIPAM_{283}$ in aqueous solution is investigated at 20 °C. At this, synchrotron small-angle X-ray scattering (SAXS) measurements are performed. A small part of this chapter is based on ”Self-Assembled Micelles from Thermoresponsive Poly(methyl methacrylate)-*b*-poly(*N*-isopropylacrylamide) Diblock Copolymers in Aqueous Solution” C.-H. Ko et al. *Macromolecules* **2021**, *54*, 384-397 [126].

6.1 Introduction

Amphiphilic diblock copolymers are polymers comprising a hydrophobic block and a hydrophilic block. Due to the amphiphilicity, they can self-assemble into micelles in aqueous solution, when the concentration is above their critical micelle concentration (CMC). Below the CMC, the polymers are exclusively present as unimers, which means that they are molecularly dissolved. Above the CMC, unimers and micelles coexist. The higher the concentration, the larger the fraction of micelles. To carry out a systematic and thorough characterization on the phase behavior and temperature-dependent morphological transition of the self-assembled micelles from $PMMA_{21}$-*b*-$PNIPAM_{283}$ aqueous solutions, a preliminarily structural investigation of the micelles and their concentration-dependence above CMC is necessary.

As shown in Section 3.6.2, the concentration-dependence of $PMMA_{21}$-*b*-$PNIPAM_{283}$ in aqueous solutions was previously studied by both DLS and UV-vis spectroscopy. There is no transition point related to a CMC down to 0.05 g L^{-1}. This confirms that $PMMA_{21}$-*b*-$PNIPAM_{283}$ form self-assembled micelles in aqueous solution when the concentration is above 0.05 g L^{-1}.

In this chapter, the self-assembled micelles formed by $PMMA_{21}$-*b*-$PNIPAM_{283}$ in aqueous solutions and their concentration-dependence above 0.05 g L^{-1} are investigated using synchrotron SAXS at ambient temperature, i.e., 20 °C.

6.2 Concentration-dependence of micellar size

6.2.1 Overview

To characterize the concentration-dependent morphology of the micelles above CMC, synchrotron SAXS measurements were performed at 20 °C. To ensure $PMMA_{21}$-*b*-$PNIPAM_{283}$ diblock

copolymers form self-assembled micelles, the concentration was chosen between 0.2 and 10 g L^{-1}, which are above its predicted CMC (0.05 g L^{-1}). In Figure 6.1a and b, the SAXS data are present. All the scattering curves feature two shoulders, which are a pronounced one at ~0.15 nm^{-1} and a second one at ~0.5 nm^{-1}. These characteristics can be tentatively assigned to the form factor scattering from the micelles. When the concentrations are in a range from 0.2 to 1 g L^{-1}, the concentration-normalized absolute intensity of the pronounced shoulder remains almost independent on concentration (Figure 6.1a). However, at concentration of 10 g L^{-1}, it decreases. This indicates that the micelles become correlated owing to larger fraction of micelles at this concentration. The SAXS data become noisier at relatively dilute concentration. It is possibly due to the smaller fraction of micelles, resulting in a rather poor scattering.

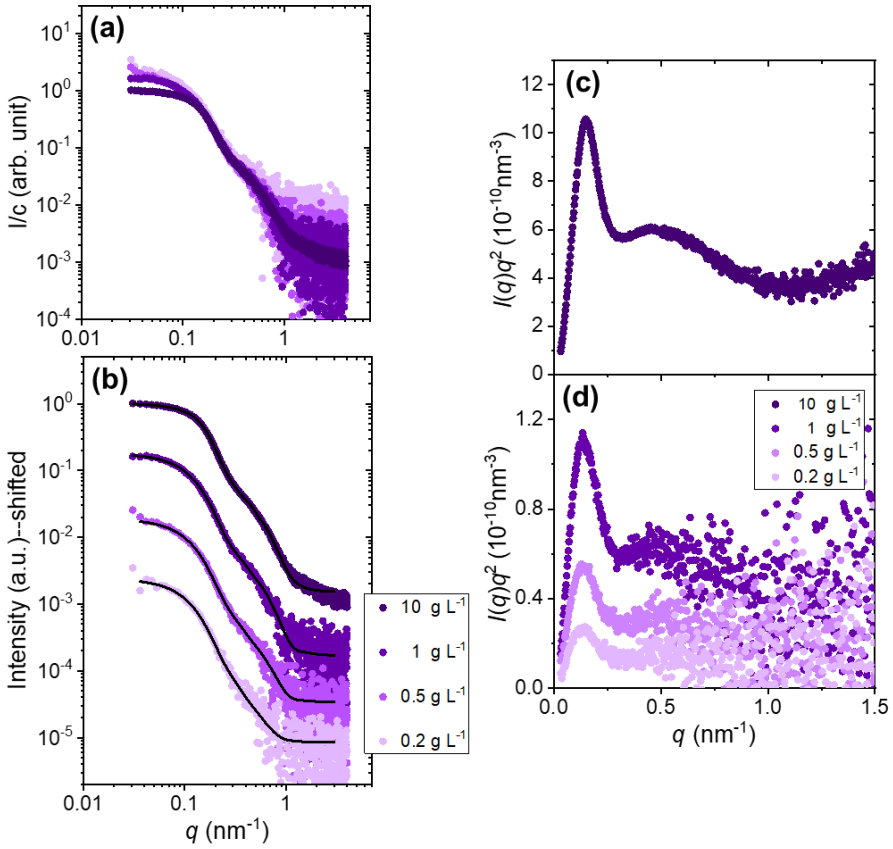

Figure 6.1 (a) Representative SAXS data of the $PMMA_{21}$-*b*-$PNIPAM_{283}$ solution in D_2O (symbols) at 20 °C at the concentrations given in (b). (b) The curves are shifted by a factor of 10 with respect to each other for clarity, and only every two point is shown. The black solid lines are the model fits. (c, d) Kratky plot of the same data, $I(q)q^2$ vs q.

In Figure 6.1c and d, the Kratky plots of the same SAXS data are shown, which yields qualitative information of the system without model fits. For all concentrations, a bell-shaped gaussian peak is

observed at q ~0.18 nm^{-1}, indicates the compact globular structures. This may be ascribed to the compact micellar core formed by hydrophobic PMMA blocks. Moreover, at a concentration of 10 g L^{-1}, a small shoulder at q ~0.5 nm^{-1} implies that the globular structure consists of multidomain, which, in this case, is the feature of the core-shell micelles. Towards high q values, the curve in Kratky plot has a short-range plateau at intermediate q range and monotonically increases. This suggests that highly flexible and swollen polymer chains, which is assigned to the hydrophilic PNIPAM blocks in the micellar shell [187]. Nevertheless, at concentration of 0.2, 0.5 and 1 g L^{-1}, these features are less prominent due to relatively weak scattering.

6.2.2 Fit model

By model fits the SAXS data, more quantitative information on the inner morphology of the self-assembled micelles can be obtained. A form factor for core-shell spheres with a homogeneous shell SLD, $P'_{CS}(q)$, does not fit the data well. This may be attributed to the relatively long hydrophilic PNIPAM blocks, resulting in non-homogeneous SLD values along the radial direction in the micellar shell. Therefore, from 0.2 to 1 g L^{-1}, the SAXS curves are modeled by the form factor for core-shell spheres, $P_{CS}(q)$, with the shell SLD profile being described by an exponential function along the radial direction. It points to that $PMMA_{21}$-*b*-$PNIPAM_{283}$ diblock copolymers dissolved in D_2O self-assemble into spherical micelles with hydrophobic PMMA core and hydrophilic PNIPAM shell. The PNIPAM shell has a radially decaying exponential density profile, meaning that the PNIPAM concentration declines radially along the direction away from the core, whereas the D_2O content raises. From $P_{CS}(q)$, the resulting fit parameters are determined: the micellar radius, R_{mic}, the micellar core radius, R_{core}, the shell thickness, t_{shell}, and the radially decaying SLD profile of micellar shell. During fitting, the SLD values of the core and the solvent are fixed, while the shell SLD values along radial direction are free fit parameters, revealing the radially increasing D_2O content in the micellar shell. Besides, the aggregation number of the micelles, N_{agg}, can be estimated based on the resulting R_{core} using eq. 4.52.

Owing to the presence of the correlations between the micelles, the SAXS curve at 10 g L^{-1} is analyzed by the following model:

$$I(q) = I_0 P_{cs}(q) S_{SHS}(q) + I_{bkg} \tag{6.1}$$

$P_{CS}(q)$ is the same form factor as described above. A sticky hard-sphere structure factor, $S_{SHS}(q)$, is applied here owing to the presence of the correlations between the micelles. I_0 is the scaling factor. In addition to the parameters obtained from the form factor, the half-distance between two correlated micelles, R_{HS}, the volume fraction of correlated micelles, ϕ, and the stickiness, τ_0, related to

interactions between correlated micelles are discovered from the structure factor. The detailed equations are listed in Section 4.5. All the SAXS data can be well fitted (Figure 6.1b).

6.2.3 Resulting structural characteristics

For all concentrations, the $PMMA_{21}$-*b*-$PNIPAM_{283}$ diblock copolymers self-assemble into spherical core-shell micelles. The resulting fit parameters are compiled in Figure 6.2 and 6.3. We firstly focus on the results at 0.2 g L^{-1}. The micellar radius R_{mic} is ~31.7 nm with a rather small core radius R_{core} of ~2.9 nm and shell thickness t_{shell} of ~28.8 nm (Figure 6.2a), which is consistent with the fact that $PMMA_{21}$-*b*-$PNIPAM_{283}$ has a relatively short hydrophobic PMMA block and a long hydrophilic PNIPAM block. The end-group effects of $PMMA_{21}$-*b*-$PNIPAM_{283}$ on the self-assembled micelles are assumed to be small and can be neglected. R_{mic} is larger than the calculated end-to-end distance of this diblock copolymers ($R_{ee,\ ideal}$ = 12.3 nm) and smaller than the calculated contour length (R_{max} = 76.6 nm). The detailed calculation is shown in Section 3.6.2. This suggests that the PNIPAM chains in micellar shell are swollen, but not fully stretched. The core polydispersity p_{core} is ~0.4 (Figure 6.2b). As calculated from R_{core} and the degree of polymerization of the PMMA block (DP_{PMMA}= 21), the aggregation number N_{agg} of the micelles is ~33 (Figure 6.2c). The large error bar of p_{core} and N_{agg} is attributed to the weak scattering caused by lower fraction of micelles at more dilute concentration.

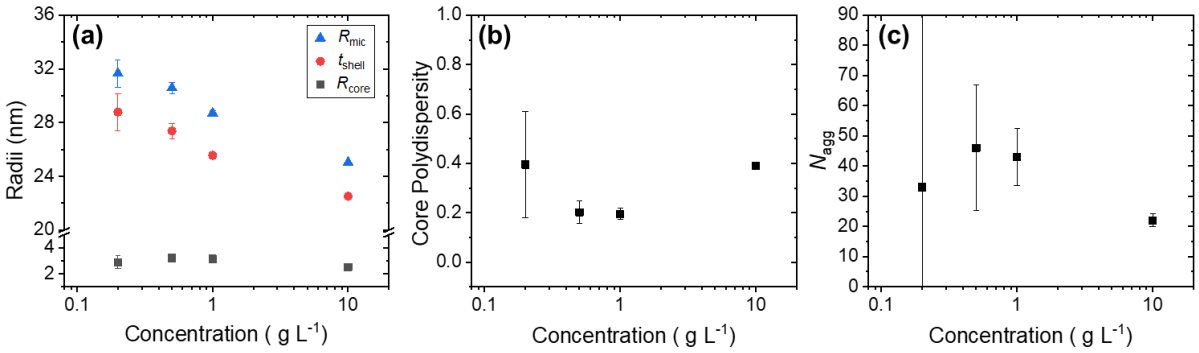

Figure 6.2 Resulting parameters from model fits: (a) micellar core radius R_{core} (black squares), shell thickness t_{shell} (red circles), micellar radius R_{mic} (blue triangles), as marked in the legend. (b) core polydispersity p_{core}. (c) aggregation number N_{agg}.

At 0.2 g L^{-1}, the SLD profile of the PNIPAM shell shows a radially exponential decaying from a value of 9.68 × 10^{-6} $Å^{-2}$ to the SLD value of D_2O (9.44 × 10^{-6} $Å^{-2}$), indicating that polymer segment concentration reduces along the radial direction. The closer to the micellar core, the denser the hydrophilic PNIPAM chains. This phenomenon is also found in the micellar shell from PS-*b*-PNIPAM diblock copolymers [107], and in the micellar shell from PNIPAM homopolymers end-capped with

hydrophobic ligand [188]. Furthermore, the D_2O content in the micellar shell can be estimated and presented in Figure 6.3b. The D_2O content at the interface between the micellar core and shell is ~0.72 (Figure 6.3c) and it rises along the micellar radius to ~1. Therefore, the inner part of the micellar shell contains less water than the outer part. The parameter v_0 is ~5.1 (Figure 6.3d), which quantifies how steeply the exponential functions decay. This not only evaluates the density distribution and the D_2O content in the micellar shell but also gives insight into the interface between micellar shell and solvent.

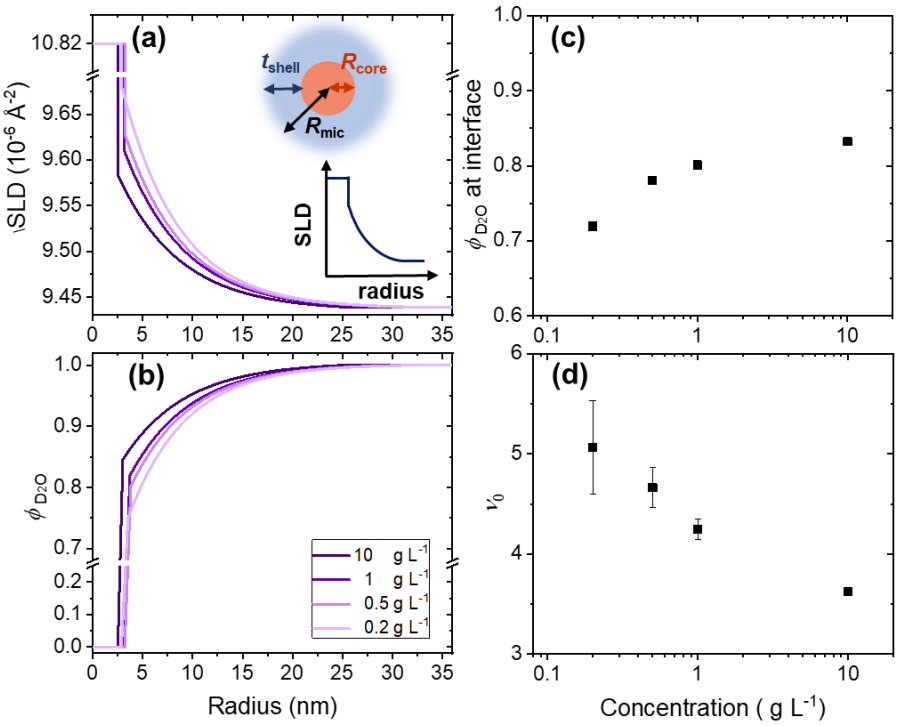

Figure 6.3 Resulting (a) scattering length density SLD profile and (b) D_2O content along the micellar radial direction at the concentrations in the legend. (c) D_2O content at the interface of micellar core and shell and (d) parameter v_0 related to shape of the exponential function for shell SLD in dependence on concentration. The inset in (a) depicts the schematic of the SLD profile along the micellar radial direction.

As the concentration increases to 10 g L^{-1}, R_{mic} decreases ~6.7 nm, resulting from a combined contribution from a subtle decrease of R_{core} and a small shrinkage of t_{shell} (Figure 6.2a). The core polydispersity p_{core} is ca. 0.2-0.4 (Figure 6.2b). From the decrease of R_{core}, a decrease of N_{agg} in dependence on concentration is deduced. From 0.5 to 10 g L^{-1}, N_{agg} decreases from 46 to 22. This alludes to a reduction of PMMA blocks within one single micellar core with increasing concentration, which may be attributed to the PMMA blocks are still mobile. This implies that chain exchange among micelles is possible. As the concentration increases, the shell SLD profiles have overall lower SLD values and decay slower with increasing concentration (Figure 6.3a), showing that the micellar shell

contains generally more D_2O at high concentrations. This is originated from that fewer N_{agg}, as the concentration increases. The D_2O content within the micellar shell along the radial direction at different concentrations is displayed in detailed in Figure 6.3b. From 0.2 to 10 g L^{-1}, the D_2O content at the interface of micellar core and shell increases from 0.72 to 0.83 (Figure 6.3c). Moreover, the parameter v_0 decreases from 5.1 to 3.6 (Figure 6.4d), implying that the interface between shell and solvent becomes indistinct at high concentrations.

At 10 g L^{-1}, the correlations of micelles appear. The hard-sphere distance R_{HS} is ~20.7 nm, which is the half-distance between two correlated micelles. R_{HS} is smaller than R_{mic}, stating that the micelles are interpenetrating with each other instead of being apart from each other with a certain distance. The volume fraction of the correlated micelles ϕ is ~0.05, meaning that the micelles are weakly correlated.

6.3 Conclusions

Based on the results, the concentration-dependent structures of $PMMA_{21}$-*b*-$PNIPAM_{283}$ in D_2O are schematically concluded in Figure 6.4. Above its critical micelle concentration, $PMMA_{21}$-*b*-$PNIPAM_{283}$ diblock copolymers form spherical core-shell micelles with a radial gradient of water content in the micellar shell. The more concentrated the solution, the smaller the micellar size. At high concentrations, the aggregation number N_{agg} is smaller and the water content in the shell is higher.

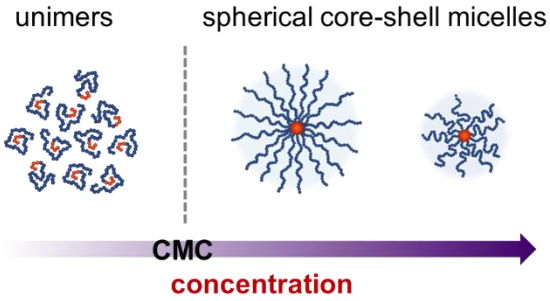

Figure 6.4 Schematic representation of the morphology of $PMMA_{21}$-*b*-$PNIPAM_{283}$ in D_2O in dependence on concentration. Red spheres represent for the micellar core made up of PMMA blocks. The blue lines stand for the PNIPAM blocks.

In this chapter, the concentration-dependence of micelles formed by $PMMA_{21}$-*b*-$PNIPAM_{283}$ in D_2O has been investigated by SAXS at 20 °C. The inner structures of the micelles are revealed in detail. Due to the thermoresponsive property of PNIPAM blocks, the temperature-induced morphological transition and the aggregation behavior of micelles formed by $PMMA_{21}$-*b*-$PNIPAM_{283}$ is also of great interest. In the following Chapters 7 and 8, the self-assembled micelles from $PMMA_{21}$-*b*-$PNIPAM_{283}$ upon heating are investigated in-depth.

7. Temperature-dependence of self-assembled micelles from PMMA-*b*-PNIPAM in dilute aqueous solution

In this chapter, the temperature-induced morphological transition of self-assembled micelles formed by $PMMA_{21}$-*b*-$PNIPAM_{283}$ in aqueous solution at 1 g L^{-1} is investigated. At this, turbidimetry, dynamic light scattering (DLS), and synchrotron small-angle X-ray scattering (SAXS) experiments are performed during heating scan.

7.1 Introduction

In Chapter 6, it has been investigated the concentration-dependence of the self-assembled micelles formed by $PMMA_{21}$-*b*-$PNIPAM_{283}$ in aqueous solution at 20 °C. PNIPAM is a thermoresponsive polymer and exhibits an LCST of 32 °C in aqueous solution. Thus, the morphology of the self-assembled micelles from $PMMA_{21}$-*b*-$PNIPAM_{283}$ is tunable by altering temperature.

In this chapter, we aim to study the temperature-dependence of self-assembled micelles from $PMMA_{21}$-*b*-$PNIPAM_{283}$ in dilute aqueous solution. To focus on the collapse mechanism of the micelles upon heating without the influence from their correlations, $PMMA_{21}$-*b*-$PNIPAM_{283}$ aqueous solution at 1 g L^{-1} is chosen. The phase behavior is characterized using turbidimetry. Furthermore, a comprehensive structural study of the self-assembled micelles is probed by DLS and synchrotron SAXS to cover a temperature range below and above the cloud point in small temperature steps.

7.2 Temperature-dependence of micellar size

For a $PMMA_{21}$-*b*-$PNIPAM_{283}$ solution in D_2O at 1 g L^{-1}, the cloud point is identified to be T_{CP} = 30.5 ± 0.5 °C by turbidimetry. Temperature-resolved DLS measurements were conducted upon heating up to 31 °C to identify the hydrodynamic radius, R_h, of the micelles, formed by the same solution. The representative normalized intensity autocorrelation functions during heating and cooling runs are presented, respectively (Figure 7.1a and b). In Figure 7.1c and d, their corresponding distribution functions are shown as well. The autocorrelation functions are characteristic of a single decay, and the corresponding distribution functions feature monomodal distribution peaks, suggesting that one type of diffusing particles dominates. The hydrodynamic radii, R_h, of the particles are assigned to single micelles. At 16 °C, the peak is centered at ~35 nm. Upon heating to 30 °C, the distributions shift slightly toward smaller sizes and become narrower (Figure 7.1c). At 31 °C, it shifts toward slightly

larger sizes. From the cooling run, the distributions shift sightly toward smaller sizes down to 26 °C and then shift slightly toward larger sizes. (Figure 7.1d).

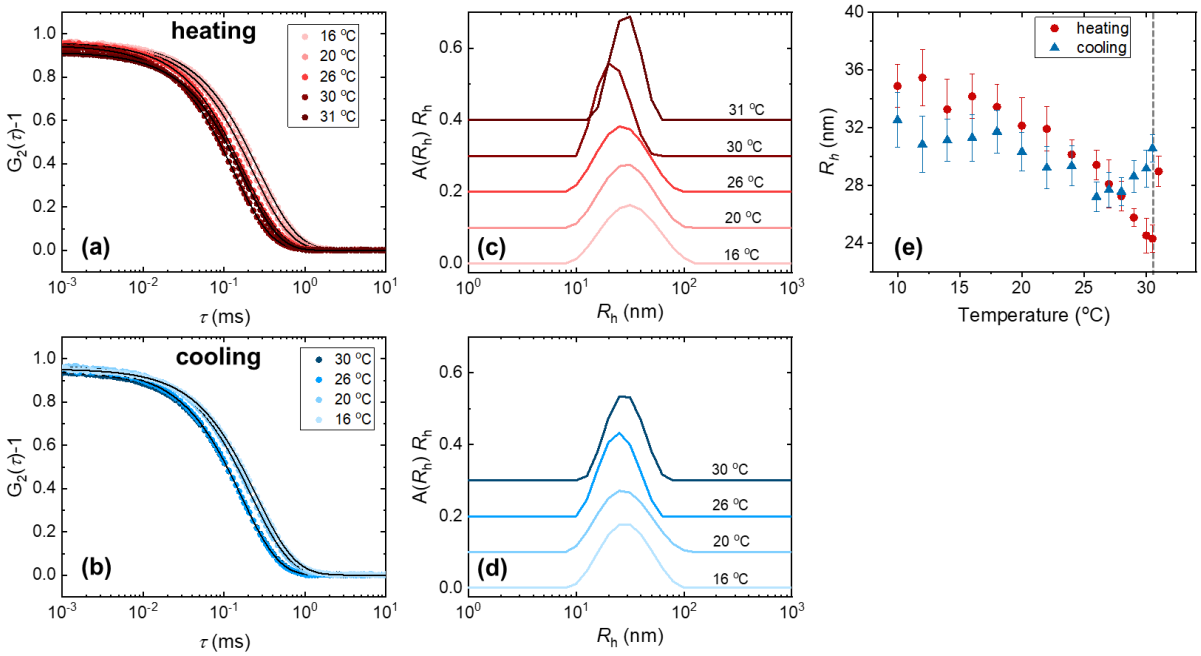

Figure 7.1 (a, b) Representative normalized intensity autocorrelation functions and (c, d) the corresponding distribution functions of hydrodynamic radii, R_h, from DLS on the 1 g L^{-1} $PMMA_{21}$-*b*-$PNIPAM_{283}$ solution in D_2O at the temperatures given in the graphs during heating and cooling. (e) the average hydrodynamic radii, R_h, of the micelles during heating (red circles) and cooling (blue triangles) runs. The grey dashed line points to the cloud point, T_{CP}, determined by turbidimetry.

The average R_h values of the micelles during heating and cooling run are summarized in Figure 7.1e. As the temperature increases upon heating, R_h decreases from 35 to 24 nm from 10 to 30 °C. This suggests that the micellar size decreases when the temperature is close to T_{CP}. This may be due to the collapse of the PNIPAM shell. At 31 °C, R_h increases from 24 nm to 29 nm, which could be attributed to either the expansion of the PNIPAM shell or an increase of the aggregation number. DLS only provides overall size information rather than the internal structure of the micelles; therefore, these possible scenarios cannot be distinguished merely by DLS. Above 31.5 °C, it is no longer possible to perform DLS measurements due to the high turbidity. As the temperature decreases upon cooling, R_h decreases from 30 nm back to ~28 nm at 26 °C, and slightly increases to ~30 nm down to 10 °C. During the cooling run, R_h is at a similar size range but slightly different from the ones during heating run, which may be ascribed to the hysteresis effect of PNIPAM block [110, 189]. This indicates that the temperature-induced transition of the micellar size is reversible with the hysteresis effect.

7.3 Morphological transition of the micelles upon heating

7.3.1 Overview

To investigate the morphological transition and the collapse mechanism of the micelles and further elucidate the remaining question from DLS, temperature-resolved synchrotron SAXS measurements were performed on the sample solution. The temperature scan was done from 19.7 to 40.0 °C to cover the range below and above T_{CP} in steps of 1 or 2 °C. The SAXS data are shown in Figure 7.2.

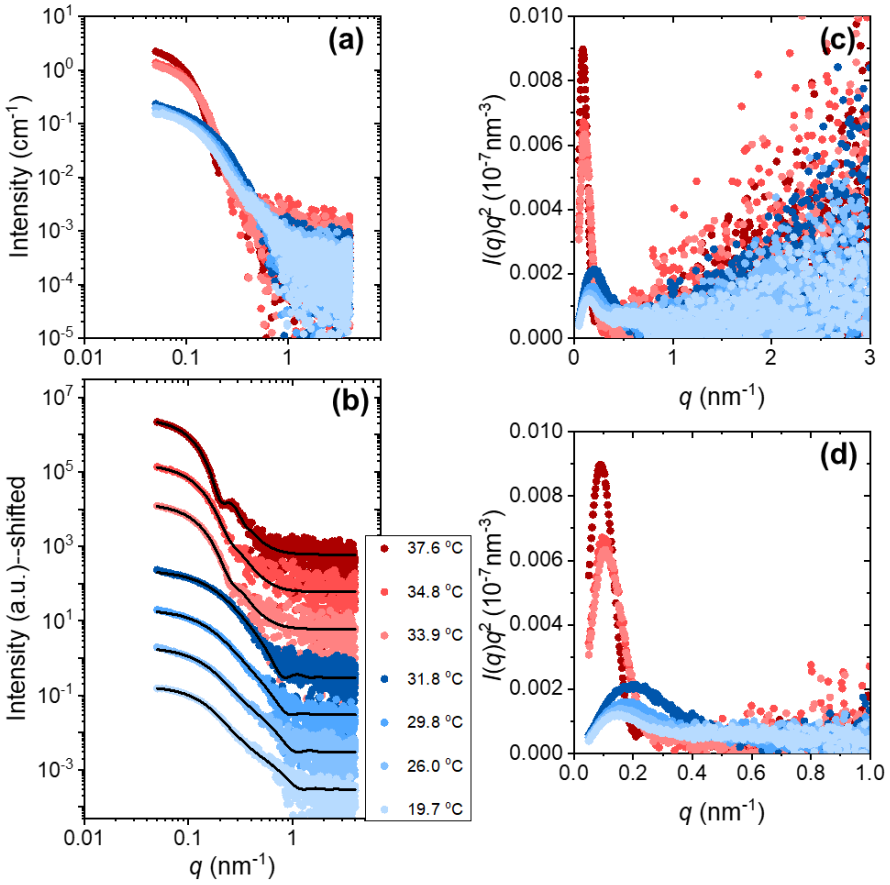

Figure 7.2 (a) Representative SAXS data of the 1 g L^{-1} PMMA$_{21}$-*b*-PNIPAM$_{283}$ solution in D_2O (symbols) at the temperatures given in (b). The blue and red color indicate regime I (below and at T_{CP}) and regime II (above T_{CP}), respectively. For clarity, in (b), the curves are shifted by a factor of 10 with respect to each other, and only every second point is shown. The black solid lines are the model fits. (c) Kratky plot, $I(q)q^2$ vs q, of the same data. (d) is a zoom of the low-q part of (c).

From 19.7 to 31.8 °C, all the scattering curves feature a first shoulder at ~0.15 nm^{-1} and a weak second shoulder at ~0.5 nm^{-1} (Figure 7.2a, b). These characteristics can be ascribed to the spherical

form factor of the micelles, which have been described in Chapter 6. Upon heating towards 31.8 °C, the first shoulder moves slightly towards larger q values (~0.2 nm^{-1}), and the second shoulder becomes even less pronounced. This may be attributed to the subtle shrinkage of the micellar size. From 33.9 to 40.0 °C, the first shoulder dominates and shifts slightly towards lower q values (~0.1 nm^{-1}), and their absolute intensity increases significantly. This might be due to the large micellar size caused by the drastic collapse of PNIPAM chains in the micellar shell. According to the features in the scattering curves, the temperature range is divided into two regimes: regime I (19.7-31.8 °C, i.e., below and just above T_{CP}) and regime II (33.9 to 40.0 °C, i.e., above T_{CP}).

In Figure 7.2c and d, the Kratky plots of these SAXS data are presented. In regime I, a bell-shaped peak at q ~0.14 nm^{-1} indicates a compact globular structure, which is attributed to the compact micellar core formed by the PMMA blocks. An additional weaker shoulder at q ~0.5 nm^{-1} demonstrates that the globular structure comprises more than one domain, which results from the core-shell structure of the micelles. Towards high q values (q > 1 nm^{-1}), the curve in the Kratky plot increases (q > 2 nm^{-1}). This suggests loosely packed chains, which is attributed to the hydrophilic PNIPAM blocks in the micellar shell [187]. In regime I, the bell-shaped peak at q ~0.14 nm^{-1} shifts slightly toward higher q values, becomes broader, and its amplitude increases. Moreover, the weak shoulder at q ~0.5 nm^{-1} disappears and becomes a decay. These changes imply a decreasing micellar size caused by a shrinkage and dehydration of the micellar shell, resulting in a vanishing contrast between the micellar core and the shell. In regime II, the prominent bell-shaped peak shifts to lower q values at q ~0.1 nm^{-1} and its amplitude abruptly increases, which might be attributed to an increase of the micellar size with denser PNIPAM shell due to strong dehydration.

7.3.2 Fit Model

As studied from Chapter 6, from 19.7 to 31.8 °C, the SAXS curves in regime I, are described by a core-shell sphere form factor, $P_{CS}(q)$, with a shell SLD profile based on an exponential function along the radial direction. All the fit parameters from this form factor are obtained as mentioned in Section 4.5. The shell thickness, t_{shell}, is defined at where the D_2O content in the micellar shell decays to 100 vol%. Due to the weak scattering, in this chapter, t_{shell} is defined at where the D_2O content in the shell of 99.5 vol%. The micellar radius, R_{mic}, can be further deduced by $R_{mic} = R_{core} + t_{shell}$.

As the temperature increases above T_{CP} in regime II, the SLD values of PMMA and dehydrated PNIPAM become very similar (SLD of PMMA: 10.82 × 10^{-6} $Å^{-2}$; SLD of dry PNIPAM: 10.30 × 10^{-6} $Å^{-2}$). Thus, it is difficult to differentiate core and shell in the micelles due to the continuous collapse and dehydration of PNIPAM. Therefore, the SAXS curves from 33.9 to 40.0 °C in regime II, are fitted

by the form factor of homogeneous spheres, $P_s(q)$, providing the overall size of the collapsed micelles. All the SAXS data are well described (Figure 7.2b).

7.3.3 Resulting temperature-dependent structural characteristics

The resulting fit parameters are compiled in Figure 7.3 and 7.4. From 19.7 to 31.8 °C in regime I, spherical core-shell micelles formed by $PMMA_{21}$-*b*-$PNIPAM_{283}$ diblock copolymers present as expected. At 19.7 °C, the micellar radius $R_{mic} \cong 26.0$ nm with a core radius R_{core} of ~3.4 nm and a shell thickness t_{shell} of ~22.6 nm (Figure 7.3a). The SAXS data in regime I can be fitted by a core-shell sphere form factor with monodisperse core. Therefore, no core polydispersity is displayed in Figure 7.3b. Upon heating from 19.7 to 31.8 °C, R_{core} increases from 3.4 to 5.0 nm, while t_{shell} remains nearly constant at 22.9 nm. In regime I, R_{mic} are at values of ~27.1 nm.

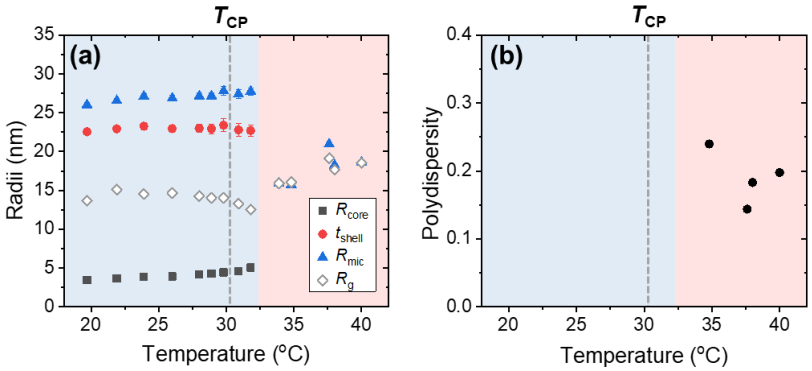

Figure 7.3 Resulting parameters from model fits: (a) micellar core radius R_{core} (black squares), shell thickness t_{shell} (red circles), micellar radius R_{mic} (blue triangles), and radius of gyration R_g identified by Guinier plots (grey open diamonds), as marked in the legend. (b) polydispersity p_{core}. The light blue and light red background colors indicate regimes I and II, respectively.

As the temperature increases from 19.7 to 31.8 °C, another change in the shell is observed. The SLD values in the shell are generally higher at high temperatures and decay much sharply (Figure 7.4a), which is an indicative of the dehydration of the shell. The D_2O content along the radial direction within shell is shown in dependence on temperature in Figure 7.4b. At the interface of the micellar core and shell, the D_2O content decreases from 0.72 to 0.48 (Figure 7.4c). Moreover, the parameter v_0 increases from 5.7 to 10 (Figure 7.4d), implying that the interface between shell and solvent becomes sharper at high temperatures. As discussed, the increase of R_{core} may be caused by either an increase of the aggregation number or the strong dehydration at the interface of the core and shell. However, due to the weak contrast of the PMMA core and the dehydrated PNIPAM shell, it is not possible to resolve this question.

Above T_{CP} in regime II, it is not feasible to differentiate between the core and shell owing to the weak SLD contrast between PMMA and dehydrated PNIPAM. At 33.9 °C, R_{mic} has shrunken abruptly to ~16 nm (Figure 7.3a). This may be attributed to the strong collapse of PNIPAM chains. Meanwhile, from 33.9 to 40.0 °C, R_{mic} increases slightly to 20 nm and is overall smaller than in regime I. This implies that the collapsed micelles slightly grow upon heating in regime II.

From the Guinier plots of the same SAXS data at low q values (0.06-0.09 nm^{-1}), the radius of gyration of the micelles, R_g, are obtained. In regime I, R_g is ~15 nm, which is smaller than R_{mic} (~27 nm). This implies that the mass of the micelles is concentrated in the inner part of the micelles. Furthermore, R_{mic} slightly decreases to 13.3 nm upon heating from 19.7 to 31.8 °C in regime I, which indicates the subtle dehydration of the inner part of the shell. This is in agreement with the results from the shell SLD profiles. At 33.9 °C, R_g increases to 16 nm. Upon heating to 40.0 °C, R_g continuously increases to 18.5 nm upon heating to 40.0 °C. Additionally, in regime II, R_g is almost same as R_{mic}, suggesting that the mass distribution in the collapsed micelles is more homogenous.

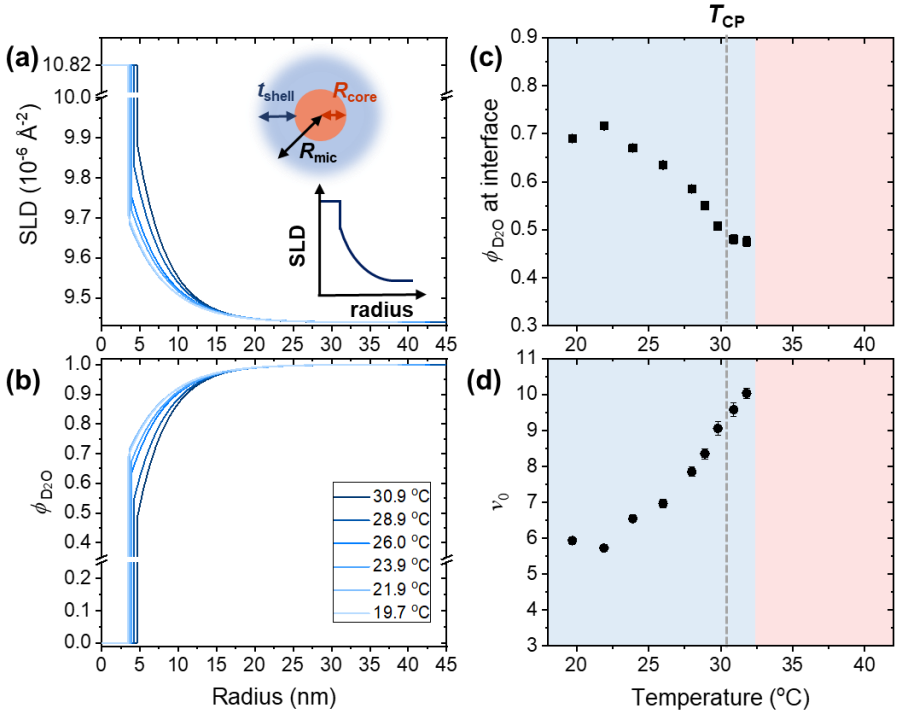

Figure 7.4 Resulting scattering length density SLD profile (a) and D_2O content (b) along the micellar radial direction at the temperatures in the legend. D_2O content at the interface of micellar core and shell (c) and parameter ν_0 related to shape of the exponential function for shell SLD (d) in dependence on concentration. The light blue and light red background colors indicate regimes I and II, respectively.

7.4 Conclusions

The purpose of this chapter is to determine the temperature-dependent morphology of the self-assembled micelles from $PMMA_{21}$-*b*-$PNIPAM_{283}$ in D_2O at 1 g L^{-1}. As stated in the SAXS results, the collapse mechanism of the micellar structure upon heating is summed up in Figure 7.5. From 19.7 to 31.8 °C, i.e., below and just above T_{CP}, the micellar size keeps almost the same, whereas the micellar shell dehydrates with increasing temperature. Additionally, based on the findings from R_g, the mass of the micelles concentrates at the center part instead of homogeneous distribution. From 33.9 to 40.0 °C, i.e., above T_{CP}, the micelles strongly collapse, as evident from a decrease of R_{mic} and an increase of R_g. As a result of weak contrast between PMMA and dehydrated PNIPAM, the mass distribution of the collapsed micelles become homogenous. Thus, distinguishing between core and shell is no longer possible. Due to the same reason, precisely determining the aggregation number is also limited.

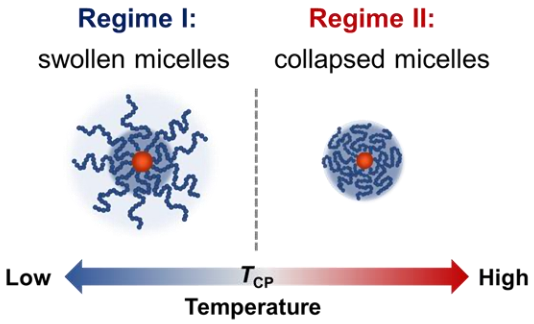

Figure 7.5 Schematic representation of the internal morphology of $PMMA_{21}$-*b*-$PNIPAM_{283}$ in D_2O at 1 g L^{-1} in dependence on temperature. Red spheres depict the micellar core made up of PMMA blocks. The blue lines serve as the PNIPAM blocks. The dark blue background colors mark where the mass concentrates in the micelles.

Another issue in this work is due to the relatively dilute concentration at 1 g L^{-1}. From the SAXS data (Figure 7.2 a and b), the data quality of the scattering features related to the shell, i.e., the second shoulder at q ~0.5 nm^{-1}, is not sufficient, which prevents us from accurately identifying the boundary between the shell and the solvent. In spite of these limitations, this work certainly adds to our understanding of the temperature-induced collapse transition of single micelle from $PMMA_{21}$-*b*-$PNIPAM_{283}$. From the results in Chapter 6, it was found that increasing the solution concentration will reduce the aggregation number and increase the water content in the micellar shell. This may raise the contrast between PMMA and dehydrated PNIPAM shell. Additionally, the choice of more concentrated concentration may also lead to a better data quality of scattering without increasing the measurement time, which may be beneficial for the characterization of micellar structure. With increasing concentration, the fraction of micelles is expected to increase. Consequently, not only the

collapse transition but also the aggregation mechanism of the micelles may be disclosed at higher concentration. In the next chapter, we will focus on the temperature-induced morphological transition of the same polymers in a semidilute aqueous solution at a concentration of 10 g L^{-1}.

8. Temperature-dependence of self-assembled micelles from PMMA-*b*-PNIPAM in semidilute aqueous solution

In this chapter, the temperature-induced morphological transition of self-assembled micelles formed by $PMMA_{21}$-*b*-$PNIPAM_{283}$ in aqueous solution at 10 g L^{-1} is investigated. At this, turbidimetry, dynamic light scattering (DLS), and synchrotron small-angle X-ray scattering (SAXS) experiments are performed during heating scan. This chapter is mainly based on ”Self-Assembled Micelles from Thermoresponsive Poly(methyl methacrylate)-*b*-poly(*N*-isopropylacrylamide) Diblock Copolymers in Aqueous Solution” C.-H. Ko et al. [126] *Macromolecules* **2021**, *54*, 384-397.

8.1 Introduction

In Chapter 7, it has been observed that the temperature-induced collapse transition of single micelle formed by $PMMA_{21}$-*b*-$PNIPAM_{283}$ in dilute aqueous solution at 1 g L^{-1}. However, due to the poor data quality of scattering resulting from the micellar shell, precisely determining the shell thickness below T_{CP} is hindered. To address this issue, we aim to perform measurements on a more concentrated solution which fraction of micelles is expected to be higher that may have stronger scattering contributed by the micelles.

In this chapter, a comprehensive structural investigation of the self-assembled micelles formed $PMMA_{21}$-*b*-$PNIPAM_{283}$ in semidilute aqueous solution at 10 g L^{-1} is done by turbidimetry, DLS and synchrotron SAXS in a temperature range around the cloud points with a good temperature resolution. Due to the more concentrated concentration, below the cloud point, not only the temperature-dependent structural transition of the micelles but also the correlations between the micelles are revealed. Furthermore, above the cloud point, the aggregation mechanism of the collapsed micelles and the structural evolution of the large aggregates are both disclosed.

Moreover, as mentioned in Section 3.3, PS-*b*-PNIPAM diblock copolymers is one of the most frequent investigated thermoresponsive amphiphilic diblock copolymers. Their self-assembled structures are usually not in equilibrium, but kinetically frozen [45]. Comparing to PS, it is known that PMMA is a hydrophobic polymer, which is more compatible and less hydrophobic [111, 112]. Therefore, PMMA can serve as an attractive alternative for hydrophobic blocks. At the end of this Chapter, a comparison between the self-assembled micelles from PS-*b*-PNIPAM and the one from PMMA-*b*-PNIPAM is made to discuss the influence of the hydrophobicity of the hydrophobic blocks on the inner structure, interactions, and the aggregation of the micelles.

8.2 Phase behavior

Figure 8.1 presents the temperature-dependent light transmission curve of a 10 g L^{-1} $PMMA_{21}$-*b*-$PNIPAM_{283}$ solution in D_2O, measured by turbidimetry at heating rate of 0.2 K min^{-1}. Upon heating, the normalized transmission is constant at ~1 up to 31 °C, shows an abruptly decays. The cloud point is determined to be T_{CP} = 31.2 ± 0.5 °C as the temperature where the normalized transmission begins to decrease. T_{CP} of $PMMA_{21}$-*b*-$PNIPAM_{283}$ is similar as the values of PNIPAM homopolymer (~32 °C) that mostly reported in the literature [15, 16]. From 31 to 32 °C, the normalized transmission drops to ~0 and remains constant ~0 above 32 °C, indicating that the phase transition is rather sharp.

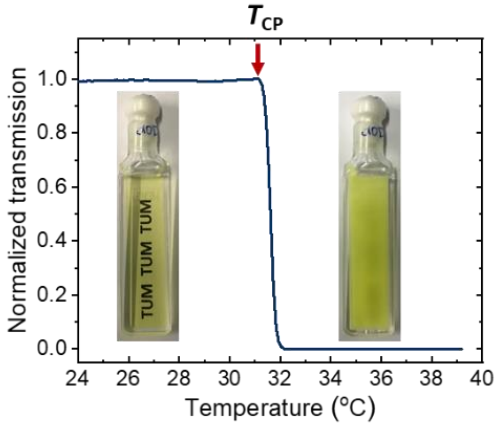

Figure 8.1 Light transmission of the 10 g L^{-1} $PMMA_{21}$-*b*-$PNIPAM_{283}$ solution in D_2O in dependence on temperature. The photos show a solution below T_{CP} (left) and above T_{CP} (right). The red arrow indicates the cloud point. (Reprinted from Ref. [126]. Copyright (2021) American Chemical Society.)

8.3 Temperature-dependence of micellar size

To investigate whether the diffusion of the micelles is translational, we performed the angular-dependent DLS measurement on 10 g L^{-1} $PMMA_{21}$-*b*-$PNIPAM_{283}$ solution in D_2O at 20 °C and in scattering angle θ range from 45° to 135° (Figure 8.2a). The decay rate Γ depends linearly on q^2. The diffusion coefficient of the micelles is determined as $D = 6.57 \times 10^{-12} \pm 9.04 \times 10^{-14}$ m^2 s^{-1} from the slope of the linear fit to Γ versus q^2 (Figure 8.2b). The hydrodynamic radius, R_h, is calculated as R_h = 26.1 ± 0.4 nm by the Stokes-Einstein equation ($R_h = k_B T/6\pi\eta_s D$), where the Boltzmann constant k_B = 1.38×10^{-23} kg m^2 s^{-2} K^{-1}, temperature T = 293.1 K, and the solvent viscosity η_s = 0.00125 kg $m^{-1}s^{-1}$. Due to the time constraint, the temperature-resolved DLS measurements from 20 °C to 31.5 °C were carried out only at scattering angle θ = 90°.

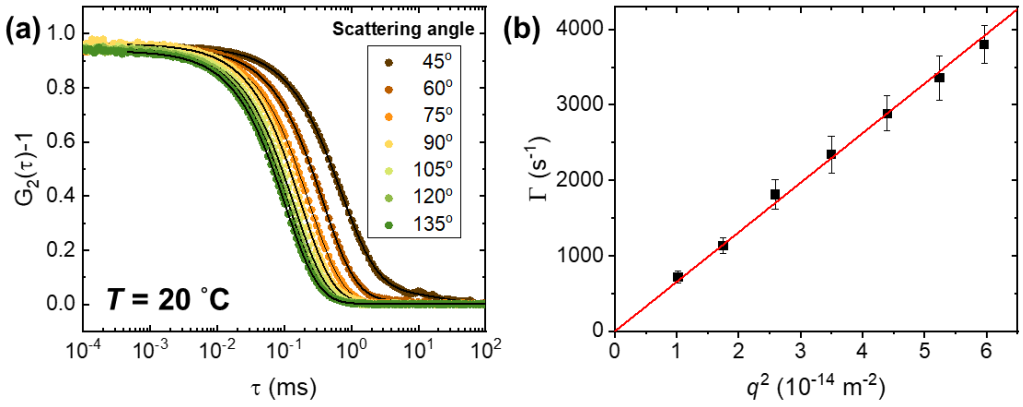

Figure 8.2 (a) Representative normalized intensity autocorrelation functions from DLS on 10 g L^{-1} $PMMA_{21}$-*b*-$PNIPAM_{283}$ solution in D_2O at $T = 20$ °C and at scattering angle, θ, given in the graphs. Black solid lines are model fits. (b) Decay rate as a function of q^2 (black squares). Red solid line is linear fit to the data. (Reprinted from Ref. [126]. Copyright (2021) American Chemical Society.)

Temperature-resolved DLS measurements were carried out to determine the hydrodynamic radius, R_h, of the micelles, formed by $PMMA_{21}$-*b*-$PNIPAM_{283}$ in D_2O in a temperature range below the cloud point. The representative normalized intensity autocorrelation functions and the corresponding distribution functions during heating and cooling are shown in Figure 8.3. The autocorrelation functions feature a single decay, and the corresponding distribution functions are monomodal distribution peaks, indicating that one type of diffusing particles prevails. The hydrodynamic radii, R_h, of the particles are assigned to single micelles. At 20 °C, the peak is centered at ~20-30 nm. Upon heating, the distributions shift toward slightly larger sizes and become narrower (Figure 8.3c). These changes are reversible, as seen in the results from the cooling run. (Figure 8.3d).

The average R_h values of the micelles during heating and cooling run are summarized in Figure 8.3e. At 20 °C, R_h is ~27 nm, which is consistent with R_h determined from the angular-resolved DLS measurement in Figure 8.2. As the temperature increases upon heating, R_h remains nearly constant at ~27 nm from 20 to 28 °C. Upon further heating from 28 to 31.5 °C, R_h slightly increases to ~32 nm, suggesting that the micellar size increases as the temperature approaches T_{CP}. This could be attributed to one of these reasons: (i) the expansion of the PNIPAM shell, (ii) an increase of the aggregation number, and (iii) the presence of aggregates consisting of several collapsed micelles. Since DLS only gives overall information on the size rather than the inner structure of the micelles and their possible aggregation, these scenarios cannot be distinguished. Above 31.5 °C, DLS measurements are no longer possible due to the high turbidity. Upon cooling, R_h decreases back to ~27 nm at 28 °C, and stays

constant at this value down to 20 °C. Between 31.5 and 28 °C, R_h is slightly larger during cooling than during heating, which may be assigned to the hysteresis effect of PNIPAM block.[110, 189] From 28 to 20 °C, the value from heating and cooling are equal, indicating that the temperature-dependent transition of the micellar size is reversible.

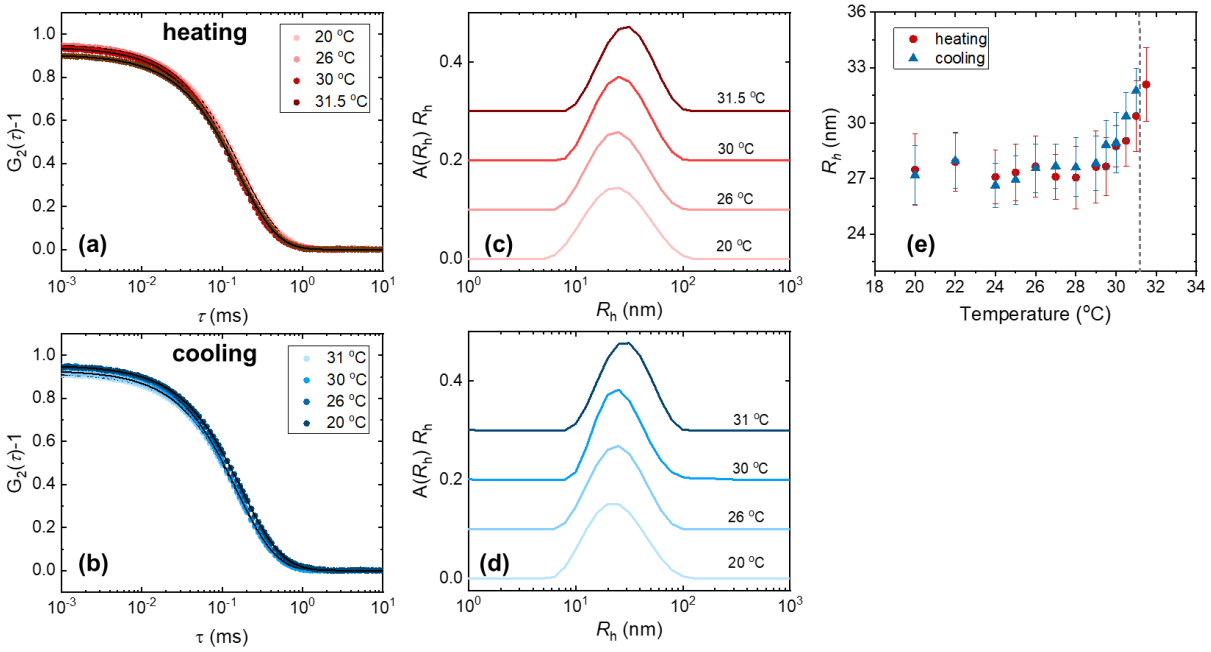

Figure 8.3 (a, b) Representative normalized intensity autocorrelation functions and (c, d) the corresponding distribution functions of hydrodynamic radii, R_h, from DLS on the 10 g L^{-1} $PMMA_{21}$-*b*-$PNIPAM_{283}$ solution in D_2O at the temperatures given in the graphs during heating and cooling runs. (e) the average hydrodynamic radii, R_h, of the micelles during heating (red circles) and cooling (blue triangles) runs. The grey dashed line points to the cloud point, T_{CP}, determined by turbidimetry. (Reprinted from Ref. [126]. Copyright (2021) American Chemical Society.)

8.4 Morphological transition and aggregation mechanism of the micelles upon heating

8.4.1 Overview

To characterize the internal morphology of the micelles and further elucidate the origin of the increase in R_h, when the temperature approached T_{CP}, temperature-resolved synchrotron SAXS measurements were performed on the sample solution. The temperature range was chosen from 20 to 38 °C to cover the range below and above T_{CP}. The SAXS data are shown in Figure 8.4.

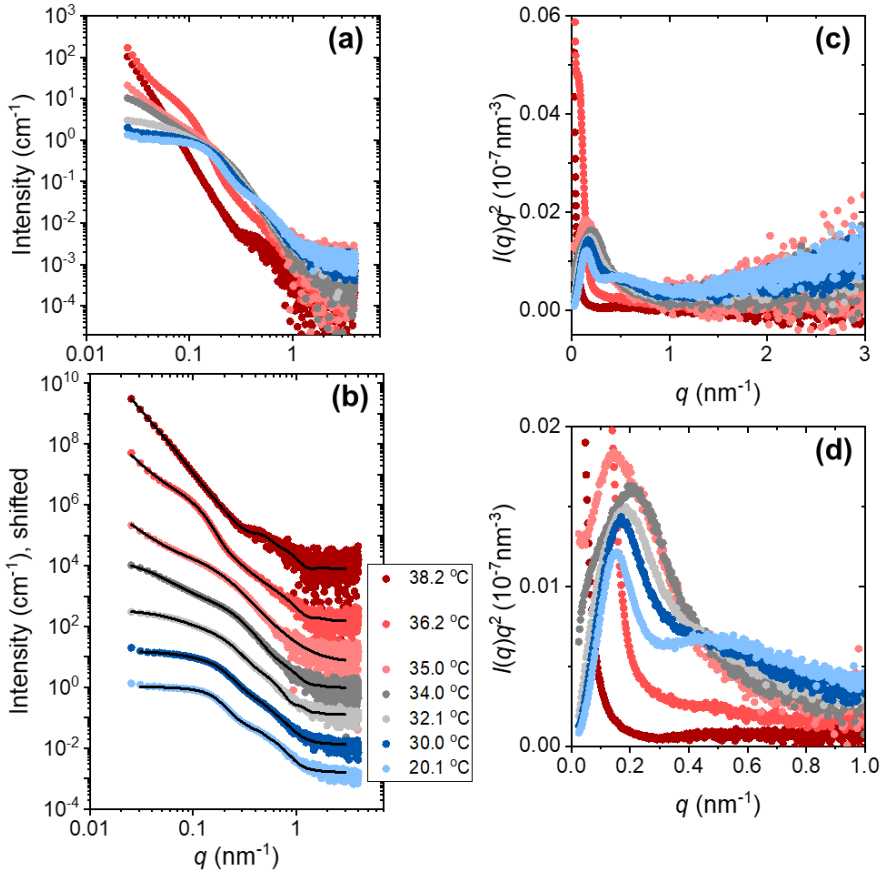

Figure 8.4 (a) Representative SAXS data of the 10 g L^{-1} PMMA$_{21}$-*b*-PNIPAM$_{283}$ solution in D_2O (symbols) at the temperatures given in (b). The blue, grey and red color indicate regime I (below T_{CP}), regime II (above T_{CP}) and regime III (far above T_{CP}), respectively. For clarity, in (b), the curves are shifted by a factor of 10 with respect to each other, and only every second point is shown. The black solid lines are the model fits. (c) Kratky plot, $I(q)q^2$ vs q, of the same data. (d) is a zoom of the low-q part of (c). (Reprinted from Ref. [126]. Copyright (2021) American Chemical Society.)

Below T_{CP} (20.1-30.0 °C), all the scattering curves feature a prominent shoulder at ~0.15 nm^{-1} and a second shoulder at ~0.5 nm^{-1} (Figure 8.4a, b). These features can be tentatively attributed to the form factor scattering of the micelles. Upon heating towards 30.0 °C, the second shoulder becomes less pronounced. Above T_{CP} (32.1-34.0 °C), the second shoulder becomes even less obvious and the prominent shoulder dominates and shifts towards slightly higher q values (~0.25 nm^{-1}), which can be assigned to the collapse of the PNIPAM blocks resulting in a shrinkage of micellar size. Furthermore, an additional shoulder appears at low q values (~0.03 nm^{-1}), and its intensity increases drastically, as the temperature is increased to 34.0 °C. This may be due to the presence and growth of large aggregates

formed by the collapsed micelles. Above 34.0 °C, this shoulder turns into a straight line, possibly because the shoulder shifts to even lower q values, which are beyond the observation window. This indicates that the aggregates continuously grow with increasing temperature. At 35.0 °C, the scattering curve shows only a slope at low q range (~0.03 nm^{-1}) and a shoulder at q ~0.20 nm^{-1}, which are attributed to the large aggregates and the collapsed micelles. At 36.2 °C, the contribution at low q values becomes even more pronounced, the shoulder shifts towards to higher q values (~0.60 nm^{-1}), revealing that the aggregates prevail and that of the collapsed micelles continue to shrink. Besides, an additional shoulder emerges at q ~0.15 nm^{-1}, which is ascribed to aggregates of intermediate size. At 38.2 °C, the contribution at low q values dominates and becomes a bit steeper, the extra shoulder q ~0.15 nm^{-1} becomes very weak, and the shoulder at q ~0.60 nm^{-1} turns into a peak, indicating that the collapsed micelles become correlated with each other. Based on the changes in the scattering curves, the temperature range is divided into three regimes: regime I (20.1-31.1 °C, below T_{CP}), regime II (32.1-34.0 °C, just above T_{CP}), and regime III (35.0-38.2 °C, far above T_{CP}).

The Kratky plots of these SAXS data are displayed in Figure 8.4c and d, providing model-free information on the micellar structures. In regime I, a bell-shaped peak at q ~0.18 nm^{-1} reveals a compact, globular structure, which is attributed to the compact micellar core formed by the PMMA blocks. An additional weaker shoulder at q ~0.5 nm^{-1} suggests that the globular structure is composed of more than one domain, which, in this case, may be due to the core-shell structure of the micelles. Towards high q values (q > 1 nm^{-1}), the curve in the Kratky plot has a plateau at intermediate q values (q ~1-1.5 nm^{-1}) and monotonically increases (q > 2 nm^{-1}). This indicates loosely packed chains, which is ascribed to the hydrophilic PNIPAM blocks in the micellar shell [187]. In regime II, the bell-shaped peak at q ~0.18 nm^{-1} becomes broader, subtly shifts toward higher q values, and its amplitude increases. Furthermore, the weak maximum at q ~0.5 nm^{-1} vanishes, and only a decay is present. These changes are indicative of a decreasing micellar size and a dehydration of the micellar shell, resulting in a disappearance of the contrast between the micellar core and the shell. In regime III, the distribution strongly changes shape: At 35.0 °C, the bell-shaped peak shifts to lower q values. At 36.2 °C, a slope at low q values and a small peak at q ~0.06 nm^{-1} are observed, and, at 38.2 °C, a deeper slope at low q values. These imply the formation and growth of large aggregates from a number of collapsed micelles. At 36.2 and 38.2 °C, the curves decay to zero at high q values, which indicates that the PNIPAM blocks in the micellar shell are compact due to strong dehydration.

8.4.2 Fit Model

Modeling the SAXS data enables us to gain detailed information on the inner structure of self-assembled micelles quantitatively. Exemplary model fits for different temperatures from the 3 regimes along with the contributions to the fitting model are displayed in Figure 8.5.

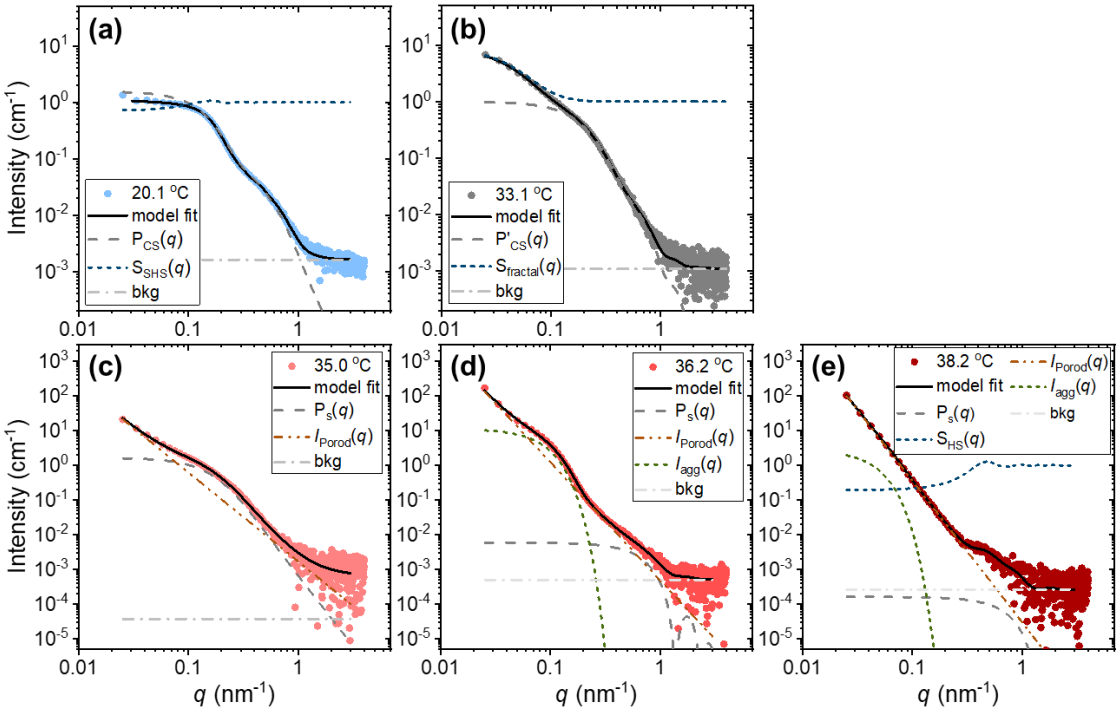

Figure 8.5 Model fits of the SAXS data. Data in regime I at 20.1 °C (a), regime II at 33.1 °C (b), and regime III at 35 °C (c), 36.2 °C (d), 38.2 °C (e), model fits (black full lines), and contributions from each term in the fitting model (dashed lines, as marked in legend). (Reprinted from Ref. [126]. Copyright (2021) American Chemical Society.)

From 20.1 to 31.1 °C, i.e., below T_{CP}, the SAXS curves in regime I, are described by a model comprising a core-shell sphere form factor, $P_{CS}(q)$, with a shell SLD profile based on an exponential function along the radial direction, and a sticky hard-sphere structure factor, $S_{SHS}(q)$, (Figure 8.5a, eq. 8.1).

$$I(q) = I_0 P_{cs}(q) S_{SHS}(q) + I_{bkg} \tag{8.1}$$

It is suggested that the diblock copolymers self-assemble into spherical micelles with a hydrophobic PMMA core and a hydrophilic PNIPAM shell. The PNIPAM shell has a radially decaying exponential concentration profile, i.e., the D_2O content varies along the radial direction. The micellar radius, R_{mic}, the micellar core radius, R_{core}, shell thickness, t_{shell}, the radially decaying SLD profile of

micellar shell are identified by the form factor. The SLD values of the core and the solvent are fixed during fitting, while the shell SLD values along radial direction are set to be free, as explained in the Section 4.5. The radially increasing D_2O content in the micellar shell can be determined by eq. 4.51. A core-shell sphere form factor, $P'_{CS}(q)$, with a homogeneous shell SLD cannot describe the data well below T_{CP}, which is possibly due to rather long hydrophilic PNIPAM blocks. The aggregation number of the micelles, N_{agg}, can be determined from the resulting R_{core} using eq. 4.52. The half-distance between two correlated micelles, R_{HS}, the volume fraction of correlated micelles, ϕ, and the stickiness, τ_0, related to interactions between correlated micelles are obtained from the structure factor and describe the correlations between micelles.

As the temperature increases above T_{CP}, from 32.1-34.0 °C (regime II), the SAXS curves are fitted by the model given in eq. 8.2 (Figure 8.5b).

$$I(q) = I_0 P'_{cs}(q) S_{fractal}(q) + I_{bkg} \tag{8.2}$$

The core-shell sphere from factor with a homogeneous shell SLD, $P'_{CS}(q)$, can now be used since the PNIPAM blocks collapse upon heating above T_{CP} resulting in rather homogeneous shell SLD. The fractal structure factor $S_{fractal}(q)$ is included to describe the shoulder appearing at low q values, which may originate from the formation of fractal clusters constituted of collapsed micelles. In addition to the detailed size information on the collapsed micelles, the radius gyration of fractal clusters, $R_{cluster}$, is determined.

Upon heating towards higher temperatures, namely above 34.0 °C (regime III), the system become more complex and be described by eq. 8.3.

$$I(q) = I_{Porod}(q) + I_{agg}(q) + I_0 P_s(q) S_{HS}(q) + I_{bkg} \tag{8.3}$$

Due to the continued collapse and dehydration of the PNIPAM shell, its SLD values is similar to the one of the PMMA core, and they can therefore not easily be differentiated. As a result, the collapsed micelles at all temperatures in regime III are described by the form factor of homogeneous spheres, $P_s(q)$, giving the overall size of the collapsed micelles. At 35.0 °C (Figure 8.5c), the model in eq. 8.3 without the $I_{agg}(q)$ term and the hard-sphere structure factor, $S_{HS}(q)$, is applied, where the $I_{Porod}(q)$ term includes the surface roughness of large aggregates. At 36.2 °C (Figure 8.5d), the SAXS curve is fitted by the model in eq. 8.3 without $S_{HS}(q)$. The $I_{agg}(q)$ term is added to model scattering from intermediate size aggregates. At 38.2 °C (Figure 8.5e), the model in eq 8.3 is used for fitting. The hard-sphere structure factor, $S_{HS}(q)$, is included here to describe the correlations between collapsed micelles. The

model fits are presented in Figure 8.4b. Complete sets of structural parameters are compiled in Tables D1-D3 in the Appendix.

8.4.3 Resulting temperature-dependent structural characteristics

The fit parameters are summarized in Figures 8.6-8.10. Below T_{CP}, the $PMMA_{21}$-*b*-$PNIPAM_{283}$ diblock copolymers form spherical core-shell micelles. At 20.1 °C, the micellar radius $R_{mic} \cong 24.4$ nm with a core radius of ~2.5 nm and a shell thickness t_{shell} of ~21.9 nm (Figure 8.6a), which is in agreement with the rather short hydrophobic PMMA block and the long hydrophilic PNIPAM block. The core polydispersity p_{core} is ~0.4 at 20.1 °C (Figure 8.6b). At the same temperature (20 °C), R_h is ~27.5 nm, which is slightly larger than R_{mic}, as expected. R_{mic} is larger than the calculated end-to-end distance of this diblock copolymer ($R_{ee,ideal}$ = 12.3 nm), while it is smaller than the calculated contour length (R_{max} = 76.6 nm), see Section 3.6.2 and Table 3.2 for the detailed calculation. This indicates that the PNIPAM blocks are swollen, but not fully stretched. The aggregation number N_{agg} of the micelles, as calculated from eq. 4.52 using R_{core} and the degree of polymerization of the PMMA block (DP_{PMMA}= 21) from ^{1}H NMR, amounts to ~23 at 20.1 °C (Figure 8.6c). The SLD profiles along the radial direction are shown in Figure 8.7a. At 20.1 °C, the SLD profile of the PNIPAM shell shows a radially exponential decay from a value of 9.59×10^{-6} Å^{-2} to the SLD value of D_2O (9.44×10^{-6} Å^{-2}), implying that the polymer segment concentration decreases along the radial direction. The closer to the micellar core, the denser the hydrophilic PNIPAM blocks, which was also previously found in PS-*b*-PNIPAM diblock copolymers [107], and in the micellar shell from PNIPAM homopolymers end-capped with hydrophobic ligand at one end [188]. The corresponding D_2O content in the micellar shell is shown in Figure 8.7b. At 20.1 °C, the D_2O content at the interface between the micellar core and shell is ~0.82 and it increases along the micellar radius to ~1. Thus, the inner part of the shell is less hydrated than the outer part shell, i.e., the PNIPAM blocks are more densely packed in the inner part of the shell, and more swollen in the outer part. At 20.1 °C, the hard-sphere radius R_{HS} is ~20.6 nm (Figure 8.6a), which is the half-distance between two correlated micelles. It is smaller than R_{mic}, meaning that the micelles interpenetrate with each other. The volume fraction of the correlated micelles ϕ is found to be ~0.06 (Figure 8.8a), i.e., the micelles are weakly correlated.

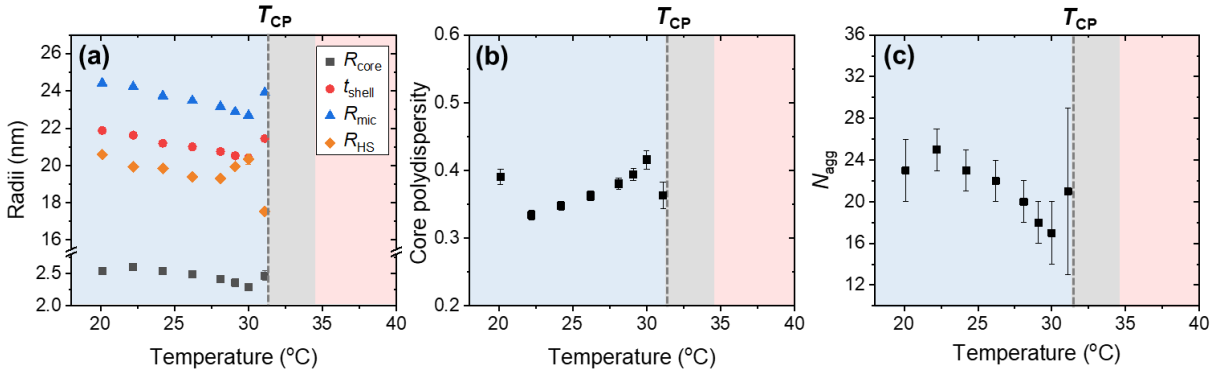

Figure 8.6 Resulting parameters from model fits in regime I: (a) micellar core radius R_{core} (black squares), shell thickness t_{shell} (red circles), micellar radius R_{mic} (blue triangles), hard-sphere radius R_{HS} (orange diamonds), as marked in the legend. (b) core polydispersity p_{core}. (c) aggregation number N_{agg}. The grey dashed line indicates T_{CP}, determined by turbidimetry. The light blue, light grey, and light red background colors indicate regimes I, II, and III, respectively. (Reprinted from Ref. [126]. Copyright (2021) American Chemical Society.)

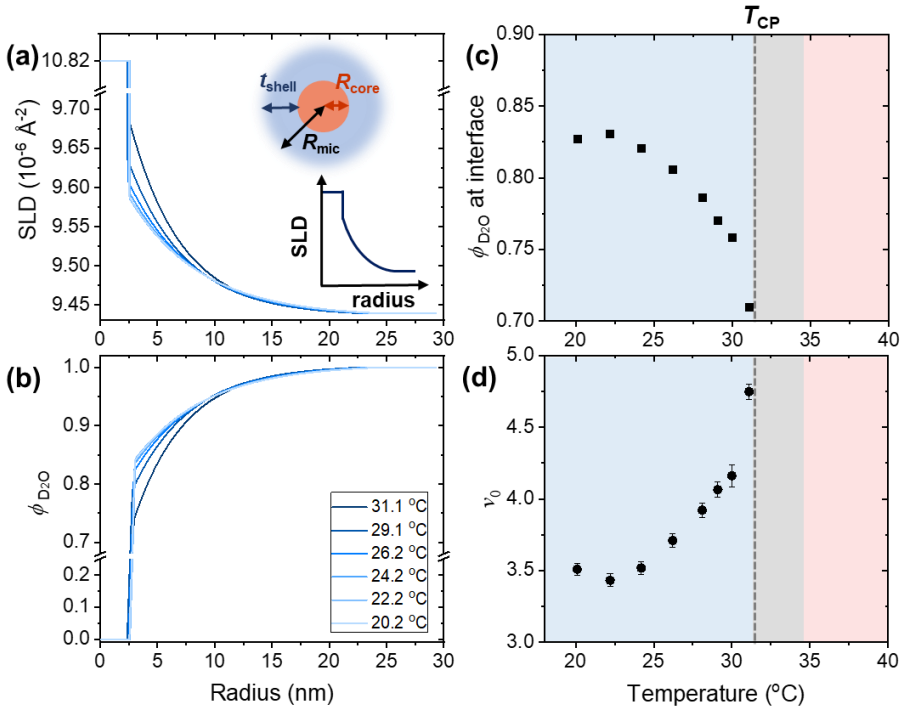

Figure 8.7 Resulting scattering length density SLD profile (a) and D_2O content (b) along the micellar radial direction at the temperatures in the legend. D_2O content at the interface of micellar core and shell (c) and parameter v_0 related to shape of the exponential function for shell SLD (d) in dependence on temperature. The inset in (a) illustrates the schematic of the SLD profile along the micellar radial direction. The light blue, light grey, and light red background colors indicate regimes I, II, and III, respectively. (Reprinted from Ref. [126]. Copyright (2021) American Chemical Society.)

As the temperature increases to 30.0 °C (still in regime I), R_{mic} decreases by ~1.7 nm, which is a result from a slight decrease of both R_{core} and t_{shell} (Figure 8.6a). The core polydispersity p_{core} increases to ~0.3-0.4 (Figure 8.6b). From the decrease of R_{core} decrease of N_{agg} to 17 is deduced (Figure 8.6c), which means that the PMMA blocks are mobile, and chain exchange among the micellar cores is possible.

Another change which takes place upon heating to 30.0 °C is that the SLD values in the shell increase and decay much steeply (Figure 8.7a), showing that the D_2O content of the micellar shell decreases. The PNIPAM blocks dehydrate gradually, and D_2O molecules are expelled from the micellar shell. The D_2O content within the micellar shell along the radial direction in regime I is displayed in dependence on temperature in Figure 8.7b. At the interface of the micellar core and shell, the D_2O content decreases from 0.83 to 0.76 between 20.1 and 30.0 °C (Figure 8.7c). Furthermore, the parameter v_0, which is related to the exponent of the shell SLD exponential function (Figure 8.7d and eq. 4.46), depicts quantitatively how steeply the functions decay. This not only characterizes the D_2O distribution in the micellar shell, but also provides hints regarding the interface between the micellar shell and solvent. In regime I, v_0 increases upon heating to 30.0 °C, implying that the interface between shell and solvent becomes sharper.

Regarding the correlations between the micelles in the temperature range of regime I, the hard-sphere radius R_{HS} remains at ~20 nm (Figure 8.6a), almost independent of temperature, indicating that the distance between the correlated micelles is more or less unchanged. The volume fraction of correlated micelles, ϕ, decreases to zero upon heating to 30.0 °C (Figure 8.8a), implying that less and less micelles are correlated. The stickiness, τ_0, stays around 0.5 from 20.1 to 26.2 °C, while it drops drastically to 0.1 from 28.0 to 30.0 °C. Smaller τ_0 values mean stronger attractive interactions between the correlated micelles. Moreover, the reduced second virial coefficient, b_2, remains at positive values of ~0.5 below 28.0 °C, and it turns into negative values above 29.1 °C (Figure 8.8b). This indicates that the interactions change from repulsive to attractive. Thus, in regime I, the interactions between the correlated micelles turn from repulsive to attractive and become stronger upon heating, despite the fact that fewer micelles are correlated with each other.

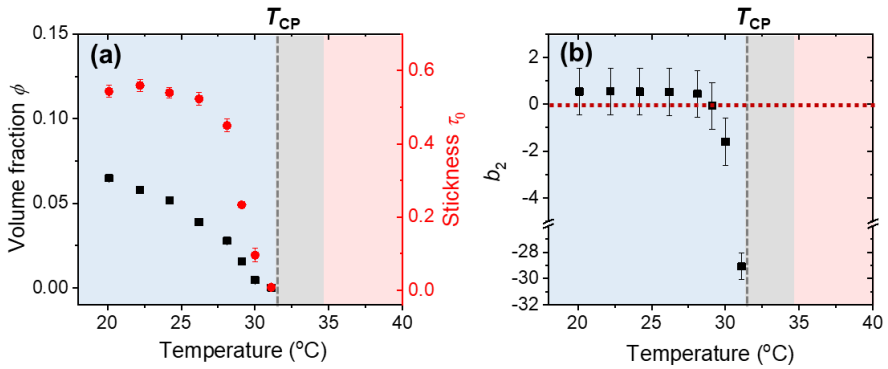

Figure 8.8 (a) Volume fraction of correlated micelles ϕ (black squares) and stickiness τ_0 (red circles) (b)The reduced second virial coefficient b_2 determined from the stickiness parameter τ_0. The red dashed line indicates $b_2 = 0$. The grey dashed line indicates T_{CP}, as determined by turbidimetry. The light blue, light grey and light red background colors indicate regimes I, II, and III, respectively. (Reprinted from Ref. [126]. Copyright (2021) American Chemical Society.)

At T_{CP} (31.1 °C), R_{mic} is 23.9 nm, which is ~1.3 nm larger than the value at 30.0 °C. Comparing to 30.0 °C, R_{core} has increased slightly by 0.3 nm, resulting in a slight increase of N_{agg} at 31.1 °C. The micellar shell swells by ~1 nm, while it significantly dehydrates at 31.1 °C. It can be observed from the D_2O content profile at 31.1 °C is generally lower than the one at lower temperatures in regime I (Figure 8.7b). Similarly, the D_2O content at the interface of micellar core and shell is only 0.70, which is 0.06 lower than at 30.0 °C (Figure 8.7c). The micellar shell has not collapsed yet, but is severely dehydrated at T_{CP}. R_{HS} changes from 20 to 17 nm, revealing that the correlated micelles are closer to each other at 31.1 °C. As evident from the parameters ϕ and τ_0 at 31.1 °C (Figure 8.8a), the amount of the correlated micelles becomes remarkably lower, yet the attractive interactions between correlated micelles are strikingly enhanced.

In regime II, i.e., above T_{CP} from 32.1 to 34.0 °C, R_{core} is ~2 nm, i.e., slightly smaller than below T_{CP}, while t_{shell} has shrunken abruptly to ~11 nm and continuously decreases with increasing temperature (Figure 8.9). Likewise, R_{mic} shrinks continuously from 13 to 9 nm and is throughout smaller than in regime I. This indicates that the decrease of the micellar size is due to the strong collapse of the PNIPAM blocks, inducing the shrinkage of micellar shell. Furthermore, fractal clusters form in regime II with the collapsed micelles being the building blocks. The fractal correlation length, ξ_f, increases from 10 to 25 nm (Figure 8.10a). The size of the fractal clusters, $R_{cluster}$, can be estimated by eq. 4.66. In regime II, $R_{cluster}$ increases from 30 to 56 nm (Figure 8.9). The fractal dimension D_f has a value of ~3 at 32.1 and 33.1 °C and 2.6 at 34.0 °C (Figure 8.10a), implying that the clusters are rather densely packed.

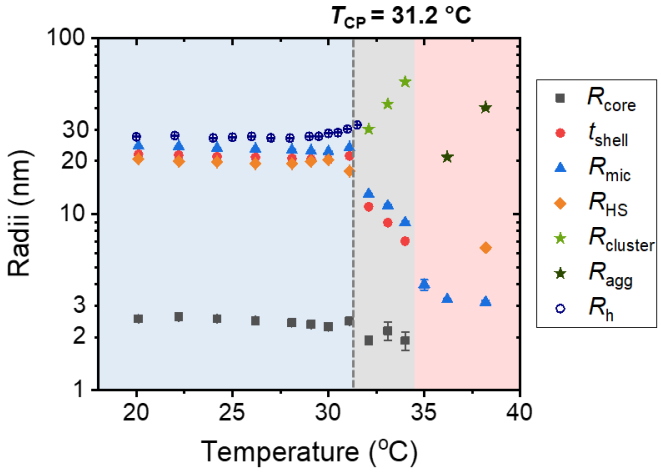

Figure 8.9 Resulting parameters obtained from model fitting to the SAXS data in dependence on temperature. Micellar core radius R_{core} (black squares), shell thickness t_{shell} (red circles), micellar radius R_{mic} (blue triangles), hard-sphere radius R_{HS} (orange diamonds), radius of gyration of the fractal clusters, $R_{cluster}$ (green stars), and radius of gyration of the aggregates, R_{agg} (dark green stars), as marked in the legend. The hydrodynamic radius R_h measured during the heating run (dark blue spheres) is plotted here again for comparison. The grey dashed line indicates T_{CP}, as determined by turbidimetry. The light blue, light grey, and light red background colors indicate regimes I, II, and III, respectively. (Reprinted from Ref. [126]. Copyright (2021) American Chemical Society.)

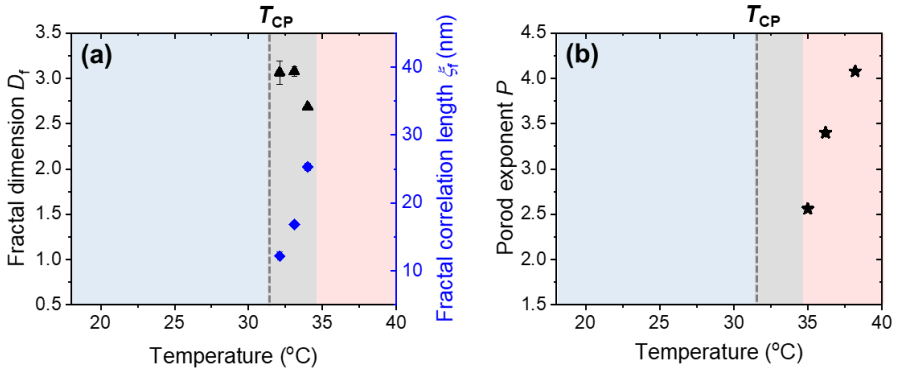

Figure 8.10 (a) Fractal dimension D_f (black triangles) and fractal correlation length ξ_f (blue diamonds). (c) Porod exponent P. The grey dashed line indicates T_{CP}, determined by turbidimetry. The light blue, light grey and light red background colors indicate regimes I, II, and III, respectively. (Reprinted from Ref. [126]. Copyright (2021) American Chemical Society.)

In regime III (35.0 to 38.2 °C), i.e., far above T_{CP}, it is no longer possible to distinguish between the core and shell, because of the weak SLD contrast between PMMA and the strongly dehydrated

PNIPAM blocks. At 35.0 °C, R_{mic} features another abrupt decrease to ~4 nm (Figure 8.9); thus, the shell is even more compact due to the continued dehydration and collapse of the PNIPAM blocks. Upon heating from 35.0 to 38.2 °C, R_{mic} slightly shrinks to ~3 nm. At 38.2 °C, R_{HS} is ~ 6 nm, suggesting that the collapsed micelles not only shrink but are also correlated with each other with a half-distance of 6 nm. In regime III, the SAXS curves feature a slope at low q values instead of a shoulder, which may be attributed to a shift of the shoulder to q values below the accessible q range. This implies that the fractal clusters grow presumably and form even larger aggregates, whose size is too large to be resolved. However, the Porod exponent P enables us to characterize their surface roughness. From 35.0 to 38.2 °C, P increases from 2.5 to 4 (Figure 8.10b), indicating that the surface of large clusters or aggregates changes from rough to smooth. Additionally, some intermediate-size aggregates with ~20 nm appears at 36.2 °C, which grows to ~40 nm at 38.2 °C. This is possibly due to heterogeneous aggregation in this temperature range.

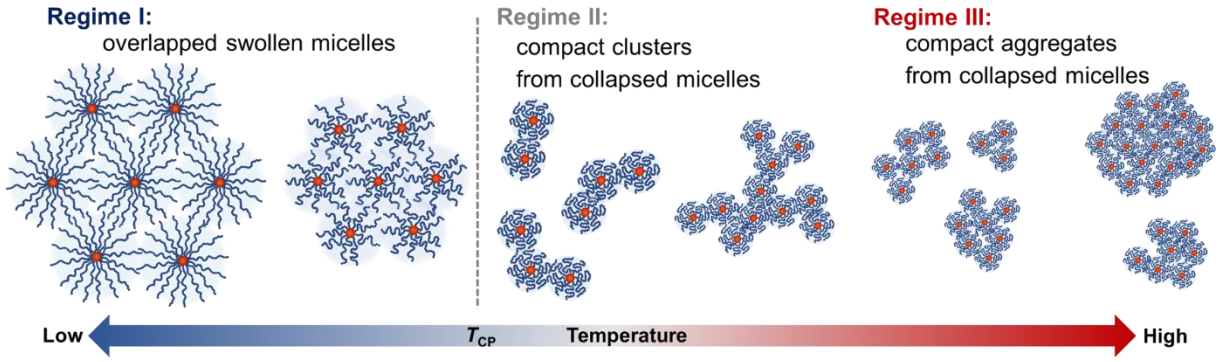

Figure 8.11 Schematic representation of the structural evolution of the self-assembled structures formed by $PMMA_{21}$-*b*-$PNIPAM_{283}$ in D_2O at 10 g L^{-1} in dependence on temperature. Red spheres represent the micellar core from the PMMA blocks. The blue lines stand for the PNIPAM blocks. (Reprinted from Ref. [126]. Copyright (2021) American Chemical Society.)

Based on the results, the temperature-dependent structural changes of $PMMA_{21}$-*b*-$PNIPAM_{283}$ in D_2O at 10 g L^{-1} are summarized schematically in Figure 8.11. Below T_{CP}, $PMMA_{21}$-*b*-$PNIPAM_{283}$ in D_2O forms spherical core-shell micelles, which feature a rather small core, formed by PMMA blocks, and a thick hydrated shell formed by the PNIPAM blocks with a radially decaying water content. The swollen micelles are overlapped and correlated with each other. As temperature increases in regime I, the micelles slightly shrink and their correlation weakens. The aggregation number of the micelles decreases upon heating, indicating that the PMMA blocks are mobile and can exchange between micelles. The overall water content in the micellar shell decreases upon heating in regime I, due to the dehydration and partial collapse of PNIPAM blocks. At T_{CP}, the micelles dramatically shrink due to

the collapse of the PNIPAM blocks, the core radius increases slightly due to an increase of the aggregation number. The collapsed micelles form fractal clusters. Upon further heating in regime II, the fractal clusters grow, while the collapsed micelles continuously shrink. As temperature is raised far above T_{CP} (regime III), the fractal clusters grow into even larger and compact aggregates. The simultaneous presence of intermediate size aggregates implies that heterogeneous aggregation occurs far above T_{CP}.

Our results from $PMMA_{21}$-*b*-$PNIPAM_{283}$ diblock copolymers with PNIPAM weight fraction w_{PNIPAM} of 0.94 may be compared with the previous reported findings from a similar sample, $PMMA_{16}$-*b*-$PNIPAM_{172}$ with w_{PNIPAM} of 0.92 [113]. Both PMMA-*b*-PNIPAM diblock copolymers form spherical micelles in aqueous solution having similar hydrodynamic radii (~30-40 nm below T_{CP}). For $PMMA_{14}$-*b*-$PNIPAM_{106}$ diblock copolymers with w_{PNIPAM} of 0.89 in 10 wt% aqueous solutions, hydrogels were found below T_{CP}, which consist of ordered packed micelles [113]. This is consistent with our results that the swollen micelles in regime I are overlapped and correlated with each other, although the concentration used by us is significantly lower (10 g L^{-1}, i.e., ~0.9 wt%).

8.5 Comparison of PMMA-*b*-PNIPAM with PS-*b*-PNIPAM

Unlike PS-*b*-PNIPAM diblock copolymers, which form spherical micelles only in a narrow range of w_{PNIPAM} [103, 105, 107], $PMMA_{21}$-*b*-$PNIPAM_{283}$ diblock copolymers with a relatively high w_{PNIPAM} of 0.94 are still capable of forming stable spherical micelles. In comparison to PS_{48}-*b*-$PNIPAM_{159}$ diblock copolymers (w_{PNIPAM} of 0.78) in aqueous solution, which also form spherical micelles [107], the overall size of the micelles from $PMMA_{21}$-*b*-$PNIPAM_{283}$ is about 18 nm larger. As expected from the shorter PMMA blocks, the micellar cores in $PMMA_{21}$-*b*-$PNIPAM_{283}$ are smaller. Below T_{CP}, the swollen micelles from $PMMA_{21}$-*b*-$PNIPAM_{283}$ are overlapped with each other, while the micelles from PS_{48}-*b*-$PNIPAM_{159}$ keep a certain distance with each other. As temperature approaches T_{CP}, the shell thickness of micelles from $PMMA_{21}$-*b*-$PNIPAM_{283}$ decreases, whereas the one from PS_{48}-*b*-$PNIPAM_{159}$ firstly increases and then decreases (Figure 8.12). This may be attributed to the lower hydrophobicity of PMMA. It is known that PS is glassy and hydrophobic which leads to enhanced interchain interactions between the PNIPAM blocks and thus hinders their collapse in the micellar shell causing the initial increase of micellar size upon heating [103, 105]. The weaker hydrophobicity of PMMA not only weakens interchain interactions between the PMMA blocks giving rise to lower aggregation number of micelles but also reduces the interchain interactions between the adjacent PNIPAM blocks in the swollen micellar shells. Therefore, the intrachain interactions within the micellar shell of $PMMA_{21}$-*b*-$PNIPAM_{283}$ dominate and cause the subtle shrinkage of micellar shell, as

temperature approaches T_{CP}. Above T_{CP}, the micelles from $PMMA_{21}$-*b*-$PNIPAM_{283}$ firstly collapse and fractal clusters are formed by collapsed micelles. These clusters grow and become compact aggregates. In contrast, for the micelles from PS_{48}-*b*-$PNIPAM_{159}$, very small clusters are formed by partially collapsed micelles already 2-3 °C below T_{CP}, their number firstly increases, and these small clusters grow with increasing temperature above T_{CP}. This may be ascribed to the difference in hydrophobicity of the hydrophobic blocks. The collapse transition and the aggregation behavior of the micelles are significantly changed by tuning the hydrophobicity of the hydrophobic blocks because of the different extent of interchain interactions in the micellar cores.

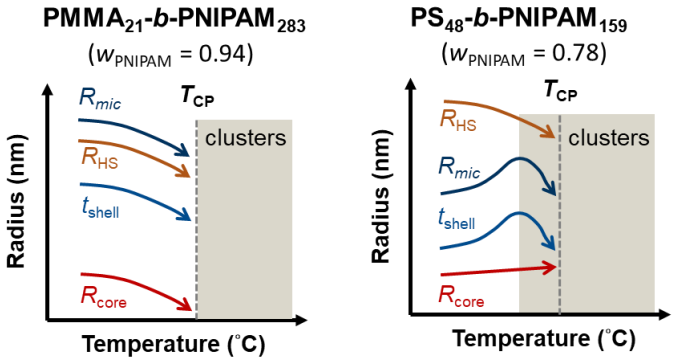

Figure 8.12 Schematic representation of the structural differences of the self-assembled structures formed by $PMMA_{21}$-*b*-$PNIPAM_{283}$ and PS_{21}-*b*-$PNIPAM_{159}$ in dependence on temperature. The light brown background color indicates the temperature range that the clusters form. (The findings from PS_{21}-*b*-$PNIPAM_{159}$ refer to Ref. [107])

8.6 Conclusions

The phase behavior in D_2O is probed by turbidimetry, revealing the cloud point T_{CP} in dilute solution to be 31.1 °C. The temperature-induced morphological transition of the micelles and their subsequent secondary aggregation behavior are investigated in detail by DLS and SAXS. The inner structure, the interactions, and the aggregation of the micelles are revealed. Comparing the findings from PMMA-*b*-PNIPAM with the ones from PS-*b*-PNIPAM, it becomes clear that the hydrophobicity of the hydrophobic blocks plays an important role on the inner structure, interactions, and the aggregation of the micelles, which is attributed to the different extent of the interchain interactions in the micellar core and shell.

Thanks to its enhanced solubility, facilitated micelle formation and improve biocompatibility compared to previously reported PS-*b*-PNIPAM polymers, the presented PMMA-*b*-PNIPAM diblock copolymer can serve as a more appropriate carrier system for drug delivery or biomedical applications. The insights into the morphological transition and the aggregation behavior of its self-assembled

micelles will facilitate the future designing of substance transport systems with a better-controlled loading and releasing capability.

9. Co-nonsolvency effect of PMMA-*b*-PNIPAM in water/methanol mixtures

In this chapter, the influence of the solvent composition on the thermal and structural properties of $PMMA_{21}$-*b*-$PNIPAM_{283}$ in D_2O/CD_3OD mixtures at 10 g L^{-1} is investigated at ambient temperature 20 °C. At this, the phase diagram is constructed using turbidimetry and differential scanning calorimetry (DSC). Dynamic light scattering (DLS) and synchrotron small-angle X-ray scattering (SAXS) experiments are performed to reveal the structural changes on $PMMA_{21}$-*b*-$PNIPAM_{283}$ at 10 g L^{-1} in dependence on the solvent composition at 20 °C.

Parts of this chapter are based on experiments performed by Patrick Wastian and Luka Gaetani for their bachelor's theses [135, 190]. A paper about the results in this chapter with the title " Co-nonsolvency Effect in Solutions of Poly(methyl methacrylate)-*b*-poly(*N*-isopropylacrylamide) Diblock Copolymers in Water/Methanol Mixtures" is currently under preparation.

9.1 Introduction

In Chapter 8, the temperature-dependent structural investigation of the self-assembled micelles formed $PMMA_{21}$-*b*-$PNIPAM_{283}$ in aqueous solution at 10 g L^{-1} has been studied. PNIPAM blocks are not only sensitive to temperature, but also to the solvent composition. Adding methanol as a cosolvent causes these blocks to collapse which reduces the transition temperature, i.e., co-nonsolvency is observed. At room temperature, PNIPAM polymer chains experience the reentrant coil-to-globule-to-coil transition with a miscibility gap range from ca. 25-65 vol% of methanol [90, 91]. However, PMMA features the co-solvency effect in water/methanol mixtures, i.e., the solubility of PMMA block is enhanced in mixtures of water and methanol with ~80-95 wt% of methanol, i.e., ca 85-98 vol% of methanol [120]. Therefore, $PMMA_{21}$-*b*-$PNIPAM_{283}$ diblock copolymers in water/methanol mixtures are responsive to both temperature and the solvent composition.

In this chapter, due to the peculiar co-nonsolvency and co-solvency effects, we focus on the influence of the solvent composition on the thermal and structural properties of $PMMA_{21}$-*b*-$PNIPAM_{283}$ at 10 g L^{-1} in different D_2O/CD_3OD mixtures. The phase diagram of $PMMA_{21}$-*b*-$PNIPAM_{283}$ in dependence on the volume fraction of CD_3OD is established by turbidimetry and DSC. DLS and SAXS disclose the structural changes of $PMMA_{21}$-*b*-$PNIPAM_{283}$ in dependence on the solvent composition at 20 °C. We explore how the co-nonsolvency and the co-solvency effects play the roles in the morphology of $PMMA_{21}$-*b*-$PNIPAM_{283}$ in deuterated water/methanol mixtures.

9.2 Phase behavior

In Figure 9.1, the temperature-dependent light transmission curves of 10 g L^{-1} $PMMA_{21}$-*b*-$PNIPAM_{283}$ solutions in D_2O/CD_3OD mixtures from turbidimetry measurements at a heating rate of 0.2 K min^{-1} are presented. In water-rich solvent mixtures, the cloud points, T_{CP}, of the samples, taken as the temperature where the normalized transmission starts to decrease, are shown in Figure 9.2. T_{CP} decreases from of 31.2 ± 0.2 °C in pure D_2O to 13.6 ± 0.2 °C in 70:30 v/v D_2O/CD_3OD. A similar trend was observed for PNIPAM homopolymer solutions [82, 191]; however, the T_{CP} values of PMMA-*b*-PNIPAM are generally ~1°C lower than the ones of PNIPAM. This may be attributed to the usage of D_2O instead of H_2O and the steric hindrances caused by the dense packing of the PNIPAM blocks near the PMMA cores of the micelles. Moreover, the decrease of the light transmission becomes slightly broader with increasing CD_3OD volume fraction, and finite values are reached above T_{CP}. In methanol-rich solvent mixtures, the polymer solutions are clear and transparent in the temperature range from 15 to 55 °C. The samples with volume fractions of CD_3OD above 70 % do not exhibit a cloud point T_{CP} within the temperature range accessible.

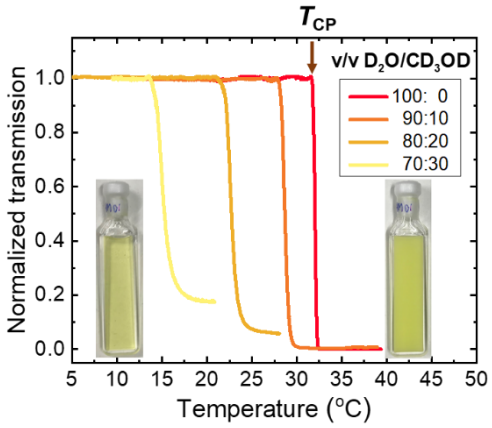

Figure 9.1 Temperature-dependent light transmission of $PMMA_{21}$-*b*-$PNIPAM_{283}$ solutions at 10 g L^{-1} in D_2O/CD_3OD mixtures in dependence on the volume fraction of CD_3OD. The red arrow points out T_{CP}. The inset photos show the solution in 90:10 v/v D_2O/CD_3OD below T_{CP} (left) and above T_{CP} (right).

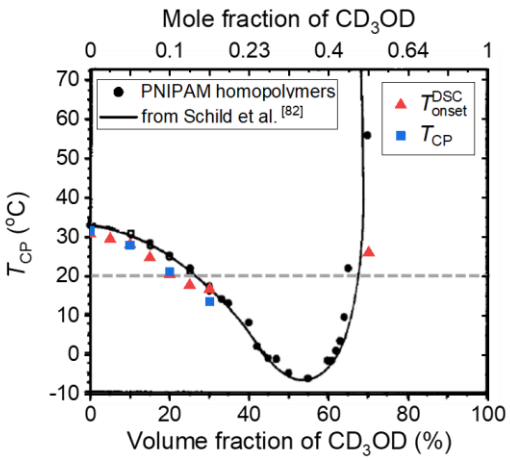

Figure 9.2 Cloud points determined by turbidimetry (blue squares) and onset temperatures from DSC (red triangles) of $PMMA_{21}$-*b*-$PNIPAM_{283}$ solutions at 10 g L^{-1} in D_2O/CD_3OD mixtures in dependence on the volume fraction of CD_3OD. For comparison, cloud points (black closed circles) and transition temperatures from DSC (black open circles) of PNIPAM homopolymers in H_2O/CH_3OH mixtures are given, which are taken from Ref. [82]. Reprinted with permission from Ref. [82]. Copyright 1991 American Chemical Society. The grey dashed line indicates the temperature at which DLS and SAXS measurements were performed.

9.3 Thermal behavior

Figure 9.3a displays the DSC thermograms from the second heating and cooling cycle at a rate of 1 K min^{-1}. The onset temperatures of the phase transition during the second heating run, T_{onset}^{DSC}, are given in Table 9.1 and Figure 9.2. In water-rich solvent mixtures, T_{onset}^{DSC} decreases as the volume fraction of CD_3OD increases, and the values are in agreement with the values of T_{CP} observed by turbidimetry. Moreover, the higher the volume fraction of CD_3OD, the broader and the more asymmetric is the endothermic peak. This broadening is in accordance with the findings from turbidimetry. From the endothermic peak areas, the enthalpies of the phase transition, ΔH, are identified and are given in Table 9.1 and Figure 9.3b. They decrease with increasing volume fraction of CD_3OD, which is in consistency with the computational [99] and experimental [100] calorimetric enthalpies of PNIPAM homopolymers in water/methanol mixtures. The endothermic enthalpy is related to the heat required to break the hydrogen bonds between the polymers and the solvent molecules [82, 99, 192]. As demonstrated in Ref. [99] and [100], the presence of CD_3OD as a cosolvent reduces the number and the strength of the hydrogen bonds between the polymers and the solvent molecules during the phase transition, giving rise to values of the enthalpy. In methanol-rich solvent mixtures, T_{onset}^{DSC} is 26.1 ± 0.2 °C at 70 vol% of CD_3OD. However, for CD_3OD volume fractions above 70 %, no phase transition temperature is observed (Figure 9.4a and b).

The resulting phase diagram (Figure 9.2) shows that, at 20 °C, solutions with volume fractions of CD_3OD up to 20 % and above 70 % are below T_{CP}, while those with 25 – 70 % are above T_{CP}.

Table 9.1 Results from turbidimetry and DSC measurements

Solvent composition v/v D_2O/CD_3OD	T_{CP} (°C)	T_{onset}^{DSC} (°C)	T_{peak}^{DSC} (°C)	ΔH (J/g$_s$)
100:0	31.2 ± 0.2	30.8 ± 0.2	31.7 ± 0.1	0.43 ± 0.02
95:5	-	29.5 ± 0.2	30.5 ± 0.1	0.33 ± 0.02
90:10	27.9 ± 0.2	28.0 ± 0.2	28.9 ± 0.1	0.34 ± 0.02
85:15	-	24.8 ± 0.2	25.7 ± 0.1	0.27 ± 0.02
80:20	21.2 ± 0.2	20.6 ± 0.2	21.4 ± 0.1	0.20 ± 0.02
75:25	-	17.8 ± 0.2	18.7 ± 0.1	0.21 ± 0.02
70:30	13.6 ± 0.2	16.7 ± 0.2	17.7 ± 0.1	0.18 ± 0.02
30:70	-	26.1 ± 0.2	27.0 ± 0.1	0.25 ± 0.02

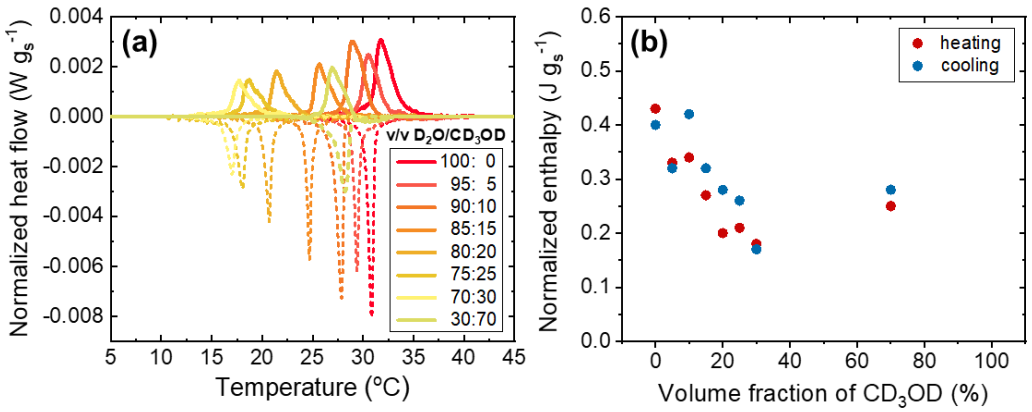

Figure 9.3 (a) DSC thermograms of 10 g L^{-1} $PMMA_{21}$-*b*-$PNIPAM_{283}$ solutions in D_2O/CD_3OD mixtures in dependence on the volume fraction of CD_3OD from second heating (solid lines) and cooling cycle (dashed lines) at a rate of 1 K min^{-1}. (b) Resulting enthalpy ΔH in dependence on the solvent composition from heating (red symbols) and cooling (blue symbols).

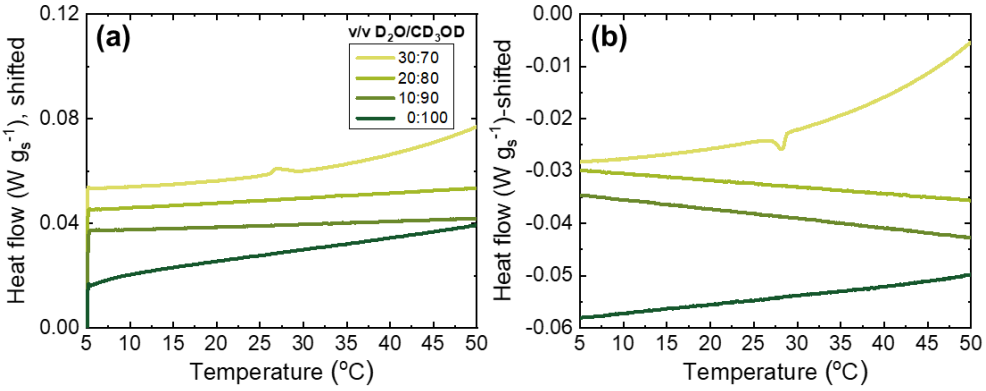

Figure 9.4 DSC thermograms of 10 g L^{-1} $PMMA_{21}$-*b*-$PNIPAM_{283}$ solutions in D_2O/CD_3OD mixtures from the second heating (a) and cooling (b) cycles at a rate of 1 K min^{-1} for the solvent compositions given in the legend.

9.4 Diffusional behavior

From the turbidimetry and DSC measurements, the phase diagram of 10 g L^{-1} $PMMA_{21}$-*b*-$PNIPAM_{283}$ solutions in D_2O/CD_3OD mixtures is established (Figure 9.2). To investigate the co-nonsolvency/co-solvency effect on the hydrodynamic radius, angle-resolved DLS measurements were performed at 20 °C in dependence on the solvent composition. The autocorrelation functions feature a single decay (Figure 9.5a). Up to CD_3OD volume fractions below 25 %, the decay time t shifts to slightly higher values. In contrast, for CD_3OD volume fractions above 70 %, τ shifts to significantly lower values with increasing CD_3OD volume fraction. The decay rates $\Gamma = 1/\tau$ depend linearly on q^2 (Figure 9.5b and c). From the slopes of the linear fits, the corresponding diffusion coefficients *D* are identified (Table 9.2). Using the Stokes-Einstein equation with the diffusion coefficients and the measured viscosity values of the solvent mixtures (Table 4.1), the hydrodynamic radius of the particles, R_h, is determined and is given in dependence on the solvent composition in Figure 9.5d and Table 9.2.

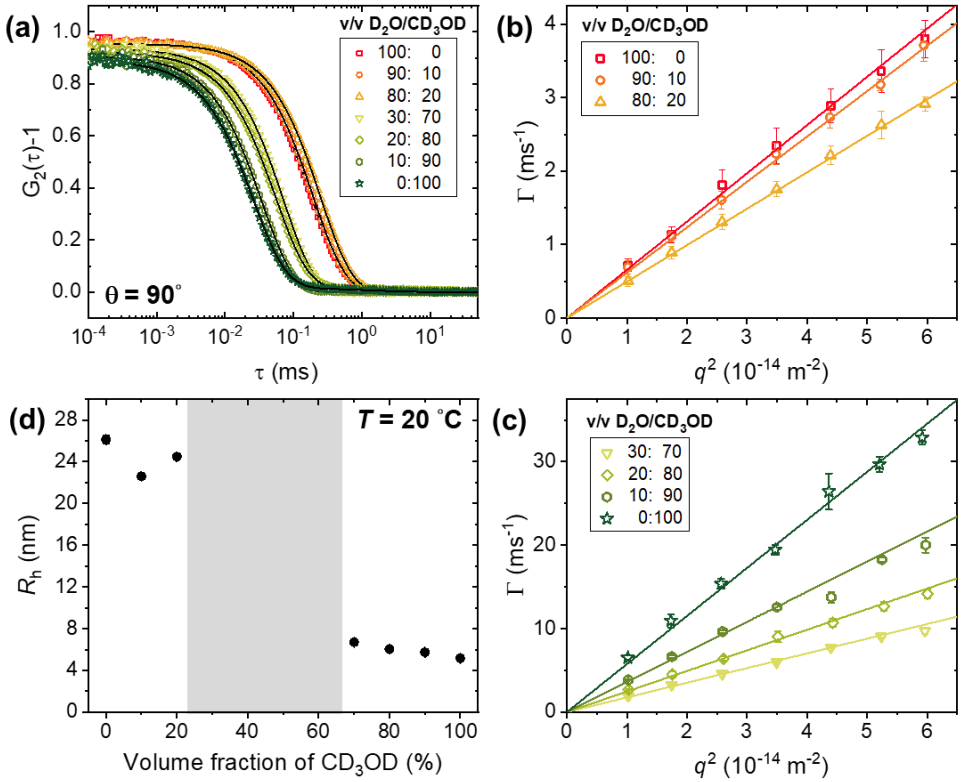

Figure 9.5 DLS results on 10 g L^{-1} $PMMA_{21}$-*b*-$PNIPAM_{283}$ solutions in D_2O/CD_3OD mixtures at 20 °C. (a) Representative normalized intensity autocorrelation functions measured at scattering angle θ = 90°. (b, c) Decay rates as a function of q^2 in dependence on the solvent composition, as given in the graph. (d) Corresponding hydrodynamic radii R_h. Black solid lines are model fits. Colored solid lines are linear fits. The grey shading indicates the two-phase region.

Table 9.2 Results from DLS measurements on the polymer solutions at 20 °C

Solvent composition D_2O/CD_3OD [v/v]	Diffusion coefficient D (10^{-11} m^2 s^{-1})	Hydrodynamic radius R_h (nm)
100:0	0.66 ± 0.01	26.1 ± 0.4
90:10	0.62 ± 0.01	22.6 ± 0.2
80:20	0.50 ± 0.01	24.5 ± 0.2
30:70	1.76 ± 0.03	6.7 ± 0.1
20:80	2.47 ± 0.04	6.0 ± 0.1
10:90	3.61 ± 0.07	5.7 ± 0.1
0:100	5.76 ± 0.10	5.2 ± 0.1

For the sample in pure D_2O, R_h is ~26 nm, which is assigned to the size of the micelles, in consistency with our previous findings that PMMA-*b*-PNIPAM diblock copolymers form self-assembled micelles in D_2O [126]. For the sample in 90:10 v/v D_2O/CD_3OD, R_h is ~22 nm, suggesting that the micellar size decreases. This may be due to the slight shrinkage of the PNIPAM shell caused by the presence of CD_3OD. For the sample in 80:20 v/v D_2O/CD_3OD, for which T_{CP} is just above 20 °C, R_h is slightly higher again, namely ~24 nm. This might be attributed to (i) an increase of the micellar size caused by the increasing aggregation number or the expansion of the micellar shell or (ii) the formation of aggregates composed of several collapsed micelles. However, by DLS, these scenarios cannot be distinguished.

For the samples with CD_3OD volume fractions of 65-100 %, i.e., on the other side of the miscibility gap, the R_h values are significantly smaller than in the range of 0-20 %. For the samples with volume fractions of CD_3OD above 70 %, R_h slightly decreases from ~7 nm to ~5 nm with increasing CD_3OD volume fraction. For PMMA having a molar mass of 14000 g/mol, a clearing point above 35 °C was reported in Ref. [121] , which is far above the measuring temperature, so micelle formation would still be expected. However, it cannot be excluded that the clearing point of the PMMA block in our PMMA-*b*-PNIPAM diblock copolymer is lower because of its lower molar mass (2700 g/mol). Moreover, from the simulation of radius of gyration R_g for PMMA with a molar mass of 3000 g/mol in Ref. [122], it is confirmed that PMMA has a co-solvency effect in water/methanol mixtures. Therefore, it may be questioned that the PMMA blocks of PMMA-*b*-PNIPAM diblock copolymer still form a micellar core. Thus, the chains may be molecularly dissolved, even though the diblock copolymers are amphiphilic in these solvent mixtures. However, this is insufficient to judge merely by the DLS results.

9.5 Micellar structures at low methanol volume fractions

9.5.1 Overview

To characterize the internal morphology of the micelles formed at CD_3OD volume fractions up to 25 %, in dependence on the solvent composition and to resolve the questions raised by the DLS results, synchrotron SAXS measurements are carried out on the same solutions at 20 °C. The SAXS data feature a pronounced shoulder at ~0.15 nm^{-1} and a second shoulder at ~0.6 nm^{-1} (Figure 9.6a and b). These characteristics can be ascribed to the form factor scattering of the micelles. With increasing CD_3OD volume fraction to 20 and 25 %, the second shoulder becomes less pronounced, while the first shoulder shift towards slightly higher *q*-values (~0.3 nm^{-1}). These changes may be attributed to a decrease of the micellar size, resulting from the collapse of the PNIPAM blocks. Moreover, an

additional shoulder emerges at very low q-values (~0.04 nm^{-1}), and its intensity increases dramatically, as the CD_3OD volume fraction is increased. This may be assigned to the formation of large clusters consisting of collapsed micelles.

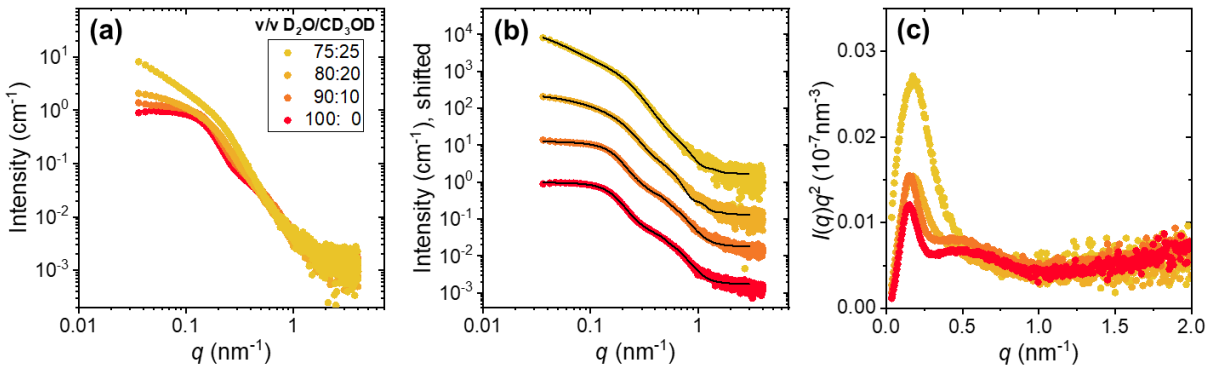

Figure 9.6 (a, b) Representative SAXS data of the 10 g L^{-1} $PMMA_{21}$-*b*-$PNIPAM_{283}$ in D_2O/CD_3OD mixtures (symbols) at 20 °C for low volume fractions of CD_3OD. The solvent compositions are given in the graph. In (b), the curves are vertically shifted by a factor of 10 with respect to each other. The black solid lines are the overall model fits. (c) Kratky plot of the same data, $I(q)q^2$ vs q. For clarity, only every two point is shown.

More information can be gained from the Kratky plots (Figure 9.6c). In pure D_2O, the bell-shaped peak at $q \cong 0.2$ nm^{-1} is an indication of a compact globular structure, which is ascribed to the compact micellar core presumably constituted by the PMMA blocks. The additional shoulder at $q \cong 0.5$ nm^{-1} reveals that the globular structure contains more than one domain, which may be due to the core-shell feature of the micelles. At q-values above 1.0 nm^{-1}, the curve increases again, suggesting loosely packed polymer chains, presumably the hydrophilic PNIPAM blocks in the micellar shell [187]. Upon increasing the CD_3OD volume fraction, the bell-shaped peak at $q \cong 0.2$ nm^{-1} becomes broader and moves towards slightly higher q-values, and its amplitude increases, indicating a shrinkage of the micellar size. Additionally, at CD_3OD volume fractions of 20 and 25 %, the weak maximum at $q \cong 0.5$ nm^{-1} disappears and becomes a decay, which is indicative of a vanishing contrast between the micellar core and shell due to deswelling of the micellar shell.

9.5.2 Fit models

To obtain detailed information on the inner structure of the micelles, the SAXS data are analyzed by fit models. Exemplary model fits and the contributions to the fit model are shown in Figure 9.7.

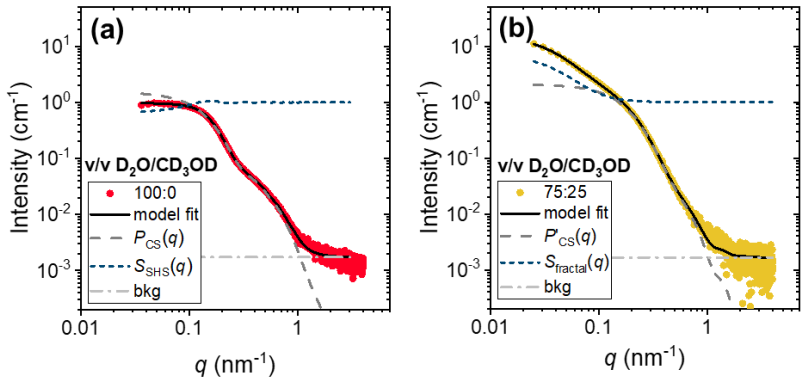

Figure 9.7 Model fits of the SAXS data. Data at 20 °C in 100:0 (a) and 75:25 (b) v/v D_2O/CD_3OD mixtures. Black full lines: overall model fits; dashed lines: contributions from each term in the fit model, see legends.

For the samples with the CD_3OD volume fractions of 0-15 %, the SAXS curves are fitted by the model in eq. 9.1, which was used by us previously to describe the scattering from the identical copolymers in pure D_2O at the same polymer concentration [126].

$$I(q) = I_0 P_{CS}(q) S_{SHS}(q) + I_{bkg} \tag{9.1}$$

It includes the form factor of core-shell spheres, $P_{CS}(q)$, with a polydisperse core and a shell SLD profile that is an exponential function along the radial direction, and the sticky hard-sphere structure factor $S_{SHS}(q)$ (Figure 9.7a). At these solvent compositions, the measuring temperature (20 °C) is far below the respective cloud points; thus, the diblock copolymers are expected to self-assemble into spherical micelles consisting of a hydrophobic PMMA core and a hydrophilic PNIPAM shell. The PNIPAM shell has a radially decaying SLD profile, indicating that the concentration of PNIPAM segments in the micellar shell decays along the radial direction from the micellar core. The data cannot be described satisfactorily by a form factor of core-shell spheres, $P'_{CS}(q)$, with a homogeneous shell SLD, presumably because of the relatively long PNIPAM blocks. From the form factor, the micellar core radius R_{core}, the shell thickness t_{shell}, the micellar radius R_{mic} and the radially decaying SLD profile of the micellar shell are determined. The aggregation number of the micelles, N_{agg}, can be deduced from R_{core}. The structure factor quantifies the correlation between the micelles, including the half-distance between two correlated micelles, R_{HS}, the volume fraction of correlated micelles, ϕ, and the stickiness parameter, τ_0. Throughout, the fits are excellent (Figure 9.6b).

For the solutions with CD_3OD volume fraction of 20 and 25 %, the forward scattering is more prominent, and the shell seems to deswell, as seen from Figure 4c. The SAXS curves are described by the model in eq. 9.2 (Figure 9.7b).

$$I(q) = I_0 P'_{\mathrm{CS}}(q) S_{\mathrm{fractal}}(q) + I_{\mathrm{bkg}} \tag{9.2}$$

The micellar shell can be described using a homogeneous shell SLD, as implemented in $P'_{\mathrm{CS}}(q)$. At theses solvent compositions, the measuring temperature is only slightly below or already above the respective cloud points (Figure 9.2 and Table 9.1), resulting in more collapsed PNIPAM blocks, due to the co-nonsolvency effect. The fractal structure factor, $S_{\mathrm{fractal}}(q)$, is used to describe the additional shoulder at low q-values, which may emanate from clusters composed of collapsed micelles. It gives the fractal correlation length ξ_{f}, the fractal dimension D_{f} and the radius of gyration of the clusters, R_{cluster}.

All the SAXS data are well described by the chosen fitting models (Figure 9.6b). In the following, the resulting fitting parameters are discussed in dependence on the volume fraction of CD_3OD with a focus on the co-nonsolvency/co-solvency effect on the micelles. The resulting fit parameters are summarized in Figures 9.8 and 9.9; complete sets of structural parameters are compiled in Tables E1-E2 in the Appendix.

9.5.3 Structural changes of the micelles

In pure D_2O, it is known that the copolymers form self-assembled spherical micelles, for a similar composition studied as here yielding a radius R_{mic} = 24.4 nm with a PMMA core having a radius R_{core} = 2.5 nm and a shell formed by the long PNIPAM blocks having a thickness t_{shell} = 21.9 nm [126]. The concentration of PNIPAM segments in the micellar shell decreased along the radial direction. Moreover, the micelles interpenetrated and were weakly correlated.

In this Chapter, we find very similar structural characteristics at 20 °C in pure D_2O. The micellar radius R_{mic} is ~24.7 nm with a core radius R_{core} = 2.7 nm and a shell thickness t_{shell} = 22.0 nm (Figure 9.8a). The core polydispersity p_{core} is 0.3. The aggregation number of the micelles N_{agg} is ~27 (Figure 9.8b). The SLD profile of the PNIPAM shell displays a radially exponential decay from a value of 9.58×10^{-6} Å^{-2} to the SLD value of the D_2O (9.44×10^{-6} Å^{-2}), as shown in Figure 9.9a. The hard-sphere radius R_{HS} is ~19.8 nm (Figure 9.8a), and the volume fraction of the correlated micelles, ϕ, is 0.07 (Figure 9.8c). These findings are consistent with our previous results [126].

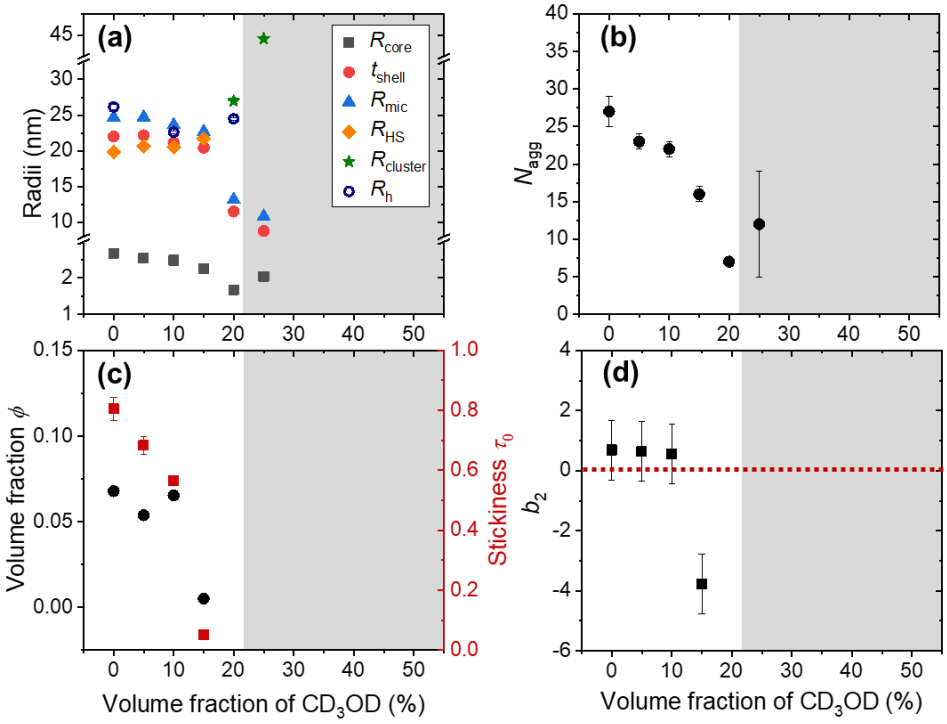

Figure 9.8 Structural parameters resulted from model fits to the SAXS data in dependence on the CD_3OD volume fraction: (a) Micellar core radius R_{core} (black squares), shell thickness t_{shell} (red circles), micellar radius R_{mic} (blue triangles), hard-sphere radius R_{HS} (orange diamonds), radius of gyration of the fractal clusters R_{cluser} (green stars), the hydrodynamic radius R_h (dark blue open circles) measured from DLS, as given in the legend. (b) Aggregation number N_{agg} (black circles). (c) Volume fraction of correlated micelles ϕ (black circles) and stickiness parameter τ_0 (red squares). (d) The reduced second virial coefficient b_2 deduced from τ_0. The grey shading indicates the two-phase region. In (a), the hydrodynamic radius R_h from DLS is added (dark blue open circles).

In the range of volume fractions of CD_3OD up to 25 %, the copolymers still form self-assembled micelles. As the CD_3OD volume fraction increases to 15 %, R_{mic} decreases by ~2 nm, originating from a subtle decrease of both, R_{core} and t_{shell}. The core polydispersity p_{core} slightly increases to ~0.4. The decrease of R_{core} by 0.5 nm implies that N_{agg} decreases to 16. This implies that the solubility of the PMMA blocks is slightly increased due to the presence of CD_3OD. This can be explained by comparing the solubility parameters δ: The solubility parameter of PMMA is closer to the one of methanol than the one of water (δ_{PMMA} = 11.1 $cal^{1/2}cm^{-3/2}$, $\delta_{methanol}$ = 14.5 $cal^{1/2}cm^{-3/2}$ and δ_{water} = 23.4 $cal^{1/2}cm^{-3/2}$) [56]. Although the co-solvency effect for PMMA is most pronounced at methanol volume fractions of 80-90 % [120-123], the intermolecular interactions between the PMMA blocks in the micellar core may already be weakened at the low fractions investigated here. This suggests that the addition of

CD_3OD softens the micellar core and promotes the micellar exchange dynamics, even though the PMMA blocks are still insoluble in the D_2O/CD_3OD mixtures.

The decrease of t_{shell} by ~1.5 nm may be attributed to the co-nonsolvency effect on the PNIPAM blocks from CD_3OD. The presence of CD_3OD reduces the solvent quality for the PNIPAM blocks, leading to a partial shrinkage of the PNIPAM blocks. Upon increasing the CD_3OD volume fraction to 15 %, the SLD profiles of the micellar shell decay in a similar manner and reach the level of the respective solvent mixture (Figure 9.9a). Likewise, the values of the parameter v_0, which describes the shape of the exponential function in the SLD profile of the shell, all lie in a range of ~3.3-3.5 (Figure 9.9b). This implies that the presence of CD_3OD has almost no influence on the segment concentration profile of PNIPAM blocks along the radial direction in the micellar shell.

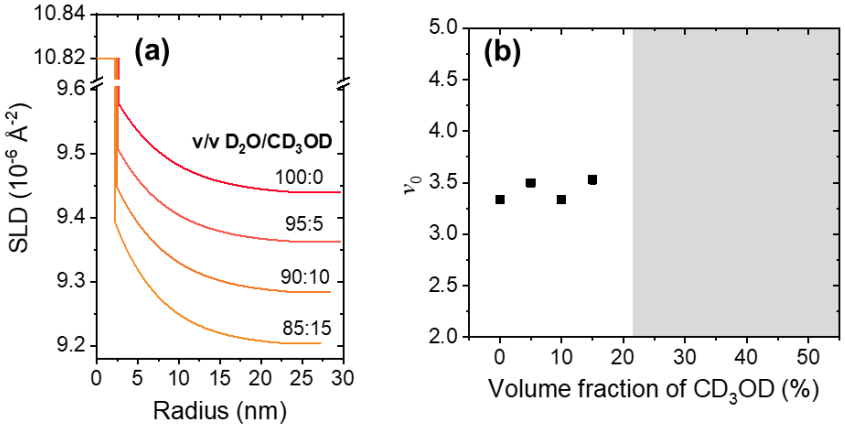

Figure 9.9 (a) The resulting scattering length density (SLD) profile. (b) Parameter v_0 related to shape of the exponential function for shell SLD. The grey shading in (b) indicates the two-phase region.

Regarding the correlation between the micelles, R_{HS} increases from 19.8 nm to 21.7 nm upon increasing the CD_3OD volume fraction from 0 to 15 %, indicating that the distance between the correlated micelles increases slightly. For all compositions in this range, R_{HS} is smaller than R_{mic}, meaning that the micelles interpenetrate. As the CD_3OD volume fraction increases, R_{mic} slightly decreases, whereas R_{HS} increases, which indicates that the micelles slightly separate from each other and become less interpenetrated. The volume fraction of correlated micelles, ϕ, remains at values of ~0.05-0.06 up to 10 vol% of CD_3OD and decreases significantly to the value of ~0.01 at 15 vol% (Figure 9.8c), implying that fewer micelles are correlated. Moreover, the stickiness parameter τ_0 decreases with increasing CD_3OD volume fraction, slightly up to 10 vol% of CD_3OD and strongly at 15 vol% (Figure 9.8c). This suggests that the attractive interactions between the correlated micelles are enhanced, despite the fact that the number of correlated micelles is reduced. The reduced second

virial coefficient b_2 (Figure 9.8d), which is deduced from τ_0, stays at a positive value of ~0.6 up to a CD_3OD volume fraction of 10 %, and becomes negative at 15 %. This indicates that, between 10 and 15 vol%, the interactions between correlated micelles change from repulsive to attractive.

For the solution with a CD_3OD volume fraction of 20 %, the measuring temperature (20 °C) is only slightly below the cloud point. R_{core} is slightly lower than at 15 %, which is due to the increased solubility of the PMMA blocks. Correspondingly, N_{agg} has decreased to 7. For this solution, the form factor of micelles with a homogeneous shell describes the data best. t_{shell} has shrunken drastically to ~11 nm, which is attributed to the collapse of the PNIPAM blocks resulting from the co-nonsolvency effect. Furthermore, the collapsed micelles form fractal clusters, having a size $R_{cluster}$ = 27 nm (Figure 9.8a) and a fractal dimension D_f = 1.5, i.e., the micelles are loosely packed.

At a CD_3OD volume fraction of 25 %, the coexistence line has been crossed, and the solution is in the two-phase state (Figure 9.2). Compared to the value at 25 %, R_{core} has slightly increased again, which may be due to a merging of the inner part of the PNIPAM shell with the PMMA-rich core, resulting in an apparent increase of N_{agg}. t_{shell} has decreased further, as expected, and the overall size, R_{mic}, has decreased as well. The size of the clusters is now $R_{cluster}$ = 45 nm (Figure 9.8a), and D_f has increased to a value of 2.8, implying that the clusters grow and become compact.

To summarize, for CD_3OD volume fractions up to 25 %, the $PMMA_{21}$-*b*-$PNIPAM_{283}$ diblock copolymers self-assemble into spherical core-shell micelles. Upon increasing the CD_3OD volume fraction, the aggregation number of the micelles decreases slightly, which is due to the presence of CD_3OD that weakens the intermolecular interactions between the PMMA blocks in the micellar core. Besides, the micellar shell thickness decreases slightly up to 15 vol% of CD_3OD and is much lower at 20 vol%, which is ascribed to a reduced solvent quality for the PNIPAM blocks, caused by the co-nonsolvency effect, that leads to a shrinkage of the PNIPAM blocks. Furthermore, as the CD_3OD volume fraction is increased, the correlated micelles slightly separate from each other, and the fraction of correlated micelles decreases, while the attractive interactions between those micelles, that are correlated, are strengthened. The clusters formed by the collapsed micelles appear at 20 vol% of CD_3OD, which is presumably due to the enhanced attractive interactions between the micelles, starting at 15 %. The SAXS results confirm that the hydrodynamic radius determined by DLS is related to the overall micellar size for CD_3OD volume fractions of 0-10 % (Figure 9.8a). In contrast, at 20 vol% of CD_3OD, the hydrodynamic radius is close to the size of the clusters (R_h ~25 nm; $R_{cluster}$ ~27 nm), while the micellar size is much smaller (R_{mic} ~13 nm).

9.6 Chain conformations at high methanol volume fractions

9.6.1 Overview

At high methanol volume fractions, DLS revealed R_h values between 5 and 7 nm, which points to molecularly-dissolved chains. Their chain conformation and the co-nonsolvency/co-solvency effect at high methanol volume fractions, synchrotron SAXS measurements are performed (Figure 9.10). At the CD_3OD volume fraction of 70 %, the SAXS curve features a strong decay at 0.03-0.09 nm^{-1} and a shoulder at ~0.5 nm^{-1}, which are associated with the forward scattering due to large-scale inhomogeneities and the chain scattering, respectively. For the samples with CD_3OD volume fractions above 70 %, the SAXS curves feature a shoulder at ~0.3 nm^{-1}, indicating that the chain scattering prevails, and only very weak forward scattering is observed at 0.03-0.05 nm^{-1}, pointing to rather homogeneous solutions of molecularly-dissolved chains.

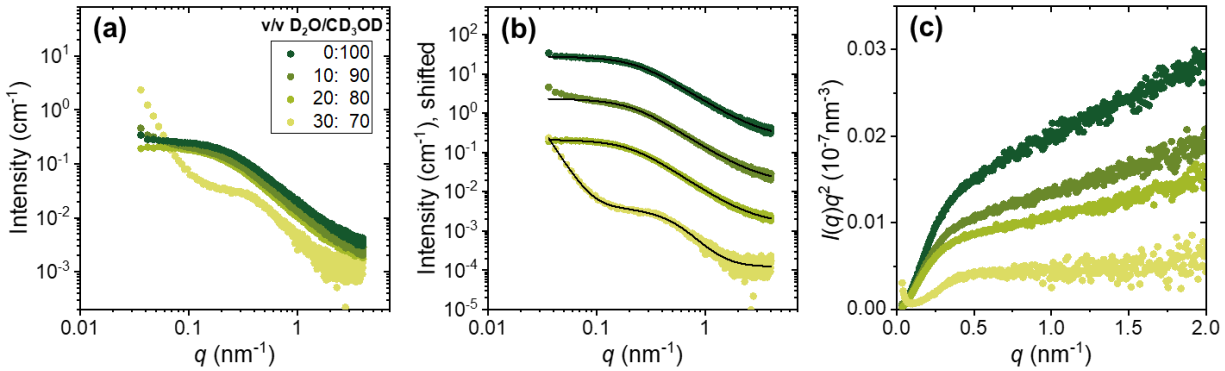

Figure 9.10 (a, b) Representative SAXS data of the 10 g L^{-1} $PMMA_{21}$-*b*-$PNIPAM_{283}$ in D_2O/CD_3OD mixtures (symbols) at 20 °C for high volume fractions of CD_3OD. The solvent compositions are given in the graph. In (b), the curves are vertically shifted by a factor of 10 with respect to each other. The black solid lines are the overall model fits. (c) Kratky plot of the same data, $I(q)q^2$ vs q. For clarity, only every two point is shown.

The Kratky plots feature a decay at low q-values and a plateau at $q \cong 0.5$ nm^{-1} at a CD_3OD volume fraction of 70 % (Figure 9.10c). Above 70 %, the decrease at low q-values vanishes and only the plateau remains, where, however, an increase is present with a slope that increases with the CD_3OD volume fraction. This confirms that, in this composition range, the diblock copolymers are molecularly dissolved, even though, at the temperature chosen, the PMMA blocks are expected to be insoluble in the solvent mixtures.

9.6.2 Fit models

To gain detailed information on the chain conformation of the molecularly-dissolved chains, the SAXS data are analyzed by the polymer excluded volume model, $P_{\text{chain}}(q)$, is applied, which describes the scattering from polymer chains exhibiting excluded volume effects. Exemplary model fits and the contributions to the fit model are displayed in Figure 9.11. Thus, the radius of gyration of the diblock copolymer chains, R_g, and the Porod exponent m, indicative of the chain conformation, are determined. For the solution with a CD_3OD volume fraction of 70 %, which is close to the phase boundary (Figure 9.2), strong forward scattering is present. The SAXS curve is modeled by eq. 9.3 (Figure 9.11a), which contains the Porod term $I_{\text{Porod}}(q)$ that describes the strong forward scattering caused by the presence of large aggregates.

$$I(q) = I_{\text{Porod}}(q) + I_0 P_{\text{chain}}(q) + I_{\text{bkg}} \tag{9.3}$$

For CD_3OD volume fractions of 80-100 %, nearly no forward scattering is present, and the SAXS curves can be fitted by the polymer excluded model alone (Figure 9.11b).

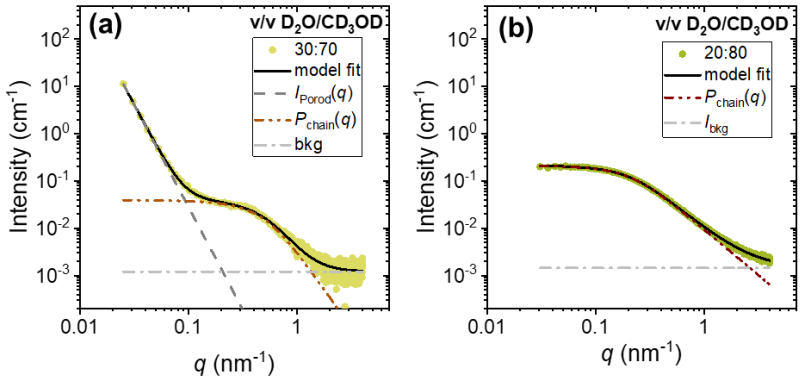

Figure 9.11 Model fits of the SAXS data. Data at 20 °C in 30:70 (a) and 20:80 (b) v/v D_2O/CD_3OD mixtures. Black full lines: overall model fits; dashed lines: contributions from each term in the fit model, see legends.

All the SAXS data are well described by the chosen fitting models (Figure 9.10b). The resulting fitting parameters are discussed in dependence on the volume fraction of CD_3OD with a focus on the co-nonsolvency/co-solvency effect on the molecularly-dissolved chains. The resulting fit parameters are compiled in Figure 9.12 and in Tables E3 in the Appendix.

9.6.3 Structural changes of the molecularly-dissolved chains

For 70 vol% of CD_3OD, the R_g values determined by SAXS is 3.6 nm (Figure 9.12a). The Porod exponent of the polymer chains, m = 3.2 (Figure 9.12b), i.e., the Flory exponent is $\nu \cong 1/3$, which indicates a collapsed chain conformation. In the SAXS curves from this solution, forward scattering is present as well with Porod exponents P slightly larger than 4, which indicates compact aggregates with a concentration gradient near their surfaces. We attribute these findings for m and P to the proximity of the coexistence line.

For the solutions with CD_3OD volume fractions of 80-100 %, R_g = 7 nm, i.e., higher than at 70 %, and m = 1.8-1.9, i.e., $\nu \cong 0.53$-0.56, suggesting that the solvent mixture has a quality between the one of a theta solvent ($\nu = 0.5$) and a good solvent ($\nu = 0.6$). Furthermore, in these solvent mixtures, R_g decreases slightly upon increasing the volume fraction of CD_3OD, which may be attributed to the co-solvency effect of the PMMA blocks [120-123]. The ratio R_g/R_h is 1.1-1.2, which is close to the value of 1.2 expected for random coils [157].

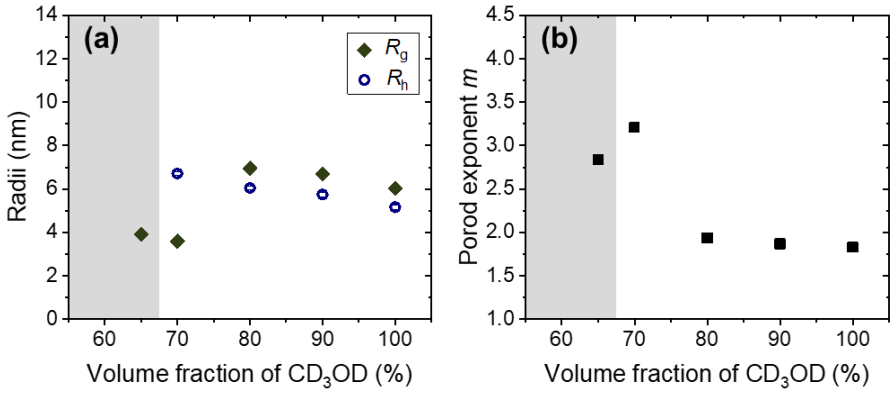

Figure 9.12 Structural parameters resulted from model fits to the SAXS data in dependence on the CD_3OD volume fraction: (a) Radius of gyration of the diblock copolymer chains R_g (dark green diamonds) (b) The Porod exponent of the diblock copolymer chains m (black squares). The grey shading indicates the two-phase region. The hydrodynamic radius R_h from DLS is added to (a) as dark blue open circles

9.7 Summary of the findings on PMMA-*b*-PNIPAM in D_2O/CD_3OD mixtures

The solvent-induced structural changes of $PMMA_{21}$-*b*-$PNIPAM_{283}$ in D_2O/CD_3OD mixtures at 20 °C are schematically depicted in Figure 9.13. The diblock copolymers form spherical core-shell micelles for CD_3OD volume fractions up to 25 %. The internal morphology of the micelles is altered by the solvent compositions in two ways: CD_3OD makes the core-forming block, PMMA, less hydrophobic, while it has a co-nonsolvency effect on the PNIPAM micellar shell. In contrast, for the CD_3OD volume fractions of 70 % and higher, the diblock copolymers are molecularly dissolved. While

they are collapsed near the coexistence line, they become random coils as the CD_3OD volume fraction increases towards 100 %.

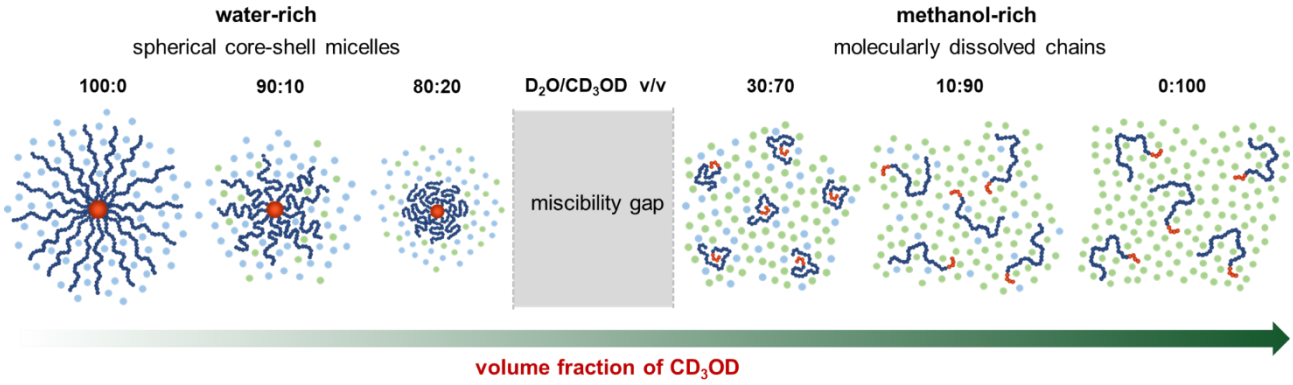

Figure 9.13 Schematic representation of the structural changes formed by $PMMA_{21}$-*b*-$PNIPAM_{283}$ in D_2O/CD_3OD mixtures at 20 °C in dependence on the CD_3OD volume fraction. Red spheres symbolize for the micellar core constituted by the PMMA blocks. Red and blue lines represent the PMMA and PNIPAM blocks, respectively. The grey shading indicates the two-phase region.

9.8 Comparison of PMMA-*b*-PNIPAM with PS-*b*-PNIPAM

In our previous study on the temperature-dependent structures in micellar solutions from $PMMA_{21}$-*b*-$PNIPAM_{283}$ in neat D_2O [126], we found by comparison with results from PS-*b*-PNIPAM [107] that the hydrophobicity of the core-forming block plays a vital role. The question arises in how far this difference is apparent in water/methanol mixtures as well. In our previous investigations of PS_{14}-*b*-$PNIPAM_{310}$ and $P(S\text{-}d_8)_{11}$-*b*-$PNIPAM_{431}$ (the PS blocks was perdeuterated) diblock copolymers, a reduction of T_{CP} was observed as the volume fraction of CD_3OD was increased from 0 to 20 % [191, 193]. For both PS-*b*-PNIPAM and PMMA-*b*-PNIPAM, the values of T_{CP} are slightly lower than the ones from PNIPAM homopolymers (Figure 9.14a), with the effect being much more significant for PS-*b*-PNIPAM. For instance, in 90:10 v/v D_2O/CD_3OD mixtures, T_{CP} is 29.5 ± 0.2 °C for a $PNIPAM_{200}$ homopolymer, 28.0 ± 0.2 °C for $PMMA_{21}$-*b*-$PNIPAM_{283}$, and 26.5 ± 0.2 °C for PS_{14}-*b*-$PNIPAM_{310}$ [191]. This is due to the fact that (i) PS is more hydrophobic than PMMA (δ_{PS} = 9.1 $cal^{1/2}cm^{-3/2}$) [56], and (ii) the solubility of PMMA is enhanced in water/methanol mixtures.

Moreover, the solvent composition affects the micellar core for PMMA-*b*-PNIPAM and PS-*b*-PNIPAM in different ways. Even though it was claimed that the addition of methanol leads to a softening the PS micellar core and an enhancement of the micellar exchange dynamics [194], for CD_3OD volume fractions of 10 and 20 %, the micellar core radius of $P(S\text{-}d_8)_{11}$-*b*-$PNIPAM_{431}$ remains almost unaffected by the presence of methanol [193]. In contrast, the micellar core radius of $PMMA_{21}$-

b-PNIPAM$_{283}$ decreases slightly with increasing methanol content in this composition range (Figure 9.14b), which can be attributed to the weaker intermolecular interactions between the hydrophobic PMMA blocks in the micellar core induced by methanol [120-123]. This implies that the addition of methanol enhances the micellar exchange dynamics of PMMA$_{21}$-*b*-PNIPAM$_{283}$ more strongly than the ones of P(S-d$_8$)$_{11}$-*b*-PNIPAM$_{431}$.

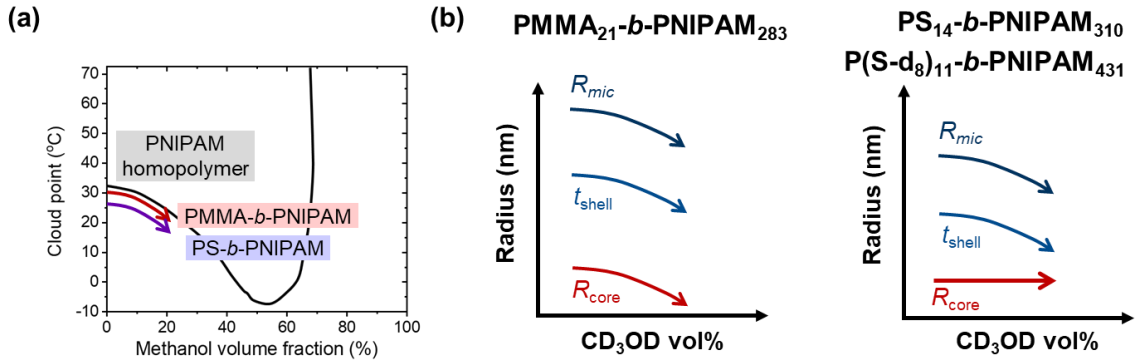

Figure 9.14 Schematic representation of the cloud points (a) and the structural differences (b) of the self-assembled structures formed by PMMA-*b*-PNIPAM and PS-*b*-PNIPAM in dependence on temperature. (The findings from PS$_{14}$-*b*-PNIPAM$_{310}$ and P(S-d$_8$)$_{11}$-*b*-PNIPAM$_{431}$ refer to Refs. [191] and [193], respectively)

9.9 Conclusions

In this chapter, the phase diagram of PMMA$_{21}$-*b*-PNIPAM$_{283}$ diblock copolymers in D$_2$O/CD$_3$OD mixtures is established by turbidimetry and DSC, revealing that, up to 25 vol% of CD$_3$OD the cloud point T_{CP} decreases. The enthalpies related to the phase transition decrease with increasing methanol volume fraction, indicating that the strength or number of the hydrogen bonds between water and polymer are weakened due to the presence of methanol. The solvent-induced morphological changes are investigated in detail at 20 °C by DLS and synchrotron SAXS. Spherical core-shell micelles are formed on the water-rich side of the miscibility gap, while the chains are molecularly dissolved on the methanol-rich side of miscibility gap. The internal structures, the correlations of the micelles, and the chain conformations of the dissolved chains are characterized in dependence on the solvent composition. Apart from the co-nonsolvency effect of PNIPAM, the overall enhancement of the solubility of PMMA by methanol and the co-solvency effect of PMMA play a crucial role for the phase behavior, thermal behavior, the morphology of the micelles and the chain conformations.

10. Dissertation summary and outlook

This thesis addresses the temperature-dependent phase behavior of novel thermoresponsive homopolymers PNIPMAM in aqueous solutions, the self-assembled micelles from thermoresponsive PMMA-*b*-PNIPAM diblock copolymers in aqueous solutions, and the co-nonsolvency/co-solvency effects in solutions of PMMA-*b*-PNIPAM diblock copolymers in water/methanol mixtures.

In the first part of this thesis, the temperature-dependent phase behavior of PNIPMAM solutions in D_2O is investigated in depth using turbidimetry, OM, DSC, SANS/VSANS, and Raman spectroscopy, covering a large concentration range. A comparison between PNIPMAM and PNIPAM is made to elucidate the influence of the additional methyl groups on the vinyl backbone. It was found that PNIPMAM chains only dehydrates 2-3 °C above the macroscopic T_{CP}. Even in the one-phase state, loosely packed, large-scale inhomogeneities and physical crosslinks are observed in PNIMAM solutions. The chain conformation of PNIPMAM is more compact than the one of PNIPAM. This is due to the attractive intermolecular interactions between the hydrophobic moieties. The phase transition of PNIPMAM is broader than the one of PNIPAM. Upon heating to the two-phase state, PNIPMAM chains collapse and form mesoglobules. These mesoglobules of PNIPMAM are larger and contain more water than those of PNIPAM. This is attributed to the steric hindrance originating from the additional methyl groups, which weaken the intrapolymer interactions in the two-phase state. As a result, the methyl groups in the backbone of the PNIPMAM chains have a significant influence on the hydration and the structural behavior around the phase transition.

In the second part of this thesis, the self-assembly behavior in aqueous solutions of the thermoresponsive amphiphilic diblock copolymer PMMA-*b*-PNIPAM with a short permanently hydrophobic PMMA block and a long thermoresponsive PNIPAM block is studied using turbidimetry, DLS, SAXS. The concentration-dependence of self-assembled micelles are investigated at 20 °C above the critical micelle concentration. From 0.2 to 10 g L^{-1}, the more concentrated the solution, the smaller the micellar size. At high concentrations, the smaller the aggregation number of micelles, N_{agg}, is smaller and the micellar shell contains more water.

The temperature-dependent phase behavior and structural transition of micelles from PMMA-*b*-PNIPAM are investigated in both dilute and semidilute aqueous solution. For a dilute aqueous solution, i.e., at 1 g L^{-1}, the T_{CP} is found at 30.5 °C. The collapse mechanism of the micelles upon heating without the influence of their correlations is observed. Below T_{CP}, spherical core-shell micelles are found, having a small PMMA core and a hydrated PNIPAM shell with a radial gradient of water content. Below T_{CP}, the micellar size remains almost unchanged, whereas the micellar shell dehydrates with

increasing temperature. In addition, the mass of the micelles concentrates at the center part rather than homogeneous distribution. Above T_{CP}, the micelles notably collapse. Due to the strong dehydration of PNIPAM shell leading to a weak contrast between core and shell, the mass distribution of collapsed micelles become homogeneous.

For a semidilute PMMA-*b*-PNIPAM aqueous solution, i.e., at 10 g L^{-1}, an LCST behavior with a T_{CP} = 31.1 °C is observed. Below T_{CP}, the micelles are interpenetrated and weakly correlated with each other. As the temperature approaches T_{CP}, the micellar core shrinks and the aggregation number decreases, indicating that the PMMA blocks are still mobile. In addition, the micellar shell strongly dehydrates above T_{CP} and the micelles notably contract. The collapsed micelles form clusters, which grow and transform into large compact aggregates as temperature is increased far above T_{CP}. By comparing the findings from PMMA-*b*-PNIPAM with the ones from PS-*b*-PNIPAM, it is found that the hydrophobicity of the hydrophobic block plays a vital role in the inner structure, interactions, and the aggregation of the micelles, which is due to the different extents of the interchain interactions in the micellar core and shell. Owing to its improved solubility, facilitated micelle formation, and enhanced biocompatibility compared to previously reported PS-*b*-PNIPAM polymers, the presented PMMA-*b*-PNIPAM diblock copolymer can serve as a more suitable carrier system for substance transportation in biomedical applications.

Additionally, the self-assembly of thermoresponsive amphiphilic diblock copolymer PMMA-*b*-PNIPAM is also investigated in mixtures of water and methanol at 10 g L^{-1}. The solvent-composition-dependent phase diagram is constructed by turbidimetry and DSC. The structural information at 20 °C in dependence on the solvent composition is revealed by DLS and SAXS. In water-rich solvent mixtures, self-assembled spherical core-shell micelles are formed. The internal structure of the micelles is tunable by the solvent compositions in two ways: methanol softens PMMA micellar core, whereas it causes the shrinkage of the PNIPAM micellar shell. In the methanol-rich solvent mixtures beyond the miscibility gap, the copolymers are molecularly-dissolved chains. The chain conformation is collapsed near the coexistence line, while it becomes swollen like random coils as the methanol content increases. The internal morphology of the micelles and the conformation of the dissolved chains depend strongly on the solvent composition, as a consequence of the superposed co-nonsolvency effect of PNIPAM and the overall enhanced solvation of PMMA when adding methanol. Furthermore, the solvent composition affects the micellar core for PMMA-*b*-PNIPAM and PS-*b*-PNIPAM in two different ways. It is found that the addition of methanol promotes the micellar exchange dynamics of PMMA-*b*-PNIPAM more strongly than the ones of PS-*b*-PNIPAM.

Form the above-mentioned results, several questions raised by this study still remain to be

answered. For instance, the water dynamics in PNIPMAM aqueous solutions would be of great interest after understanding the temperature-dependent phase behavior of PNIPMAM. The role of water during the phase transition in PNIPMAM aqueous solutions would be possible to further investigate by quasi-elastic neutron scattering (QENS) experiments. Besides, the segmental dynamics and the micellar diffusion of PMMA-*b*-PNIPAM diblock copolymers in D_2O would be an area for further research. These could be further investigated by neutron spin-echo (NSE) spectroscopy. Another point that would be of significant interest is the influence of methanol on the temperature-dependent morphological transition and aggregation dynamics of PMMA-*b*-PNIPAM diblock copolymers in pure D_2O, in 90:10 and 80:20 v/v D_2O/CD_3OD mixtures. This could be further carried out by time-resolved SAXS during temperature scans and temperature jumps.

In conclusion, although more aspects are required to be considered in the future, a comprehensive fundamental understanding of the phase behavior of PNIPMAM with the focus on the structural investigation is beneficial for understanding the phase transitions of more complex systems containing PNIPMAM polymers. Besides, the detailed insights into the structural transition and the aggregation behavior of self-assembled micelles from PMMA-*b*-PNIPAM will facilitate the future designing of substance transport or delivery systems with a better-controlled loading and releasing capability. This work has paved the way for designing materials based on these novel thermoresponsive polymers that are advantageous for potential applications.

Appendix

A. Supporting information for Chapter 5

Cloud points

The cloud points were identified by three different, independent methods: turbidimetry, neutron transmission, and in-situ optical microscopy (Table A1). The protocols to extract the T_{CP} from three methods are described in the following.

Turbidimetry was performed using a 10 mW HeNe laser with a wavelength of 632.8 nm and a photodiode (Thorlabs, CITY). The samples were mounted in quartz glass cells (Hellma Analytics) with a light path of 1 mm. The cell was inserted into an aluminum sample stage connected to a Julabo F12 thermostat. Temperature scans were carried out at a heating rate of 0.2 K min^{-1}. A Pt100 resistance thermosensor was directly attached to the sample cell. The transmitted light intensity was normalized to the maximum intensity in the actual sample measurement to give the transmission. The transmission decreases abruptly at the cloud point temperature T_{CP}, which was taken as the onset temperature of the decrease.

Neutron transmission was measured during the VSANS measurements due to the direct beam on the detector. At the cloud points, the transmission decreases drastically. T_{CP}^{VSANS} was defined as the temperature at which the transmission starts to decay. The values of T_{CP}^{VSANS} are equal to the values of T_{CP} identified by turbidimetry.

Optical microscopy was conducted using the same sample holder as for Raman spectroscopy. The OM images were taken in situ along with the Raman measurements. The OM images were taken by an Olympus X41 microscope equipped with a CCD camera. The micro capillary was embedded in a copper stage and a copper foil cover was used to improve the thermal conductivity and temperature homogeneity. The temperature of the copper stage was controlled by a circulating water bath thermostat and was measured by a Pt100 resistance thermosensor inserted into the copper stage. The rate of the temperature change was maintained below 0.5 K min^{-1} to maintain thermal equilibrium between the sample and the copper stage. T_{CP}^{OM} was determined as the average temperature between the temperature just before mesoglobules appeared and the temperature at which mesoglobules were present. Examples just below T_{CP}^{OM} and at T_{CP}^{OM} are shown in Figure 5.3a and 5.3b in the main text. However, there is an offset between T_{CP}^{OM} and T_{CP} determined by turbidimetry, which may due to the radiation losses originated from the vicinity of the microscope objective and the thermal conductivity difference between the copper sample holder from OM and the aluminum one in turbidimetry.

Table A1. Characteristic transition temperatures of PNIPMAM solutions in D_2O from turbidimetry, DSC, SANS, VSANS, and OM

Concentration ($g\ L^{-1}$)	T_{CP} (°C)	T_{onset}^{DSC} (°C)	T_{peak}^{DSC} (°C)	T_{CP}^{VSANS} (°C)	T_s (°C) from I_{OZ}	T_s (°C) from ξ_{OZ}	T_P^{SANS} (°C)	T_{CP}^{OM} (°C)
2	45.0 ± 0.5	-	-	-	-	-	-	-
5	44.4 ± 0.5	46.9 ± 0.2	47.4 ± 0.1	-	-	-	-	-
10	44.0 ± 0.5	46.6 ± 0.2	47.2 ± 0.1	-	-	-	-	-
30	43.5 ± 0.5	46.0 ± 0.2	46.6 ± 0.1	44.0 ± 1.0	-	-	41.0 ± 0.5	-
100	42.2 ± 0.5	45.0 ± 0.2	45.9 ± 0.1	42.0 ± 1.0	44.4 ± 0.4	44.4 ± 0.6	38.5 ± 0.5	-
150	41.7 ± 0.5	44.5 ± 0.2	45.7 ± 0.1	42.0 ± 1.0	44.6 ± 0.6	43.9 ± 0.7	38.0 ± 0.5	39.0

B. Supporting information for Chapter 6

Structural parameters from model fits of the SAXS data

Table B1. Fitting results for $PMMA_{21}$-*b*-$PNIPAM_{283}$ solution in D_2O at 20 °C at concentrations from 0.2 to 10 g L^{-1}.

Concentration [g L^{-1}]	$P_{CS}(q)$					$S_{SHS}(q)$		
	R_{core} (nm)	p_{core}	t_{shell} (nm)	ρ_{shell}^{o} (10^{-6} Å^{-2})	ν_0	R_{HS} (nm)	ϕ	τ_0
0.2	2.88 ± 0.49	-	28.78 ± 1.37	9.68 ± 0.02	5.06 ± 0.47	-	-	-
0.5	3.20 ± 0.11	-	27.38 ± 0.56	9.63± 0.01	4.66 ± 0.20	-	-	-
1	3.14 ± 0.05	-	25.65 ± 0.26	9.61 ± 0.01	4.24 ± 0.10	-	-	-
10	2.51 ± 0.02	0.39 ± 0.01	22.52 ± 0.07	9.58 ± 0.01	3.62 ± 0.03	20.70 ± 0.10	0.054 ± 0.001	0.54 ± 0.02

C. Supporting information for Chapter 7

Structural parameters from model fits of the SAXS data

Table C1. Fitting results for $PMMA_{21}$-*b*-$PNIPAM_{283}$ solution in D_2O at 1 g L^{-1} below T_{CP} and at T_{CP} in regime I.

T [°C]	$P_{CS}(q)$				
	R_{core} (nm)	p_{core}	t_{shell} (nm)	ρ_{shell}^{o} (10^{-6}Å^{-2})	ν_0
19.7	3.45 ± 0.03	-	28.69 ± 0.35	9.71± 0.01	5.93 ± 0.10
21.9	3.65 ± 0.03	-	28.89 ± 0.31	9.68 ± 0.01	5.73 ± 0.09
23.9	3.84 ± 0.04	-	31.23 ± 0.44	9.72 ± 0.01	6.54 ± 0.11
26.0	3.91 ± 0.05	-	31.73 ± 0.48	9.75 ± 0.01	6.97 ± 0.12
28.0	4.14 ± 0.06	-	33.93 ± 0.54	9.80 ± 0.01	7.85 ± 0.12
28.9	4.26 ± 0.07	-	34.97 ± 0.62	9.83 ± 0.01	8.35 ± 0.14
29.8	4.43 ± 0.10	-	37.06 ± 0.82	9.86 ± 0.01	9.06 ± 0.18
30.9	4.62 ± 0.11	-	37.16 ± 0.87	9.89 ± 0.01	9.58 ± 0.19
31.8	5.05 ± 0.10	-	37.80 ± 0.67	9.89 ± 0.01	10.04 ± 0.15

Table C2. Fitting results for $PMMA_{21}$-*b*-$PNIPAM_{283}$ solution in D_2O at 1 g L^{-1} above T_{CP} in regime II.

T [°C]	$P_s(q)$		
	R_{mic} (nm)	p_{mic}	ρ_{shell} (10^{-6}Å^{-2})
33.9	15.96 ± 0.07	0.21 ± 0.01	9.51 ± 0.01
34.8	15.73 ± 0.12	0.24 ± 0.01	9.51 ± 0.01
37.6	20.96 ± 0.03	0.14 ± 0.01	9.52 ± 0.01
38.0	18.24 ± 0.03	0.18 ± 0.01	9.52 ± 0.01
40.0	18. 61 ± 0.03	0.19 ± 0.01	9.52 ± 0.01

D. Supporting Information for Chapter 8

Structural parameters from model fits of the SAXS data

Table D1. Fitting results for $PMMA_{21}$-*b*-$PNIPAM_{283}$ solution in D_2O at 10 g L^{-1} below T_{CP} in regime I.

T [°C]	$P_{CS}(q)$					$S_{SHS}(q)$		
	R_{core} (nm)	p_{core}	t_{shell} (nm)	ρ_{shell}^{o} (10^{-6}Å^{-2})	ν_0	R_{HS} (nm)	ϕ	τ_0
20.1	2.54 ± 0.03	0.39 ± 0.01	21.88 ± 0.10	9.59 ± 0.01	3.51 ± 0.04	20.59 ± 0.11	0.065 ± 0.001	0.54 ± 0.02
22.2	2.60 ± 0.02	0.33 ± 0.01	21.62 ± 0.10	9.59 ± 0.01	3.43 ± 0.05	19.93 ± 0.11	0.058 ± 0.001	0.56 ± 0.02
24.2	2.54 ± 0.02	0.35 ± 0.01	21.19 ± 0.09	9.59 ± 0.01	3.52 ± 0.04	19.84 ± 0.10	0.052 ± 0.001	0.54 ± 0.01
26.2	2.48 ± 0.02	0.36 ± 0.01	21.00 ± 0.10	9.61 ± 0.01	3.71 ± 0.05	19.40 ± 0.14	0.039 ± 0.001	0.52 ± 0.02
28.1	2.42 ± 0.02	0.38 ± 0.01	20.75 ± 0.11	9.62 ± 0.01	3.92 ± 0.05	19.30 ± 0.16	0.028 ± 0.001	0.45 ± 0.02
29.1	2.36 ± 0.02	0.39 ± 0.01	20.52 ± 0.10	9.64 ± 0.01	4.06 ± 0.05	19.95 ± 0.14	0.016 ± 0.001	0.23 ± 0.01
30.0	2.29 ± 0.03	0.42 ± 0.01	20.40 ± 0.14	9.65 ± 0.01	4.16 ± 0.08	20.34 ± 0.26	0.005 ± 0.001	0.10 ± 0.02
31.1	2.47 ± 0.07	0.36 ± 0.01	21.45 ± 0.11	9.69 ± 0.01	4.75 ± 0.05	17.54 ± 0.15	0.000 ± 0.001	0.01 ± 0.01

Table D2. Fitting results for $PMMA_{21}$-*b*-$PNIPAM_{283}$ solution in D_2O at 10 g L^{-1} above T_{CP} in regime II.

T [°C]	$P'_{CS}(q)$				$S_{fractal}(q)$		
	R_{core} (nm)	p_{core}	t_{shell} (nm)	ρ_{shell} (10^{-6} Å^{-2})	η_f	D_f	ξ_f (nm)
32.1	1.93 ± 0.11	0.87 ± 0.04	11.02 ± 0.06	9.47 ± 0.00	0.137 ± 0.010	3.06 ± 0.13	12.17 ± 0.62
33.1	2.18 ± 0.25	0.79 ± 0.07	8.95 ± 0.06	9.48 ± 0.00	0.075 ± 0.010	3.08 ± 0.06	16.84 ± 0.49
34.0	1.91 ± 0.22	0.89 ± 0.08	7.03 ± 0.09	9.49 ± 0.00	0.048 ± 0.003	2.69 ± 0.03	25.34 ± 0.54

Table D3. Fitting results for $PMMA_{21}$-*b*-$PNIPAM_{283}$ solution in D_2O at 10 g L^{-1} far above T_{CP} in regime III.

T [°C]	$I_{Porod}(q)$	$I_{agg}(q)$	$P_S(q)$		$S_{HS}(q)$	
	m	R_{agg} (nm)	R_{mic} (nm)	p_{mic}	R_{HS} (nm)	η
35.0	2.56 ± 0.01	-	3.97 ± 0.27	0.70 ± 0.04	-	-
36.2	3.40 ± 0.01	21.04 ± 0.09	3.27 ± 0.04	-	-	-
38.2	4.08 ± 0.01	40.25 ± 0.35	3.16 ± 0.08	-	6.40 ± 0.17	0.211 ± 0.016

E. Supporting Information for Chapter 9

Structural Parameters from Model Fits of the SAXS Data

Table E1. Fit results for $PMMA_{21}$-*b*-$PNIPAM_{283}$ solution at 10 g L^{-1} for volume fractions of CD_3OD between 0 and 15 %

D_2O/CD_3OD [v/v]	$P_{CS}(q)$						$S_{SHS}(q)$		
	R_{core} [nm]	p_{core}	t_{shell} [nm]	$\rho_{solvent}$ [10^{-6} Å^{-2}]	ρ_{shell}^{o} [10^{-6} Å^{-2}]	ν_o	R_{HS} [nm]	ϕ	τ_0
100:0	2.69 ± 0.02	0.31 ± 0.01	21.99 ± 0.09	9.44	9.58 ± 0.01	3.34 ± 0.04	19.82 ± 0.13	0.068 ± 0.001	0.84 ± 0.04
95:5	2.55 ± 0.02	0.33 ± 0.01	22.17 ± 0.09	9.36	9.51 ± 0.01	3.50 ± 0.04	20.63 ± 0.13	0.054 ± 0.001	0.68 ± 0.03
90:10	2.49 ± 0.02	0.36 ± 0.01	21.15 ± 0.07	9.28	9.45 ± 0.01	3.34 ± 0.04	20.50 ± 0.79	0.065 ± 0.001	0.57 ± 0.01
85:15	2.24 ± 0.02	0.43 ± 0.01	20.44 ± 0.08	9.20	9.39 ± 0.01	3.53± 0.04	21.70 ± 0.82	0.005 ± 0.001	0.05 ± 0.01

Table E2. Fit results for $PMMA_{21}$-*b*-$PNIPAM_{283}$ solution in D_2O at 10 g L^{-1} for volume fractions of CD_3OD between 20 and 25 %

D_2O/CD_3OD [v/v]	$P'_{CS}(q)$					$S_{fractal}(q)$		
	R_{core} [nm]	p_{core}	t_{shell} [nm]	$\rho_{solvent}$ [10^{-6} Å^{-2}]	ρ_{shell} [10^{-6} Å^{-2}]	η_f	D_f	ξ_f [nm]
80:20	1.68 ± 0.09	0.89 ± 0.01	11.50 ± 0.04	9.12	9.16 ± 0.01	0.120 ± 0.011	1.52 ± 0.11	19.54 ± 0.20
75:25	2.05 ± 0.13	0.93 ± 0.05	8.77 ± 0.06	9.04	9.09 ± 0.01	0.055 ± 0.004	2.84 ± 0.05	19.08 ± 0.58

Table E3. Fit results for $PMMA_{21}$-*b*-$PNIPAM_{283}$ solution in D_2O at 10 g L^{-1} for volume fractions of CD_3OD between 70 and 100 %

D_2O/CD_3OD [v/v]	$I_{Porod}(q)$	$P_{chain}(q)$	
	P	R_g [nm]	m
30:70	4.33 ± 0.01	3.59 ± 0.02	3.20 ± 0.05
20:80	-	6.95 ± 0.01	1.94 ± 0.01
10:90	-	6.70 ± 0.01	1.87 ± 0.01
0:100	-	6.02 ± 0.01	1.83± 0.01

Bibliography

1. Roy, D.; Brooks, W. L. A.; Sumerlin, B. S. New Directions in Thermoresponsive Polymers. *Chem. Soc. Rev.* **2013,** *42*, 7214-7243.
2. De, P.; Gondi, S. R.; Sumerlin, B. S. Folate-Conjugated Thermoresponsive Block Copolymers: Highly Efficient Conjugation and Solution Self-Assembly. *Biomacromolecules* **2008,** *9*, 1064-1070.
3. Li, G.; Song, S.; Guo, L.; Ma, S. Self-assembly of Thermo- and pH-responsive Poly(acrylic acid)-*b*-poly(N-isopropylacrylamide) Micelles for Drug Delivery. *J. Polym. Sci. A Polym. Chem.* **2008,** *46*, 5028-5035.
4. Liu, Y.; Cao, X.; Luo, M.; Le, Z.; Xu, W. Self-assembled Micellar Nanoparticles of a Novel Star Copolymer for Thermo and pH Dual-responsive Drug Release. *J. Colloid Interface Sci.* **2009,** *329*, 244-252.
5. Sun, X. L.; Tsai, P. C.; Bhat, R.; Bonder, E. M.; Michniak-Kohn, B.; Pietrangelo, A. Thermoresponsive Block Copolymer Micelles with Tunable Pyrrolidone-based Polymer Cores: Structure/Property Correlations and Application as Drug Carriers. *J. Mater. Chem. B* **2015,** *3*, 814-823.
6. Yan, Q.; Yuan, J.; Yuan, W.; Zhou, M.; Yin, Y.; Pan, C. Copolymer Logical Switches Adjusted Through Core–shell Micelles: from Temperature Response to Fluorescence Response. *Chem. Commun.* **2008**, 6188-6190.
7. Roy, D.; Cambre, J. N.; Sumerlin, B. S. Triply-responsive Boronic Acid Block Copolymers: Solution Self-assembly Induced by Changes in Temperature, pH, or Sugar Concentration. *Chem. Commun.* **2009**, 2106-2108.
8. Wang, Y.; Wei, G.; Zhang, W.; Jiang, X.; Zheng, P.; Shi, L.; Dong, A. Responsive Catalysis of Thermoresponsive Micelle-supported Gold Nanoparticles. *J. Mol. Catal. A Chem.* **2007,** *266*, 233-238.
9. Patterson, J. P.; Cotanda, P.; Kelley, E. G.; Moughton, A. O.; Lu, A.; Epps, I. I. I. T. H.; O'Reilly, R. K. Catalytic Y-tailed Amphiphilic Homopolymers – Aqueous Nanoreactors for High Activity, Low Loading SCS Pincer Catalysts. *Polym. Chem.* **2013,** *4*, 2033-2039.
10. Wu, Q.; Tian, P. Adsorption of Cu^{2+} Ions with Poly(*N*-isopropylacrylamide-co-methacrylic acid) Micro/nanoparticles. *J. Appl. Polym. Sci.* **2008,** *109*, 3470-3476.
11. Lokuge, I.; Wang, X.; Bohn, P. W. Temperature-Controlled Flow Switching in Nanocapillary Array Membranes Mediated by Poly(N-isopropylacrylamide) Polymer Brushes Grafted by Atom Transfer Radical Polymerization. *Langmuir* **2007,** *23*, 305-311.
12. Ballauff, M.; Lu, Y. "Smart" Nanoparticles: Preparation, Characterization and Applications. *Polymer* **2007,** *48*, 1815-1823.
13. Hogan, K. J.; Mikos, A. G. Biodegradable Thermoresponsive Polymers: Applications in Drug Delivery and Tissue Engineering. *Polymer* **2020,** *211*, 123063.
14. Pamies, R.; Zhu, K.; Kjøniksen, A. L.; Nyström, B. Thermal Response of Low Molecular Weight Poly-(*N*-isopropylacrylamide) Polymers in Aqueous Solution. *Polym. Bull.* **2009,** *62*, 487-502.

15. Halperin, A.; Kröger, M.; Winnik, F. M. Poly(*N*-isopropylacrylamide) Phase Diagrams: Fifty Years of Research. *Angew. Chem. Int. Ed.* **2015,** *54*, 15342-15367.

16. Schild, H. G. Poly(*N*-isopropylacrylamide): Experiment, Theory and Application. *Prog. Polym. Sci.* **1992,** *17*, 163-249.

17. Kojima, H.; Tanaka, F. Cooperative Hydration Induces Discontinuous Volume Phase Transition of Cross-Linked Poly(*N*-isopropylacrylamide) Gels in Water. *Macromolecules* **2010,** *43*, 5103-5113.

18. Terada, T.; Inaba, T.; Kitano, H.; Maeda, Y.; Tsukida, N. Raman-Spectroscopic Study on Water in Aqueous-Solutions of Temperature-Responsive Polymers - Poly(*N*-Isopropylacrylamide) and Poly[*N*-(3-Ethoxypropyl)Acrylamide]. *Macromol. Chem. Phys.* **1994,** *195*, 3261-3270.

19. Lin, S.-Y.; Chen, K.-S.; Liang, R.-C. Thermal Micro ATR/FT-IR Spectroscopic System for Quantitative Study of the Molecular Structure of Poly(*N*-isopropylacrylamide) in Water. *Polymer* **1999,** *40*, 2619-2624.

20. Katsumoto, Y.; Tanaka, T.; Sato, H.; Ozaki, Y. Conformational Change of Poly(*N*-isopropylacrylamide) during the Coil-Globule Transition Investigated by Attenuated Total Reflection/Infrared Spectroscopy and Density Functional Theory Calculation. *J Phys Chem A* **2002,** *106*, 3429-3435.

21. Futscher, M. H.; Philipp, M.; Müller-Buschbaum, P.; Schulte, A. The Role of Backbone Hydration of Poly(*N*-isopropyl acrylamide) Across the Volume Phase Transition Compared to its Monomer. *Sci Rep-Uk* **2017,** *7*, 17012.

22. Gorelov, A. V.; Du Chesne, A.; Dawson, K. A. Phase Separation in Dilute Solutions of Poly (*N*-isopropylacrylamide). *Physica A* **1997,** *240*, 443-452.

23. Aseyev, V.; Hietala, S.; Laukkanen, A.; Nuopponen, M.; Confortini, O.; Du Prez, F. E.; Tenhu, H. Mesoglobules of Thermoresponsive Polymers in Dilute Aqueous Solutions above the LCST. *Polymer* **2005,** *46*, 7118-7131.

24. Balu, C.; Delsanti, M.; Guenoun, P.; Monti, F.; Cloitre, M. Colloidal Phase Separation of Concentrated PNIPAm Solutions. *Langmuir* **2007,** *23*, 2404-2407.

25. Niebuur, B.-J.; Claude, K.-L.; Pinzek, S.; Cariker, C.; Raftopoulos, K. N.; Pipich, V.; Appavou, M. S.; Schulte, A.; Papadakis, C. M. Pressure-Dependence of Poly(*N*-isopropylacrylamide) Mesoglobule Formation in Aqueous Solution. *ACS Macro Lett.* **2017,** *6*, 1180-1185.

26. Lee, L.-T.; Cabane, B. Effects of Surfactants on Thermally Collapsed Poly(N-isopropylacrylamide) Macromolecules. *Macromolecules* **1997,** *30*, 6559-6566.

27. Du, H.; Wickramasinghe, R.; Qian, X. Effects of Salt on the Lower Critical Solution Temperature of Poly (N-Isopropylacrylamide). *J. Phys. Chem. B* **2010,** *114*, 16594-16604.

28. Shibayama, M.; Tanaka, T., Volume Phase Transition and Related Phenomena of Polymer Gels. In *Responsive Gels: Volume Transitions I*, Dušek, K., Ed. Springer Berlin Heidelberg: Berlin, Heidelberg, 1993; pp 1-62.

29. Chen, G.; Hoffman, A. S. Graft Copolymers that Exhibit Temperature-induced Phase Transitions over a Wide Range of pH. *Nature* **1995,** *373*, 49-52.

30. Feil, H.; Bae, Y. H.; Feijen, J.; Kim, S. W. Effect of Comonomer Hydrophilicity and Ionization on the Lower Critical Solution Temperature of N-isopropylacrylamide copolymers. *Macromolecules* **1993,** *26*, 2496-2500.

31. Aseyev, V.; Tenhu, H.; Winnik, F. M. Non-ionic Thermoresponsive Polymers in Water. *Adv Polym Sci* **2011,** *242*, 29-89.

32. Fujishige, S.; Kubota, K.; Ando, I. Phase-Transition of Aqueous-Solutions of Poly(*N*-isopropylacrylamide) and Poly(*N*-isopropylmethacrylamide). *J Phys Chem-Us* **1989,** *93*, 3311-3313.

33. Chytrý, V. N., M.; Bohdanecký, M.; Ulbrich, K. Phase Transition Parameters of Potential Thermosensitive Drug Release Systems Based on Polymers of *N*-alkylmethacrylamides. *J Biomat Sci-Polym E* **1997,** *8*, 817-824.

34. Netopilík, M.; Bohdanecký, M.; Chytrý, V.; Ulbrich, K. Cloud Point of Poly(*N*-isopropylmethacrylamide) Solutions in Water: Is It Really a Point? *Macromol Rapid Comm* **1997,** *18*, 107-111.

35. Djokpé, E.; Vogt, W. *N*-isopropylacrylamide and *N*-isopropylmethacrylamide: Cloud Points of Mixtures and Copolymers. *Macromol. Chem. Phys.* **2001,** *202*, 750-757.

36. Kano, M.; Kokufuta, E. On the Temperature-Responsive Polymers and Gels Based on *N*-Propylacrylamides and *N*-Propylmethacrylamides. *Langmuir* **2009,** *25*, 8649-8655.

37. Kubota, K.; Hamano, K.; Kuwahara, N.; Fujishige, S.; Ando, I. Characterization of Poly(*N*-isopropylmethacrylamide) in Water. *Polym J* **1990,** *22*, 1051-1057.

38. Tang, Y. C.; Ding, Y. W.; Zhang, G. Z. Role of Methyl in the Phase Transition of Poly(*N*-isopropylmethacrylamide). *J. Phys. Chem. B* **2008,** *112*, 8447-8451.

39. Dybal, J.; Trchova, M.; Schmidt, P. The Role of Water in Structural Changes of Poly(*N*-isopropylacrylamide) and Poly(*N*-isopropylmethacrylamide) Studied by FTIR, Raman Spectroscopy and Quantum Chemical Calculations. *Vib Spectrosc* **2009,** *51*, 44-51.

40. Pang, J.; Yang, H.; Ma, J.; Cheng, R. S. Understanding Different LCST Levels of Poly(*N*-alkylacrylamide)s by Molecular Dynamics Simulations and Quantum Mechanics Calculations. *J Theor Comput Chem* **2011,** *10*, 359-370.

41. Tiktopulo, E. I.; Uversky, V. N.; Lushchik, V. B.; Klenin, S. I.; Bychkova, V. E.; Ptitsyn, O. B. Domain Coil-Globule Transition in Homopolymers. *Macromolecules* **1995,** *28*, 7519-7524.

42. Maeda, Y.; Nakamura, T.; Ikeda, I. Changes in the Hydration States of Poly(*N*-*n*-propylmethacrylamide) and Poly(*N*-isopropylmethacrylamide) during Their Phase Transitions in Water Observed by FTIR Spectroscopy. *Macromolecules* **2001,** *34*, 8246-8251.

43. Spěváček, J.; Dybal, J. Temperature-Induced Phase Separation and Hydration in Aqueous Polymer Solutions Studied by NMR and IR Spectroscopy: Comparison of Poly(*N*-vinylcaprolactam) and Acrylamide-Based Polymers. *Macromol Symp* **2014,** *336*, 39-46.

44. Dimitrov, I.; Trzebicka, B.; Müller, A. H. E.; Dworak, A.; Tsvetanov, C. B. Thermosensitive Water-soluble Copolymers with Doubly Responsive Reversibly Interacting Entities. *Prog. Polym. Sci.* **2007,** *32*, 1275-1343.

45. Laschewsky, A.; Müller-Buschbaum, P.; Papadakis, C. M. Thermo-responsive Amphiphilic Di- and Triblock Copolymers Based on Poly(N-isopropylacrylamide) and Poly(methoxy diethylene glycol acrylate): Aggregation and Hydrogel Formation in Bulk Solution and in Thin Films. *Prog. Colloid Polym. Sci.* **2013,** *140*, 15-34.

46. Luo, G.-F.; Chen, W.-H.; Zhang, X.-Z. 100th Anniversary of Macromolecular Science Viewpoint: Poly(*N*-isopropylacrylamide)-Based Thermally Responsive Micelles. *ACS Macro Lett.* **2020,** *9*, 872-881.

47. Papadakis, C. M.; Müller-Buschbaum, P.; Laschewsky, A. Switch It Inside-Out: "Schizophrenic" Behavior of All Thermoresponsive UCST-LCST Diblock Copolymers. *Langmuir* **2019,** *35*, 9660-9676.

48. Rösler, A.; Vandermeulen, G. W. M.; Klok, H.-A. Advanced Drug Delivery Devices via Self-assembly of Amphiphilic Block Copolymers. *Adv. Drug Deliv. Rev.* **2012,** *64*, 270-279.

49. Hocine, S.; Li, M.-H. Thermoresponsive Self-assembled Polymer Colloids in Water. *Soft Matter* **2013,** *9*, 5839-5861.

50. Kotsuchibashi, Y.; Ebara, M.; Aoyagi, T.; Narain, R. Recent Advances in Dual Temperature Responsive Block Copolymers and Their Potential as Biomedical Applications. *Polymers (Basel)* **2016,** *8*, 380.

51. Hussein, Y. H. A.; Youssry, M. Polymeric Micelles of Biodegradable Diblock Copolymers: Enhanced Encapsulation of Hydrophobic Drugs. *Materials (Basel)* **2018,** *11*, 688.

52. Rubinstein, M.; Colby, R. H., *Polymer Physics*. Oxford University Press: Oxford, 2003.

53. Yuan, G.; Wang, X.; Han, C. C.; Wu, C. Reexamination of Slow Dynamics in Semidilute Solutions: Temperature and Salt Effects on Semidilute Poly(*N*-isopropylacrylamide) Aqueous Solutions. *Macromolecules* **2006,** *39*, 6207-6209.

54. de Gennes, P. G., *Scaling Concepts in Polymer Physics*. Cornell University Press: Ithaca, NY, 1979.

55. Teraoka, I., *Polymer Solutions: An Introduction to Physical Properties.* John Wiley and Sons, Inc.: 2002.

56. Brandrup, J.; Immergut, E. H.; Grulke, E. A., Solubiliy Parameter Values. In *Polymer Handbook*, 4th ed.; Grulke, E. A., Ed. Wiley: 2004; Vol. 2.

57. Graziano, G. On the Temperature-induced Coil to Globule Transition of Poly-*N*-isopropylacrylamide in Dilute Aqueous Solutions. *Int. J. Biol. Macromol.* **2000,** *27*, 89-97.

58. Zhang, Q. L.; Weber, C.; Schubert, U. S.; Hoogenboom, R. Thermoresponsive Polymers with Lower Critical Solution Temperature: from Fundamental Aspects and Measuring Techniques to Recommended Turbidimetry Conditions. *Mater Horiz* **2017,** *4*, 109-116.

59. Riess, G. Micellization of Block Copolymers. *Prog. Polym. Sci.* **2003,** *28*, 1107–1170.

60. Gohy, J.-F., *Block Copolym. II*. Springer Berlin Heidelberg: Berlin, Heidelberg 2005.

61. Halperin, A. Polymeric Micelles: A Star Model. *Macromolecules* **1987,** *20*, 2943-2946.

62. Zhulina, Y. B.; Birshtein, T. M. Conformations of Block-copolymer Molecules in Selective

Solvents (Micellar Structures). *Polymer Science U.S.S.R.* **1985,** *27*, 570-578.

63. Zhulina, E. B.; Adam, M.; LaRue, I.; Sheiko, S. S.; Rubinstein, M. Diblock Copolymer Micelles in a Dilute Solution. *Macromolecules* **2005,** *38*, 5330-5351.

64. Zhulina, E. B.; Borisov, O. V. Theory of Block Polymer Micelles: Recent Advances and Current Challenges. *Macromolecules* **2012,** *45*, 4429-4440.

65. Hamley, I. W., *Introduction to Soft Matter*. John Wiley & Sons, Ltd: 2007.

66. Israelachvili, J. N.; Mitchell, D. J.; Ninham, B. W. Theory of Self-Assembly of Hydrocarbon Amphiphiles into Micelles and Bilayers. *J. Chem. Soc., Faraday Trans. 2,* **1976,** *72*, 1525-1568.

67. Blanazs, A.; Armes, S. P.; Ryan, A. J. Self-Assembled Block Copolymer Aggregates: From Micelles to Vesicles and their Biological Applications. *Macromol. Rapid Commun.* **2009,** *30*, 267-277.

68. Choucair, A.; Eisenberg, A. Control of Amphiphilic Block Copolymer Morphologies Using Solution Conditions. *Eur. Phys. J. E* **2003,** *10*, 37-44.

69. Cameron, N. S.; Corbierre, M. K.; Eisenberg, A. 1998 E.W.R. Steacie Award Lecture Asymmetric Amphiphilic Block Copolymers in Solution: a Morphological Wonderland. *Can. J. Chem.* **1999,** *77*, 1311-1326.

70. Lodge, T. P. Block Copolymers: Past Successes and Future Challenges. *Macromol. Chem. Phys.* **2003,** *204*, 265-273.

71. Jain, S.; Bates, F. S. Consequences of Nonergodicity in Aqueous Binary PEO−PB Micellar Dispersions. *Macromolecules* **2004,** *37*, 1511-1523.

72. Motornov, M.; Roiter, Y.; Tokarev, I.; Minko, S. Stimuli-responsive Nanoparticles, Nanogels and Capsules for Integrated Multifunctional Intelligent Systems. *Prog. Polym. Sci.* **2010,** *35*, 174-211.

73. Sistach, S.; Beija, M.; Rahal, V.; Brûlet, A.; Marty, J.-D.; Destarac, M.; Mingotaud, C. Thermoresponsive Amphiphilic Diblock Copolymers Synthesized by MADIX/RAFT: Properties in Aqueous Solutions and Use for the Preparation and Stabilization of Gold Nanoparticles. *Chem. Mater.* **2010,** *22*, 3712-3724.

74. Ge, Z.; Xie, D.; Chen, D.; Jiang, X.; Zhang, Y.; Liu, H.; Liu, S. Stimuli-Responsive Double Hydrophilic Block Copolymer Micelles with Switchable Catalytic Activity. *Macromolecules* **2007,** *40*, 3538-3546.

75. Rao, J.; Xu, J.; Luo, S.; Liu, S. Cononsolvency-Induced Micellization of Pyrene End-Labeled Diblock Copolymers of N-Isopropylacrylamide and Oligo(ethylene glycol) Methyl Ether Methacrylate. *Langmuir* **2007,** *23*, 11857-11865.

76. Zhou, H.; Lu, Y.; Zhang, M.; Guerin, G.; Manners, I.; Winnik, M. A. PFS-b-PNIPAM: A First Step toward Polymeric Nanofibrillar Hydrogels Based on Uniform Fiber-Like Micelles. *Macromolecules* **2016,** *49*, 4265-4276.

77. Tanaka, H. Appearance of a Moving Droplet Phase and Unusual Network-Like or Sponge-Like Patterns in a Phase-Separating Polymer-Solution with a Double-Well-Shaped Phase-Diagram. *Macromolecules* **1992,** *25*, 6377-6380.

78. Wu, C.; Li, W.; Zhu, X. X. Viscoelastic Effect on the Formation of Mesoglobular Phase in Dilute

Solutions. *Macromolecules* **2004,** *37*, 4989-4992.

79. Tanaka, H. Viscoelastic Phase Separation. *J Phys-Condens Mat* **2000,** *12*, R207-R264.

80. Tanaka, F.; Koga, T.; Kaneda, I.; Winnik, F. M. Hydration, Phase Separation and Nonlinear Rheology of Temperature-sensitive Water-soluble Polymers. *J. Phys.: Condens. Matter* **2011,** *23*, 284105.

81. Okada, Y.; Tanaka, F. Cooperative Hydration, Chain Collapse, and Flat LCST Behavior in Aqueous Poly(*N*-isopropylacrylamide) Solutions. *Macromolecules* **2005,** *38*, 4465-4471.

82. Schild, H. G.; Muthukumar, M.; Tirrell, D. A. Cononsolvency in Mixed Aqueous Solutions of Poly(*N*-isopropylacrylamide). *Macromolecules* **1991,** *24*, 948-952.

83. Costa, R. O. R.; Freitas, R. F. S. Phase Behavior of Poly(*N*-isopropylacrylamide) in Binary Aqueous Solutions. *Polymer* **2002,** *43*, 5879-5885.

84. Hao, J.; Cheng, H.; Butler, P.; Zhang, L.; Han, C. C. Origin of Cononsolvency, Based on the Structure of Tetrahydrofuran-water Mixture. *J. Chem. Phys.* **2010,** *132*, 154902.

85. Hore, M.-J. A.; Hammouda, B.; Li, Y.; Cheng, H. Co-Nonsolvency of Poly(*n*-isopropylacrylamide) in Deuterated Water/Ethanol Mixtures. *Macromolecules* **2013,** *46*, 7894-7901.

86. Scherzinger, C.; Schwarz, A.; Bardow, A.; Leonhard, K.; Richtering, W. Cononsolvency of Poly-*N*-isopropyl acrylamide (PNIPAM): Microgels versus Linear Chains and Macrogels. *Curr. Opin. Colloid Interface Sci.* **2014,** *19*, 84-94.

87. Zhu, P.-w.; Chen, L. Effects of Cosolvent Partitioning on Conformational Transitions and Chain Flexibility of Thermoresponsive Microgels. *Phys. Rev. E* **2019,** *99*, 022501.

88. Schroer, M. A.; Michalowsky, J.; Fischer, B.; Smiatek, J.; Grübel, G. Stabilizing Effect of TMAO on Globular PNIPAM States: Preferential Attraction Induces Preferential Hydration. *Phys. Chem. Chem. Phys.* **2016,** *18*, 31459-31470.

89. Winnik, F. M.; Ringsdorf, H.; Venzmer, J. Methanol-water as a Co-nonsolvent System for Poly(*N*-isopropylacrylamide). *Macromolecules* **1990,** *23*, 2415-2416.

90. Zhang, G.; Wu, C. The Water/Methanol Complexation Induced Reentrant Coil-to-Globule-to-Coil Transition of Individual Homopolymer Chains in Extremely Dilute Solution. *J. Am. Chem. Soc.* **2001,** *123*, 1376-1380.

91. Pang, J.; Yang, H.; Ma, J.; Cheng, R. Solvation Behaviors of *N*-Isopropylacrylamide in Water/Methanol Mixtures Revealed by Molecular Dynamics Simulations. *J. Phys. Chem. B* **2010,** *114*, 8652-8658.

92. Zhang, G.; Wu, C. Reentrant Coil-to-Globule-to-Coil Transition of a Single Linear Homopolymer Chain in a Water/Methanol Mixture. *Phys. Rev. Lett.* **2001,** *86*, 822-825.

93. Mukherji, D.; Kremer, K. Coil–Globule–Coil Transition of PNIPAm in Aqueous Methanol: Coupling All-Atom Simulations to Semi-Grand Canonical Coarse-Grained Reservoir. *Macromolecules* **2013,** *46*, 9158-9163.

94. Tanaka, F.; Koga, T.; Winnik, F. M. Temperature-Responsive Polymers in Mixed Solvents: Competitive Hydrogen Bonds Cause Cononsolvency. *Phys. Rev. Lett.* **2008,** *101*, 028302.

95. Tanaka, F.; Koga, T.; Kojima, H.; Xue, N.; Winnik, F. M. Preferential Adsorption and Co-nonsolvency of Thermoresponsive Polymers in Mixed Solvents of Water/Methanol. *Macromolecules* **2011,** *44*, 2978-2989.

96. Mukherji, D.; Marques, C. M.; Kremer, K. Polymer Collapse in Miscible Good Solvents is a Generic Phenomenon Driven by Preferential Adsorption. *Nat. Commun.* **2014,** *5*, 4882.

97. Rodríguez-Ropero, F.; Hajari, T.; van der Vegt, N. F. A. Mechanism of Polymer Collapse in Miscible Good Solvents. *J. Phys. Chem. B* **2015,** *119*, 15780-15788.

98. Pica, A.; Graziano, G. An Alternative Explanation of the Cononsolvency of Poly(*N*-isopropylacrylamide) in Water-methanol Solutions. *Phys. Chem. Chem. Phys.* **2016,** *18*, 25601-25608.

99. Dalgicdir, C.; Rodríguez-Ropero, F.; van der Vegt, N. F. A. Computational Calorimetry of PNIPAM Cononsolvency in Water/Methanol Mixtures. *J. Phys. Chem. B* **2017,** *121*, 7741-7748.

100. Grinberg, V. Y.; Burova, T. V.; Grinberg, N. V.; Moskalets, A. P.; Dubovik, A. S.; Plashchina, I. G.; Khokhlov, A. R. Energetics and Mechanisms of poly(*N*-isopropylacrylamide) Phase Transitions in Water–Methanol Solutions. *Macromolecules* **2020,** *53*, 10765-10772.

101. Tavagnacco, L.; Zaccarelli, E.; Chiessi, E. Molecular Description of the Coil-to-Globule Transition of Poly(N-isopropylacrylamide) in Water/Ethanol Mixture at Low Alcohol Concentration. *J. Mol. Liq.* **2020,** *297*, 111928.

102. Nikoofard, N.; Maghsoodi, F. Amphiphilic Block Copolymer Nano-micelles: Effect of Length Ratio of the Hydrophilic Block. *Phys. Chem. Res.* **2015,** *3*, 239-245.

103. Zhang, W.; Zhou, X.; Li, H.; Fang, Y.; Zhang, G. Conformational Transition of Tethered Poly(*N*-isopropylacrylamide) Chains in Coronas of Micelles and Vesicles. *Macromolecules* **2005,** *38*, 909-914.

104. Kessel, S.; Urbani, C. N.; Monteiro, M. J. Mechanically Driven Reorganization of Thermoresponsive Diblock Copolymer Assemblies in Water. *Angew. Chem. Int. Ed.* **2011,** *50*, 8082-8085.

105. Nuopponen, M.; Ojala, J.; Tenhu, H. Aggregation Behaviour of Well Defined Amphiphilic Diblock Copolymers with Poly(*N*-isopropylacrylamide) and Hydrophobic Blocks. *Polymer* **2004,** *45*, 3643-3650.

106. Cao, M.; Nie, H.; Hou, Y.; Han, G.; Zhang, W. Synthesis of Star Thermoresponsive Amphiphilic Block Copolymer Nano-assemblies and the Effect of Topology on Their Thermoresponse. *Polym. Chem.* **2019,** *10*, 403-411.

107. Adelsberger, J.; Meier-Koll, A.; Bivigou-Koumba, A. M.; Busch, P.; Holderer, O.; Hellweg, T.; Laschewsky, A.; Müller-Buschbaum, P.; Papadakis, C. M. The Collapse Transition and the Segmental Dynamics in Concentrated Micellar Solutions of P(S-*b*-NIPAM) Diblock Copolymers. *Colloid Polym. Sci.* **2011,** *289*, 711-720.

108. Ke, X.-X.; Wang, L.; Xu, J.-T.; Du, B.-Y.; Tu, Y.-F.; Fan, Z.-Q. Effect of Local Chain Deformability on the Temperature-induced Morphological Transitions of Polystyrene-*b*-poly(*N*-isopropylacrylamide) Micelles in Aqueous Solution. *Soft Matter* **2014,** *10*, 5201-5211.

109. Wang, W.; Gao, C.; Qu, Y.; Song, Z.; Zhang, W. In Situ Synthesis of Thermoresponsive

Polystyrene-*b*-poly(*N*-isopropylacrylamide)-*b*-polystyrene Nanospheres and Comparative Study of the Looped and Linear Poly(*N*-isopropylacrylamide)s. *Macromolecules* **2016,** *49*, 2772-2781.

110. Troll, K.; Kulkarni, A.; Wang, W.; Darko, C.; Bivigou Koumba, A. M.; Laschewsky, A.; Müller-Buschbaum, P.; Papadakis, C. M. The Collapse Transition of Poly(styrene-*b*-(*N*-isopropyl acrylamide)) Diblock Copolymers in Aqueous Solution and in Thin Films. *Colloid Polym. Sci.* **2008,** *286*, 1079-1092.

111. Shastri, V. P. Non-degradable Biocompatible Polymers in Medicine: Past, Present and Future. *Curr. Pharm. Biotechnol.* **2003,** *4*, 331-7.

112. Frazer, R. Q.; Byron, R. T.; Osborne, P. B.; West, K. P. PMMA: an Essential Material in Medicine and Dentistry. *J. Long Term Eff. Med. Implants* **2005,** *15*, 629-39.

113. Tang, T.; Castelletto, V.; Parras, P.; Hamley, I. W.; King, S. M.; Roy, D.; Perrier, S.; Hoogenboom, R.; Schubert, U. S. Thermo-responsive Poly(methyl methacrylate)-block-poly(N-isopropylacrylamide) Block Copolymers Synthesized by RAFT Polymerization: Micellization and Gelation. *Macromol. Chem. Phys.* **2006,** *207*, 1718-1726.

114. Razavi, B.; Abdollahi, A.; Roghani-Mamaqani, H.; Salami-Kalajahi, M. Light- and Temperature-responsive Micellar Carriers Prepared by Spiropyran-initiated Atom Transfer Polymerization: Investigation of Photochromism Kinetics, Responsivities, and Controlled Release of Doxorubicin. *Polymer* **2020,** *187*, 122046.

115. Wei, H.; Zhang, X.-Z.; Zhou, Y.; Cheng, S.-X.; Zhuo, R.-X. Self-assembled Thermoresponsive Micelles of Poly(*N*-isopropylacrylamide-*b*-methyl methacrylate). *Biomaterials* **2006,** *27*, 2028-2034.

116. Kelarakis, A.; Tang, T.; Havredaki, V.; Viras, K.; Hamley, I. W. Micellar and Surface Properties of a Poly(methyl methacrylate)-block-poly(*N*-isopropylacrylamide) Copolymer in Aqueous Solution. *J. Colloid Interface Sci.* **2008,** *320*, 70-3.

117. Wei, H.; Cheng, C.; Chang, C.; Chen, W.-Q.; Cheng, S.-X.; Zhang, X.-Z.; Zhuo, R.-X. Synthesis and Applications of Shell Cross-Linked Thermoresponsive Hybrid Micelles Based on Poly(*N*-isopropylacrylamide-*co*-3-(trimethoxysilyl)propyl methacrylate)-*b*-poly(methyl methacrylate). *Langmuir* **2008,** *24*, 4564-4570.

118. Chang, C.; Wei, H.; Wu, D.-Q.; Yang, B.; Chen, N.; Cheng, S.-X.; Zhang, X.-Z.; Zhuo, R.-X. Thermo-responsive Shell Cross-linked PMMA-*b*-P(NIPAAm-*co*-NAS) Micelles for Drug Delivery. *Int. J. Pharm.* **2011,** *420*, 333-340.

119. Mukherji, D.; Marques, C. M.; Kremer, K. Collapse in Two Good Solvents, Swelling in Two Poor Solvents: Defying the Laws of Polymer Solubility? *J. Phys.: Condens. Matter* **2017,** *30*, 024002.

120. Cowie, J. M. G.; Mohsin, M. A.; McEwen, I. J. Alcohol-water Cosolvent Systems for Poly(methyl methacrylate). *Polymer* **1987,** *28*, 1569-1572.

121. Hoogenboom, R.; Becer, C. R.; Guerrero-Sanchez, C.; Hoeppener, S.; Schubert, U. S. Solubility and Thermoresponsiveness of PMMA in Alcohol-Water Solvent Mixtures. *Aust. J. Chem.* **2010,** *63*, 1173-1178.

122. Mukherji, D.; Marques, C. M.; Stuehn, T.; Kremer, K. Depleted Depletion Drives Polymer

Swelling in Poor Solvent Mixtures. *Nat. Commun.* **2017,** *8*, 1374.

123. Hoogenboom, R.; Rogers, S.; Can, A.; Becer, C. R.; Guerrero-Sanchez, C.; Wouters, D.; Hoeppener, S.; Schubert, U. S. Self-assembly of Double Hydrophobic Block Copolymers in Water–ethanol Mixtures: from Micelles to Thermoresponsive Micellar Gels. *ChemComm* **2009**, 5582-5584.

124. Ko, C.-H.; Claude, K.-L.; Niebuur, B.-J.; Jung, F. A.; Kang, J.-J.; Schanzenbach, D.; Frielinghaus, H.; Barnsley, L. C.; Wu, B.; Pipich, V.; Schulte, A.; Müller-Buschbaum, P.; Laschewsky, A.; Papadakis, C. M. Temperature-Dependent Phase Behavior of the Thermoresponsive Polymer Poly(*N*-isopropylmethacrylamide) in an Aqueous Solution. *Macromolecules* **2020,** *53*, 6816-6827.

125. Moad, G.; Rizzardo, E.; Thang, S. H. Toward Living Radical Polymerization. *Acc. Chem. Res.* **2008,** *41*, 1133-1142.

126. Ko, C.-H.; Henschel, C.; Meledam, G. P.; Schroer, M. A.; Müller-Buschbaum, P.; Laschewsky, A.; Papadakis, C. M. Self-Assembled Micelles from Thermoresponsive Poly(methyl methacrylate)-*b*-poly(*N*-isopropylacrylamide) Diblock Copolymers in Aqueous Solution. *Macromolecules* **2021,** *54*, 384-397.

127. Booth, C.; Attwood, D. Effects of Block Architecture and Composition on the Association Properties of Poly(oxyalkylene) Copolymers in Aqueous Solution. *Macromol. Rapid Commun.* **2000,** *21*, 501-527.

128. Zeng, F.; Tong, Z.; Sato, T. Molecular Chain Properties of Poly (*N*-isopropyl acrylamide). *Sc. China Ser. B-Chem.* **1999,** *42*, 290-297.

129. Brown, W., *Dynamic Light Scattering: The Method and Some Applications*. Clarendon Press: New York, 1993.

130. Schärtl, W., *Light Scattering from Polymer Solutions and Nanoparticle Dispersions*. Springer-Verlag Berlin Heidelberg: 2007.

131. *Neutron, X-rays and Light. Scattering Methods Applied to Soft Condensed Matter*. Elsevier: 2002.

132. Jakeš, J. Regularized Positive Exponential Sum (REPES) Program - A Way of Inverting Laplace Transform Data Obtained by Dynamic Light Scattering. *Collect. Czech. Chem. Commun.* **1995,** *60*, 1781–1797.

133. Štěpánek, P., Data Analysis in Dynamic Light Scattering. In *Dynamic Light Scattering: The Method and Some Applications (Monographs on the Physics and Chemistry of Materials)*, Brown, W., Ed. Clarendon Press: New York, 1993; pp 177–241.

134. Ivanov, E. V.; Abrossimov, V. X. Volumetric Properties of Mixtures of Water and Methanol H/D-isotopomers between 5 and 45°C. *J. Solution Chem.* **1996,** *25*, 191-201.

135. Wastian, P. Cononsolvency in Novel Thermoresponsive Polymers. Bachelor's thesis. Technical University of Munich, 2018.

136. Feigin, L. A., Svergun, D. I., *Structure Analysis by Small-Angle X-Ray and Neutron Scattering*. Plenum Press: New York, 1987.

137. Svergun, D. I.; Koch, M. H. J.; Timmins, P. A.; May, R. P., *Small Angle X-Ray and Neutron Scattering from Solutions of Biological Macromolecules*. Oxford University Press: 2013.

138. NCNR, Neutron scattering lengths and cross sections. https://www.ncnr.nist.gov/resources/n-lengths/

139. Pedersen, J. S.; Posselt, D.; Mortensen, K. Analytical Treatment of the Resolution Function for Small-Angle Scattering. *J. Appl. Cryst.* **1990,** *23*, 321-333.

140. Frielinghaus, H.; Feoktystov, A.; Berts, I.; Mangiapia, G. KWS-1: Small Angle Scattering Diffractometer. *Journal of Large-Scale Research Facilities.* **2015,** *1*, A28.

141. Feoktystov, A. V.; Frielinghaus, H.; Di, Z. Y.; Jaksch, S.; Pipich, V.; Appavou, M. S.; Babcock, E.; Hanslik, R.; Engels, R.; Kemmerling, G.; Kleines, H.; Ioffe, A.; Richter, D.; Bruckel, T. KWS-1 High-resolution Small-Angle Neutron Scattering Instrument at JCNS: Current State. *J Appl Crystallogr* **2015,** *48*, 61-70.

142. Pipich, V.; Fu, Z. KWS-3: Very Small Angle Scattering Diffractometer with Focusing Mirror. *Journal of Large-Scale Research Facilities.* **2015,** *1*, A31.

143. Blanchet, C. E.; Spilotros, A.; Schwemmer, F.; Graewert, M. A.; Kikhney, A.; Jeffries, C. M.; Franke, D.; Mark, D.; Zengerle, R.; Cipriani, F.; Fiedler, S.; Roessle, M.; Svergun, D. I. Versatile Sample Environments and Automation for Biological Solution X-ray Scattering Experiments at the P12 Beamline (PETRA III, DESY). *J. Appl. Cryst.* **2015,** *48*, 431-443.

144. Round, A.; Felisaz, F.; Fodinger, L.; Gobbo, A.; Huet, J.; Villard, C.; Blanchet, C. E.; Pernot, P.; McSweeney, S.; Roessle, M.; Svergun, D. I.; Cipriani, F. BioSAXS Sample Changer: a Robotic Sample Changer for Rapid and Reliable High-throughput X-ray Solution Scattering Experiments. *Acta Crystallogr. D* **2015,** *71*, 67-75.

145. Franke, D.; Kikhney, A. G.; Svergun, D. I. Automated Acquisition and Analysis of Small Angle X-ray Scattering Data. *Nucl. Instrum. Methods Phys. Res* **2012,** *689*, 52-59.

146. Porod, G. Die Röntgenkleinwinkelstreuung von dichtgepackten kolloiden Systemen. *Kolloid-Zeitschrift* **1951,** *124*, 83-114.

147. Teixeira, J. Small-Angle Scattering by Fractal Systems. *J. Appl. Cryst.* **1988,** *21*, 781-785.

148. Evmenenko, G.; Theunissen, E.; Mortensen, K.; Reynaers, H. SANS Study of Surfactant Ordering in Kappa-carrageenan/Cetylpyridinium Chloride Complexes. *Polymer* **2001,** *42*, 2907-2913.

149. Hammouda, B.; Ho, D. L.; Kline, S. Insight into Clustering in Poly(ethylene oxide) Solutions. *Macromolecules* **2004,** *37*, 6932-6937.

150. Shibayama, M.; Tanaka, T.; Han, C. C. Small-Angle Neutron-Scattering Study on Poly(*N*-isopropyl acrylamide) Gels near Their Volume-Phase Transition-Temperature. *J. Chem. Phys.* **1992,** *97*, 6829-6841.

151. Beaucage, G.; Schaefer, D. W. Structural Studies of Complex-Systems Using Small-Angle Scattering - a Unified Guinier Power-Law Approach. *J Non-Cryst Solids* **1994,** *172*, 797-805.

152. Beaucage, G. Approximations Leading to a Unified Exponential Power-law Approach to Small-Angle Scattering. *J Appl Crystallogr* **1995,** *28*, 717-728.

153. Koberstein, J. T.; Morra, B.; Stein, R. S. The Determination of Diffuse-Boundary Thicknesses of Polymers by Small-Angle X-ray Scattering. *J. Appl. Cryst.* **1980,** *13*, 34-45.

154. Schmidt, P. Interpretation of Small-Angle Scattering Curves Proportional to a Negative Power of the Scattering Vector. *J. Appl. Cryst.* **1982,** *15*, 567-569.
155. Hammouda, B., SANS from Homogeneous Polymer Mixtures: A Unified Overview. In *Polymer Characteristics*, Springer Berlin Heidelberg: Berlin, Heidelberg, 1993; pp 87-133.
156. Benoit, H. The Diffusion of Light by Polymers Dissolved in a Good Solvent. *Comptes Rendus.* **1957,** *245*, 2244−2247.
157. Flory, P., *Principles of Polymer Chemistry*. Cornell University Press: Ithaca, NY, 1953.
158. Guinier, A.; Fournet, G., *Small-Angle Scattering of X-Rays*. John Wiley and Sons: New York, 1955.
159. Kotlarchyk, M.; Chen, S. H. Analysis of Small Angle Neutron Scattering Spectra from Polydisperse Interacting Colloids. *J. Chem. Phys.* **1983,** *79*, 2461-2469.
160. Kotlarchyk, M.; Stephens, R. B.; Huang, J. S. Study of Schultz Distribution to Model Polydispersity of Microemulsion Droplets. *J. Chem. Phys.* **1988,** *92*, 1533-1538.
161. Poly(methyl methacrylate). https://polymerdatabase.com/polymers/polymethylmethacrylate.html (September 17, 2020).
162. Percus, J. K.; Yevick, G. J. Analysis of Classical Statistical Mechanics by Means of Collective Coordinates. *Phys. Rev.* **1958,** *110*, 1-13.
163. Baxter, R. J. Percus–Yevick Equation for Hard Spheres with Surface Adhesion. *J. Chem. Phys.* **1968,** *49*, 2770-2774.
164. Menon, S. V. G.; Manohar, C.; Rao, K. S. A New Interpretation of the Sticky Hard Sphere Model. *J. Chem. Phys.* **1991,** *95*, 9186-9190.
165. Möller, J.; Grobelny, S.; Schulze, J.; Bieder, S.; Steffen, A.; Erlkamp, M.; Paulus, M.; Tolan, M.; Winter, R. Reentrant Liquid-Liquid Phase Separation in Protein Solutions at Elevated Hydrostatic Pressures. *Phys. Rev. Lett.* **2014,** *112*, 028101.
166. Schroer, M. A.; Schulz, F.; Lehmkühler, F.; Möller, J.; Smith, A. J.; Lange, H.; Vossmeyer, T.; Grübel, G. Tuning the Interaction of Nanoparticles from Repulsive to Attractive by Pressure. *J. Phys. Chem. C* **2016,** *120*, 19856-19861.
167. Kline, S. Reduction and Analysis of SANS and USANS Data using IGOR Pro. *J. Appl. Cryst.* **2006,** *39*, 895-900.
168. *Thermal Analysis in Practice Handbook: Fundamental Aspects of Thermal Analysis*. METTLER TOLEDO.
169. *DSC 3 Product Brochure: Differential Scanning Calorimetry for Routine Analysis*. METTLER TOLEDO.
170. McCreery, R. L., *Raman Spectroscopy for Chemical Analysis*. John Wiley & Sons, Inc.: Canada, 2000.
171. Schulte, A.; Guo, Y., Applications of Laser Raman Spectroscopy. In *Handbook of Applied Solid State Spectroscopy*, Springer US: 2006.
172. Siesler, H. W., 2.09-Vibrational Spectroscopy. In *Polymer Science: A Comprehensive Reference*,

Matyjaszewski, K., Möller, M., Eds. Elsevier: Amsterdam, 2012; pp 255-300.
173. Siebert, F.; Hildebrandt, P., *Vibrational Spectroscopy in Life Science*. Wiley: 2007.
174. Fenn, M. B.; Xanthopoulos, P.; Pyrgiotakis, G.; Grobmyer, S. R.; Pardalos, P. M.; Hench, L. L. Raman Spectroscopy for Clinical Oncology. *Adv. Opt. Technol.* **2011,** *2011*, 213783.
175. Demtröder, W., *Laser Spectroscopy 1*. Springer-Verlag Berlin Heidelberg: 2014.
176. Vishnevetskaya, N. S.; Hildebrand, V.; Niebuur, B.-J.; Grillo, I.; Filippov, S. K.; Laschewsky, A.; Müller-Buschbaum, P.; Papadakis, C. M. "Schizophrenic" Micelles from Doubly Thermoresponsive Polysulfobetaine-*b*-Poly(*N*-isopropylmethacrylamide) Diblock Copolymers. *Macromolecules* **2017,** *50*, 3985-3999.
177. Sánchez, M. S.; Hanyková, L.; Ilavský, M.; Pradas, M. M. Thermal Transitions of Poly(*N*-isopropylmethacrylamide) in Aqueous Solutions. *Polymer* **2004,** *45*, 4087-4094.
178. Meier-Koll, A.; Pipich, V.; Busch, P.; Papadakis, C. M.; Müller-Buschbaum, P. Phase Separation in Semidilute Aqueous Poly(*N*-isopropylacrylamide) Solutions. *Langmuir* **2012,** *28*, 8791-8798.
179. Maeda, Y.; Higuchi, T.; Ikeda, I. Change in Hydration State during the Coil-Globule Transition of Aqueous Solutions of Poly(*N*-isopropylacrylamide) as Evidenced by FTIR Spectroscopy. *Langmuir* **2000,** *16*, 7503-7509.
180. Ramon, O.; Kesselman, E.; Berkovici, R.; Cohen, Y.; Paz, Y. Attenuated Total Reflectance/Fourier Transform Infrared Studies on the Phase-Separation Process of Aqueous Solutions of Poly(*N*-isopropylacrylamide). *J. Polym. Sci. Pol. Phys.* **2001,** *39*, 1665-1677.
181. Ahmed, Z.; Gooding, E. A.; Pimenov, K. V.; Wang, L. L.; Asher, S. A. UV Resonance Raman Determination of Molecular Mechanism of Poly(*N*-isopropylacrylamide) Volume Phase Transition. *J. Phys. Chem. B* **2009,** *113*, 4248-4256.
182. Sun, B. J.; Lin, Y. A.; Wu, P. Y. Structure Analysis of Poly(*N*-isopropylacrylamide) using Near-Infrared Spectroscopy and Generalized Two-Dimensional Correlation Infrared Spectroscopy. *Appl. Spectrosc.* **2007,** *61*, 765-771.
183. Chaikin, P. M.; Lubensky, T. C., *Field Theories, Critical Phenomena, and the Renormalization Group. In Principles of Condensed Matter Physics*. Cambridge University Press: Cambridge, 1995; Chapter 5.
184. Onuki, A., *Critical Phenomena and Scaling. In Phase Transition Dynamics*. Cambridge University Press: Cambridge, 2002; Chapter 2.
185. Maiorano, A.; Martín-Mayor, V.; Ruiz-Lorenzo, J. J.; Tarancón, A. Weak First-order Transition in the Three-dimensional Site-diluted Ising Antiferromagnet in a Magnetic Field. *Phys. Rev. B* **2007,** *76*, 064435.
186. Deshmukh, S. A.; Sankaranarayanan, S. K. R. S.; Suthar, K.; Mancini, D. C. Role of Solvation Dynamics and Local Ordering of Water in Inducing Conformational Transitions in Poly(*N*-isopropylacrylamide) Oligomers through the LCST. *J. Phys. Chem. B* **2012,** *116*, 2651-2663.
187. Hsu, H.-P.; Paul, W.; Binder, K. Scattering Function of Semiflexible Polymer Chains under Good Solvent Conditions. *J. Chem. Phys.* **2012,** *137*, 174902.

188. Patterson, J. P.; Kelley, E. G.; Murphy, R. P.; Moughton, A. O.; Robin, M. P.; Lu, A.; Colombani, O.; Chassenieux, C.; Cheung, D.; Sullivan, M. O.; Epps, T. H.; O'Reilly, R. K. Structural Characterization of Amphiphilic Homopolymer Micelles Using Light Scattering, SANS, and Cryo-TEM. *Macromolecules* **2013,** *46*, 6319-6325.

189. Wang, X.; Qiu, X.; Wu, C. Comparison of the Coil-to-Globule and the Globule-to-Coil Transitions of a Single Poly(*N*-isopropylacrylamide) Homopolymer Chain in Water. *Macromolecules* **1998,** *31*, 2972-2976.

190. Gaetani, L. Co-nonsolvency Effect in Novel Thermoresponsive Homo- and Block Copolymers. Bachelor's thesis. Technical University of Munich 2020.

191. Kyriakos, K.; Philipp, M.; Adelsberger, J.; Jaksch, S.; Berezkin, A. V.; Lugo, D. M.; Richtering, W.; Grillo, I.; Miasnikova, A.; Laschewsky, A.; Müller-Buschbaum, P.; Papadakis, C. M. Cononsolvency of Water/Methanol Mixtures for PNIPAM and PS-b-PNIPAM: Pathway of Aggregate Formation Investigated Using Time-Resolved SANS. *Macromolecules* **2014,** *47*, 6867-6879.

192. Heskins, M.; Guillet, J. E. Solution Properties of Poly(*N*-isopropylacrylamide). *J. Macromol. Sci. A* **1968,** *2*, 1441-1455.

193. Kyriakos, K.; Philipp, M.; Lin, C.-H.; Dyakonova, M.; Vishnevetskaya, N.; Grillo, I.; Zaccone, A.; Miasnikova, A.; Laschewsky, A.; Müller-Buschbaum, P.; Papadakis, C. M. Quantifying the Interactions in the Aggregation of Thermoresponsive Polymers: The Effect of Cononsolvency. *Macromol. Rapid Commun.* **2016,** *37*, 420-425.

194. Schaeffel, D.; Kreyes, A.; Zhao, Y.; Landfester, K.; Butt, H.-J.; Crespy, D.; Koynov, K. Molecular Exchange Kinetics of Diblock Copolymer Micelles Monitored by Fluorescence Correlation Spectroscopy. *ACS Macro Lett.* **2014,** *3*, 428-432.

Scientific contributions

Publication related to this thesis

- C.-H. Ko, K.-L. Claude, B.-J. Niebuur, F. A. Jung, J.-J. Kang, D. Schanzenbach, H. Frielinghaus, L. C. Barnsley, B. Wu, V. Pipich, A. Schulte, P. Müller-Buschbaum, A. Laschewsky, C. M. Papadakis, Temperature-dependent Phase Behavior of the Thermoresponsive Polymer Poly(*N*-isopropylmethacrylamide) in Aqueous Solution, *Macromolecules* **2020**, *53*, 6816–6827.
- C.-H. Ko, C. Henschel, G. P. Meledam, M. A. Schroer, P. Müller-Buschbaum, A. Laschewsky, C. M. Papadakis, Self-Assembled Micelles from Thermoresponsive Poly(methyl methacrylate)-*b*-poly(*N*-isopropylacrylamide) Diblock Copolymers in Aqueous Solution, *Macromolecules* **2021**, *54*, 384-397.
- C.-H. Ko, C. Henschel, G. P. Meledam, M. A. Schroer, R. Guo, L. Gaetani, P. Müller-Buschbaum, A. Laschewsky, C. M. Papadakis, Co-nonsolvency Effect in Solutions of Poly(methyl methacrylate)-*b*-poly(*N*-isopropylacrylamide) Diblock Copolymers in Water/Methanol Mixtures, *Macromolecules* **2021**, (March submitted).

Further publications

- C. Tsitsilianis, G. Serras, C.-H. Ko, F. Jung, C. M. Papadakis, M. Rikkou-Kalourkoti, C. S. Patrickios, R. Schweins, C. Chassenieux, Thermoresponsive Hydrogels Based on Telechelic Polyelectrolytes: From Dynamic to "Frozen" Networks, *Macromolecules* **2018**, *51*, 2169–2179.
- N. S. Vishnevetskaya, V. Hildebrand, N. M. Nizardo, C.-H. Ko, Z. Di, A. Radulescu, L. C. Barnsley, P. Müller-Buschbaum, A. Laschewsky, C. M. Papadakis, All-In-One "Schizophrenic" Self-Assembly of Orthogonally Tuned Thermoresponsive Diblock Copolymers, *Langmuir* **2019**, *35*, 6441–6452.
- F. A. Jung, P. A. Panteli, C.-H. Ko, J.-J. Kang, L. C. Barnsley, C. Tsitsilianis, C. S. Patrickios, C. M. Papadakis, Structural Properties of Micelles Formed by Telechelic Pentablock Quaterpolymers with pH-Responsive Midblocks and Thermoresponsive End Blocks in Aqueous Solution, *Macromolecules* **2019**, *52*, 9746–9758.
- B.-J. Niebuur, C.-H. Ko, X. Zhang, K.-L. Claude, L. Chiappisi, A. Schulte, C. M. Papadakis, Pressure Dependence of the Cononsolvency Effect in Aqueous Poly(*N*-isopropylacrylamide) Solutions: A SANS Study, *Macromolecules* **2020**, *53*, 3946–3955.
- J.-J. Kang, F. A. Jung, C.-H. Ko, K. Shehu, L. C. Barnsley, F. Kohler, H. Dietz, J. Zhao, S. Pispas, C. M. Papadakis, Thermoresponsive Molecular Brushes with Propylene Oxide/Ethylene Oxide Copolymer Side Chains in Aqueous Solution, *Macromolecules* **2020**, *53*, 4068–4081.

- M. M. S. Lencina, C.-H. Ko, F. A. Jung, R. Schweins, M. Rikkou-Kalourkoti, C. S. Patrickios, C. M. Papadakis, C. Tsitsilianis, Effect of pH on the Dynamics and Structure of Thermoresponsive Telechelic Polyelectrolyte Networks: Impact on Hydrogel Injectability. *ACS Appl. Polym. Mater.* **2021**, *3*, 819–829.
- J.-J. Kang, K. Shehu, C. Sachse, F. A. Jung, C.-H. Ko, L. C. Barnsley, R. Jordan, C. M. Papadakis, A Molecular Brush with Thermoresponsive Poly(2-ethyl-2-oxazoline) Side Chains: A Structural Investigation, *Colloid Polym. Sci.* **2021**, *299*,193–203.

Conference talks

- C.-H. Ko, J.-J. Kang, S. Xia
  Dynamic Investigation on Polymer Solutions by DLS and FCS
  Polymer Physics Summer School, Obertauern, Austria, 12 – 15 Jun 2018
- C.-H. Ko, K.-L. Claude, D. Schanzenbach, B.-J. Niebuur, F. Jung, J.-J. Kang, H. Frielinghaus, L. Barnsley, V. Pipich, B. Wu, A. Schulte, P. Müller-Buschbaum, A. Laschewsky, C. M. Papadakis
  The Structural, Thermal and Dynamic Behavior of the Thermoresponsive Polymer Poly(N-isopropylmethacrylamide)
  14th European Summer School on Scattering Methods Applied to Soft Condensed Matter, Bombannes, 19 – 26 Jun 2018
- C.-H. Ko, K.-L. Claude, D. Schanzenbach, B.-J. Niebuur, H. Frielinghaus, L. Barnsley, V. Pipich, A. Schulte, P. Müller-Buschbaum, A. Laschewsky, C. M. Papadakis
  The Structural and Dynamic Behavior of the Thermoresponsive Polymer Poly(N-isopropylmethacrylamide)
  DPG-Frühjahrstagung, Regensburg, 31 Mar – 5 Apr 2019
- C.-H. Ko, C. Henschel, L.C. Barnsley, J.-J. Kang, A. Laschewsky, P. Müller-Buschbaum, C. M. Papadakis
  Thermal Behavior and Cononsolvency of the Thermoresponsive Diblock Copolymers PMMA-b-PNIPAM and PMMA-b-PNIPMAM in Aqueous Solution
  4th internal biennial science meeting of the MLZ, Grainau, 24 – 27 Jun 2019
- C.-H. Ko, C. Henschel, G. P. Meledam, M. A. Schroer, A. Laschewsky, P. Müller-Buschbaum, C. M. Papadakis
  Self-Assembled Micelles from Thermoresponsive Poly(methyl methacrylate)-b-poly(N-isopropylacrylamide) Diblock Copolymers in Aqueous Solution
  EMBL Hamburg P12 Virtual User Meeting, 17 – 19 November 2020
- C.-H. Ko, K.-L. Claude, D. Schanzenbach, B.-J. Niebuur, F. A. Jung, J.-J. Kang, H. Frielinghaus, L. C. Barnsley, V. Pipich, B. Wu, A. Schulte, P. Müller-Buschbaum, A. Laschewsky, C. M. Papadakis

Temperature-Dependent Phase Behavior of Thermoresponsive Polymer Poly(N-isopropylmethacrylamide) in Aqueous Solution
MLZ Virtual User Meeting 2020, 08 – 09 December 2020

Conference poster presentations

- C.-H. Ko, M. A. Dyakonova, K. Raftopoulos, S. Gkermpoura, M. M. Soledad Lencina, M. Rikkou-Kalourkoti, C. S. Patrickios, C. Tsitsilianis, C. M. Papadakis
  Multiresponsive Hydrogels from Telechelic Polyelectrolytes
  Kolloid-Tagung "Multiresponsive systems", Garching, 9 – 11 Oct 2017
- C.-H. Ko, K.-L. Claude, D. Schanzenbach, B.-J. Niebuur, X. Zhang, D. Aravopoulou, A. Kyritsis, H. Frielinghaus, P. Müller-Buschbaum, A. Laschewsky, C. M. Papadakis
  The Structural, Thermal and Dynamic Behavior of the Thermoresponsive Polymer Poly(N-isopropylmethacrylamide)
  DPG-Frühjahrstagung, Berlin, 11 – 16 Mar 2018
- C.-H. Ko, K.-L. Claude, D. Schanzenbach, B.-J. Niebuur, F. Jung, J.-J. Kang, H. Frielinghaus, L. Barnsley, V. Pipich, B. Wu, A. Schulte, P. Müller-Buschbaum, A. Laschewsky, C. M. Papadakis
  The Structural, Thermal and Dynamic Behavior of the Thermoresponsive Polymer poly(N-isopropylmethacrylamide)
  32th European Colloid and Interface Society ECIS, Ljubljana, 2 – 9 Sep 2018
- C.-H. Ko, K.-L. Claude, D. Schanzenbach, B.-J. Niebuur, F. Jung, J.-J. Kang, H. Frielinghaus, L. Barnsley, V. Pipich, B. Wu, A. Schulte, P. Müller-Buschbaum, A. Laschewsky, C. M. Papadakis
  The Structural, Thermal and Dynamic behavior of the Thermoresponsive Polymer Poly(N-isopropylmethacrylamide)
  4th German SNI Conference, Garching, 17 – 19 Sep 2018
- C.-H. Ko, K.-L. Claude, D. Schanzenbach, B.-J. Niebuur, F. A. Jung, J.-J. Kang, H. Frielinghaus, L. C. Barnsley, V. Pipich, B. Wu, A. Schulte, P. Müller-Buschbaum, A. Laschewsky, C. M. Papadakis
  The Structural and Thermal Behavior of the Thermoresponsive Polymer Poly(N-isopropylmethacrylamide) in Aqueous Solution
  French-German Opportunities of Cooperation to Fact the European Revolution in Neutron Science, Garching, Germany, 14 – 16 May 2019
- C.-H. Ko, C. Henschel, L. Barnsley, J.-J. Kang, A. Laschewsky, P. Müller-Buschbaum, C. M. Papadakis
  Thermal Behavior and Cononsolvency of the Amphiphilic Diblock Copolymers PMMA-b-PNIPAM and PMMA-b-PNIPMAM in Aqueous Solution

European Polymer Congress (EPF 2019), Heraklion Crete, Greece, 9 – 14 Jun 2019

- C.-H. Ko, C. Henschel, G. P. Meledam, M. Schroer, A. Laschewsky, P. Müller-Buschbaum, C. M. Papadakis
  Thermal Behavior and Cononsolvency of the Amphiphilic Diblock Copolymer PMMA-b-PNIPAM in Aqueous Solution
  Kolloid-Tagung Complex Fluids/49th Conference of the German Colloid Society, Stuttgart, Germany, 23 – 25 Sep 2019
- C.-H. Ko, K.-L. Claude, D. Schanzenbach, B.-J. Niebuur, F. A. Jung, J.-J. Kang, H. Frielinghaus, L. C. Barnsley, V. Pipich, B. Wu, A. Schulte, P. Müller-Buschbaum, A. Laschewsky, C. M. Papadakis
  The Structural and Thermal Behavior of the Thermoresponsive Polymer Poly(N-isopropylmethacrylamide) in Aqueous Solution
  MLZ User Meeting 2019, München 10/11 Dec 2019
- C.-H. Ko, K.-L. Claude, D. Schanzenbach, B.-J. Niebuur, F. A. Jung, J.-J. Kang, H. Frielinghaus, L. C. Barnsley, V. Pipich, B. Wu, A. Schulte, P. Müller-Buschbaum, A. Laschewsky, C. M. Papadakis
  Temperature-Dependent Phase Behavior of Thermoresponsive Polymer Poly(N-isopropylmethacrylamide) in Aqueous Solution
  MLZ User Meeting 2020, 08 – 09 December 2020
- C.-H. Ko, C. Henschel, G. P. Meledam, M. A. Schroer, R. Guo, L. Gaetani, P. Müller-Buschbaum, A. Laschewsky, C. M. Papadakis
  Thermal Behavior and Co-nonsolvency Effect of Poly(methyl methacrylate)-b-poly(N-isopropylacrylamide) Thermoresponsive Diblock Copolymers in Aqueous Solution and Water/Methanol Mixtures
  Virtual Conference on osmolyte and cosolvent effects, 25 – 26 February 2021

Acknowledgments

I would like to thank all the people that provide me help and support in various forms. Without them, it would be impossible to successfully complete this work.

Firstly, I would like to express my genuine gratitude to my supervisor Prof. Dr. Christine M. Papadakis for offering me this valuable opportunity to undertake my PhD study in her group and to work on such an interesting topic. I am grateful for her professional guidance, deep knowledge on polymer physics, continuous support, great patience, and enormous help throughout this time that make me grow as a better scientist and a better person.

I would like to thank Prof. Dr. André Laschewsky (University of Potsdam, Fraunhofer IAP) for the great collaboration on this project. His deep knowledge from the chemist's perspective is always useful and informative for me. Through the scientific discussions with him, my understanding of polymer chemistry is vastly enriched.

I would like to thank Dr. Dirk Schanzenbach and Cristiane Henschel (University of Potsdam) for their efforts on synthesizing all the high-quality polymer materials for the collaborative project. Special thanks go to Cristiane Henschel for her invaluable help in chemical aspects. Her enthusiasm and the fruitful discussions with her regarding the project always give me a lot of inspiration.

I am also grateful to Prof. Dr. Peter Müller-Buschbaum (Chair of Functional Materials). The suggestions and comments within the framework of our collaborative project are very helpful. I would also like to thank Christina Geiger for exchanging idea and sharing insights on our collaborative project.

Special thanks go to Prof. Dr. Alfons Schulte (University of Central Florida) for offering the chance to perform Raman experiments in Orlando. I truly appreciate for his great support, helpful discussions regarding data analysis, and crucial comments on the results.

Furthermore, I am thankful to all the beamline scientists: Dr. Henrich Frielinghaus and Dr. Lester C. Barnsley from the KWS-1 SANS instrument (MLZ, Garching); Dr. Vitaliy Pipich and Dr. Baohu Wu from the KWS-3 VSANS instrument (MLZ, Garching); Dr. Martin A. Schroer, Dr. Dmitry Molodenskiy and Dr. Stefano Da Vela from P12 SAXS instrument (EMBL, Hamburg). Without their tremendous help and guidance for the measurements, it would be impossible to complete the present work.

I thank all the students that I collaborated with, either during their Master and Bachelor theses or during their work in the group. I truly appreciate Patrick Wastian, Luka Gaetani, Shu-Hsien Huang and William Berthou for their efforts. Their works contribute both directly and indirectly to the present thesis. It was a great pleasure to work with you all.

I would like to especially thank my former and current colleagues from the Soft Matter Physics Group: Dr. Konstantinos N. Raftopoulos, Dr. Anatoly Berezkin, Dr. Margarita A. Dyakonova, Dr. Natalya S. Vishnevetskaya, Dr. Xiaohan Zhang, Kora-Lee Claude, Dr. Bart-Jan Niebuur, Dr. Florian A. Jung, Jia-Jhen Kang, Kaltrina Shehu, Shu-Hsien Huang, Dr. Geethu P. Meledam, Yanan Li, Bahar Yazdanshenas. Thank you all for the kindly help, support, and encourage in all aspects during the journey of my PhD. It was a fantastic time as colleagues with all of you.

In addition, I would like to express my gratitude to all the members of the Chair of Functional Materials for the positive and pleasant working atmosphere. It was a great time to be at the chair with all of you during all these years. Special thanks go to Carola Kappauf and Marion Waletzki, who were always there for us and provided the help with bureaucratic and administrative works. I am also thankful to Reinhold Funer for his support with building and optimizing the sample stage for the in-house experimental setup.

Moreover, I would like to thank Deutsche Forschungsgemeinschaft (DFG) for the financial support of this project (Pa 771/20-1, MU1487/29-1, LA 611/16-1).

Finally, I am deeply grateful to my lovely family for their love and constant support.